Politecnico di Milano

Department of Energy
Doctoral Programme in Energy and Nuclear Science and Technology (STEN)

Start-up and shut-down of PEMFC in real conditions: local experimental investigation and development of a new accelerated stress test protocol

Doctoral Dissertation of:
Andrea Bisello

Supervisor:
Dott. Andrea Baricci

Tutor:
Prof. Andrea Casalegno

The Chair of the Doctoral Program:
Prof. Vincenzo Dossena

Year 2019/2020 - Cycle XXXII

Start-up and shut-down of PEMFC in real conditions: local experimental investigation and development of a new accelerated stress test protocol

Andrea Bisello

May 2020

Contents

List of Figures

List of Tables

Abstract

An experimental investigation of Start-up and shut-down operation in polymer electrolyte membrane (PEM) fuel cells is presented. An array of reference Hydrogen Electrodes is implemented both at the anode and at the cathode, on a segmented-cell hardware to collect local potentials and currents during Start-up/shut-down. A two dimensional transient model of the operation is also developed, to investigate the impact of the operating conditions and materials properties.

The key role of the oxygen at the anode side has emerged. Moreover, the temperature and hydrogen flow-rate impact on mitigation of degradation during start-up and shut-down was quantified.

Local degradations resulting from repeated start-ups and shut-downs was evaluated with and without mitigation strategies. A good correlation between Support DoE Accelerated Stress Test (AST) and un-mitigated protocol was found: one cycle of Start-up/Shut-down is well described by 10 cycles of Support AST, while AST accelerates the process of a 10.3 factor in time.

Instead, under mitigated protocol, a strong heterogeneous degradation was observed at cathode inlet zone (i.e. anode outlet), compatible with platinum dissolution mechanism (i.e -37% ECSA loss and -15 mV voltage loss). A new differential hardware, called Zero-Gradient cell, designed to study materials behaviour in a reliable and representative way was then introduced. A new AST protocol (named Start-up AST) was proposed, to correlate the degradation observed in Zero-Gradient cell to start-up/shut-down operation in segmented-cell.

This study combines large amount of experimental electrochemical data clarifying the dominant effect of platinum dissolution and diffusion/precipitation within the polymer electrolyte, under wide voltage cycling at low temperature, like in mitigated Start-up operation.

Keywords: Polymer Electrolyte Fuel Cells, Start-up/shut-down, Modeling, Reference Hydrogen electrode, Accelerated Stress Test

Introduction

For the automotive industry, hydrogen polymer electrolyte membrane fuel cells (PEMFC) are among the most promising sustainable technologies for replacing fossil fuel based systems. While the first passenger vehicles are already entering the market, the durability issues must be overcome in order to reach a competitive commercialization: lifetime and degradation targets (set by the U.S. Department of Energy at 5000 h with a 10% loss in performance for the 2020) must be met under conditions and operations typical for automotive driving, which include dynamic operation, dry air and hydrogen and harsh conditions in particular start/stop. With the goal of lowering the cost of PEM systems, highly dispersed and carbon supported catalysts have been developed. One of their drawbacks is the loss of stability induced by carbon support corrosion and catalyst dissolution.

So far is known that carbon corrosion in the electrodes of MEAs (membrane-electrode assembly) is the major cause for voltage degradation during start(stop) cycles, when a H_2/air front flow in the anode opposite to an air(hydrogen) filled cathode leads to reverse-current mechanism[72] which increases cathode electrode potential as high as 1.5 V vs RHE. It entails accelerated carbon corrosion and catalyst degradation in the local regions exposed to air in the anode compartment the longest: degradations will be more severe near the hydrogen outlet (inlet) in the case of startup (shutdown)[26, 47]. A description of the reverse-current mechanism underlying start/stop operation is depicted in Figure 1. Despite this corrosion process is now relatively characterized from an experimental point of view, the influence of experimental parameters (stressors) such as gas inlet flow rate, gas humidification, gas concentration and anode and cathode catalyst loading are not yet fully understood or accepted in the scientific community (see Ref. [57, 58] for operating parameters influence and Ref. [40] for materials degradation impact).

Estimating lifetime of components requires considerable effort, time and resources that hinder the rate of R& D activities. Nowadays, materials benchmark is thus based on Accelerated Stress Tests (AST), focused on specific aging mechanisms that are promoted on their physics. For the

catalyst layer, two different types of ASTs are normally used. First of all, a carbon support AST is available: carbon oxidation, thermodynamically allowable but kinetically inhibited in case of standard cell functioning, is promoted exploiting voltages as high as those reached during start/stop (>1 V). On the other hand, the electrocatalyst AST strengthens the platinum dissolution, redeposition and coagulation by the way of voltage cycling in FC normal range (<1 V)[86]. However, D.o.E. ASTs are performed at very specific parameters (e.g. 80 °C, 100% RH), not representative of real-world operations, which are instead characterized by a high heterogeneity of conditions that make the degradation heterogeneous too. Its quantification, in dependence on the local factors that subsist in a stack, is scarcely established at present. In addition, ASTs don't reproduce the typical parameters of the today-adopted operative modes, like the mitigation procedures for start-up/shut-down (based on low temperatures[57, 58], external loads[9], and oxygen consumption).

In the above-mentioned scenario, the research project deals with PEMFC durability, focusing on degradation occurring during start-up/shut-down operation with a locally resolved investigation. The understanding about the main mechanisms originating the uneven distribution of local potentials and currents will have to be improved, by focusing on the major stressors (e.g. temperature, relative humidity, ...), permitting then: (I) to quantify the impact of the start-up/shut-down on performance degradation; (II) to develop a specific AST able to reproduce start-up operation; (III) and to validate its relevance by correlation to real world ageing. Modeling simulation will support either interpretation and validation activity in order to predict the impact on heterogeneity of ageing under stressing operating conditions and to relate causes to performance losses. The research project has been carried-out within EU Project ID-FAST (H2020 framework) whose purpose is the investigations of degradation mechanisms and the definition of protocols for PEM Fuel cells Accelerated Stress Testing.

The dissertation is organized in the following chapters:

- Chapter 1 - State of Art

  The working principles and the structure of polymer electrolyte membranes fuel cells are explained. Particular attention has been paid to explain the main current challenges for the technology and durability issues. The framework and the scope of the work are here clarified.

- Chapter 2 - Experimental methodology

  Information about both the experimental configuration and the procedures of testing are provided. The three different used hardware are described: the reference hydrogen electrodes, the segmented-cell,and

the newly realized Zero-Gradient Cell. Degradation protocols and characterization techniques are presented.

- Chapter 3 - Experimental and modelling investigation of start-up and shut-down transients

  The physics of the mechanisms of reverse-current during start-up and shutdown are analysed. The goal of the task is to evaluate the impact of specific stressors, on start-up and shut-down operation, such as the temperature, the flow rate, the reactants concentration. Through a dedicated experimental campaign performed with reference hydrogen electrodes different start-up (shutdown) operating conditions are evaluated. Thus, modeling investigation is carried out to distinguish the current contributions to the reverse-current mechanism underlying start-up (shutdown) operation.

- Chapter 4 - Start-up and shut-down cycling without mitigation strategies

  A comparison between performance degradation under repetitive start-up and shut-down operation and ASTs are preliminary performed using SoA protocols. The degradation mechanisms under Start-up/shut-down operation in un-mitigated cycles (at 80°C – small flow rate) are clarified and a clear quantitative correlation with DoE Support AST are found.

- Chapter 5 - Start-up and Shut-down cycling with mitigation strategies

  A specific protocol, developed in the framework of ID-FAST project (introducing mitigation strategies to mimic real automotive stack start-up/shut-down) is investigated and local performance losses are analyzed in segmented-cell. The most degraded zone of the MEA is defined, and detailed local characterization is conducted.

- Chapter 6 - Experimental characterization of AST in Zero-gradient cell

  As a basis for the development of the new AST protocols for start-up/shut-down impact evaluation, SoA ASTs are evaluated. All material testing results have been realized adopting new single cell design (named Zero-gradient cell hardware), designed to characterize material properties under uniform operating conditions, without any effect of the flow-field design. The effect of temperature on performance degradation is elucidated and specific performance indicator are found to distinguish the effects of platinum dissolution and carbon support oxidation on performance loss.

- Chapter 7 - Design of an accelerated stress test for start-up operation

First of all, a new Start-up AST (SU-AST) has been developed and transfer functions correlating degradation to real world operation at full-scale cell is determined. The degradation mechanisms, underlying Start-up/Shut-down operation under mitigation strategies, are clarified, by in-situ and ex-situ analyses. The impact of platinum dissolution mechanisms is quantified and an accelerated protocol is then proposed.

Chapter 1

State of Art

1.1 Introduction

This Chapter aims to introduce the structure and the working principles of a polymer electrolyte membranes fuel cell.
Then, being ones of the main current challenges for the technology, durability issues are described. First, an overview of the most relevant degradation mechanisms is provided: these information are useful to understand how aging mechanisms are involved during real fuel cells operations, like start-up and shut-down operations.
Accelerated Stress Tests are therefore described, in particular focusing on their limits: overcoming these drawbacks is the core objective of the Horizon 2020 European project ID-FAST, in the frame of which this work is developed.
Finally, the targets of the thesis work are clarified, reporting both the adopted research tools and a comprehensive literature review of how the problem of start-up/shut-down was addressed.

1.2 Fundamentals of fuel cells

The proton exchange membrane fuel cell (PEMFC) are electrochemical devices in which hydrogen and oxygen separately react to produce an electric current and water as the only byproduct. Hydrogen is oxidezed at the anode (Hydrogen Oxidation Reaction HOR, see (1.1)), while the oxygen is reduced at the cathode (Oxygen Reduction Reaction, see ORR (1.2)). Depending on the operating temperature, two type of PEMFCs can be distinghuished: Low-Temperature FCs that operates below 100 °C, and High-Temperature FCs that operates in a range of 110-180 °C. These systems run at low temperatures, and this is an advantage because it means a rapid start-up process

and rapid load changes, very useful for automotive applications, but also a disadvantage because it leads to slow reaction rates, which require a precious catalyst and sophisticated electrodes.

$$H_2 \longrightarrow 2H^+ + 2e^- \qquad E^0 = 0\,V \tag{1.1}$$

$$\frac{1}{2}O_2 + 2H^+ + 2e^- \longrightarrow H_2O \qquad E^0 = 1.229\,V \tag{1.2}$$

1.2.1 PEMFC structure

The typical testing structure of a PEM fuel cell is represented in Figure 1.1.

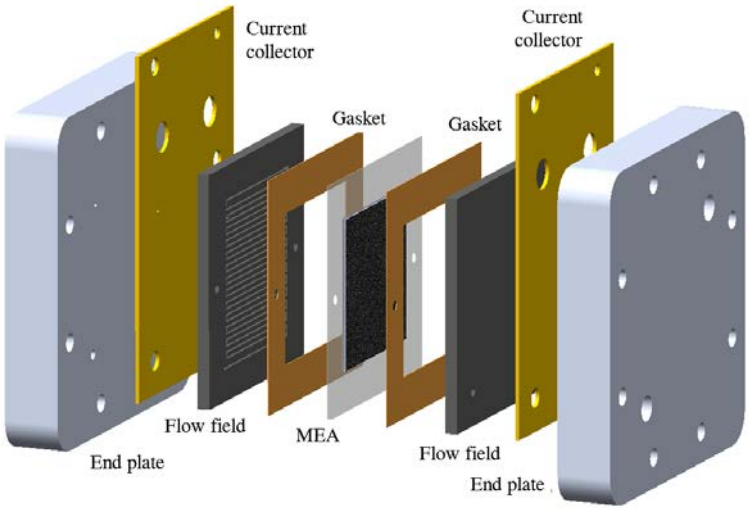

Figure 1.1 – Structure of a PEM fuel cell

Protons are transported from the anode to the cathode through the electrolyte membrane and the electrons are carried though an external circuit load. From the structural point of view the central component of a PEMFC is the ionically conductive polymer electrolyte membrane, which has two essential functionalities. The membrane must ensure a spatial separation of the electrodes, by preventing direct recombination of the reactants and thus gas permeability has to be as low as possible. Moreover, the electrons must move in the external circuit and therefore the membrane must possess both high proton conductivity and electrical insulation. The standard electrolyte material used is a fluorinated material, first produced by DuPont in the 1960s, which is commonly called Nafion®. A high hydration of the membrane is essential to ensure an optimal ionic transport, and it's achieved by careful

control of both the water production at the cathode and the feeding of humidified reactants.

The single-cell structure can be here summarized: The anodic and cathodic reactions described in Equations (1.1) and (1.2) occur in the catalyst layers (CLs), which are attached at both sides of the membrane. The catalyst layers consist of platinum nanoparticles dispersed on a carbon support impreganted with electrolyte solution that ensures the connection between the proton conducting phase. The electrochemical reactions occurs at the triple-phase boundary between the proton conducting phase, the electrically conducting phase and the gas phase. The electron transport is ensured by highly conductive carbon support while gas access is provided by the porous structure of the CL. The assembly of catalyst layers and electrolyte membrane is called as catalyst coated membrane (CCM).

To achieve a homogeneous supply of reactant gases to the catalyst layer, a gas diffusion layer (GDL) is attached to the CLs. Gas diffusion layers are a porous material composed of a dense array of carbon fibers, which also provides an electrically conductive pathway for current collection between the bipolar plate with channel-land structure and the electrode. To facilitate the removal of product water from the cell, the gas diffusion layers are typically impregnated with PTFE solution that provides hydrophobicity. Additionally, a micro porous layer (MPL) can be inserted between GDL and the catalyst layer. The functional unit of membrane, catalyst layer, and gas diffusion layer is usually referred to as Membrane Electrode Assembly (MEA). Another key feature of the GDL is to provide enough mechanical strength to hold membrane electrode assembly from extension caused by water absorbance.

To provide mechanical stability and to supply the reactant gases, flow field plates are attached at both sides of the MEA. The flow fields distribute the gases across the entire active area of the fuel cell; for laboratory applications they are made of graphite, which ensures excelent electron transport and chemical stability. The layout of the channel and land structure (rib) significantly affects gas distribution, water management and the electric contact to the MEA and thus various flow field designs have been developed in order to improve fuel cell performance.

The single cell setups used in laboratories also include a couple of current collectors, that provide connections to the electrical load, and end plates, that assure the proper compression of the multi-layer and the control of the cell temperature.

1.2.2 Current challenges in PEMFC

Automotive PEMFCs have finally reached an high technology readiness level, so much so several major companies are leasing and selling fuel cell electric vehicles (FCEV), like Toyota (Mirai, 2015) , Hyundai (Tucson, 2014 and Nexo, 2018) and Honda (Clarity, 2016). FCEVs offer many advantages over Battery electric vehicle (BEV), like fast refueling time (i.i. 3-5 min), long range with up to 600 km thanks to high-pressure hydrogen tank and longevity. However BEVs, already now, sales exceed 1 million annually, whereas FCEVs are just starting to be sold in small quantities and in limited areas, in part because the hydrogen infrastructure is behind BEV recharging stations, but also due to higher capital and operating costs. The high cost is primarily due to the use of platinum catalysts and current low production volume.

Therefore, in the light of the above, the main challenges of the fuel cell research can be here summarized:

- Cost reduction. The 2020 U.S. Department of Energy (DOE) targets for fuel cell systems are a cost of $40/kW and with 12.5 gramms of Pt, based on 500,000 fuel cell system produced per year. While a cost of $30/kW is considered necessary to be competitive with alternative powertrains, including future advanced gasoline engines [86]. The current fuel cell electric vehicles cost is estimated to be $53/kW, when the production volume reach 500,000 units/year (for a 80kW system). As said above, the larger portion of the cost is due to the precious metal group (PMG) catalyst, usually platinum, and it can also be attributed to the material processing costs, which lead Pt catalyst to be more expensive than untreated Pt metal. For this reason a big research effort is oriented to the development of low Pt-loaded fuel cells. In particular, ultra-low Pt loading or non-precious metal catalysts, coupled with high mass production, could achieve cost parity with concurrent technologies.

- Durability increase. The durability under a wide range of operating conditions is another technical barrier for the acceptance of fuel cells. The target for durability is set by the DOE to 5000 hours of functioning with a loss of performance lower than 10%. Recent tests show the actual useful life of a system being at best around 80% of the target [86]. The dynamic nature of the operating condition that a FCEV have to face is by itself detrimental for the longevity of the system, and the membrane and the catalyst layer are the most stressed components. The most studied degradation phenomena taking place in the catalyst layer are Pt instabilities and carbon support deterioration, that are thoroughly described in the following section.

Reduce the PGM-loading and increase the power density are the main challenges for that technology. Most of the research and development effort are addressed to the cathodic electrode, where the oxygen reduction reaction is sluggish compared to the hydrogen oxidation reaction at the anode side, limiting the performance and increasing the needed catalyst loading. Actually, ORR catalyst with competitive performance exist, such as they meet the required mass activity (0.44 mA/cm^{-2} at 0.9 V), however the power density goal is far to be reach (1000 mW/cm^{-2} at 150kPa), in real operating conditions. Limiting mass transport phenomena are the key issues, at high power density, and the underlying mechanisms are still to be fully clarified, so much effort must be applied on this topic.

1.2.3 Cost Analysis

Currently, a fuel cell electric vehicle, with a limited production of 3000 units, reach a cost of 45000 €for vehicle[8], equal to 500 $/kW$ (i.e. for a system of 90 kW_{gros}). Under this assumption, the system cost is break down in between components as: 25-30% for the hydrogen tank, 20-25% for the Balance of Plant (which includes the humidifier, the valves and the compressor), 5-10% the bipolar-plate, and 35-45% the MEA. The main cost is then principally attributable to the stack (i.e. 40-55% of total cost). Considering also, the *Technology Readiness Level* (TRL) of auxiliary components and hydrogen tank, the MEA development is the leading task for cost reduction.

As defined in section 1.2.1 the MEA can be described as an assembly of three main components: the polymer electrolyte membrane, the catalyst layers and the gas diffusion layers. Regards the membrane, the most common used material is a polymeric plastic (i.e. a sulfonated tetrafluoroethylene-based fluoropolymer–copolymer with conductive properties) commercially known under the common name Nafion. The cost of Perfluorosulfonic acid (PFSA) polymer, that can be obtained in a single step from the co-polymerization of *Tetrafluoroethylene* (TFE) and a co-monomer PSEPVE, depend for 62% from the cost of precursors[8]. Due to the complexity and risk for the production and management of such a chemical materials, the production of polymer electrolyte, is limited to large producers[91].

Gas diffusion layers are a porous material composed of a dense array of carbon fibers. The production of GDL is the easiest and cheapest between MEA components, and its economic weight is limited.

The catalyst layer is the most expensive component of the MEA, due to the cost of catalyst ink production (i.e. 2500 $/kg_{ink}$). The total cost of an MEA is 141.7 $/m^2$ or 6.6 $/unit$ (considering an area of 466 cm^2 for each MEA). Assuming an ink consumption of 6.67 mg_{ink}/cm^2, with catalyst content of 15

g_{Pt}/kg_{ink}, the total catalyst loading is around 0.4 mg/cm^2[8]. The reported analysis is valid for a stack cost of 2500 and an annual production of 300000 units. Due to the high price and price volatility of platinum, changes in the platinum loading have the greatest effect on cost[41].

1.2.4 Performance Analysis

In this section, the targets for fuel cell electric vehicle are summarized. data are reported from DoE Technical document[86]. In Figure 1.3, technical targets for fuel cell system for transportation are reported. The costs of hydrogen tank, power electronics and electric motor are excluded. Considering fuel cell durability, two main targets are here reported: the durability in automotive drive cycle (i.e. 5000 hour in real operation) with a maximum performance loss of 10% at nominal power, and a maximum of performance loss after 5000 start-up/shut-down cycles (i.e. 5% voltage loss at high current density equal to 1.2 A/cm^2).

Table 3.4.4. Technical Targets: 80-kW_e (net) Transportation Fuel Cell Stacks Operating on Direct Hydrogen[a,b]

Characteristic	Units	2015 Status	2020 Targets	Ultimate Targets
Stack power density[c]	W / L	3,000[d]	2,250	2,500
Stack specific power	W / kg	2,000[e]	2,000	2,000
Performance @ 0.8 V[f]	mA / cm^2	–	300	300
Cost[g]	$ / kW_{net}	26[h]	20	15
Durability in automotive drive cycle[i]	hours	3,900[j]	5,000	8,000
Start-up/shutdown durability[k]	cycles	–	5,000	5,000
$Q/\Delta T_i$[l]	kW/°C	1.9[m]	1.45	1.45
Robustness (cold operation)[n]	see footnote	–	0.7	0.7
Robustness (hot operation)[o]	see footnote	–	0.7	0.7
Robustness (cold transient)[p]	see footnote	–	0.7	0.7

Figure 1.2 – DoE Technical target for fuel cell system[86].

The nominal performance of a generic stack, is properly defined by $Q/\Delta T_i$ parameter (see eq. 1.3). It define the maximum producible power, for an automotive stack, that works at a specific cooling temperature.

$$\frac{Q}{\Delta T_i} = \frac{P_{stack} \cdot \left(\frac{E_{th,LHV} - \Delta V_{P_{rated}}}{\Delta V_{P_{rated}}}\right)}{T_{stack} - T_{amb}} \tag{1.3}$$

Assuming a stack power of 90 kW (equal to a net power of 80 kW), $E_{th,LHV}$ of 1.25 V and ambient temperature of 40 °C, the constraint $Q/\Delta T_i$ <=

$1.45kW/C$, define a clear relationship between the maximum operating temperature of the stack (or MEA) and the minimum nominal voltage.

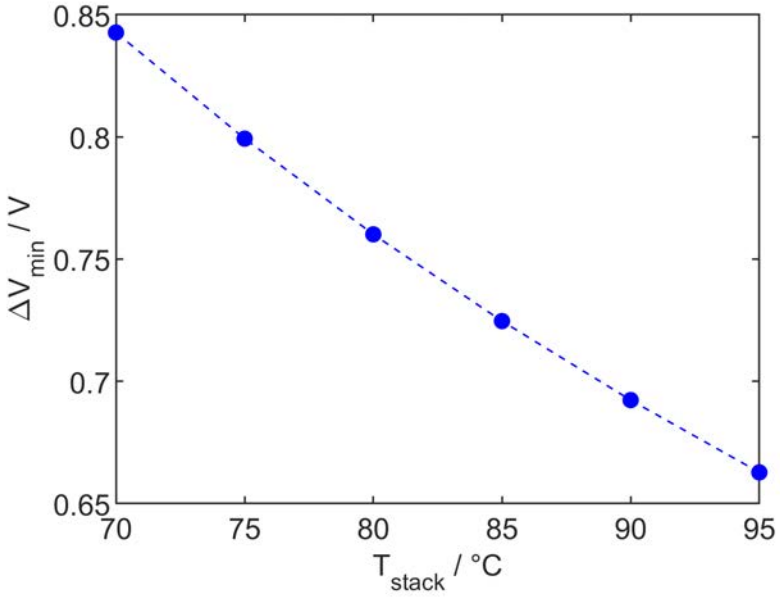

Figure 1.3 – Minimum target voltage at fixed stack temperature

Assuming a specific target of 1 W/cm^2, and a maximum temperature of 90 °C, the performance constraint $Q/\Delta T_i <= 1.45kW/C$ define the nominal current density (1.45 A/cm^2) and voltage (0.69 V) for stack/single MEA.

1.3 Fuel cell durability

The performance of a PEM fuel cell is limited by many internal and external factors, such as flow-field design and assembly, degradation of materials, operating conditions, and impurities or contaminats. In general performance degradation is unavoidable, but the aim is to minimize the degradation rate through the understanding of degradation mechanisms and failure modes.

In order to clarify the evolution of performance decay of PEMFC discussed in the next in this thesis, several terms must be here clarified:

- Durability: is the capability of a fuel cell to mantain a performance over time. Durability does not lead to a failure but to a decrease in performance that could be reversible or not reversible. This parameter is mainly related to ageing of materials;

- Stability: is the capability to recover performance loss (i.e. power loss) during continuos or cyclical operations. Stability decay is in general link to reversible material changes and is managed by operating conditions (e.g. water management, refresh due to stop of operation);

- Reliability: is the capability to perform a specific operation for a certai period of time. This term include failure modes that lead to discontinuos performance decay at an unacceptable level.

Usualy performance decay rate during driving cycle, is the sum of both stability and durability decay and specific targets are fixed for the automotive application. The U.S. Department of Energy set the durability target at 5000 h of operation under real automotive conditions (i.e. dynamic driving cycle operation with changes of current density, gas feeding relative humidity, and fuel cell temperature and pressure) with a maximum performance loss of 10% at nominal power (i.e. 10% voltage loss at maximum current density), that correspond to around 10 $\mu V/h$. In addition, off-load transient operation occurs such as Start-up/Shut-down and cold start, that accelerate the degradation mechanisms. For this specific off-load events, proper durability targets are fixed, in harsh operating conditions (i.e. without system mitigation strategies), design to evaluate materials stress.

Among the fuel cell components, the main durability issue regards the cathode catalyst layer. It is indeed subjected to several degradation mechanisms that are here described drawing a distinction based on the involved element: deterioration processes concern both electrocatalyst and carbon support. Both the mechanisms are strongly accelerated due to operating conditions cycling (i.e. voltage, temperature, relative humidity cycling).

1.3.1 Catalyst layer degradation

In the past years the main efforts were concentrated to understand the degradation mechanisms underlying the voltage cycling operations of platinum catalyst carbon supported electrode (Pt/C electrode). The performance of this materials depends primarily to the available catalytic active surface (ECSA m^2_{Pt}/g_{Pt}) and the catalyst loading (mg_{Pt}/cm^2_{geo}).

The CCL degradation is mainly due to platinum dissolution/deposition mechanisms, that occurs during voltage cycling and are stressed at high temperature and relative humidity (i.e. high dissolution kinetics).

Platinum instabilities can be divided in the following main parallel mechanisms. All of them result in reduction of electrochemically active platinum surface area (ECSA) and reduce performances because of the boosted kinetic

losses. All of them result from the main process of Platinum dissolution, considered of larger impact in typical PEMFC operations.

- At micro-scale, e.g. Ostwald ripening-based coarsening.
  Small particles of Pt dissolve, diffuse through the ionomer at nanometer scale and finally deposit on larger particles, that are energetically favored. The result is a change in particles size distribution - the average diameter increases - and a reduction of available Pt surface[36, 94]. Such mechanism prevails during voltage cycling operations, in particular at high potentials. Many parameters play a determinant role in such a mechanisms: voltage cycling (accelerate nanoparticle agglomeration), temperature and humidity (increases the kinetics of Pt dissolution and the Pt^{2+} ion mobility in the electrolyte)[23, 67, 74, 81, 101].

- At macro-scale, the diffusion/migration of Pt^{2+} ions play a key role. Pt^{2+} ions, produced by Pt dissolution in the catalyst layer, migrate into the polymer electrolyte membrane, and successively are reduced by hydrogen permeated in the membrane (i.e. H_2 crossover) from anode electrode, to form large Pt agglomerate at membrane/CCL interface (Pt-band formation). This Pt agglomerate are no more in electric contact with the electrode, and doesn't result active[38, 46, 81].

1.3.2 Carbon corrosion

Catalyst support is made by carbon, that could be corroded following reaction (1.4):

$$C + 2H_2O \longrightarrow CO_2 + 4H^+ + 4e^- \; E^0 = 0.207\,V \tag{1.4}$$

The reaction develops in two steps: oxide species are formed on the carbon surface (1.5) and then they are further oxidized to carbon dioxide (1.6): this is the rate determining step.

$$C + H_2O \longrightarrow CO_{ad} + 2H^+ + 2e^- \tag{1.5}$$

$$CO_{ad} + H_2O \longrightarrow CO_2 + 2H^+ + 2e^- \tag{1.6}$$

Considering the typical operating potentials of a PEMFC (< 1 V), the reaction is thermodinamically allowable. Nevertheless, the low temperatures slow down the kinetics so much to make this process almost negligible. However, some events like fuel starvation and start up/shut down processes - later described in Section 3.4 - can result in high cathode potentials, larger than 1 V, that enhance the reaction significantly.

In presence of Pt, according to Maas et al. [51], the reaction is largely catalyzed, as expressed by the following reaction pathway:

$$Pt + H_2O \longrightarrow Pt - OH_{ad} + H^+ + e^- \tag{1.7}$$

$$Pt - OH_{ad} + CO_{ad} \longrightarrow Pt + CO_2 + H^+ + e^- \tag{1.8}$$

Since the corrosion of carbon is accelerated by the presence of platinum, the attachment of catalyst to support surface is weakened, making easier Pt dissolution. Support corrosion enhances sintering and agglomeration of particles; deterioration could finally cause Pt detachments, isolating some catalyst particles that do not participate in electrochemical reactions anymore. ECSA loss is therefore strengthen.
The cell morphology can be deeply modified: proton transport and, possibly, even the electronic transport to the triple-phase boundary could become more critical. Cathode carbon structure collapse strongly weakens both transport of oxygen and removal of product water. The disappearance of void volume in CL and the hydrophobicity loss of porous layers, make detrimental effects mainly visible at high current densities: indeed, the amount of consumed oxygen is directly proportional to the current itself.
Even though the most detrimental effects are consequence of high voltages, some researches highlighted that corrosion also occurs at lower potentials in presence of Pt, as shown in Figure 1.4. Three additional peaks have been identified: around 0.7 - 0.8 V, when reduction of platinum oxides formed at higher potentials leads to OH-like species formation that, as seen, promote corrosion. Secondly, increasing potential over 0.55 V, CO_2 is produced as consequence of the oxidation of carbon monoxide, previously formed as adsorbed species on the support surface. Finally, even at potentials lower than 0.2 V CO_2 is detected: in this case, chemical oxidation by hydrogen peroxide of carbon is conjectured.

1.3.3 Influence of operating conditions on catalyst layer degradation

Different stressors concur in promoting platinum and carbon degradation in the catalyst layer. The conditions that enhance these phenomena are very similar, as shown in Scheme 1.5, hence they are hard to disentangle. Both are indeed promoted by the high temperatures[49], because of boosted kinetics of reactions, by high relative humidity[1, 49, 88] and high voltages[90]. About this latter, the two processes have different sensitivities: potential cycling below 1 V emphasizes degradation of the metal[34, 101], mainly because

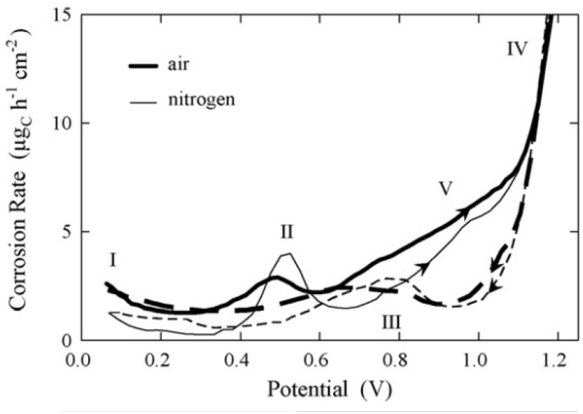

Figure 1.4 – Potentiodynamic corrosion measurements of CO_2 on Pt/C-electrodes in air (thick lines) and nitrogen (thin lines) [51].

of consequent oxidation/reduction of the electrode surface that promotes dissolution. At higher potentials instead, at which surface reduction hardly occurs, carbon corrosion is more encouraged (Figure 1.4).

1.4 Start-up and shut-down processes

Usually, shut-down in PEMFCs is realized by purging the anode compartment, filled with hydrogen, using air. At the opposite for start-up: hydrogen is introduced into the anode substituting air. During both these processes, the creation of the air/hydrogen front in the anode generates the so called reverse current decay mechanism, proposed for the first time in 2005 by Reiser et al. [72].

As shown in Figure 1.6, the half of the cell filled with fuel works normally with HOR and ORR: it has an active role. The other half, where anode is rich in air, is instead passive: ORR takes place at the anode and oxidation reactions like COR and OER occur at the cathode. The simultaneous generation and consumption of protons at the same electrode causes a reverse proton flow in the air/air and the hydrogen/air regions, leading to a circular current flow in the cell. To explain the mechanism, fuel-filled regions, that operate normally as a power supply, are considered to polarize the remaining part. Potentials distribution along direction of gas path is depicted in Figure 1.7. Due to the high electric conductivity of the electrode materials, the absolute metal potentials ϕ_s^+ and ϕ_s^- are assumed uniform. The cell voltage V_{cell} is consequence of reactions occurring in the normal fuel cell region: since the large difference in equilibrium potentials between oxygen and hydrogen, a

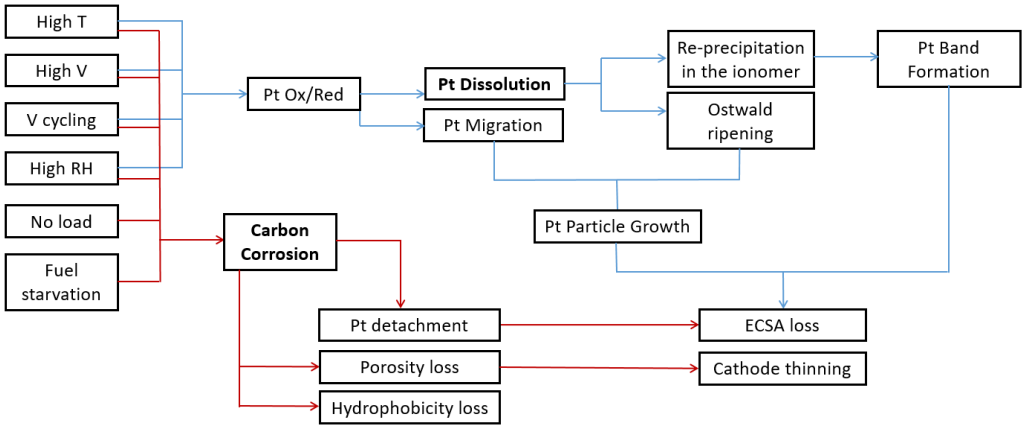

Figure 1.5 – Most influencing operating conditions on catalyst layer degradation (inspired by [66]).

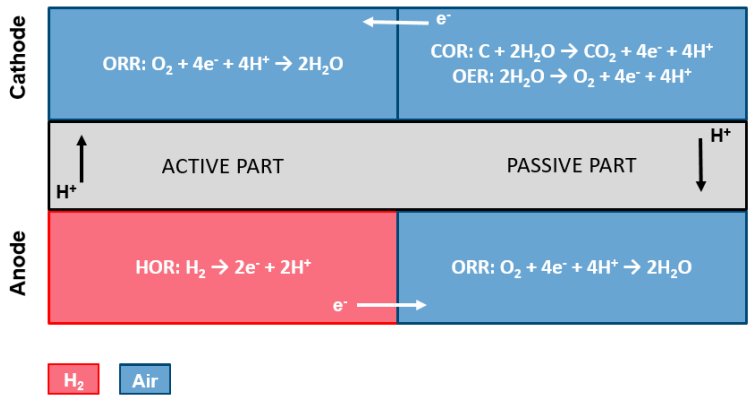

Figure 1.6 – Schematic of reverse-decay reactions and currents.

drop of the electrolyte potential in the air/air region is caused. Indeed, the increase of ϕ_s^- - ϕ_l, driven by the active part, moves ϕ_l down. As a result, ϕ_s^+ - ϕ_l increases to values that significantly exceed the oxygen equilibrium potential: this condition makes the carbon oxidation reaction (COR) and oxygen evolution reaction (OER) occur at cathode.
This description, that imagines the cell as divided in two halves and in steady-state conditions, is not thorough: during the effective start-up and shut-down the cell voltage, and thus both metal and electrolyte potentials, are not constant but progressively change during the transients. Their values should depend on the location of the boundary between the two parts, that evolves in time. Process therefore lasts as the two gases at the anode co-exist.

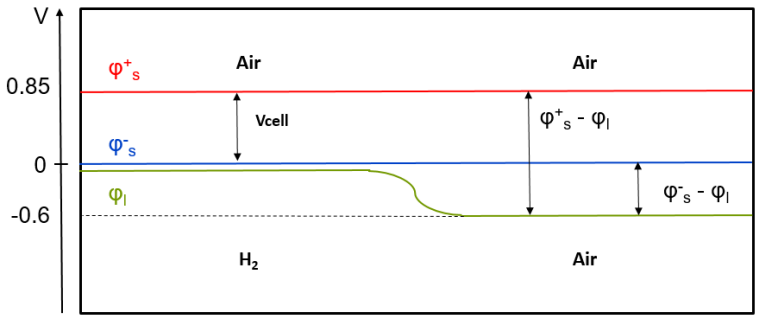

Figure 1.7 – Potential distribution along the anodic flow path during the reverse current decay mechanism. Values reported are suggested by [72].

In reality, other current sources play a role during start-up and shut-down processes, as explained by Gu et alt. [31]. Contributions come from double-layer capacitance and pseudo-capacitance. The former is the result of the accumulated ionic and electronic charges at the electrolyte and metal interfaces. The latter is instead the result of platinum oxidation state and its redox reactions, that can either provide or consume protons. In steady-state conditions, normally their contributions are neglected. However, in these transitory events they can participate in the balancing.

The combination of elevated potentials and rapid potential changes at the positive electrode leads both to a significant carbon corrosion and to platinum dissolution. Clear variations in structure morphology are reported in Figure 1.8. Mass transport resistance is boosted, number and dimension of pores are reduced, cathode electrode is made thinner. ECSA loss is induced at cathode, increasing kinetic ORR overpotentials; a summary of type of losses encountered by catalyst layer is in Table 1.1.

Table 1.1 – Major failure modes of catalyst layer in a PEMFC

Type of loss	Causes
Kinetic losses	Electrocatalyst dissolution/sintering/detachment
Mass transport and conductivity losses	Carbon support corrosion
Worsen water management	Decrease in hydrophobicity Structure collapse

The magnitude of the phenomenon is not uniform along the cell: active and passive sections depicted in Figure 1.6 change progressively their dimensions during the front passage, such that carbon corrosion impact more on

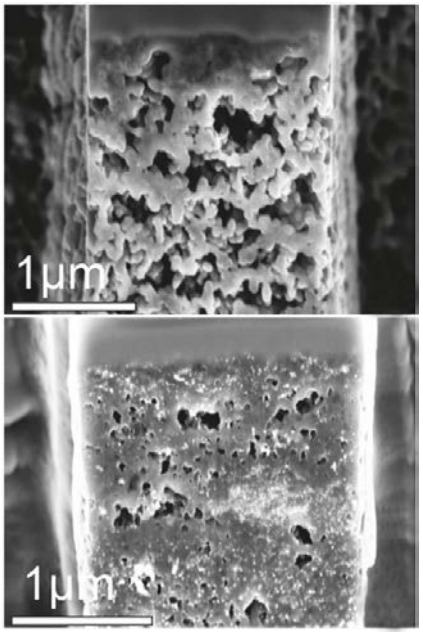

(a) CL porosity reduction [78]

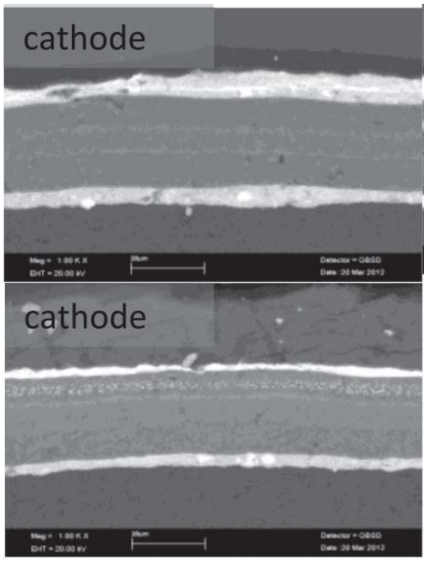

(b) Thinning of CL and Pt band formation in the membrane [47]

Figure 1.8 – (a) Pristine catalyst layer (top) and after start/stop procedure (bottom) (b) Difference between the least (top) and most (bottom) affected region of cathode catalyst layer after start-up degradation; less affected portion faces anode inlet, while most affected anode outlet.

the extremities of the cell. Most affected regions are either inlet or outlet, labelled with respect to anode flow direction, during shut-down and start-up respectively: these MEA portions are expected to be more damaged than the middle.

Large efforts have been spent in order to mitigate start-up and shut-down. First of all, operating on materials, researchers offered partial attenuation based on promotion or inhibition of specific reactions. The use of graphitized carbon supports has been proved to better resist to corrosion [31, 58], while alternative catalysts, typically alloy-based, are evaluated to reduce ORR activity at anode [27] and boost OER activity at cathode [4], in order to favor this oxidation reaction in place of support corrosion. This is anyway not enough: the choice of suitable operating conditions has revealed fundamental to decrease the start/stop degradation and use the state-of-art technology. The commonly conditions studied to be controlled are temperature, humidity and, most of all, purging flow [19, 39, 43, 50, 58]. Indeed, low temperature and humidity inhibit the kinetics of reactions and proton conductivity. High purging flows instead reduce the co-existence time of the two different anodic

gases: this is a well known mitigation way, reported in patents [96]. Patent review evidenced also system-based mitigation strategies, such as the application of dummy loads to reduce the driving force generated by the active side of the fuel cell and consequently the maximum potentials reached by the cathode [7, 87].
Even though these procedures have revealed effective in lab analysis, their implementation on real stacks may be not easy: practical feasibility should be verified. For a more complete collection of known attenuation mechanisms, refer to the review by Yu et al. [97].

In the past years, researchers largely focused as well on platinum dissolution and carbon corrosion mechanisms, but only a limited number investigated start-up and shut-down processes.
About the reverse current decay mechanism, the experimented direct imposition of high voltages - working with H_2/N_2 - and the use of a dual cell configuration [72, 84] have given some explanations, but it is necessary to work with real transients for a deeper understanding of the limiting and/or boosting factors. These have been investigated mainly checking the amount of carbon dioxide produced [31, 43] as well as the internally circulating currents [48, 83], through the use of segmented hardware. Only limited attempts to measure local potentials have been done [82], mostly due to the practical limitations of using reference electrodes (RHE) in PEMFCs. In contrast to measurements carried out in presence of hydrogen, where the counter electrode could be used as reference electrode too, the potential at the positive electrode is not directly accessible in an air/air configuration from cell voltage since polarization at anode cannot be neglected. RHEs are thus necessary to investigate how potentials evolve during the transients, because they highlight ϕ_s - ϕ_l variations.

Since the first description of the reverse current mechanism, efforts has been made to develop mathematical models that can describe the phenomena. One of the first models was presented by Meyers and Darling [56]: this is a transient 1-D model that focuses on the kinetics of the three main reactions (HOR, ORR/OER, COR). It was an important first step towards the comprehension of the different mechanisms but it neglects both double layer and oxidation state and it takes important simplifications in the species transport through diffusion media.
Gu et al. [31] first introduced the pseudo-capacitive effects. In their model, they included a pseudo-capacitance to represent Pt oxidation and reduction reactions, and by doing so they successfully described the asymmetry between start-up and shut-down. Later, the same authors presented an useful review and classification of the different modelling studies [32]: these successfully describe the carbon corrosion due to fuel starvation or start-up/shut-down, but

do not describe quantitatively the local potentials and the internal currents that can be experimentally observed by the techniques introduced in Section 2.3.2. A new model by Maranzana et al. [54] tried to fill this gap. The authors implemented a transient "pseudo 2D" model that attempted to mimic the experiments performed on the segmented cell used by the same group. In this case, it was added a comprehensive modelling of the different Pt oxidation reactions, that were previously lumped in the only pseudo-capacitance. Nevertheless, mass transport was considered just in the through-plane direction while the gas concentration in-plane is imposed as boundary condition and thus the channels are not modeled.

1.5 Accelerated stress testing

The development and the comparison of new components to reach the objectives of cost reduction and increase in durability, explained in Section 1.3, require proper ways of testing.
In order to study how fuel cell degrades, accelerated life tests (AST) are commonly used: they amplify single mechanisms of degradation while real conditions can require thousands of hours, permitting to reduce both time and costs. Acceleration is guaranteed by a higher stress level and/or a more frequent stress application, that concentrates on a single component, as membrane or catalyst layer. In the specific case of CL, focus is on a single mechanism, i.e. electrocatalyst or carbon support degradation: acceleration of these processes is carried out through those parameters shown in Section 1.3.3. Until today, ASTs have been mainly used in a qualitative way, for a fast benchmark and development of new materials, to understand why units fails and to study mitigation strategies.
Anyway, three main drawbacks have become evident:

- Lack of reliability.
  Results of ASTs depend on the bench test, in particular on the setup geometries. Generated results are not directly comparable, even opposed, in case of different used hardware;

- Lack of representativeness.
  AST represents degradation at a very specific operating conditions: it does not consider the influence of real working parameters in failure modes. Even more so, this limit raises in case of heterogeneous and dynamic mechanisms, that have a different local impact, as start-up and shut-down.

- Lack of predictability.
  Until today, it does not exist a clear transfer function that permits to predict the lifetime of components from ASTs results: ASTs aging and real world degradation have not been linked yet.

1.6 Aim of the work

The research project deals with PEMFC durability, focusing on degradation occurring during start-up/shutdown operation with a locally resolved investigation.
The understanding about the main mechanisms originating the uneven distribution of local potentials and currents will have to be improved, by focusing on the major stressors (e.g. temperature, relative humidity, . . .). In particular, the present work uses a recent technique for local potential tracking, applied not only to the cathode [35], but also to the anode side. This tool permits to control also how long the process lasts and which are the variations caused by changes in operating conditions. In addition, the evolution of degradation on voltage profiles during start-up/shutdown is researched. Modeling simulation will support either interpretation and validation activity to predict the impact on heterogeneity of ageing under stressing operating conditions and to relate causes to performance losses. This has been permitted to: **(I) to quantify the impact of the start-up/shutdown on performance degradation**;

Since the objective of this research project is to reproduce real-world operation (such as start-up) by the use of ASTs, a comparison between degradation under repetitive start-up and shutdown operation and ASTs was preliminary performed using SoA protocols. Firstly, start-up/shutdown operation in unmitigated cycles (at 80°C – small flow rate) were compared with DoE ASTs, then a specific protocol, developed in the framework of ID-FAST project (introducing mitigation strategies to mimic real automotive stack start-up/shutdown, see 1.7) was investigated and local performance losses were analyzed. Besides a Single Cell with through-plate reference electrodes, a Segmented cell is used (see Rabissi et al. [69]), with the aim to improve local study. An in-house custom hardware has been on purpose modified for introducing an array of RHEs: it is the first time that these setups have been coupled to perform start/stops analysis. In addition to the pointy tracking given by RHEs, segments ensure information about how local degradation evolves. From the literature review indeed, it is known the heterogeneity of the process: inlet and outlet are the most affected regions [20, 31, 55], rather than the middle region of the MEA.

In order to improve reliability of the AST results (see 1.5), a new testing

hardware has been designed (the so-called Zero-gradient test cell) under the coordination of JRC (Joint Research Centre of the European Union), and tested with the aim of defining a common standard to be used for single cell testing. As part of this work, the POLIMI prototype is used to test the materials under different AST protocols to accelerate the catalyst layer degradation. In this way, it was possible to highlight the influence of one single degradation mechanism or operating condition stressor. Finally, the results of are compared with data collected during start-up and shut-down operation in the most affected MEA regions of the segmented-cell, to elucidate the effect of degradation heterogeneity during real operating conditions. The main results obtained were: **(II) to develop a specific AST able to reproduce start-up operation; (III) and to validate its relevance by correlation to real world ageing.**

The research project has been carried-out within EU Project ID-FAST (H2020 framework) whose purpose is the investigations of degradation mechanisms and the definition of protocols for PEM Fuel cells Accelerated Stress Testing (see Section 1.7).

The rest of this dissertation is organized as follows:

- **Fundamental study of start-up and shut-down processes**, in order to better understand the physics of phenomena. This first part wants to clarify the main aspects related to the basics of starts/stops and the impact of different operating conditions. To achieve this objective, innovative reference hydrogen electrodes are experimentally adopted, as described in Section 2.3.2. To overcome experimental limits and reach a higher level of comprehension, a model is developed too, as described in Section 3.3. It is a true 2D transient model developed in COMSOL Multiphysic® in order to get insight about the circulating currents and to confirm the conclusions drawn by the experimental studies (see Section 3.1).

- The second module starts from DOE Accelerated Stress Testing: to understand the degradation induced by real **unmitigated SUSD**, results should be correlated with single-emphasized CL failure modes, in a quantitative point of view. In addition, trying to complete the study of phenomena, it is investigated how start-up and shut-down are modified as consequence of a specific degradation, induced by AST: this suggests how the damaging impact of start/stops evolves with the state of materials aging (see Section 4.1). The next Section shares the purposes of the second, but in this case **real mitigated start-up** and shut-down are tested, in accordance with the mitigated procedure proposed by project partners. To guarantee the representability of non-uniform phenomena

like start-up and shut-down, the most affected MEA portion should be analysed in detail: for this purpose, a Segmented-Cell is used (see Section 5.1).

- Since the mitigation modifies the operating conditions, a stressor analysis, is performed on the DoE AST protocol; the effectiveness of adopted parameters is verified by the way of material response and through a specifically-developed hardware that ensures reliable results, called Zero-Gradient Cell Hardware (see Section 6.1). Finally, a new AST protocol is proposed to reproduce in Zero-Gradient Cell the Start-up mechanism under mitigation strategies (see Section 7.1).

1.7 The ID-FAST project

This dissertation work was done under the framework of the European project ID-FAST (European Union's Framework Program Horizon 2020 - H2020/2014-2020 - for the Fuel Cells and Hydrogen Joint Technology Initiative under grant agreement n°779565 - FCH-JU project ID-FAST): *Investigations on degradation mechanisms and Definition of protocols for PEM Fuel cells Accelerated Stress Testing*.
ID-FAST aims to support and promote the deployment of fuel cell vehicles, through the development of appropriate ASTs for PEMFC components, able to overcome the issues introduced in Section 1.2. Transfer functions, allowing to predict the performance degradation during real world operation, should be developed, to accelerate the introduction of innovative materials in next generation designs. The project tries to achieve its goals by 4 steps:

1. Identification and quantification of degradation phenomena involved in real ageing;
2. Analysis of stressors and of their accelerating factor for each single mechanism AST;
3. Analysis and development of combined AST protocols;
4. Validation of combined ASTs and development of transfer functions to link ASTs ageing in single cell to real ageing in stack, with realistic lifetime estimation.

The Politecnico di Milano is tasked to analyze the existing single mechanism ASTs and then improve them or develop new ones, and between the different components it will focus mainly on the catalyst layer.

The partner of the project are: CEA (France, project coordiantor), BMW (Germany), DLR (Germany), Fraunhofer (Germany), Freudenberg (Germany), Politecnico di Milano (Italy), Symbio (France), ZSW (Germany).

Chapter 2

Experimental methodology

2.1 Introduction

The purpose of Chapter 2 is to describe the adopted methodology. In particular, the experimental tecniques and the procedure of testing for the study of reverse-current mechanism and degradation associated to start-up/shut-down operation are extensively described. This chapter contains the following main sections:

In the first part, the samples properties are described. Then, the tecniques of reference hydrogen electrodes (RHEs) and macro-segmented cell hardware are introduced. The purpose was the evaluation of local performance under operations object of the study. In the last part the design of the new differential cell hardwware, named Zero-Gradient cell is illustrated with a description of its features.

Finally, the single cell test protocols are presented, with the exception of the specific procedures adopted for start-up shut-down analysis, that are detailed later, in the next chapters.

2.2 MEA samples

All the tests presented in this work have been realized in single-cell hardware. For the purpose, two catalyst Catalyst-coated membranes (CCMs) were used: a commercially available CCM (ION-POWER®), named Type A, with Pt loading of 0.3 mg cm for both anode and cathode side. Nafion® XL membrane was used for this CCM. A commercial CCM, for automotive application, supplied by Johnson Matthey, named Type B CCM. The Pt loading is of 0.4 mg cm^{-2} for cathode and 0.08 for anode. The Type A CCM was assembled with Sigracet® 29BC GDL (235 μm) without hot-pressing

cells. The type B CCM was assembled with Freudenberg GDL H14CX483 without hot-pressing into single-cell hardware. Compression was obtained using rigid gaskets in PTFE and an optimal compression value of 80% of initial thickness was kept for all the samples. The active area was controlled using Mylar sub-gasket, such to be fixed at value of 25 cm^2 for both Single and Segmented Cell and at 10 cm^2 for Zero-Gradient Cell (Section 2.3).

The samples tested in the frame of the work are:

- Type A CCM
  - for Accelerated stress test in Chapter 4;
  - for unmitigated Start-up/Shut-down operation;
  - for physical study in Chapter 3.
- Type B CCM
  - for automotive Start-up/Shut-down operation with mitigation strategies;
  - for Accelerated Stress Test in chapter 6-7;
  - for physical study in Chapter 3.

2.3 Experimental setup

2.3.1 Structure of Single and Segmented-Cell Hardware

The flow field

In order to permit a thorough investigation of performance under Start-up/Shut-down mode a single-cell reference setup has been adopted. Two specific configurations have been taken into account, a Single and a macro-Segmented Fuel Cell. The purpose of the Segmented cell is to permit localized electrochemical characterization. Both the setup, the same flow pattern design has been maintained. It's based on three serpentine channels 0.8 mm wide and 1/0.8 mm deep respectively.
For Segmented hardware, both at anode and cathode, the distributors are divided into four parts. Segmentation cuts were realised in correspondence of the ribs to avoid changes in channel cross section. The preheating of gases is guaranteed by the way of a first serpentine line, not in contact with the MEA. The local resolution of the segmented setup has been limited to minimize measurments uncertainty due to currents cross-section.

Current collectors

The distributors are directly in contact with the current collectors. While in case of Single Cell these are unique pieces, in case of Segmented Cell they are divided into four segments, as the distributors; the collection of the local generated currents is thus allowed.
Sources and senses cables connect the electronic load with the hardware. A data acquisition system collect voltages for both the single cell and for each segment in the Segmented cell. In addittion, one pair of cables is connected with each Reference Hydrogen electrode with current collector. A total of 8 cables, i.e. 4 per side, are then necessary; in case of Segmented Cell this configuration must be repeated for each segment.

End plates

All the cell parts are finally kept together by two aluminium end plates; for the Segmented Cell, inside them are displaced two thermocouples and two heating cartridges controlled by PID logic that ensures the temperature control of the cell. In case of Single Cell instead, only the end plate at cathode side is directly regulated.

2.3.2 Reference Hydrogen Electrodes

An innovative tecnique as been adopted for dynamical measurment of local potentials. It's based on reference hydrogen electrodes with a through-plane configuration. This technique is innovative, used in the recent years by Piela et alt. [68] and by Brightman and Hinds [35]. The new design is more complex than traditional solutions but permits to overcome some issues. Actually, the conventional sandwiched references are thin films put inside two membranes, therefore they modify inevitably the membrane characteristics. Regarding the external edge type, that has a salt bridge connection, the distance between the reference electrode and the MEA introduces potential drops effects. Notably, in case of start-up shut-down study, it must be considered that reference potential needs the presence of hydrogen: if the measurement is based on incorporating RHE in the ionomer phase, the air/air configuration should be problematic. Dynamic hydrogen electrodes, for example, try to overcome the problem by a local generation of H_2 through a small cathodic current: anyway, accuracy of measurement could be affected.

The adopted setup is shown in Figure 2.2. The salt bridge consists on a Nafion tubing (Perma Pure, NJ, USA. Internal diameter of 0.6 mm, external diameter of 0.8 mm), placed inside a PTFE tubing, both of approximately 0.1

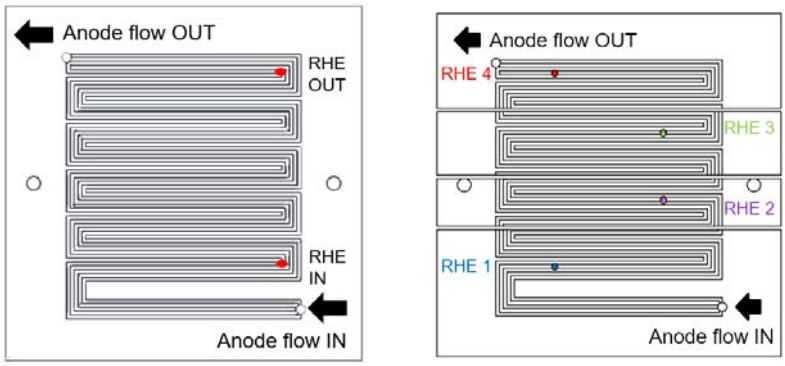

(a) Single Cell **(b)** Segmented Cell

Figure 2.1 – Cathode flow field with RHEs positions. Anode flow field is symmetric to cathode one. Labels of RHEs and segments is assigned with respect to anode flow direction; cell is worked in co-flow mode, with the only exception of Chapter 5 analysis, as there specified.

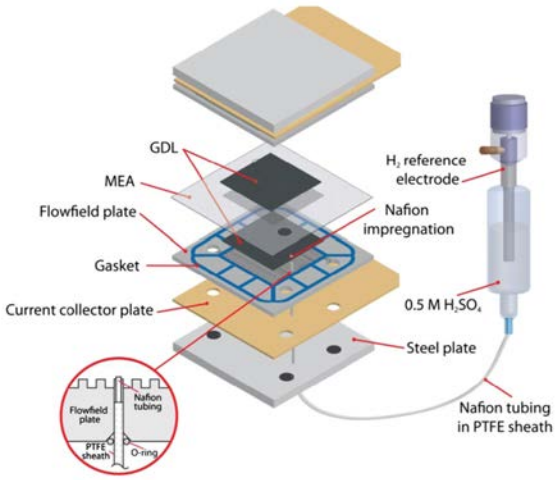

Figure 2.2 – Ionic connection between the catalyst layer and the reference electrode [35]

m length. The end plates, current collectors and flow fields present some holes, the position of which is reported in Fig 2.1: the first is the Single Cell while the second is an in-house custom Segmented Cell specifically modified for this work, to ensure the use of RHEs. The former was used with Type A CCM, to understand the physics of the phenomena and perform ASTs/unmitigated SUSD. The latter was adopted with Type B CCM, for a deeper analysis of the transients and to investigate real aging.

The tube is placed inside the hole and, on one side, it gets in touch with the GDL, while the other end is immersed in a vessel. On the GDL extremity, a PEEK filament (0.45 mm diameter) is plugged in to ensure better mechanical properties. On the external surface of the flow-field, an O-ring arrangement works as gastight, preventing leakages. The vessel is full of 0.5 M H_2SO_4 and holds the hydrogen reference electrode (Reference Electrode HydroFlex by Gaskatel®); it works through a H_2 cartridge, connected to a Platin-Palladium-electrode. To avoid dehydration and maintain thus a good ion-conductive path, the Nafion tubing is filled by the same 0.5 M H_2SO_4 acid.
As configuration improvement, to ensure a more direct ionic connection till the electrode, some very small holes have been made in the GDL (d = 0.9 mm), filled up by a mixture of liquid Nafion and propanol. Holes are so small that their influence on MEA performances is assumed negligible.

2.3.3 Zero-Gradient Cell

The Zero-Gradient cell hardware is conceived to keep the operative conditions as homogeneous as possible along the MEA, and all its different part were designed in order to achieve this objective. It was designed to provide a 10 cm^2 active area and comprehends the gas flow fields, the current collectors, the liquid cooling distributors and the end-plates, as shown in Figure 2.3.

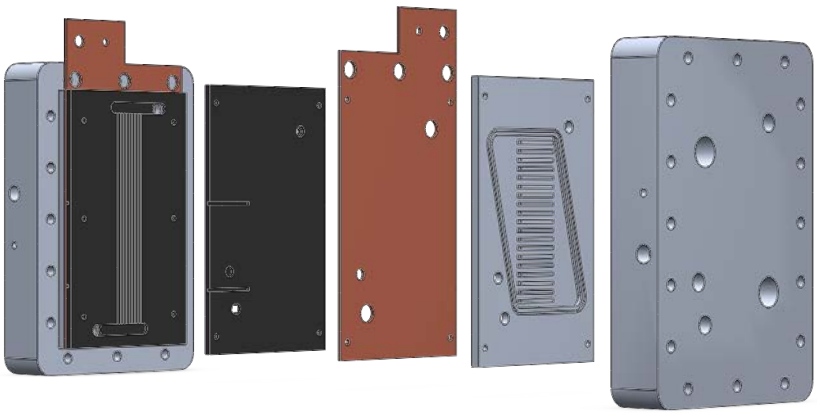

Figure 2.3 – Render of the Zero-Gradient hardware.

The flow field

The flow fields are designed to provide an uniform gas distribution in the GDL while keeping the pressure drops to a minimum and also assuring an

effective electric contact. The main design parameters of the flow field are summarized in Table 2.1.
One of the most crucial characteristic is the pattern of the gas channels: a parallel flow design was chosen as it is the one that minimizes the pressure drops. However, this type of flow field is not optimal for gas distribution and water management, but these drawbacks are overcome by the effects of the high stoichiometric ratios utilized. As a matter of fact, a λ higher than usual is necessary to ensure an homogeneous concentration along the whole MEA, where λ is defined as the ratio between reactant feed into the cell and reactant consumption inside the cell.
From the pressure drops point of view, large channels with slow velocities were preferable, but this would have caused a poor and non-homogeneous electrical contact and a higher ohmic drop, since the rib area would have be small; from the low velocities would be derived poor water management and gas distribution in the GDL. For these reasons, it was preferred to implement an high number of channels, with a relative small channel and a rib width able to assure an uniform current distribution, while the small depth results in high velocities.
While the total width of the channels (20 mm) was imposed by the desired active area, the length of the channels was chosen to be significantly longer than the one of the MEA in order to assure a complete preheating and flow development prior to the gas reaching the GDL. To ensure an uniform gas distribution in all the channels, two manifolds, both at the inlet and outlet, were implemented.

Table 2.1 – Flow field characteristics of the Zero-Gradient Cell

	Cathode	**Anode**
Number of channels	24	25
Channel Depth	0.4 mm	0.3 mm
Channel Width	0.6 mm	0.3 mm
Rib Width	0.25 mm	0.55 mm
Channel Length	123.5 mm	96 mm

Six $^1/_8$" slots are disposed along the edge of the flow field to hold PFA centering pins, which provide assistance in the correct assembling of the MEA and gaskets, and for the alignment of the two flowfields. In addition, two squared slots for the insertion of thermocouples has been added on the back of the graphite plate. They are placed close to ends of the active area and are used to ensure the absence of temperature gradient.

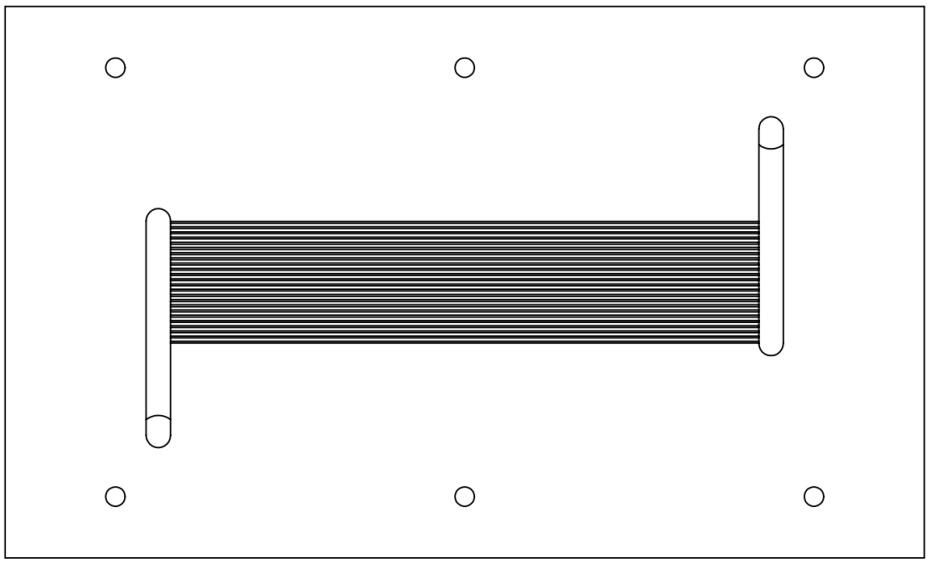

Figure 2.4 – CAD sketch of the anode flow field.

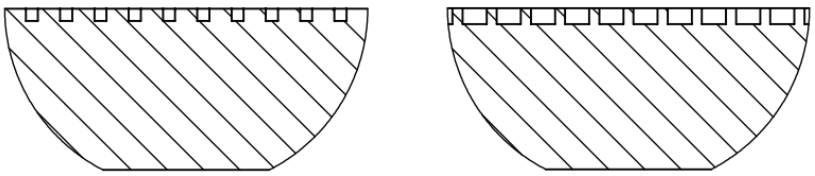

(a) Anode **(b)** Cathode

Figure 2.5 – Section detail for anode and cathode flow fields. Relative dimensions of ribs/channels are highlighted.

The current collector

The current collectors have been made with a 2 mm thick copper plate and present holes for the alignment pins and for the gas tubes going to the flowfields, that are sized to restrain also the O-ring that prevents gas leakages. Attention has been paid to the end portion of the plate, in which the connections to the wiring are placed. It is designed to keep the cross section area as big as possible, in order to limit the ohmic drop, while allowing an easy assembly procedure.

The liquid cooling plate

For the temperature control of the cell it was chosen to use a liquid system. In comparison with the more traditional electrical cartridge heater, the liquid system allows a more uniform heat exchange and temperature distribution; it also allows the cooling of the cell, if needed. The obvious drawback is a higher system complexity. The heat exchanger plate was designed to be mounted between the end-plate and the current collector. The open flow field employs a simple parallel channel design, perpendicular to the direction of the gas in the graphite flow field, to make the temperature profile as uniform as possible. There are 26 channels at the cathode and 20 at the anode, they are 2.5 mm deep and 2.5 mm/2.6 mm wide, respectively at the cathode and at anode.
The open channels face the end plate, this is not the most efficient way for the heat exchange but it was chosen to prevent the liquid from touching the copper plate, and thus preventing corrosion. It also makes the electrical insulation of the cell easier.
A rectangular slot was milled outside of the flow field to accommodate an O-ring, necessary for preventing liquid leakages.

The end plate

The end plates have the main function of keeping the different components together and assure the proper compression of the MEA. Sixteen 10 mm bolts are distributed along the edges and are tighten with a torque wrench to 12 Nm. The aluminum plates were designed thicker than usual to prevent bending, that could have been accentuated by the water pressure. They are fitted with all the different connection for the gases ($^3/_8$" and $^1/_4$" borethrough connections, respectively for cathode and anode) and the liquid cooling (12 mm NPT). In addition, they are already prepared to accommodate the heating cartridges, if necessary.

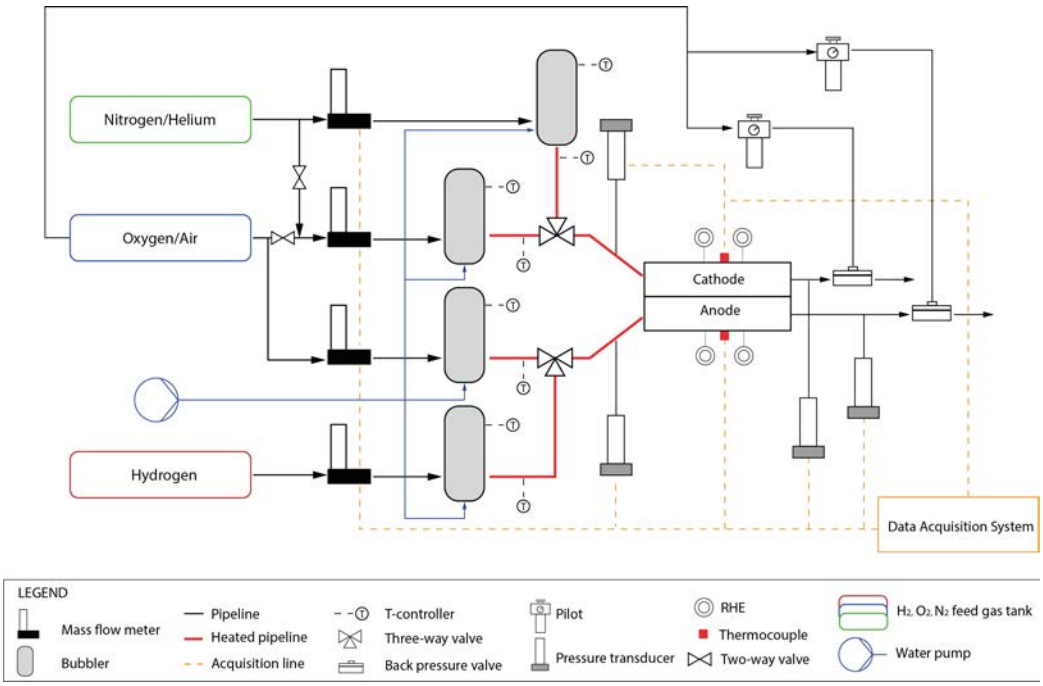

Figure 2.6 – Schematic experimental setup of station 1 for both Single and Segmented Cell hardware with implementation of RHEs.

2.3.4 Basic plant layout

In the frame of this work, two different working stations were necessary. A first station was provided by the necessary tools for start-up shut-down study: RHEs and, afterward, segmented structure were used. A second station instead was organized for the operation of Zero-Gradient Cell. A short description of their plants is done in this part; to check the most relevant characteristics of the following mentioned components, refer to Appendix 7.7. The basic layout of the first station is shown in Figure 2.6, where the solid lines indicate fluid pipelines, while the dashed ones are electric connections. Moving from the left side of the scheme, the first depicted part is necessary to furnish the properly heated and humidified streams to the cell. The used gaseous reactants and inerts are hydrogen, oxygen, nitrogen, helium - stored in pressurized tanks - and air. The purity level is 6.0 for N_2, 3.5 for O_2, 5.0 for H_2 and 5.5 for He. The amount of gases is set by electronic flow meters, that ensure a fast control. Some upstream valves, not drawn, allow to switch from one gas to the other, in case they share the same flow meter. The two-way valves are instead useful to match the full-scale required for N_2 by different testing procedures.
The fluids move then inside the bubblers: their aim is to saturate the flow

before getting into the cell. The dew point temperature is chosen and fixed by the way of a T-controller; in other words, this system keeps the relative humidity to the desired value. A pump fills the bubblers any time the level of water, provided by a float, drops down. Heated ducts are used immediately downstream to avoid the decrease of flow temperature as it exits the bubbler, preventing condensation. They are managed, here again, by T-controllers.
The two three-way valves have different aims. At the cathode, it simply allows the switching of gases avoiding that some O_2 might influence the process when N_2 is used. At the anode it is crucial instead for the start-up shut-down test, in order to form a front H_2/air - or vice versa.
Around the cell, a set of RHEs is highlighted; they represent the most relevant feature in the frame of this work. The reference electrode array is based on a through-plate configuration that is deeply described in Section 2.3.2.
Pressure is another parameter to regulate: to increase it properly upstream, the gases encounter back pressure valves before being discharged to the environment. Pilots, either manual or electronic, make possible such operation. Both the upstream and the downstream pressures are marked out by means of transducers, connected both to anode/cathode inlet and outlet. Data Acquisition System passes through National Instrument DAQmx.
A second plant has been arranged to settle Zero-Gradient hardware; the configuration is close to the first, as evidence in Figure 2.7; some simplifications are however here allowed since no gas switching at the anode is necessary and no RHEs are implemented. The element of complexity, as described previously, consists in the temperature control by a liquid system: water temperature is set through a thermo-circulating bath in place of electrical cartridge heater, that could be in any case implemented at need.

The experimental procedures are described in the second part of this chapter (see Section 2.4). Anyway, a concise introduction is here necessary to explain how they are performed. The electric load Chroma®63600 sets currents - in galvanostatic operations - through sources cables, while senses measure the voltage that is thus not affected by cables resistance. This is done generally during *Operando* tests with H_2/air or H_2/O_2 feed, such as polarization curves and EIS. The load could also work in a potentiostatic mode and the power that is produced is dissipated. These *in-operando* tests are managed by some LabView System Design Softwares. When inerts (H_2/N_2) are used for the protocol, the potentiostat is required, commanded by NOVA Autolab user interface. The potentiostat works either in galvanostatic operation or in a potentiostatic manner (AST, CV). In addition, to conform to the request of high current at low potentials during Limiting Current Measurement (see 2.4.5), Autolab with 20 A Booster has been used in place of Chroma load.

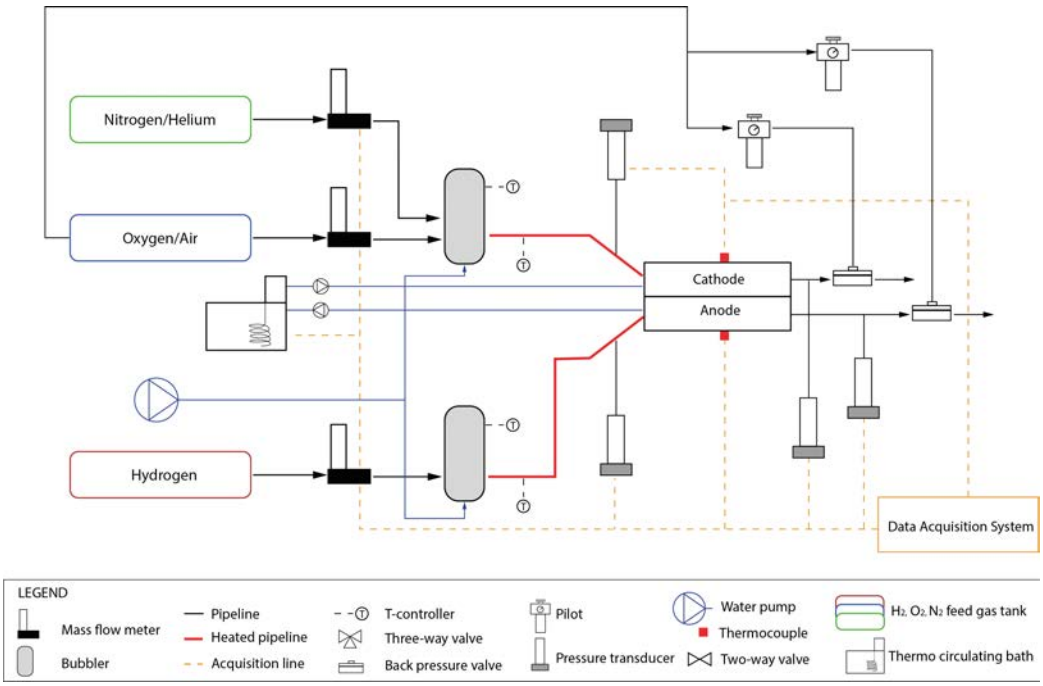

Figure 2.7 – Schematic experimental setup of station 2 for settlement of Zero-Gradient Cell.

In the case of segmented hardware, at need, the multi-potentiostat could be utilized.
The collected raw data are saved and then post-processed using Matlab®. Only the reliable data are identified, cleaning the set of results from outliers, undesired transients and noisy-affected points.

2.4 Experimental procedures

2.4.1 Cyclic Voltammetry

The Cyclic Voltammetry is an *in-situ* test performed using nitrogen at working electrode and hydrogen at counter electrode. Temperature, flows and RH are held constant. Thanks to a potentiostat, the working electrode potential is increased at a constant rate from a minimum value to a maximum and then decreased back to the initial value. Current is recorded in the meanwhile and the plot of current versus potential is constructed, which is known as a *voltammogram* [15].
In the low potential range, from OCV to around 0.35 V, the positive current is generated by hydrogen desorption reaction, while the negative current is

the result of the opposite adsorption reaction, that occurs when voltage is decreased. Integrating the current in time under the desorption peak, the total charge passed is obtained, from which the electrochemical surface area (ECSA) can be estimated. The hypothesis done commonly in literature are: a 1:1 ratio between hydrogen atoms adsorbed and used catalyst surface and a conversion factor σ_{m} of 210 μC cm^{-2}. Defining the potential at which the current has a minimum in the positive half of the chart as $\mathrm{E_{dl}}$, the scan rate [mV s^{-1}] as Sc and Pt loading as $\mathrm{L_{Pt}}$ [$\mathrm{mg_{Pt}}$ cm^{-2}]:

$$ECSA = \frac{\int_{OCV}^{E_{dl}} i\, dV}{\sigma_m\, L_{Pt}\, e\, Sc}\ [m^2 g_{Pt}^{-1}] \tag{2.1}$$

From 0.35 V to 0.60 V a flat current is observed: only charging/discharging of double layer is occurring. This part permits so to estimate the double capacitance ($\mathrm{C_{dl}}$).
Above 0.6 V, Pt is oxidized by both water and oxygen: adsorbed OH groups, chemisorbed oxygen and oxides are generated (PtOH, PtO, $\mathrm{PtO_2}$). Typically CV is stopped at either 0.6 V or 1.2 V; increasing further potential means to enter in a favourable carbon corrosion region, in accordance to what explained in Section 1.3. During the negative sweep, the potential at which PtOx reduction occurs is shifted towards lower values compared to oxidation (main reduction peak around 0.6 V - 0.8 V, but part of reduction occurs towards very low potential values).

In case of Single Cell and Zero-Gradient, the Autolab potentiostat has been used. In case of segmented setup instead, each segment could be independently controlled using NI PXIe-4139, a multi-channel potentiostat that ensures local measurement of ECSA.

2.4.2 Linear Sweep Voltammetry

Linear Sweep Voltammetry is the most common method to determine hydrogen crossover; due to its practicability and convenience it has become a basic technique. It permits also to quantify the membrane electric resistance. In particular, the gas crossover evolution during degradation tests is indicative of membrane modifications, so it is helpful for clarifying failure modes like pinholes formation and short-circuits.

As well as for CVs, temperature and RH conditions are kept constant. Fully humidified streams are used to ensure a good membrane hydration and fluxes are both set at minimum values. The potential of the working electrode is increased from a minimum to a maximum (e.g. 0.05 V - 0.60 V), thanks to a potentiostat able to operate at very low scan rates. When moved to

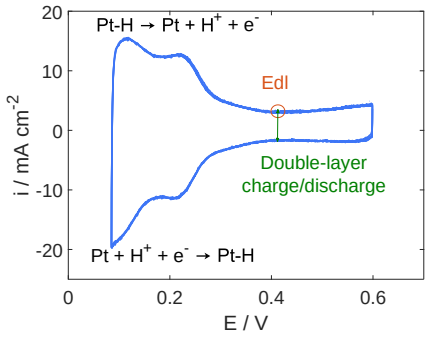

Figure 2.8 – Example of CV performed on Type A CCM. LPL = OCV, UPL = 0.6 V, Sc = 50 mV s^{-1}, both anode and cathode flow set at 60 ml min^{-1}. Different relevant regions for the analysis are put in evidence: adsorption/desorption peaks and double-layer charge/discharge.

high potentials, hydrogen that has crossed from anode to cathode is fully oxidized under mass transfer-limiting conditions; the current generated is solely attributable to the crossover of hydrogen since only inerts are introduced in the cell [99].
The LSV result could be visualized in a chart that reports current as function of voltage. A very fast initial current increase is then followed by a plateau, when the adsorption/desorption on platinum is not anymore relevant (from about 0.3 V). It is in this second part that ohmic resistance could be computed, as the ratio between voltage and current variations: in other words, it coincides with the inverse of the tangent slope to the chart. At the same time, tangent intersection with y-axis indicates the hydrogen crossover.

As seen for CV, in case of Single Cell and Zero-Gradient the Autolab potentiostat has been used for LSV. For the segmented setup instead, the multi-channel potentiostat ensures local measurement of both ohmic resistance and crossover current.

2.4.3 Polarization curve

The traditionally used technique to assess fuel cell performance is the polarization curve. By sweeping out a range of imposed current densities through an external load, the voltage drop is expressed as a function of the current itself, obtaining the V-i chart. The result is very helpful to understand both the chemistry and the physics associated with fuel cell operation: indeed, its shape strictly depends on the kind of losses at each current level. There are three major types of overpotential in fuel cells, namely: kinetic, ohmic and mass transport. During an aging protocol, categorizing what overpotentials have

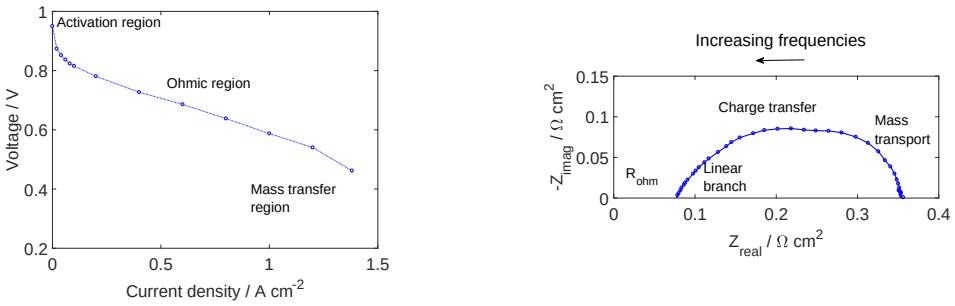

(a) Polarization Curve **(b)** Nyquist Plot

Figure 2.9 – (a) Example of polarization curve recorded for Type A CCM at BOT. T = 80 °C, RH = 100 %, $\lambda_a/\lambda_c = 2/4$, $p_{out} = p_{atm}$. The three different regions related to type of losses are put in evidence. (b) Nyquist plot from EIS in H_2/air for Type A CCM, at BOT. Frequency ranges between 0.07 Hz to 20 kHz, current is fixed at 0.4 A cm^{-2}.

changed since BOT is a powerful way to determine the causes of performance loss.

At open circuit no current flows; chemical reaction equilibrium prevails at the electrodes and the voltage is a direct measure of the difference in chemical activity at anode and cathode. Then voltage drops rapidly with increasing current; the steep initial decrease is attributed to the barrier for the electron transfer reactions occurring at the electrodes [98]. This is referred to as the ORR activation polarization region.

In a middle range of currents, the voltage decreases almost linearly. The internal protonic and electric resistances, mainly related to membrane and CL, dominate. This is the so-called ohmic region, where the cell should desirably work.

As the current increases, and finally reaches a limiting value, it is the mass transfer of reactants that limits the reactions. This is known as the concentration, or mass transfer, polarization region. The situation is particularly critical at the cathode, where water obstacles oxygen in reaching the active sites.

The procedure for recording i-V curve is straightforward in case of Single-Cell structure. In case instead of Segmented-Cell hardware, this behaves like a parallel configuration of resistors. The overall current is imposed and the voltage of each part is forced to be the same. At the same time, the current generated by each region is recorded, obtaining thus four local polarization curves. They are a valuable tool to discern how phenomena, with respect to the local position, evolve.

2.4.4 Electrochemical Impedance Spectroscopy

The impedance of the cell, resulting from both resistive and capacitive effects, is measured as a function of current density by electrochemical impedance spectroscopy. This technique can be applied *in-operando*, with both H_2/air and H_2/O_2, as done in the frame of this work. Cell conditions (temperature, humidity, flows) are held constant. A low-magnitude sinusoidal current signal is superimposed over a range of frequencies and the voltage response is measured. Since the sinusoidal perturbation is small - maximum current oscillation of 10% - the linear relationship between voltage and current is satisfied, allowing the simple computation of impedance as their ratio. The imaginary component of the impedance is then plotted against the real component for any frequency and the outcome is called Nyquist plot, an example of which is in Figure 2.9.b.

Information regarding mass transfer resistances, kinetics and ionic resistances can be extracted from the Nyquist plot [98]. The impedance response of a full cell is a combination of both the responses of anode and cathode half-cells, so individual electrode cannot be obtained directly. Anyway, the anode polarization is negligible against to cathode polarization during fuel cell operation, therefore it has only little effect, as explain after.
The main arc accounts for the charge transfer of the cathode catalyst layer (ORR). It decreases with increasing polarization due to the increased rapidity of the electrochemical kinetic [44]. At low frequencies, another arc may be present: it raises when mass-transport effect becomes significant, in both GDL and electrodes (e.g. at high current density, during flooding). At very high frequencies, the plot has only real contributions. The intercept of impedance arc on the real axis represents the total ohmic resistance, which can be expressed as the sum of contact resistances and ohmic resistances of membrane, catalyst layer, gas diffusion layer, and bipolar plates [44]. Always at high frequencies, an extra feature may be visible as a incomplete semicircle. It is linked to HOR that results in a small capacitive element thanks to its high kinetic; it merges, at least partially, with the cathodic circle.
Another distortion of the impedance spectra in the same region should be present: it is prescribed as a straight line at 45° angle. This so-called linear branch comes from the coupling between ionic resistance and capacitance in the catalyst layer; as proton transport resistance decreases, this linear part disappears, while deviations from the ideal 45° value are the result of an increased ionic resistance profile.

Comparing EIS at fixed currents during MEA aging is a powerful way to identify which changes are occurring; nevertheless this method fails to separate phenomena that have similar time constants, thus keeping open

various interpretations.

2.4.5 Limiting current measurement and O_2 mass transport resistance

The limiting current is the maximum current that can be produced by a cell as the concentration of reactant O_2 at the electrode working surface approaches zero [5]. Excess amount of H_2 is used while O_2 is amply diluted in N_2.
The limiting current is measured working in the low cell voltage region of polarization curve. The profiles at different O_2 concentrations resemble a vertical line, as could be seen in the example Figure 2.10; the recorded currents values are therefore simply averaged. The limiting current measurement is then converted into O_2 mass transport resistance. Indeed, the flux of oxygen (N_{O_2}) could be related on one hand to the current density and on the other hand to the concentration difference between channel ($C_{O_2,GC}$) and catalyst surface ($C_{O_2,Pt}$).

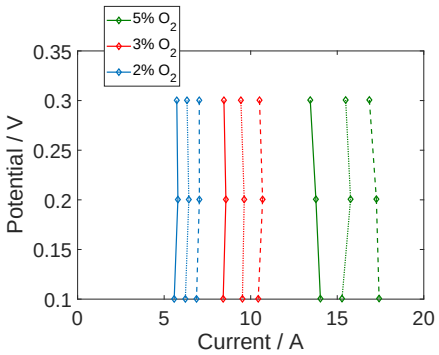

Figure 2.10 – Example of V-i chart obtained during limiting current measurement on Type A CCM (25 cm^2). Three O_2 concentrations are tested, as reported in the legend. Moreover, full lines are recorded at 115 kPa, dotted lines at 150 kPa and broken line at 200 kPa.

$$N_{O_2} = \frac{i}{4F} = \frac{C_{O_2,GC} - C_{O_2,Pt}}{R_{MT}} \tag{2.2}$$

where R_{MT} is the total mass transport resistance. In limiting current operation, as told at the beginning, the concentration of oxygen at platinum becomes null:

$$R_{MT} = 4F\frac{C_{O_2,GC}}{i_{lim}} = 4F\frac{x^{dry}_{O_{2,in}}}{i_{lim}}\frac{p - p_w}{RT} \tag{2.3}$$

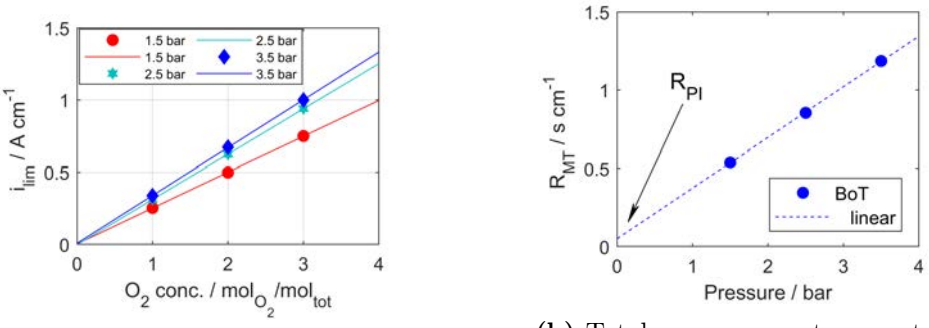

(a) Limiting current vs. % O_2

(b) Total oxygen mass transport resistance vs. pressure

Figure 2.11 – Limiting current test for Type B CCM at BOT on Zero-gradient hardware: the current recorded at the different dilutions (1, 2, 3 %) are used to evaluate, at each pressure (150, 250, 350 kPa), the total oxygen mass transport resistance.

where p is the total gas pressure while p_w is the water vapour pressure, dependent only on T. The total resistance is the outcome of different contributions. In this work, pressure is one of the main parameters let vary, allowing the separation into a pressure-dependent component, equivalent to intermolecular gas diffusion, and a pressure-independent component, i.e. Knudsen diffusion and transport through ionomer/liquid water layers. At the same time, R_{MT} could be seen as the summation of single-layer resistances; since it is the pore size that determines the gas diffusion type, molecular phenomena are dominant in the GDL and flow-fields, while Knudsen diffusion weights for the majority in the catalyst layer, where also ionomer-related resistances count. Following the procedure proposed by Baker et al. [5], limiting current should be related to the oxygen fraction by a linear correlation at each pressure condition, in accordance with Equation 2.3: the obtained straight lines should pass through the origin (Figure 2.11.a). Once the average ratio at each p is found, this value is used for computing total oxygen mass transport resistance. Thereafter, pressure independent and dependent components are disentangled thanks to a linear regression versus the absolute pressure (Figure 2.11.b).

$$R_{MT} = R_{MT,PD} + R_{MT,PI} \tag{2.4}$$

In the contest of the present work, operating conditions have been adopted during limiting current test, for the different hardware configuration adopted. The choice was taken to overcome the limitation of using RHEs under high pressure operation. The operating conditions are summarized:

- Single-cell hardware with RHEs (Chapters 3 and 4)

  - Temperature: 80 °C;
  - Pressure range: 115/150/200 kPa;
  - Dry oxygen concentration: 2/3/5 %;

- Segmented-cell and Zero-gradient cell hardware (Chapters 5/6/7)
  - Temperature: 80 °C;
  - Pressure range: 150/250/350 kPa;
  - Dry oxygen concentration: 1/2/3 %;

2.4.6 Mass activity of Pt catalyst

Catalyst activity measurement requires a purely kinetic current due to the ORR. For this reason, MEAs are tested using H_2/O_2 as reactants in order to minimize mass transport resistances. Moreover, as done by Gasteiger et al. [25] and suggested by DOE protocols [86], activities are evaluated at 0.9 V: here the overpotential losses, due to resistance, mass transport, current distribution and effects of oxygen utilization, are all expected to be small. Making the fuel cell work for a sufficient long time at low currents, the exchange current density at 0.9 V could be obtained by a linear regression of fully corrected polarization curve. This is the iR-free voltage versus the logarithm of the H_2-crossover corrected current density (i_{eff}).
The resistance-corrected cell voltage $E_{i\text{R-free}}$ is computed starting from high-frequency resistance measurements:

$$E_{iR-free} = V + i \cdot HFR \tag{2.5}$$

while the effective current results from the summation of cell current density and hydrogen crossover:

$$i_{eff} = i + i_x \tag{2.6}$$

A near theoretical Tafel slope should be found, that is 70 mV/decade at 80 °C to ensure reliable results. Then, mass activity $i_{m,(0.9\ V)}$ is computed as:

$$i_{m,(0.9V)} = \frac{i_{eff,(0.9V)}}{L_{Pt}}\ [A\, mg_{Pt}^{-1}] \tag{2.7}$$

The standardized procedure proposed by DoE, have been adapted in this work to specific operating conditions of interest. The tafel curve was Collected under oxygen feeding polarization curves as discussed in the next section.

2.5 Testing Protocols

2.5.1 Break-in and conditioning protocol

The break-in protocol is fundamental for the correct activation of the MEA, as first step after the mounting of the structure, and it is generally provided by the manufacturer. For the used MEAs in this work two different procedures have been adopted:

- Type A CCM.
  For this CCM, specifications are not given, therefore the suggestions of the EU Harmonised Test Protocols [85] are observed, with few secondary changes.
  The whole procedure is carried out with anode/cathode stoichiometry of 2/4. Initially, cell temperature is increased to 80 °C, inlet temperature of reactants to 85 °C and RH to 100 % - i.e. bubblers temperature equal to 80 °C. During this first step the gas inlet dew point is avoided to exceed reactants inlet and cell temperatures. The cell outlet works at atmospheric conditions. Starting from OCV, the current density is increased in steps of 100 mA cm^{-2} up to 800 mA cm^{-2}, being careful the cell voltage remains always larger than 400 mV. Each current is maintained for 30 min and the cell is finally let stabilize for 6 hours. Thereafter, reactants RH is fixed at 50% and the current is increased again up to 1.00 A/cm^{-2}, as done for the first part. The cell is hold in these conditions for at least 2 hours. At this point, the voltage at 1.00 A cm^{-2} is recorded as reference for 5 min and then stability validation by voltage cycling is performed. Potential is moved up to 0.8 V and held for 5 min. Subsequently it is decreased to the low level of 0.4 V and hold for 5 min also. These jumps are repeated to have three high voltage and two low voltage measurements. Moving back to a galvanostatic operation, current is set at 1.00 A cm^{-2} for 30 min; after this span, 5 min of recording are compared to the reference measurement realized before. Two conditions must be satisfied now: voltage fluctuations lower than ± 5 mV in the second recording and differences between the two 5 min-references must not be larger than ± 10 mV. In case these requirements are not satisfied, cycles are repeated again.

- Type B CCM.
  In this case, the procedure indicated in the Stack-Test Master Document (http://stacktest.zsw-bw.de/partners.html) has been followed. Load must be progressively increased in 300 s to nominal holding of 500 mA cm^{-2}, and kept for at least 60 min. Thereafter, load is decreased to 200

mA cm^{-2} and hold for 2 min. Then, moved to the high value of 800 mA cm^{-2} and hold for 2 min again. This has been repeated for set of 10 cycles, separated by 20 min of nominal holding. As stability criterion, it has been checked if, during the application of 500 mA cm^{-2}, voltage does not deviate for more than 5 mV within 3 min.

2.5.2 Diagnostic protocol

A general-purpose diagnostic protocol, adopted for all the aging procedures, is reported in Figure 2.12. It is based on two main modules: the electrochemical characterization executed in H_2/N_2,i.e. inert conditions, and the performance characterization, that consists of polarization curves performed under a variation of test conditions and the limiting current tests.

The first part concerns cyclic voltammetry (Section 2.4.1) and linear

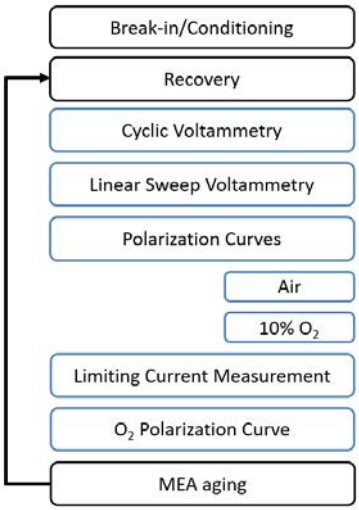

Figure 2.12 – Overview of the characterization testing procedure for the MEA. Here is reported the complete characterization, that could be performed only in part in dependence on the aging point and the type of test.

sweep voltammetry (Section 2.4.2); both are carried out with minimum fluxes of 60 ml min^{-1} at fully humidified conditions. Cell temperature is 80 °C and the outlets work in atmospheric pressure. Every time the gas of the working electrode is switched from air to nitrogen, it is necessary to wait about 30 min in order to reach a stable voltage value, that evidences the complete oxygen removal.

1. Cyclic voltammetry. First of all, the OCV is determined and 5 mV are added to this quantity. From such value, voltage is increased to a

Table 2.2 – Polarization curve operating conditions.

Parameter	Unit	Operating Condition
Nominal cell operating temperature	°C	80
Anode		
Fuel gas inlet temperature	°C	85
Fuel gas inlet humidity	%	100
Fuel gas outlet pressure (absolute)	kPa	101
Fuel gas inlet stoichiometry	-	2
Cathode		
Oxidant gas inlet temperature	°C	85
Oxidant gas inlet humidity	%	100
Oxidant gas outlet pressure (absolute)	kPa	101
Oxidant gas inlet stoichiometry	-	4

maximum of 0.600 V (UPL) and decreased back to a OCV (LPL), of 0.085 and 0.075 V for Type A and Type B respectively, using a constant rate of 50 mV s^{-1}. This cycling between UPL and LPL is repeated 3 times.

2. Linear sweep voltammetry. Voltage is linearly increased from the minimum value of 0.050 V to the maximum of 0.600 V with a constant rate of 1 mV s^{-1}.

The performance characterization is composed by polarization curves (Section 2.4.3) and limiting current measurements (Section 2.4.5). For sake of brevity, the protocols adopted in Chapter 4 are here described. Conversely, the details of characterization protocols used in Segmented-cell and Zero-gradient cell are extensively described in Sections 5.2-6.2.

1. Polarization curves are obtained in the following way:

   - H_2/air polarization curve. Polarization curve is recorded as reported in Table 2.2: The minimum flow rate is set at 0.2 A cm^{-2}, meaning that for lower currents the test is performed at fixed streams. After a waiting time of 5 min at 0.2 A cm^{-2}, current loads are imposed as reported in Table 2.3, in accordance with EU Harmonised Test Protocols [85].
     The polarization test is cut in terms of maximum current from time to time, to avoid voltage decreasing under 0.3 V. Moreover, only the descending points are used for the i-V curve and the initial

transient from one imposition to the next is depleted during data analysis.
EIS are usually obtained at 0.8, 0.4 and 0.1 A cm^{-2}, with frequency range from 0.07 Hz to 20 kHz.

- H_2/10% O_2 polarization curve. Same procedure described in case of air. There is a quite large increase in flows since air is diluted.
- H_2/O_2 polarization curve. The procedure is almost the same of the air case also in presence of oxygen. The only difference consists in stoichiometries: the flows of O_2 are set equal to the air ones at each current point, meaning that stoichiometry is much larger at the cathode now (≈ 19). However, this permits to remove pressure effects between the two curves.
  In case mass activity is evaluated (Section 2.4.6), some extra points are added at the end of polarization: 0.020, 0.010, 0.005, 0.002, 0.001 A cm^{-2}, held for 5 min per each.

2. Limiting Current Measurement. Cell works at 80 °C and 100% RH. The tested average pressures are 115 kPa, 150 kPa and 200 kPa. This test is carried out at fixed flows: for Type A CCM 240 ml min^{-1} of H_2 at anode and a total of 3000 ml min^{-1} at cathode, while flow rates are increased to 500 ml min^{-1} and 4000 ml min^{-1} for Type B CCM. Dilutions of 2 %, 3 % and 5 % of O_2 in inert N_2 are taken into account; note that flow rates are such high that the influence of stoichiometric variations on results is assumed negligible. As described in Section 2.4.5, limiting current is identified working in a low voltage region: potential is held by the potentiostat at 0.3 V, 0.2 V , 0.1 V for 180 s per each.

2.5.3 AST: Electrocatalyst Accelerated Stress Test

The electrocatalyst protocol used in this work is in accordance with DOE 2016 Fuel Cell Program [86]. The procedure has been designed as a voltage square wave, where the consecutive oxidations and reductions make the cathode catalyst degrade faster compared to real operations. This should be useful to assess electrocatalyst durability. In this AST, voltages are similar to those expected for an automotive drive cycle and test seeks to maximize catalyst degradation while minimizing the corrosion of the carbon support. Both the test structure and the frequency of performance evaluation are summarized in Table 2.4.

Table 2.3 – Polarization curve set-points.

Current density [A cm^{-2}]	**Dwell time [s]**
0.00	60
0.02	60
0.04	60
0.06	60
0.08	60
0.10	60
0.20	120
0.40	120
0.60	120
0.80	120
1.00	120
1.20	120
1.40	120
1.60	120
1.80	120
2.00	180
1.80	180
1.60	180
1.40	180
1.20	180
1.00	180
0.80	180
0.60	180
0.40	180
0.20	180
0.10	60
0.08	60
0.06	60
0.04	60
0.02	60
0.00	60

2.5.4 AST: Support Accelerated Stress Test

In this AST, the carbon support corrosion is enhanced while reducing as much as possible the electrocatalyst degradation. The potential range is increased to match the typical values encountered during unmitigated start-up and shut-down. Furthermore, potentiodynamic conditions boost the process: a very rapid triangle shape is so used. Specifications, as suggested by DOE, are collected in Table 2.5.

Table 2.4 – Electrocatalyst Cycle AST.

Cycle	Square wave between 0.6 V and 0.95 V. Holding time at each potential: 3 s. Rising time of 0.5 s.
Total number of cycles	30,000 cycles
Total cycle time	7 s
Cell temperature	80 °C
Gas inlet temperature	85 °C
Relative humidity	100 %
Outlet Pressure	Atmospheric
H_2/N_2	60/60 ml min^{-1}

Metric	Frequency
Polarization curves	0, 1k, 5k, 10k, 30k cycles
CV	0, 10, 100, 1k, 3k, 5k, 10k, 20k, 30k cycles

2.5.5 Zero-Gradient Cell specific protocols

As already mentioned, the Zero-Gradient cell was designed to achieve an homogeneous condition along the MEA. To attain this objective, specific testing protocols are also necessary.
In agreement with the other ID-FAST partners, a specific polarization curve protocol was implemented with the scope of facilitating the comparison between the results from different hardware: parameters are collected in Table 2.6. The main differences in operating conditions from the standard protocol previously described are:

- very high stoichiometric ratios, to ensure an homogeneous reactant concentration and high velocities.

Table 2.5 – Carbon Support Cycle AST.

Cycle	Triangular wave between 1.0 V and 1.5 V. Scan rate of 500 mV s^{-1}
Total number of cycles	5,000 cycles
Total cycle time	2 s
Cell temperature	80 °C
Gas inlet temperature	85 °C
Relative humidity	100 %
Outlet Pressure	Atmospheric
H_2/N_2	60/60 ml min^{-1}

Metric	Frequency
Polarization curve / air	0, 10, 100, 200, 500, 1k, 2k, 5k cycles
Polarization curve / O_2 Mass activity	0, 100, 500, 1k, 2k, 5k cycles
CV	0, 10, 100, 200, 500, 1k, 2k, 5k cycles
Limiting current	0, 100, 500, 1k, 2k, 5k cycles

- pressurized condition, the anode and cathode inlet pressure has been set respectively to 2.5/2.3 bar in order to have conditions closer to real automotive stack.

Table 2.6 – Zero-Gradient polarization curve operating conditions.

Parameter	**Unit**	**Operating Condition**
Nominal cell operating temperature	°C	80
Anode		
Fuel gas inlet temperature	°C	85
Fuel gas inlet humidity	%	100
Fuel gas inlet pressure (absolute)	kPa	250
Fuel gas inlet stoichiometry	-	8
Cathode		
Oxidant gas inlet temperature	°C	85
Oxidant gas inlet humidity	%	100
Oxidant gas inlet pressure (absolute)	kPa	230
Oxidant gas inlet stoichiometry	-	10

Minimum flow has been set at 0.5 A cm^{-2}, due to limits of the back-pressure valves. The current loads are imposed at 0, 0.02, 0.05, 0.1, 0.15, 0.2, 0.4 cm^{-2}

and, from this point forward, at steps of 0.2 A cm^{-2} until cell voltage reaches 0.3 V. EIS are obtained at 1.4, 0.8, 0.4 and 0.1 A cm^{-2}.

Chapter 3

Experimental and modelling investigation of start-up and shut-down transients

3.1 Introduction

This chapter is dedicated to the development of experimental tecnique and models to clarify the reverse-current mechanism underlying Start-up/Shut-down operation. This part is useful to understand the physical mechanisms involved and determining the influence of the operating conditions on the degradation process.

The elusive process of reverse-curent mechanism was elucidated by the mapping of local potentials thanks to the adoption of Reference Hydrogen Electrode arrays at the anode and cathode. Then a degradation model of carbon corrosion was implmented in a 2D transient PEM fuel cell model with the aim of providing insight into the dynamics of start-up and shut-down process. The model permit to simulate the different phenomena that contribute to the reverse-current because of transient hydrogen/air front at anode side. This permit to evaluate the most promising mitigation strategies, which are adopted in real stack. The most relevant tested parameters are:

- Operating cell temperature;
- Mass flow rates;
- Oxygen concentration at anode side;
- Molecular weight of dilution gas.

In the last section, the platinum oxides reaction has been introduced in the model to quantify the pseudo-capacitive contributions, and to improve the accuracy of the numerical forecasts.

3.1.1 Start-up and shut-down: methodological approach

Start-up/Shut-Down operations requires gas switching at the anode compartment, as described in Figure 3.1. At the anode side a H_2/air front is created, while the cathode continuous on operating with air. The switch between the humidified gas is permited by a three-way valve (see Figure 2.6). The operation is a very fast transient, so the acquisition is set every 10 ms.
No load is applied: starting from H_2/air OCV, maintained for 60 s, the shut-down is reproduced as soon as air arrives at the anode. After 60 s, when air/air condition is almost stabilized, valve is switched again to let the passage of hydrogen. The cycle is then repeated.
To ensure a reliable set of measurements, five Start-up/Shut-down are reproduced in a row and the third has been used in charts that compare results at different operating conditions. This makes comparison as fair as possible. In order to understand what changes in the processes using different stressors and/or materials, it has been observed:

- The minimum potential of cathodic ORR;
- The maximum COR/OER potential;
- The duration of SU/SD processes (i.e. residence time);
- The rate of change of potentials;
- Anode polarization.

3.2 Start-up and shut-down: process description by experimental results

First of all, the shutdown process is analyzed and results are depicted in Figure 3.2. Starting from Open Circuit Voltage condition, i.e. H_2/air feeding, the anode electrode is close to the equilibrium potential of 0 V, thus cathodic potential is around 0.9 V, that is almost the cell OCV. When the fuel cell is switched off, the gas is switched from hydrogen to air, and the voltage of the fuel cell, represented in black, drops rapidly. The potential of cathode inlet increases, while cathode outlet drops. During air front, and for each time

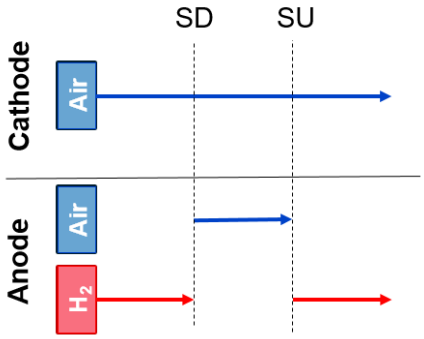

Figure 3.1 – Schematic representation of the procedure for unmitigated start-up and shut-down process.

interval, it is possible to divide the fuel cell into two parts: one active region at the anode outlet, which is filled with H_2 thus it operates as a fuel cell; one passive region at anode inlet, instead where the electrodes operates with Air/Air, where anode electrode works in ORR mode causing a high potential at cathode and boosting COR/OER (see Section 1.4). Almost all the points of anode operate with HOR as the front gets inside and they progressively change to ORR: such transition is highlighted by a variation in concavity and in the rate of potentials increase. the RHEs measurments indicates that cathode potential is 0.7-0.8 V vs RHE in the active region, while 1.5-1.6 V vs RHE in the passive region. At this point, the whole cell is filled with air: V_{cell} is around 0 V and the RHEs are at 1-1.1 V. Then, hydrogen is introduced to simulate start-up (Figure 3.3). The process is symmetric to shut-down in the procedure but not in all the results. First of all, the duration of Start-up is lower. Cathodic outlet is now in the passive region, characterized by high potential values, even larger than Shut-down. Cathodic inlet instead operates with ORR: note that since the analysed point is not really at the entrance of the channel, a transition from passive to active operation is here visible. Transition instead never appears at outlet. Both the anodic potentials go down while the cell comes back to H_2/air OCV.
For Type A CCM, collected results are based on 2 per side RHEs in the Single Cell hardware, while for Type B CCM the setup has been improved: 4 per side RHEs and the Segmented Cell have permitted to make a more complete investigation at local scale. In this second case, recorded transients are like Figure 3.4. For middle references, transitions from passive to active behaviour, and vice versa, are visible.

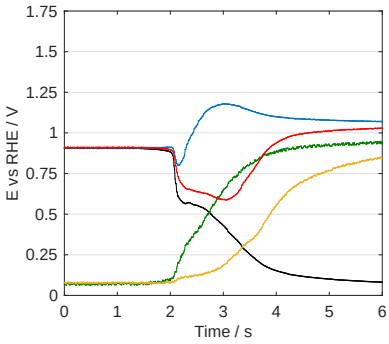

(a) Trend of voltages

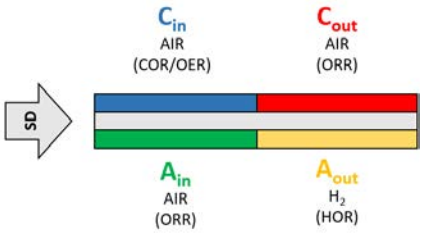

(b) Schematic representation

Figure 3.2 – Example of shut-down process on Ketjen black support material (Type A CCM 2.2). Potential profiles obtained at T = 40 °C, RH = 100%, $air_{cathode}$ = 200 ml min^{-1}, air_{anode} = $H_{2,anode}$ = 100 ml min^{-1}, p_{out} = atm. Position of RHE is specified by the schematic representation (b), while black curve represents cell voltage.

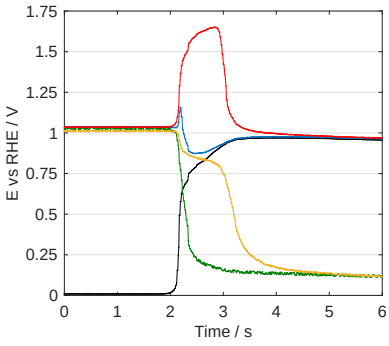

(a) Trend of voltages

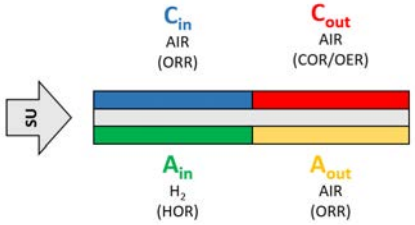

(b) Schematic representation

Figure 3.3 – Example of start-up process on Ketjen black support material (Type A CCM 2.2). Potential profiles obtained at T = 40 °C, RH = 100%, $air_{cathode}$ = 200 ml min^{-1}, air_{anode} = $H_{2,anode}$ = 100 ml min^{-1}, p_{out} = atm. Position of each RHE is specified by the schematic representation (b), while black curve represents cell voltage.

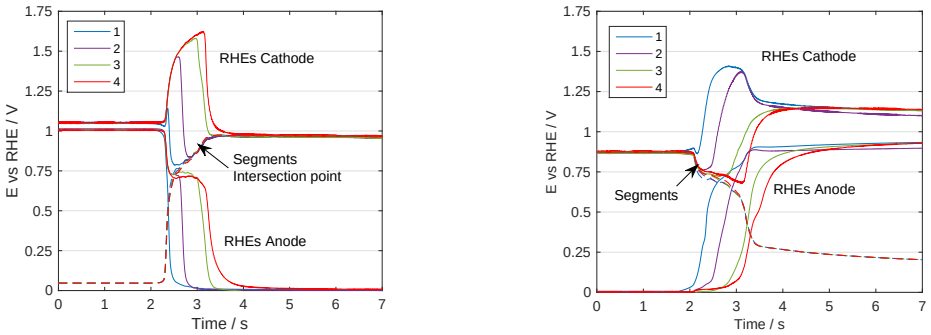

(a) Start-up **(b)** Shut-down

Figure 3.4 – Potential profiles obtained for Graphitized material (Type B CCM 2.2 at T = 40 °C, RH = 100%, $air_{cathode}$ = 200 ml min^{-1}, air_{anode} = H_{2anode} = 100 ml min^{-1}, p_{out} = p_{atm}.

3.3 Numerical model of start-up and shut-down

In order to get insights about the circulating currents and to support the conclusion drawn from the experimental tests, a numerical model of the Start-up/Shut-down process was developed. A transient 2D model was implemented in Comsol Multiphysics; it comprehends anodic and cathodic channels, gas diffusion layers, catalyst layers and the polymer membrane. It implements the main electrochemical reactions taking place during a Start-up/Shut-down event, namely hydrogen oxidation reaction (HOR), oxygen reduction reaction (ORR), oxygen evolution reaction (OER) and carbon oxidation reaction (COR), as well as the Platinum oxides formation/reduction and double-layer currents. It models the fluid dynamics in the channel and in the MEA in a continuous way. The model relies on the following assumptions:

1. Local effects over the MEA surface are considered along the channel and through the active layers, while differences between fluxes in the channel, and under the ribs of the gas distributor are neglected.

2. Liquid water transport and energy conservation are not solved, neglecting the blocking effect of liquid water on species transport and heating of porous media.

3. Conservation of water in the ionomer phase is not solved, thus water crossover across polymer membrane is neglected and ionic conductivity is calibrated as a constant parameter, consistently with the fully humidified condition that is set in the experiment.

4. Platinum oxides formation/reduction and interaction with oxygen reduction reaction is neglected.

Assumptions 2 and 3 are acceptable, as first approximation, in the light of fast dynamic behaviour that were investigated in this work (< 5 s). The model is described in the following subsection and it is able to simulate both steady state operation (polarization curves) and the transient operation (voltammetries and start-up/shut-down operation). The model is based on the Type A CCM, from which some geometrical and chemical parameters are obtained.

3.3.1 Pre-processing

The solved domain consists of seven parts, to study both anode and cathode channels, gas diffusion layers (GDLs), catalyst layers (CLs) and the polymeric membrane.
The use of a 2D model had the consequence of being able to simulate up to a single straight channel, the length of which was set to be 50 mm. A longer channel would have request more memory usage and longer computational time, without improving much the representativeness of the simulations, as it will still lack the 3D effects of the real cell (e.g. ribs, bends).
Anode and cathode are symmetrical, as in the Type A CCM. The geometric parameters of the domains are summarized in Table 3.1.

Table 3.1 – Model geometrical parameters

Parameter	**Symbol**	**Value**
Channel Length	L_{ch}	50 mm
Channel Height	d_{ch}	0.8 mm
GDL Height	d_{GDL}	135 µm
GDL Porosity	$\epsilon_{p,GDL}$	0.6
GDL Tortuosity	τ_{GDL}	4
CL Height	d_{CL}	20 µm
CL Porosity	$\epsilon_{p,CL}$	0.4
CL Tortuosity	τ_{CL}	9
Membrane Height	d_{MEM}	50 µm

A rectilinear grid mapped mesh was used, it is regularly distributed along the channel direction while it gets finer going in the through cell direction from the channel to the polymeric membrane, to ensure a proper discretization of the thin catalyst layers and of the membrane.

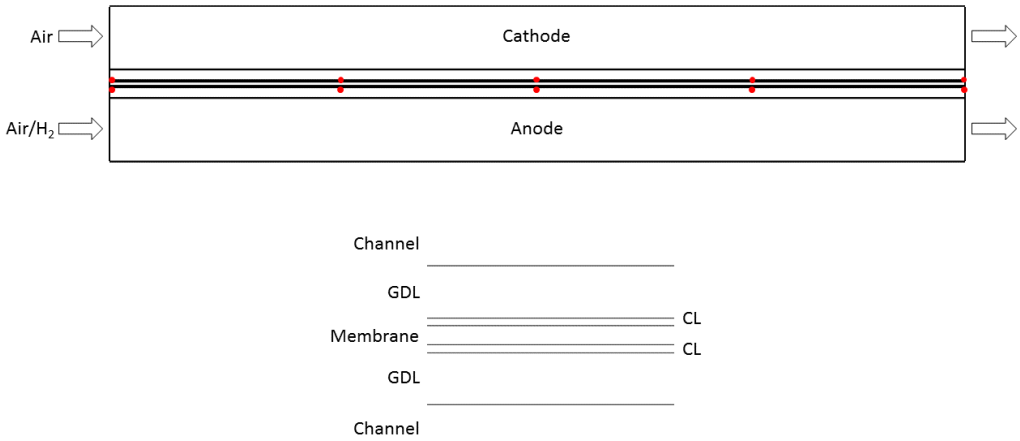

Figure 3.5 – Scheme of the simulated domain with a detail of the MEA layers. The red dots represent the points were probes have been placed; they are labelled with numbers from 1 to 5, with respect to flows direction.

Probe points have been implemented on the interface between CLs and GDLs along the channel length (at start, $\frac{1}{4}$, $\frac{1}{2}$, $\frac{3}{4}$, end of the channel, see Figure 3.5) to mimic the measurement performed with the local RHEs.

3.3.2 Equations

The velocity $\mathbf{u}$, pressure p and concentration ω_i of O_2, N_2, H_2O and H_2 (this last only at the anode) are the variables considered for the flow study. The concentration of CO_2 was not analysed as it is expected to be around some ppm at best, and thus it will not affect much the mass transport behaviour of the system. The temperature is kept constant and the energy conservation was neglected, as temperature variations and heat transfer were not considered of relevance in the short time scale of the phenomena.
The channels are modeled as free media and the left boundary is the inlet, where volumetric flow and concentrations are imposed, while the outlet is posed on the the right boundary: here the back pressure is imposed. The channel side opposite to the MEA is treated as a wall boundary condition while the remaining side is the open interface between the channel and the porous medium, where continuity of velocity and pressure, as well as species concentration, is enforced.
The mass and momentum balance of the Navier-Stokes equations are solved,

Eqn.(3.1), together with the mass balance for each species, Eqn.(3.2). The mass flux relative to the mass averaged velocity $\mathbf{J}_i$, that in our case is only due to molecular diffusion, is calculated using the Fick's law approximation, as in Eqn.(3.3).

$$\frac{\partial \rho}{\partial t} + \nabla \cdot (\rho \mathbf{u}) = 0 \tag{3.1a}$$

$$\rho \frac{\partial u}{\partial t} + \rho(\mathbf{u} \cdot \nabla)\mathbf{u} = \nabla \cdot \left[-p\mathbf{I} + \mu\big(\nabla \mathbf{u} + (\nabla \mathbf{u})^T\big) - \frac{2}{3}\mu(\nabla \cdot \mathbf{u})\mathbf{I} \right] \tag{3.1b}$$

$$\rho \frac{\partial \omega_i}{\partial t} + \nabla \cdot \mathbf{j}_i + \rho(u \cdot \nabla)\omega_i = 0 \tag{3.2}$$

$$\mathbf{j}_i = -\left(\rho D_i^F \nabla \omega_i + \rho \omega_i D_i^F \frac{\nabla M_n}{M_n} \right) \tag{3.3}$$

The GDLs and CLs are instead modeled as porous media. All sides, except the interface with the channel and between GDL and CL, are considered as impermeable walls, and thus the crossover between anode and cathode is also neglected. A volumetric molar source R_i, to which a mass source Q_m corresponds, is placed in the CLs, in order to mimic the species consumption/production due to the electrochemical reactions. It is calculated by summing all the flux contributions from the electrode reactions, of index m, according to Faraday's law:

$$R_i = -\sum_m \frac{\nu_{i,m} i_{v,m}}{n_m F} \tag{3.4}$$

where $i_{v,m}$ is the local current volumetric density of the electrochemical reaction, n_m the number of participating electrons and F is Faraday's constant; the mass exchange is assumed to occur at zero velocity.
To study the fluid dynamics in the porous media, the Brinkman Equations are used, Eqn. (3.5).

$$\frac{\partial (\epsilon_p \rho)}{\partial t} + \nabla \cdot (\rho \mathbf{u}) = Q_m \tag{3.5a}$$

$$\frac{\rho}{\epsilon_p}\left(\frac{\partial u}{\partial t} + (\mathbf{u} \cdot \nabla)\frac{\mathbf{u}}{\epsilon_p} \right) = \nabla \cdot \left[-p\mathbf{I} + \frac{\mu}{\epsilon_p}\big(\nabla \mathbf{u} + (\nabla \mathbf{u})^T\big) - \frac{2\mu}{3\epsilon_p}(\nabla \cdot \mathbf{u})\mathbf{I} \right] - \left(\mu \kappa^{-1} + \frac{Q_m}{\epsilon_p^2} \right)\mathbf{u} \tag{3.5b}$$

Similarly to the channel, species mass balances are implemented, Eqn. (3.6), and the Fick's Law approximation is also used, Eqn. (3.7).

$$\epsilon_p \rho \frac{\partial \omega_i}{\partial t} + \nabla \cdot \mathbf{j}_i + \rho(u \cdot \nabla)\omega_i = R_i \tag{3.6}$$

$$\mathbf{j}_i = -\left(\rho D^F_{i,eff} \nabla \omega_i + \rho \omega_i D^F_{i,eff} \frac{\nabla M_n}{M_n} \right) \tag{3.7}$$

The effective diffusivities ($D^F_{i,eff}$) are used to take into account the effects of the porosity of the media ϵ_p, as the matrix of solid material lowers the volume available for transport, and of the tortuosity τ, that increases the transport length. To calculate them, the values for a non-porous domain (D^F_i) are multiplied for a corrective factor f_{eff}, as in Eqn.(3.8).

$$D^F_{i,eff} = f_{eff} D^F_i \quad f_{eff} = \frac{\epsilon_p}{\tau} \tag{3.8}$$

Other than the gas phase, the electron conducting solid phase (indicated with subscript s) and the ion conducting ionomer phase (indicated with subscript l) are modeled. The electronic potential ϕ_s and the electrolyte potential ϕ_l are the model variables.
The GDL is only electronically conductive and current is conserved. Electron conduction is modeled using Ohm's law, Eqn. (3.9), and the electron conservation is implemented by Eqn. (3.10):

$$\mathbf{i}_s = -\sigma_s \nabla \phi_s \tag{3.9}$$

$$\nabla \cdot \mathbf{i}_s = 0 \tag{3.10}$$

In the CLs there is a current generation due to the electrochemical reactions, thus the electron conservation equation is changed to:

$$\nabla \cdot \mathbf{i}_s = -\sum_m \frac{i_{loc,m}}{d_{CL}} \tag{3.11}$$

The membrane is considered as a perfect electronic insulator and thus the electronic potential is neglected. Instead, both in the membrane and in the CLs, the electrolyte potential is studied and assuming electroneutrality, negligible concentration gradients of the current-carrying ion and approximately constant composition of charge carriers; the following expression can be used for the current density vector in an electrolyte:

$$\mathbf{i}_l = -\sigma_l \nabla \phi_l \tag{3.12}$$

This equation takes the same form as Ohm's law, and so, due to the assumptions above, we consider charge transport in an electrolyte as ohmic.
Similarly to the electric current, also the ionic current balance is implemented, with Eqn. (3.13) for the membrane and Eqn. (3.14) for the CLs.

$$\nabla \cdot \mathbf{i}_l = 0 \tag{3.13}$$

$$\nabla \cdot \mathbf{i}_l = \sum_m \frac{i_{loc,m}}{d_{CL}} \tag{3.14}$$

To simulate the OCV condition of the cell during the Start-up/Shut-down process and to have the internal current circulation typical of the phenomenon, all the external boundary have been set to be electronic and ionic insulators.

Table 3.2 – Model transport parameters

Parameter	Value	Source
$\sigma_{s,GDL}$	$10^7 \frac{S}{m}$	assumed
$\sigma_{s,CL}$	$100 \frac{S}{m}$	typical
$\sigma_{l,CL}$	$2.459 \frac{S}{m}$	typical
$\sigma_{l,MEM}$	$8.197 \frac{S}{m}$	typical
D_{H_2}	$5 \times 10^{-5} \frac{m^2}{s}$	assumed
D_{O_2}	$1 \times 10^{-5} \frac{m^2}{s}$	assumed
D_{N_2}	$1 \times 10^{-5} \frac{m^2}{s}$	assumed
D_{H_2O}	$1 \times 10^{-5} \frac{m^2}{s}$	assumed

The reactions considered in the model are HOR and ORR at the anode and ORR, OER and COR at the cathode. Moreover the double-layer capacitance has been modeled at both electrodes. Each reaction has a different overpotential η calculated as:

$$\eta = \phi_s - \phi_l - E_j^{eq} \tag{3.15}$$

To study the hydrogen oxidation reaction kinetics at the anode, a linearized Butler-Volmer equation (3.16) is used, the linear approximation can be used since HOR kinetics is fast and overpotentials are expected to be low [14, 31, 32, 58].

$$i_{HOR} = i_{0,HOR}\, ECSA_{Pt}\, L_{Pt}\, \frac{c_{H_2}}{c_{H_2,ref}} \left(\frac{(\alpha_c + \alpha_a)F}{RT} \right) \eta \tag{3.16}$$

Here, i_{HOR} is the local current density due to the HOR reaction (the convention for the sign of local currents was set to be positive for oxidation reaction and negative for reduction), $i_{0,HOR}$ is the exchange current density, $ECSA_{Pt}$ and L_{Pt} are the electrochemical surface area and Pt loading of the electrode. The influence of hydrogen concentration is also considered by the ratio $\frac{c_{H_2}}{c_{H_2,ref}}$, which represents the activity of hydrogen. α_c and α_a are the cathodic and anodic transfer coefficient.
The equilibrium potential of the HOR, E^{eq}_{HOR} , and similarly for the other reactions, is obtained from the Nerst equation:

$$E^{eq}_{HOR} = E^{0}_{HOR} + \Delta E_{HOR}(T - 298.15) + \frac{RT}{2F} ln(a_{H_2}) \tag{3.17}$$

Here the term E^0_{HOR} is the standard electrode potential (at $T = 298K$ and $a_{H_2} = 0$) and ΔE_{HOR} is its temperature coefficient. The activity of H_2, a_{H_2}, is defined as the gas partial pressure divided by the standard pressure.
The ORR and OER reactions are described by Tafel kinetics:

$$i_{ORR} = i_{0,ORR}\, ECSA_{Pt}\, L_{Pt}\, \frac{c_{O_2}}{c_{O_2,ref}} \left(- exp\left(\frac{\alpha_c F \eta}{RT} \right) \right) \tag{3.18}$$

$$i_{OER} = i_{0,OER}\, ECSA_{Pt}\, L_{Pt} \left(exp\left(\frac{\alpha_a F \eta}{RT} \right) \right) \tag{3.19}$$

$$E^{eq}_{ORR/OER} = E^{0}_{ORR/OER} + \Delta E_{ORR/OER}(T - 298.15) + \frac{RT}{4F} ln\left(\frac{a_{O_2}}{(a_{H_2O})^2} \right) \tag{3.20}$$

The equations parameters are similar to the one in (3.16) and (3.17), and have already been explained. The activity of water was set equal to 1, in accordance to the fully humidified condition of the simulation.
For the COR, a single-step kinetics is used and thus a Tafel kinetic law is also used:

$$i_{COR} = i_{0,COR}\, (1 - \Theta)^m\, ECSA_C\, L_C \left(exp\left(\frac{\alpha_a F \eta}{RT} \right) \right) \tag{3.21}$$

$$E^{eq}_{COR} = E^{0}_{COR} + \Delta E_{COR}(T - 298.15) + \frac{RT}{4F} ln\left((a_{H_2O})^2 \right) \tag{3.22}$$

In equation (3.21), Θ describes the fraction of the carbon-support that has already been oxidized and m describes the COR rate dependence on Θ. This contribution was suggested by Gu et al. [32] and in this work an average

value for $(1-\Theta)^m$ is used, as in [58]. A maximum carbon loss of 10% is expected at end of life for conventional carbon support and averaging along the lifetime it yields a value of $(1-\Theta)^m = 0.61$, using $m = 10.4$. $ECSA_C$ and L_C are the electrochemical surface area of carbon and the carbon loading of the electrode. L_C relates to L_{Pt} via $r_{Pt/C}$, the weight ratio of platinum over carbon support. In our work COR is assumed to follow a catalyzed path and thus its rate depends on the available Pt surface, for this reason $ECSA_C$ is assumed to be linked to $ECSA_{Pt}$, in a proportional way, even if not explicitly stated.
The double-layer capacitance was modeled at both electrodes and it acts as an additional current source in the CLs, to be added to the ones linked to the electrochemical reactions. It is described as:

$$i_{dl} = -c_{dl}\frac{\partial(\phi_s - \phi_l)}{\partial t} \tag{3.23}$$

The parameters used in the model are summarized in Table 3.3.

3.3.3 Solver

The model is solved with COMSOL Multiphysics® 5.4 with secondary current distribution module and reacting flow in porous media module. The numerical solver needs to find a stationary convergent solution before it can continue. By doing so, the starting condition, with both anode and cathode filled with air, is reached and the flow profiles are fully developed. The stationary problem and each time step of the transient problem are solved using a fully coupled method with direct MUMPS solver. The time-dependent study uses a generalized-α method for the time stepping.

Table 3.3 – Thermodynamic and kinetic parameter values. Values of E_i^0 (at 25 °C) and $i_{0,i}$ (at 80 °C) are referenced to 101.3 kPa gaseous reactant partial pressure

Parameter	**Value**	**Source**
HOR		
$i_{0,HOR}$	$0.3\ \frac{A}{cm^2 Pt}$	[32]
E^0_{HOR}	$0\,V$	[32]
ΔE_{HOR}	$0\ \frac{V}{K}$	[32]
$\alpha_c + \alpha_a$	1	[14]
ORR		
$i_{0,ORR}$	$2.47 \times 10^{-5}\ \frac{A}{cm^2}$	[32]
$E^0_{ORR/OER}$	$1.2291\,V$	[32]
ΔE_{ORR}	$-0.8456 \times 10^{-3}\ \frac{V}{K}$	[32]
α_c	0.5	[14]
OER		
$i_{0,OER}$	$1.89 \times 10^{-9}\ \frac{A}{cm^2}$	[32]
ΔE_{OER}	$-0.8456 \times 10^{-3}\ \frac{V}{K}$	[32]
α_a	0.12	assumed
COR		
$i_{0,COR}$	$1.03 \times 10^{-18}\ \frac{A}{cm^2}$	[32]
E^0_{COR}	$0.2073\,V$	[32]
ΔE_{COR}	$-0.8530 \times 10^{-3}\ \frac{V}{K}$	[32]
α_c	0.67	[32]
T	80°C	–
p_{out}	$101325\,Pa$	–
$ECSA_{Pt}$	$65\ \frac{m^2}{g}$	Voltammetry
L_{Pt}	$0.3\ \frac{mg}{cm^2}$	CCM specification
$ECSA_C$	$800\ \frac{m^2}{g}$	[32]
$r_{Pt/C}$	$0.75\ \frac{g_{Pt}}{g_C}$	Assumed
c_{dl}	$25\ \frac{F}{m^2}$	Voltammetry

3.4 Start-up and shut-down: process description by simulations

Model implementation guarantees information that could not be obtained from experiments, like the circulating currents, and thus the carbon dioxide produced, and indications about how species evolve in time/space. Note that, even if in literature experimental setups for currents measurement have been realized, it is not however possible to distinguish single contributions without a proper modelling.

First of all, potential profiles provided by the model, in Figure 3.6, approximately match with experiments. All main differences are consequence of the real geometry and of 3D effects: in particular ribs/bends cause fluxes alterations with respect to channels, which can weight significantly [77]. In addition, Pt redox reactions are not included in this model version. They could have an impact different from double-layer capacitance, even though, as first approximation, contributions may be considered comparable [32].

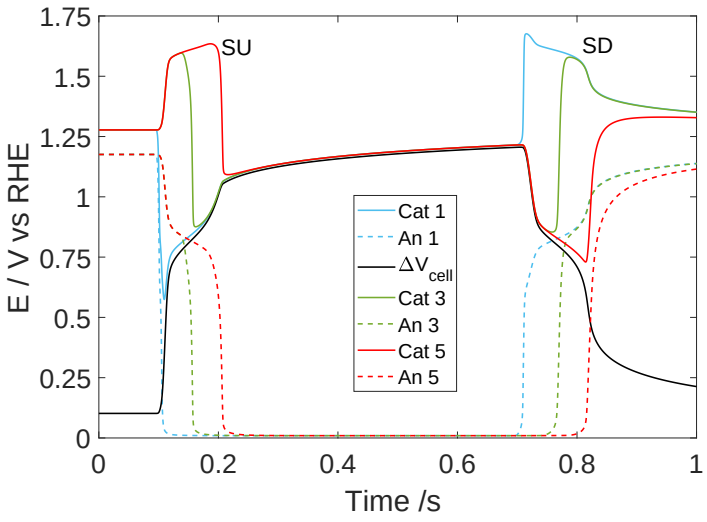

Figure 3.6 – Simulated potentials of cathode and anode in probe positions 1, 3 and 5 during both start-up and shut-down.

Considering start-up, when hydrogen arrives at the inlet of anode side (probe position 1 in Figure 3.6), the potential drops quickly to zero as reduction occurs through the catalyst by hydrogen. Potential of the other probes, for which hydrogen has not come yet, decreases too: reduction reactions are developing thanks to the supply of protons by the cathode, in accordance with the reverse current mechanism. Anyway, rate of decrease is slower in

this case.
At the cathode side, the potential of the inlet goes down, because of oxygen reduction reaction overpotentials, due to both kinetic and mass transport losses. As consequence of the driving force supplied by the active region, the potentials of the passive portion of the cathode go up. During shut-down the configuration is the reverse: the anode inlet potential starts to increase because of oxidation by air. Note that here potential at anode moves significantly only when air has effectively arrived, otherwise H_2 keeps potential close to 0 V. At cathode side, all the points in the H_2-filled region fall, because they operate as a normal fuel cell; the only exception is the cathode inlet, that moves up as a consequence.
During their increase/decrease, anode potentials change concavity when also cathode does. In addition, they show a plateau that is related to ORR, reason for which the only anode point that always work with hydrogen, probe 1 and 5 for Start-up/Shut-down respectively, never present it.
As previously introduced, the model allows to get information about the circulating currents during the Start-up/Shut-down event. It allows to perform analysis with different level of detail, starting from total electronic and ionic current to localized currents arising from one specific reaction. In Figure 3.7 it is possible to see the electric and ionic current circulating in the cell during the start-up process. The direction of the currents is the one typical of the reverse-current mechanism, as described in 1.4.

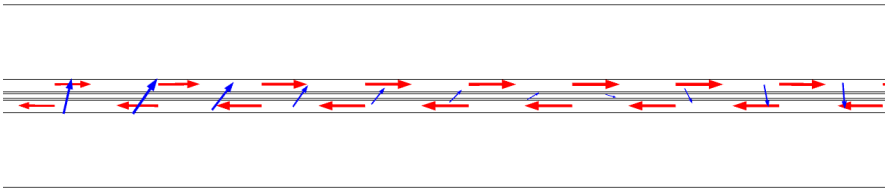

Figure 3.7 – Simulated electric (red) and ionic (blue) current density vector. The arrows do not represent all computed currents vector to improve readability. The image is taken at $t = 0.14\,s$ and represents the portion of the domain going from $x = 13\,mm$ to $x = 26\,mm$.

Figure 3.8 illustrates the total current for each probe position: during start-up, cathode inlet generates a very high local current because it supplies the entire remaining MEA, which works as passive. Indeed, while the first

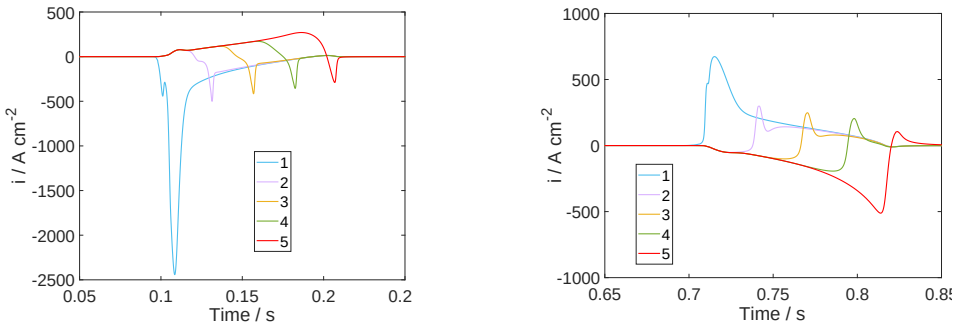

(a) Start-up **(b)** Shut-down

Figure 3.8 – Simulated total currents at each probe of cathode side for both start-up and shut-down. Charts report the summation of faradaic currents due to ORR_{cat}/COR and double-layer capacitive currents. Note the different y-axis.

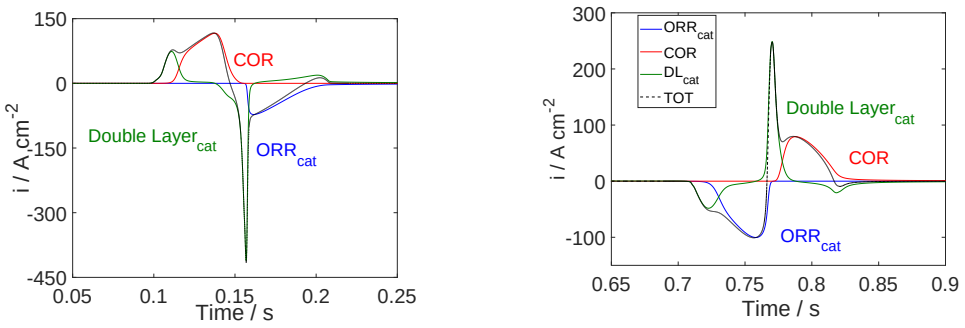

(a) Start-up **(b)** Shut-down

Figure 3.9 – Simulated local currents at probe 3 of cathode side, for both start-up and shut-down. Charts report faradaic currents due to ORR_{cat}/COR and double-layer capacitive currents. Note the different y-axis.

portion fed by hydrogen is always active, all the others become successively active once in presence of H_2. During shut-down peak is not so pronounced: first segment produces the highest COR current, sustained by the major part working as fuel cell.

As told, model allows to discern different current contributions. Considering for example the cathodic side, Figure 3.9 makes evident the weight of capacitance in this non-steady phenomenon: capacitance gives its contribution every time potential starts to increase/decrease. Focusing on start-up, middle probe potential is boosted initially: cathode sustains the raise by, first of all, double-layer capacitive currents and thereafter by carbon corrosion. Note that, for sake of simplicity, oxygen evolution reaction is not depicted in the chart because of its almost negligible contribution at 80 °C for non-graphitized

(a) H_2 molar fraction **(b)** O_2 molar fraction

Figure 3.10 – Simulated concentration of hydrogen (left) and oxygen (right) during the start-up process. The images are taken at $t = 0.14\,s$ and both represent the same relevant portion of the domain, from $x = 11\,mm$ to $x = 24\,mm$.

carbon, as here simulated. When hydrogen arrives, it moves rapidly down the potential, therefore capacitance generates the high negative current peak. This MEA portion starts so to operate with usual ORR; this reaction progressively fades because of the lower and lower passive region to sustain as front proceeds. Potential of this specific point hence raises, changing the sign of capacitive current till leasing, in the end, the overall current to flow in the opposite direction. This is the outcome of charge redistribution, as better described later, in Section 3.6. Figure 3.9.b evidences the inversion in the order of COR/ORR during shut-down, but phenomena are unchanged. Note that COR current is a little lower compared to start-up.

The concentration of the different reactants in time and space is also studied. In Figure 3.10.a, it is possible to see how, during Start-up, the movement of the hydrogen front in the channel is not matched by the hydrogen progress in the catalyst layer, in disagreement with the plug-flow assumption usually used in the literature (see Section 3.5.1). The displacement of the oxygen is also shown in Figure 3.10.b; it is visible how the consumption of O_2 in the CL affects the profile of the outgoing oxygen front in the catalyst layer, as examined later.

3.5 Operating conditions analysis

Some experimental tests and model simulations have been carried on to evidence influences of operating conditions. In this section, the most relevant results are gathered: they are useful to better understand how the process develops and how mitigation is possible.

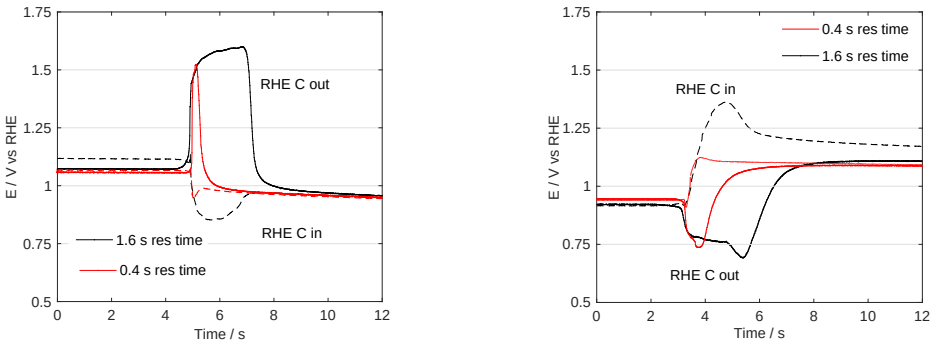

(a) Start-up **(b)** Shut-down

Figure 3.11 – Cathodic potential profiles obtained at different dry flow rates during start-up (a) and shut-down (b) processes, Type A CCM. RH = 100%, $air_{cathode}$ = 200 ml min^{-1}, p_{out} = atm, T = 40 °C. In red: air_{anode} = $H_{2,anode}$ = 200 ml min^{-1}. In black: air_{anode} = $H_{2,anode}$ = 50 ml min^{-1}

.

3.5.1 Effect of purging flow rates and transient duration

An earlier well known mitigation strategy consists in using high purge flow rates [96]. Different dry flows have been tested, while keeping constant the relative humidity. All the operating conditions are the same but dry anode gases are changed by a factor of 4. This procedure has positive effects: tests results highlight decreased detrimental conditions both in terms of lasting of phenomenon and in terms of maximum reached potentials, as clearly visible in Figure 3.11. In addition, the minimum voltage increases, suggesting a reduced overpotential of cathodic ORR.

Residence time

In Figure 3.11 it has been reported the so-called residence time. In literature, this commonly used parameter assumes the plug-flow model for gas replacement at anode side during Start-up/Shut-down. It represents the time necessary for the wet gas flow to completely fill the available volume, given by the combination of flow field ($V^{FF,\ single\ cell}$ = 1.46 cm^3 and $V^{FF,\ segmented\ cell}$ = 1.05 cm^3) and compressed GDL ($V^{GDL,\ Type\ A} \approx$ 0.28 cm^3 and $V^{GDL,\ Type\ B} \approx$ 0.18 cm^3). Its computation is thus expressed as [58]:

$$t_{Res} = \frac{V^{FF} + V^{GDL}}{\dot{V}^{wet}_{T,p,RH}} = \frac{V^{FF} + V^{GDL}}{\dot{V}^{dry}_{0} \frac{p_0}{p_{gas}} \frac{T}{T_0}} \tag{3.24}$$

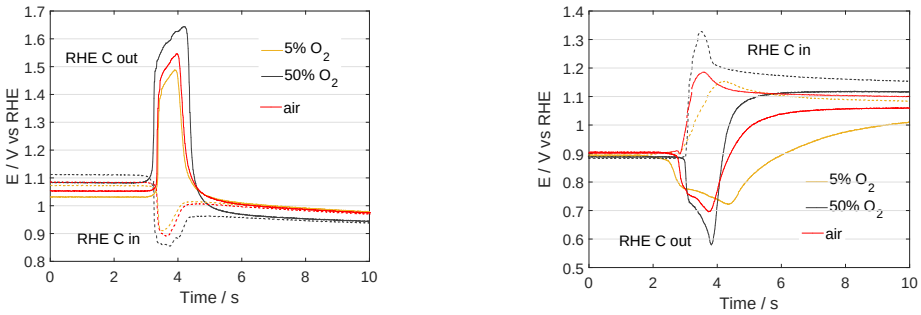

(a) Start-up **(b)** Shut-down

Figure 3.12 – Experimental transients in case of different anode oxidant dilutions for Type A CCM. RH = 100 %, T = 40 °C, air_{anode} = $H_{2,anode}$ = 100 ml min^{-1}, $air_{cathode}$ = 200 ml min^{-1}, res time = 0.8 s.

where T_0 = 273.25 K, p_0 = 101.3 kPa and p_{gas} = p - p_w. From this first example it is clear the discrepancy between the real phenomenon duration and the computed time: phenomena go on 2/3 times more and, mainly for low flow shut-down, the final part for equilibrium reaching seems very long. Thus, representation by a simple gas substitution does not seem thorough.

3.5.2 Oxygen dilutions at anode

Both experimented and simulated dilutions of O_2 at anode have revealed its key role. Tests done on Type A CCM, in Figure 3.12, highlight an impact on both start-up and shut-down:

- Increase of maximum potential at cathode during both start-up and shut-down as $\%O_2$ increases;
- Increase in the overpotential of the cathodic ORR as $\%O_2$ increases. Since the active part of the cell have not been altered in these tests, such result hints at a larger reverse current;
- An increase in the duration of the phenomenon as $\%O_2$ increases, in particular for shut-down.

Impact on potentials

Briefly aforementioned results of Type A CCM have been confirmed by Type B CCM: a decreased oxygen concentration generally weakens maximum potentials, hence the driving force for carbon corrosion. Figure 3.13 shows clearly

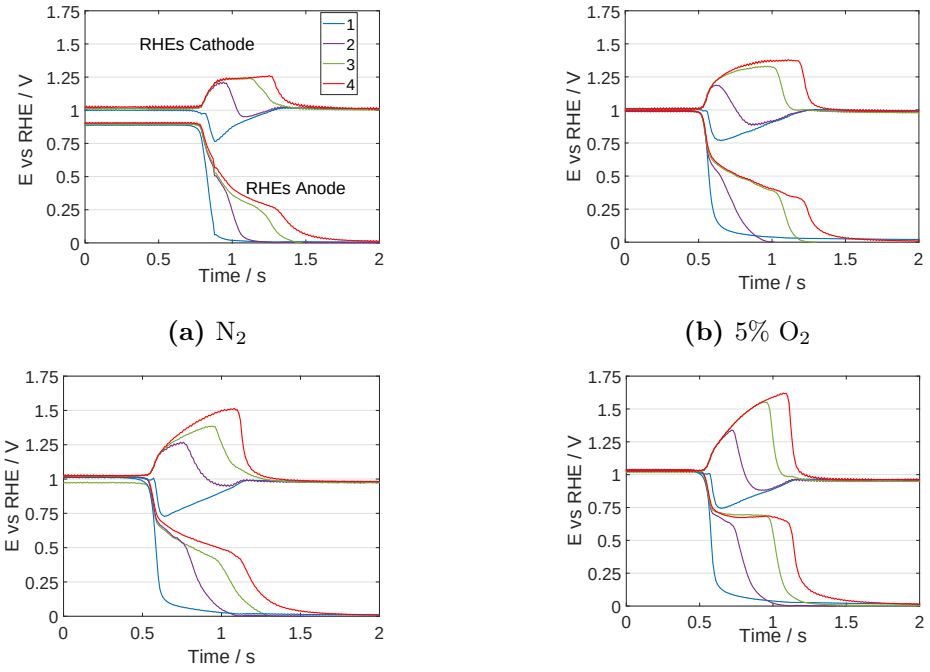

(a) N_2 **(b)** 5% O_2

(c) 20.9% O_2 **(d)** 50% O_2

Figure 3.13 – RHEs potential profiles obtained at different anode oxidant dilutions during start-up for Type B CCM. RH = 100%, T = 30°C, $flow_{anode}$ = 175 ml min^{-1}, $air_{cathode}$ = 417 ml min^{-1}, p_{out} = p_{atm}.

anodic profiles: a plateau is present when ORR reaction is expected to develop. Due to the strong effect of ORR kinetics, a lower oxygen concentration significantly decreases the potential drop at the fuel cell anode thus reducing the potential developing at the positive electrode. This part of the anodic curve becomes flatter as $\%O_2$ moves up, suggesting that abundant reactants sustain the reaction. At the opposite, at low percentages of oxidant, anode polarization progressively vanishes as if O_2 is extinguishing. Unpredictably, process still exists even when only nitrogen is present at anode side, probably because of capacitive effects, contributions of which are better explained in Section 3.6, and/or gas crossover. Maximum is however lower and cathodic potential stays around 1.25 V. Anodic plateau does not exist; only a change in the decreasing rate is evident. Dillet et. al [19] have recorded currents in case of N_2 anode-filled, in agreement with our results, but specific contributions should be clarified.
In literature, there is no focus on recordings of anode potentials; however, as seen, they could be useful to understand how process is developing and to add further information against cathode. Model results are in accordance with experiments. Voltage profiles are coherently modified at both the electrodes as oxygen dilution is changed (Figure 3.14.b): all the overpotentials are boosted as well as currents, thus the total carbon corroded significantly increases with $\%O_2$, as in Figure 3.14.c.

Impact on duration

Both Figure 3.12 and Figure 3.14, that means experiments and model, evidence longer persisting events as oxygen is moved up. This happens even though the wet volumetric flow is unchanged; in other words, residence time has not been varied.

The modelled events suggest that species reactions take part in lasting. In absence of reactions (Figure 3.14.a), phenomenon is longer because in MEA regions where diffusion prevails - catalyst layer above all - H_2 substitutes air quite difficultly. In case of electrochemical reactions, the first decreasing part of the O_2 molar fraction curve indicates species consumption by ORR reaction. Then, the second change in concavity coincides with a progressive substitution by hydrogen, as summarized in Figure 3.15. When the amount of reactant is low, the process ends even before the front has gone out (computed residence time is 0.105 s). In practice, what happens along the channel differs from the catalyst layer mainly because of species reactions: as the amount of oxygen to consume is larger, process continues for longer.
Oxygen concentration effect becomes even more evident in case of shut-down, as seen before in experimental results. When air enters, oxygen must consume

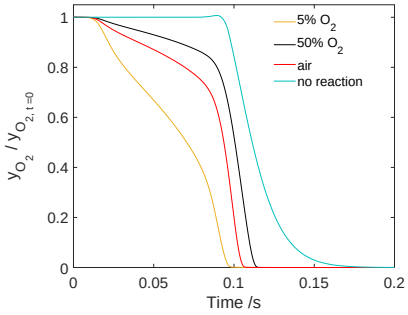

(a) Normalised molar oxygen fractions at outlet (probe 5)

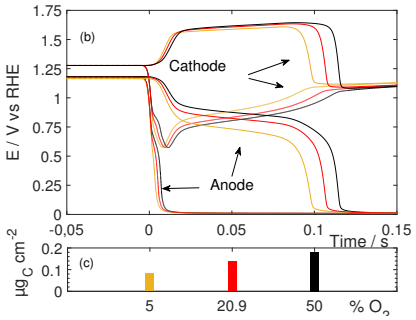

(b) Voltage profiles at probes 1 and 5, for both anode and cathode and (c) corroded carbon

Figure 3.14 – Simulated Start-up in case of different $\%O_2$ at anode. Volumetric flows are fixed. Results are for the catalyst layer/GDL interface.

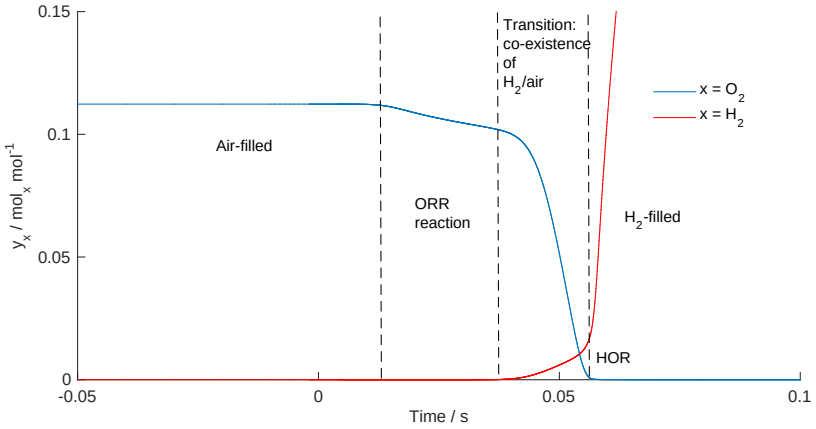

Figure 3.15 – Simulated molar fractions of H_2 and O_2 at middle point of anode catalyst layer/GDL interface during start-up (probe 3). Subdivision in main operating steps.

the abundant hydrogen that fills the anode: active part accounts for the majority of the cell. In broad terms, one mole of oxygen should react with two of hydrogen but O_2 volume is just a fifth of the total dry flow, such that transition in catalyst layer is decelerated compared to start-up: this is a possible contribution in explaining time differences between the two processes.

As seen for oxygen, hydrogen dilution can modify the transient as well. A tested 70% hydrogen in N_2 has shown a significant reduction of maximum COR/OER peak for shut-down, from 1.40 to 1.25 V. The total amount of hydrogen in the anode, to be consumed by coming oxygen, has caused the

alteration. In the meanwhile, no relevant changes are visible during start-up probably because hydrogen is enough to react with the already present oxygen, that is thus more limiting. More detailed investigations about this case were not carried on since, as explained in Chapter 5, start-up is the relevant process to mitigate, on which we concentrated.

3.5.3 Gas diffusion

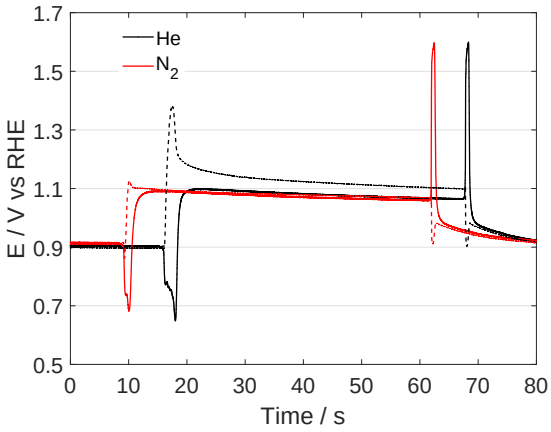

Figure 3.16 – Potential profiles during shut-down and start-up processes in case of different dilution gases (He and N_2) at anode side, Type A CCM. RH = 100%, T = 40°C, $air_{cathode}$ = 200 ml min^{-1}, $\%O_{2,anode}$ = 20.9, p_{out} = p_{atm}.

Another dissimilarity should be considered to explain the asymmetry between Start-up/Shut-down: through-plane diffusion differs in case of H_2 and O_2. As seen previously in simulations, residence time and phenomenon lasting in absence of reactions are not equivalent, hence porous media has an impact in the developing of the event. Perpendicularly to the channel, species transport is primarily diffusion controlled, thus gradient of concentrations and diffusion coefficients - that are both larger for H_2 than O_2 - could have effect.
The slower changes of potentials from hydrogen to air could be also the result of gas phase mass transport limitation for oxygen: voltage at cathode increases at a lower rate as $\%O_2$ is reduced, as visible in Figure 3.12.b. Limitations are instead not evident for hydrogen during start-up. Note that diffusion has an impact similar to species consumption, described in the previous section, in explaining Start-up/Shut-down divergences. Discerning the contributions of the two effects is not easy; they change for sure also in dependence on specific material characteristics.

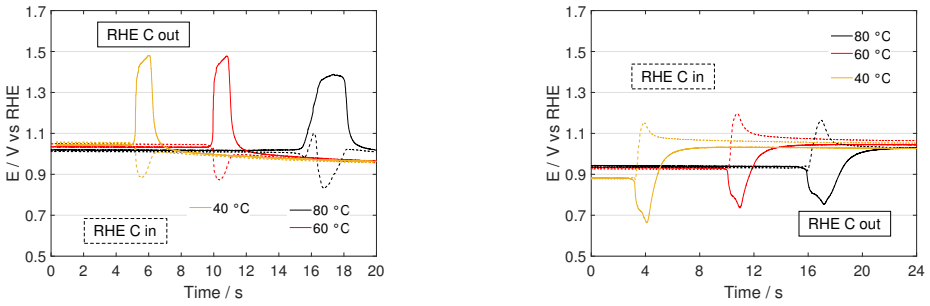

(a) Start-up **(b)** Shut-down

Figure 3.17 – Cathodic potential profiles obtained at different temperatures during start up (a) and shut down (b) processes. RH = 100%, res. time = 0.8 s, $\text{air}_{\text{cathode}}$ = 200 ml min^{-1}, p_{out} = atm.

About the weight of diffusion, it may be observed in Figure 3.17 that duration of the event seems longer in case of high temperature compared to low, in spite of the same wet mass flow rate. If total flow and RH are fixed, at high temperatures the amount of water is larger thus the reduction of reactants molar fractions and so the reduced driving force for diffusion. This is a possible cause in a case in which the proportion between reactants has been kept constant and thus no alterations due to species consumption are expected.

Furthermore, to test the effect of oxygen transport, nitrogen has been substituted with helium as dilution gas. Their molecular weights (M_{He}=4 g/mol while M_{N_2}=28 g/mol) bring about other molecular transport; the ratio between binary diffusion coefficients, evaluated in Chapman-Enskog theory, is slightly larger than three[73]. Note that the diluent does not affect Knudsen diffusion. As clearly visible, the molecular transport of O_2 through the anode modifies the voltage peak in shut-down, while start-up transient characteristics remain the same between the H_2/Helox and the H_2/air cases. O_2 mass transport limitations are thus not relevant when hydrogen is introduced in the cell and oxidant is still present, but transport of molecular oxygen to the electrode during shut-down is strongly dependent on the diluting inert gas. Proof of described results are by Schneider et al. [77].

3.5.4 Operating cell temperature

Since the kinetics of electrochemical reactions is strongly influenced by the temperature, this parameter has been taken into account. As well known in literature, carbon corrosion is lower at low temperatures [43, 58, 96]. Anyway, it has been found that a reduced current due to corrosion is not associated

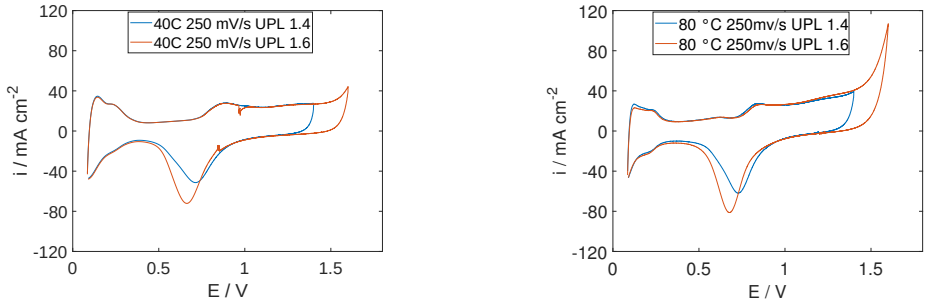

(a) 40 °C **(b)** 80 °C

Figure 3.18 – CVs obtained at different temperatures (40 °C and 80 °C) and UPL (UPL = 1.4 / 1.6 V), LPL = OCV, RH = 100%, H_{2anode} = 60 ml min^{-1}, $N_{2,cathode}$ = 60 ml min^{-1}, Sc = 250 mV s^{-1}. Sc has been set to be reasonably comparable to real start-up rate of change.

to lower cathode maximum voltages, as visible in Figure 3.17. It is the cathodic ORR overpotential at high temperature that suggests a boosted reverse current: kinetic losses are indeed reduced as temperature goes up hence the even lower potential for cathodic ORR during start-up signs how the process is altered. The behaviour during shut-down is instead more difficult to interpret. Note that to compare results the wet volumetric flow rate has been set constant. Therefore, while increasing the temperature, the gases dry flow rates are reduced because relative humidity is unchanged. Thus gases partial pressures vary a lot and this should be considered in the physical interpretation of results.

To quantify how much temperature could weight in carbon corrosion, a different type of test has been carried out. Some CVs were realised till high voltages to highlight current evolution. In case of real start-up, voltage is not fixed. Anyway, to generate a certain current, mainly determined as seen by anodic ORR and thus by anodic oxygen, COR/OER peak changes: as visible from the plots, voltage can raise even though current is lower at a different temperature.

3.6 Double-layer and pseudo-capacitance contributions

As briefly introduced in Section 1.4 and seen in simulation results (Section 3.4), capacitive effects, due to both double-layer and pseudo-capacitance, may be non negligible. They can significantly influence the charge balance in

start-up as well as during shut-down. Double-layer capacitance (c_{dl}) is due to an accumulation of ionic and electronic charges at the interface between electrolyte and metal, thus it should be described as:

$$i_{dl} = -c_{dl}\frac{\partial \phi}{\partial t} \tag{3.25}$$

Pseudo-capacitance is instead more complicate, since it comes from Pt redox reactions and it is therefore affected by catalyst state of oxidation. Reactions that occur in air regions are, for example:

$$Pt + H_2O \leftrightarrow Pt(OH) + H^+ + e^- \tag{3.26}$$

$$Pt(OH) \leftrightarrow PtO + H^+ + e^- \tag{3.27}$$

while in presence of hydrogen:

$$2Pt(OH) + H_2 \rightarrow 2Pt + 2H_2O \tag{3.28}$$

The model highlights non-secondary currents for both cathode and anode capacitance. Even PtOx are not included, Figure 3.19 suggests a quite large input.
A first visible effect of capacitive contributions consists in the Start-up/Shut-down asymmetry of voltage peaks. Oxidation of platinum at cathode electrode reduces carbon corrosion both during start up and shut down because it supplies parts of the protons required by the anode in place of support corrosion [31]. The anode capacitance instead plays two different roles. During start-up the surface is reduced (moving from air to hydrogen) thus it represents a further requirement of charges that promotes cathodic reactions. At the opposite during shut-down surface is oxidized (moving from hydrogen to air), so part of charges are internally supplied at the anode side. This is one of the main cause of lack of symmetry between the two processes.

Figure 3.19 displays the results: the different anodic contribution is evident and in case it has the same sign of COR, this is an advantage. Here cathodic double-layer changes globally its sign, since it depends on voltage increase/decrease, representing thus not always a positive contribution in reducing COR; consider that pseudo-capacitance, not simulated, behaves differently since, at high voltages, cathode surface reduction is not expected. In addition, note that COR global current during shut-down does not increase as much as in start-up. Furthermore, as visible comparing the results for the two different CCMs (Figures 3.3 and 3.2 versus Figure 3.4), maximum voltages are closer between start-up and shut-down if the anodic catalytic loading is

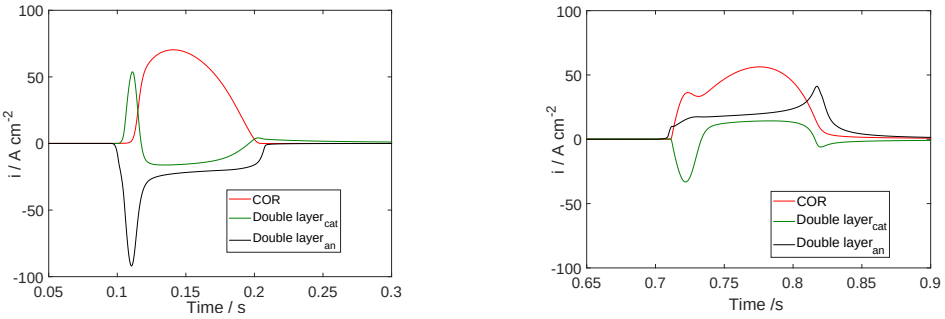

(a) Start-up **(b)** Shut-down

Figure 3.19 – Simulated global currents both during start-up and shut-down. Here faradaic COR and capacitive currents, due to double-layer of both anode and cathode, are reported in time.

reduced, that is the Type B CCM case. Indeed, a change of cathodic loading affects, in theory, Start-up/Shut-down in almost the same way, while less catalyst at anode reduces the counterposed pseudo-capacitive contributions in the two processes. In addition, in Figure 3.20, the effect of the oxidation state, that inevitably alter the PtOx reactions, is visible during consecutive start and stops processes: an increase in the maximum potential, with an almost logaritmic trend, is detected.

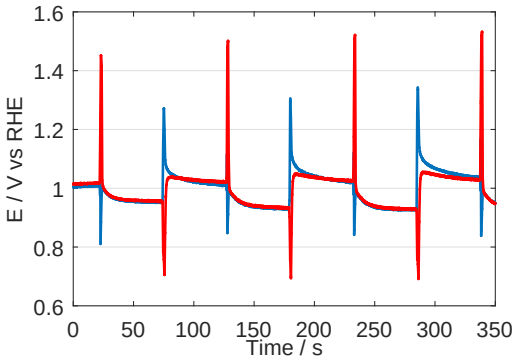

Figure 3.20 – Example of voltages trend in consecutive Start-up/Shut-down, Type A CCM. In blue: $RHE_{C,in}$, in red: $RHE_{C,out}$. RH = 100%, T = 80°, $air_{cathode}$ = 200 ml min^{-1}, $air_{anode} = H_{2,anode}$ = 50 ml min^{-1}.

From one cycle to the consecutive, cathode is just partially reduced because it is moved to potentials lower than H_2/air OCV only when it operates with ORR during the transient. We suppose that oxidation state is the major contribution to the peaks alteration: after being refreshed at low potentials

indeed, cathode shows the same trend again. The effect of retention at high voltages could be explained performing some cyclic voltammetries. The results are reported in Figure 3.21: fixing the LPL and the UPL at 1 V and 1.6 V respectively, the produced current is progressively reduced till an almost stabilised value. During a real transient, instead, no potential profile is directly imposed. The operating conditions are fixed hence the amount of oxygen to consume is unvaried; that circulating current is imagined not to change, so reached potentials are progressively higher. Notably, profiles obtained cycling at high voltages are almost equivalent for N_2 and air.

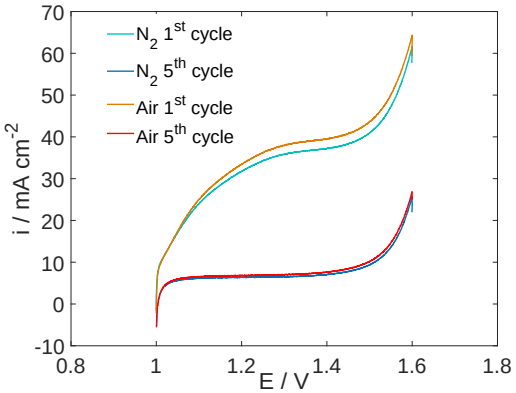

Figure 3.21 – CV: potential profiles during 5 cycles between 1 V and 1.5 V on Type A CCM, both in nitrogen and air. T = 80 °C, RH = 100 %, Sc = 250 mV s^{-1}, N_2 and air flow set equal to 200 ml min^{-1} while H_2 flow is 50 ml min^{-1}, as in Start-up/Shut-down test.

In case of very slow transition (Figure 3.22), it's remarkable the more symmetric behaviour between start/stop, in particular for the cathode inlet. Indeed slow fronts reduce the weight of capacitive effects, that run out in a short time: as seen in Section 3.4, as capacitance supply expires, COR develops. As duration increases, the peaks attenuation during shut-down is not ensured, justifying the closer similarity. For this particular test it was necessary to increase the holding time in air/air and in H_2/air to 180 s, to guarantee equilibrium OCV before gas switching. Process lasted much more than residence time, approximately 10 times: diffusion should prevail.

3.6.1 Balancing phenomenon

The use of the segmented cell hardware and the related analysis of segments voltages have been useful to partly understand time discrepancies. Start-up process has been reproduced both using short-circuited and not short-circuited segments, as in Figures 3.23 and 3.24.

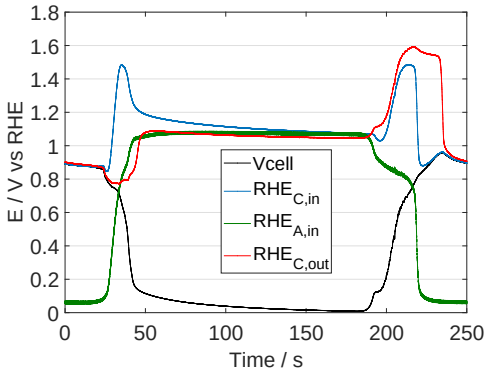

Figure 3.22 – Slow SUSD, Type A CCM. RH = 100 %, T = 40°, $air_{cathode}$ = 200 ml/min, air_{anode} = $H_{2,anode}$ = 6 ml/min.

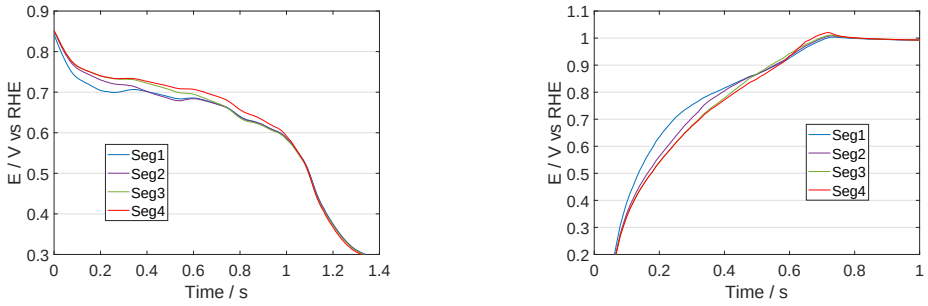

(a) Shut-down **(b)** Start-up

Figure 3.23 – Experimental segments voltages obtained with short circuiting on CCM Type B. RH = 100%, T = 30°C, air_{anode} = H_{2anode} = 100 ml min^{-1}, $air_{cathode}$ = 200 ml min^{-1}, p_{out} = p_{atm}.

Focusing the attention on segments voltages, it is evident a point of intersection. Referring to Start-up, at the beginning the potential of the first segment increases faster as the electrons flow in-plane from the outlet to the inlet at cathode side. Then, potential differences arrives at zero, meaning that current is no more present. Anyway, cell is not at equilibrium yet: points close to the anode outlet have been at high potentials longer needing to be reduced, while the opposite situation is found close to the inlet. The adjustment necessary to reach a new stable state occurs through capacitive contributions. They determine a current flowing in the other way round (Figure 3.25) and thus the inversion of segments potentials. Capacitive effects represent so an inertia that let the cathode stay at high voltages for a longer time compared to what expected by the reverse current decay mechanism. Phenomenon is seen both during start-up and shut-down. However, inversion

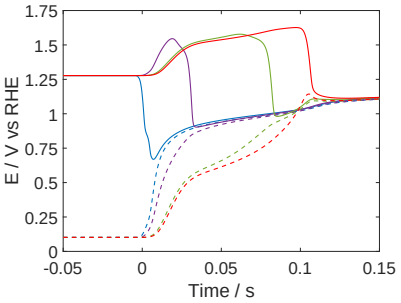

(a) Model, reduced conductivity

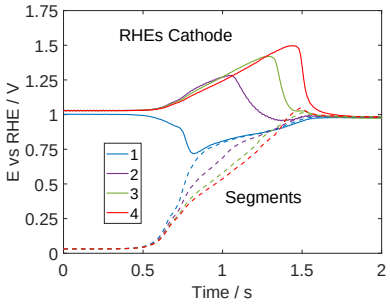

(b) Experimental, not short-circuited segments

Figure 3.24 – For model result, electric conductivity has been reduced in GDL. In experiments, cathode and segments potential profiles obtained without short circuiting, Type B CCM. RH = 100%, T = 30 °C, $\text{air}_{\text{anode}}$ = $\text{H}_{2\text{anode}}$ = 175 ml min^{-1}, $\text{air}_{\text{cathode}}$ = 417 ml min^{-1}, p_{out} = p_{atm}.

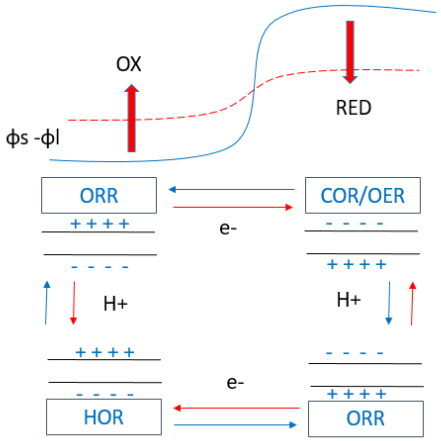

Figure 3.25 – Schematic of balancing phenomenon. In blue, the reverse-current mechanism during transient. In red, the balancing occurring after front have passed: current inversion. Qualitative ϕ_s-ϕ_l is referred to the cathode electode.

is not so pronounced in the latter case, perhaps because of lower voltages reached due to minor currents: in this way, the leading force is lessened.

The developed model, as told, permits to estimate the currents generated by the event. Even though it does not consider the Pt redox reactions but double-layer capacitance only, it shows the inversion of current flow near the process end, that is visible in the total current change of sign, as clear in Figure 3.26.b. The experimentally visible phenomenon is thus confirmed. In greater detail, considering start-up, the inversion does not occur instantaneously

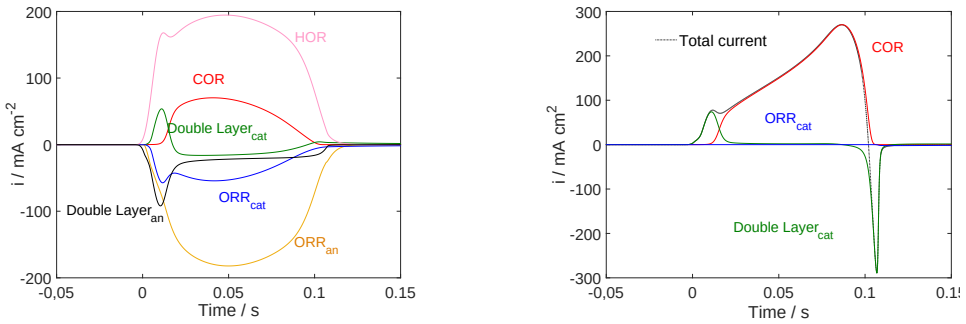

(a) Evolution of global currents

(b) Local currents for cathode outlet

Figure 3.26 – Simulated currents, global (a) and local (b), for H_2/air start-up.

for the whole MEA but the inlet portion starts reducing before H_2 has got out. In addition, an acknowledgment has been found in work of Dillet et alt. [48], that evidences the existence of balancing contributions measuring local currents.

In Type B CCM, the balancing seems to last for about the 25% - 35% of the total process duration, slightly depending also on the maximum reached voltages. In addition, the computed start-up residence time, in the test campaign on Type B CCM, is very close to the intersection point. During shut-down, the voltage trend of segments is complementary, but the process lasts longer. Residence time is not even able to predict the intersection point in this second case.

The previously introduced Figure 3.24 reveals also larger deviations in segments voltages as they are not short-circuited. Currents, that are expected to normally flow in the flow field, are probably forced in the GDL which has a lower conductivity: in-plane resistance hence increases. By the way of the model, this configuration is simulated lowering the GDL conductivity of 3 orders of magnitude. Voltage profiles thus open and segments undergo a more pronounced overshoot, that fits experimental trends. It is concluded that the overshoot that appears in experiments - even in single cell hardware - occurs during balancing phenomenon and it is affected by electronic conductivity.

3.7 Model upgrade with platinum oxides reactions

In the previous sections the contribution of platinum oxides reaction was clarified. Pt oxides formation have a positive effect at cathode passive zone, during Start-up, due to anodic current contribution that limits the COR

currents required to close the charge balance. Despite, at anode electrode, the Pt oxides reduction have a negative effect, during Start-up, because the charge associated to Pt reduction must be sum to the oxygen one, to provided the total reduction charge at the passive zone of anode electrode. Moreover, during balancing phenomena, the PtOx reaction reverse their contributions, i.e. oxide formed must be reduced when potential decrease, or, conversely Pt free site are oxidised when potential increases at active cathode part. In addition, as observed in temperature stressor section, due to the change of operating conditions, the potential at the cathode electrode increases during Start-up at ambient temperature, despite, the carbon oxidation kinetics is inhibited. A fine-tuning of platinum oxides reaction and carbon corrosion reaction is therefore needed, to improve model reliability.

In order to investigate the PtOx contributions and the influence of the operating conditions two multiscale models which includes the formation and reduction of platinum oxides, were developed. A 0-dimensional model of cathode catalyst layer was developed, to use experimental data from cyclic voltammetry to calibrate the platinum oxides and carbon oxidation reactions. To achieve the final goal the coupling between the spatially resolved start-up model and the PtOx kinetics submodel which accurately describes all relevant mechanisms from the nanometre scale up to the cell level was realised.

Platinum oxides reactions

Platinum electrochemistry comprises of three well-known phenomena, platinum oxide formation and reduction in cyclic voltammetry (CV) at different scan rate [71], at different maximum potentials [75] and potentiostatic platinum oxide growth [16]. The growth of oxide films on platinum in the absence of oxygen has been studied for decades. The oxide growth phenomenon is typically studied considering the oxidation of water on platinum. In the potential range 0.6-1.2 V, the products of platinum oxidation from water are either Oxides [42] or both Oxides and Hydroxide [3] or Super-Oxide [71]. The characteristic features of oxide film growth are the logarithmic growth of oxide with time observed in potentiostatic experiments. In order to explain this characteristic response during platinum oxide formation, some amount of surface reconstruction is considered to occur at the interphase between metal and oxide. The reconstruction refers to the formation of sub-surface oxide within the platinum lattice. These surface reconstruction steps could be considered as post electrochemical steps that cause irreversibility of oxide formation seen during CV.

Although this background review makes no claim to be exhaustive, it provides brief information on the most important phenomena connected with

platinum oxides currents that contributes during Start-up process.

The calibration of platinum oxides started from experimental cyclic voltammetries in inert atmosphere (i.e. H_2/N_2 operations). Cyclic voltammetry is a common electrochemical technique used to study platinum oxides formation and reduction, under varying scan rates and upper potential limits (UPLs). Specific protocols has been adopted to evaluate three main features related to PtOx phenomenon:

- **Protocol 1 - Cyclic Voltammetry at different Upper Potential Limits:** under dynamic conditions, the effect of upper potential limits was studied. The CVs were performed at fixed scan rate of 100 mV/s^1 between lower potential limit of 0.076 V vs RHE (OCV in H_2/N_2) and varying the UPL from 0.7 to 1.6 V vs RHE for ten points evenly spaced. The tests were repeated four times for the following temperatures: 30-40-60-80 °C;

- **Protocol 2 - Holding Test:** the characteristic logarithmic growth of oxide film was investigated with time in potentiostatic experiments. Holding tests, at fixed potential of 1 V vs RHE (OCV in H_2/Air operation), were performed in time array from 30 s till one hour. Anodic surface oxidation as a function of time was studied during reduction of the oxide film in a cathodic linear potential sweep experiment (at fixed scan rate of 50 mV/s^1). The protocol is designed to assess oxide extent in an electrochemically more stable (place-exchanged) state than the oxide formed more rapidly.

- **Protocol 3 - Fast Cyclic Voltammetry:** another characteristic of the experimental CV is the nearly constant position of the reduction peak, regardless of the UPL and scan rate. During fast CV the scan rate was varied from 125 to 1000 mV/s^1 over a wide potential range from 0.076 to 1.5 V vs RHE. The test was repeated at 30 and 80 °C.

Data collected from protocol one and two were used for model calibration, instead experimental results from protocol three were compared with simulation to validate the model. In figure 3.27 the CVs collected at different UPLs and temperatures were depicted.

Due to the effect of varying the upper potential limit at a constant scan rate, the position of the reduction peak significantly decreases from 0.8 V to 0.7 V, indicating that more stable oxides were formed or a more irreversible reaction is occurring. Despite, temperature usually exponentially increases the kinetics of electrochemical reactions, the rate of Pt oxides formation has barely changed with increasing the temperature. Conversely, the rate of

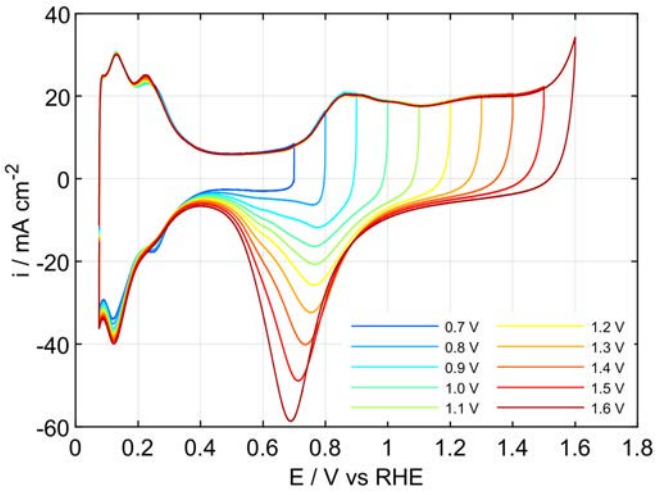

(a) Temperature 30 °C

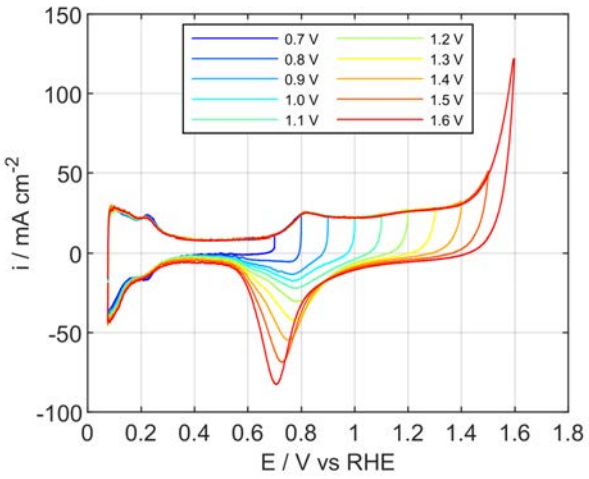

(b) Temperature 80 °C

Figure 3.27 – Experimental CVs for a commercial MEA with a Pt/C catalyst under dynamic conditions in inert atmosphere. Operating conditions: 100/100% RH, $p_{out,anode} = p_{out,cathode} = p_{amb}$, $N_{N2} = N_{H2} = 60$ ml min^{-1}.

carbon oxidation reaction has strongly increased. Results of protocol two and three are depicted below when comparison with simulation is highlighted.

Model equations

Many researchers have attempted to simulate cyclic voltammetries to gain a better understanding of the platinum oxides reactions. Each study is able to replicate some features, but none have achieved the correct shape and behaviour of CVs over a wide range of operating conditions. In a fundamental work, Conway et al. [16], proposed a simple mathematical law, in which the rate equation has no coverage-dependent preexponential term (i.e. $1-\theta_{PtOH}$), in anodic reaction (in Tafel form), so that the coverage dependence during the growth process, is only described through the term: $\exp(-g \cdot \theta_{OH})$. With further assumptions, this model can predict direct oxide growth in time over one monolayer of Pt (i.e. place-exchange mechanism). Darling and Meyers [18] utilized this idea and added a cathodic term to the place exchange model to derive a modified Butler-Volmer rate equation, to describe platinum oxide formation from water oxidation and reconversion to water. However, replicating their model and simulating under proposed protocols yields only one oxidation/reduction peak, while during holding tests and fast CVs a peaks separation was clearly visible, with the effect of a wider current's reduction zone. Additionally, a new re-parametrization of the entire model is necessary to accurately reproduce PtOx currents during Start-up operation.

To overcome such limitations, a semi-empirical two-step oxidation mechanism is proposed. One fast reversible oxidation step:

$$Pt + H_2O \rightleftarrows PtOH + H^+ + e^- \tag{3.29}$$

followed by a second, slower, reversible oxidation step:

$$PtOH \rightleftarrows PtO + H^+ + e^- \tag{3.30}$$

The place-exchange is not explicitly model but is taken into account by the semi-empirical formulation. The kinetics of these reactions is described by:

$$i_{PtOH} = i_0 \cdot \exp\left(\left(1 - \frac{T_{OP}}{T_{ref}}\right) \cdot \left(\frac{E_{act,PtOH}}{R \cdot T_{OP}}\right)\right) \cdot \left\{\exp\left(-\frac{\omega_{PtOH} \cdot \theta_{PtOH}}{R \cdot T_{OP}}\right) \cdot \exp\left(\frac{\alpha_{PtOH} \cdot F \cdot \eta_{PtOH}}{R \cdot T_{OP}}\right) - \theta_{PtOH} \cdot \exp\left(\frac{(1-\alpha_{PtOH}) \cdot F \cdot \eta_{PtOH}}{R \cdot T_{OP}}\right)\right\} \tag{3.31}$$

$$i_{PtO} = i_0 \cdot \exp\left(\left(1 - \frac{T_{OP}}{T_{ref}}\right) \cdot \left(\frac{E_{act,PtO}}{R \cdot T_{OP}}\right)\right) \cdot \left\{\theta_{PtO} \cdot \exp\left(-\frac{\omega_{PtO} \cdot \theta_{PtO}}{R \cdot T_{OP}}\right) \cdot \exp\left(\frac{\alpha_{PtO} \cdot F \cdot \eta_{PtO}}{R \cdot T_{OP}}\right) - \theta_{PtO} \cdot \exp\left(\frac{(1 - \alpha_{PtO}) \cdot F \cdot \eta_{PtO}}{R \cdot T_{OP}}\right)\right\} \quad (3.32)$$

And overpotential is obtained by:

$$\eta = \phi_s - \phi_l - E^0 \quad (3.33)$$

Standard electrode potentials has been fitted by cyclic voltammetries data while temperature effect are considered into kinetics (i.e. activation energy terms). The temperature coefficients and the activity corrections on Nernst equations were neglected. The surface coverage has been calculated as

$$\frac{d\theta_{PtOH}}{dt} = \frac{i_{PtOH}}{N_{Pt} \cdot F} - \frac{i_{PtO}}{N_{Pt} \cdot F} \quad (3.34)$$

And

$$\frac{d\theta_{PtO}}{dt} = \frac{i_{PtO}}{N_{Pt} \cdot F} \quad (3.35)$$

The maximum surface coverage for platinum is calculated by:

$$N_{Pt}\left[\frac{mol}{m^3}\right] = \frac{2.1\left[\frac{C}{m^2_{Pt}}\right] \cdot rf\left[\frac{m^2_{Pt}}{m^2_{GEO}}\right]}{F\left[\frac{C}{mol}\right] \cdot d_{CL}[m]} \quad (3.36)$$

The production of CO_2 is considered by a direct path (not catalyzed). Carbon oxidation kinetics is expressed by a Tafel law:

$$i_{COR} = i_0 \cdot \exp\left(\left(1 - \frac{T_{OP}}{T_{ref}}\right) \cdot \left(\frac{-E_{act,COR}}{R \cdot T_{OP}}\right)\right) \cdot \exp\left(\frac{\alpha_{COR} \cdot F \cdot \eta_{COR}}{R \cdot T_{OP}}\right) \quad (3.37)$$

$$E^0_T = E^0_{298} + (T - 298.15) \cdot \left(\frac{dE^0}{dT}\right)_{298} \quad (3.38)$$

Model optimization

Starting from the 0D model described above the identification of physical model parameters was based on particle swarm optimization (PSO). PSO mimics the swarming behaviours of living creatures in avoiding predators and food search. This is achieved through constant communication and

coordinated decision making between all the particles in the swarm. The algorithm is conceptually simple and computationally efficient. The following steps summarize the PSO algorithm's procedure:

- Initialize a population of particles with predefined positions xi and velocities vi on a N dimensional space;
- Evaluate the fitness function for each particle with respect to the initial N variables;
- Compare the particles fitness values with the personal best fitness (p_{best}) value a particle has achieved in previous iteration. If current value is better, then update p_{best} and set particle to equal the current position in the N space;
- Identify the particle with the best success in the swarm and assign its fitness value to global best variable (g_{best}) and its position to global best position of the swarm (variable G);
- Change the velocities and positions of each particle in the swarm according to *particleswarm* routine implemented in Matlab 2019b;
- Iterate from point two until a sufficiently satisfactory fitness value or a maximum number of iterations is reached.

The PSO fitness function is based on calculation of mean squared error, that is the average squared difference between the simulated values and the experimental values.

$$MSE = \frac{1}{n}\sum_{i=1}^{n}(Y_{\text{mod}} - Y_{\text{exp}})^2 \tag{3.39}$$

To accelerate the procedure, single experiments simulation were parallelized on 4 cores on i7 workstation with 16 GB RAM.

Results of the optimization are reported in table 3.4:

Firstly, the effect of potential and temperature over dynamic operations is evaluated. In figure 3.28, simulation results were compared with experimental data. Looking the voltammogramms depicted, the main feautures such as: anodic peak current and plateau response and cathodic peak current are closely matched by simulation. The initial anodic peak around 0.8 V, followed by the broad plateau current is characteristic of Temkin isotherm. This behaviour is better described at low temperature while at higher temperature the experimental peak is more pronounced. However, the current associated to Pt oxides is well reproduce for all the operating conditions. Probably a

Table 3.4 – 0D submodel parameters

Parameters	Values	Units	Source
E_{PtOH}	0.7619	V	Fitted
E_{PtO}	1.0025	V	Fitted
E_{COR}	0.2073	V	Ref.[12]
DE/DT_{COR}	-8.53e-4	V/K	Ref.[12]
$i_{0,PtOH}$	1.1258	A/m^2_{Pt}	Fitted
$i_{0,PtO}$	8.869e-5	A/m^2_{Pt}	Fitted
$i_{0,COR}$	8e-10	A/m^2_{C}	Fitted
α_{PtOH}	0.7076	-	Fitted
α_{PtO}	0.3562	-	Fitted
α_{COR}	0.3620	-	Fitted
ω_{PtOH}	1.712e4	J/mol	Fitted
ω_{PtO}	3.281e4	J/mol	Fitted
$E_{act,PtOH}$	2.675e3	J/mol	Fitted
$E_{act,PtO}$	9.483e4	J/mol	Fitted
$E_{act,COR}$	7.4091e4	J/mol	Fitted
rf_{Pt}	160	m^2_{Pt}/m^2_{GEO}	Measured
rf_{C}	640	m^2_{C}/m^2_{GEO}	Assumed
d_{CCL}	10e-6	m	Measured
$H_{2,xover}$	1.6e6	A/m^3	Measured
C_{dl}	46e6	F/m^3	Measured

much more detailed model that considers site specific kinetics could capture the peak shift observed when potential increased, on the other hand a more complex submodel will not be solvable with acceptable computational costs when implemented in the Start-up model. Moreover, the rate of carbon oxidation reaction is adeguately calibrated without the need to measure carbon dioxide formation in harsh conditions (i.e. very low concentration and fast dynamics).

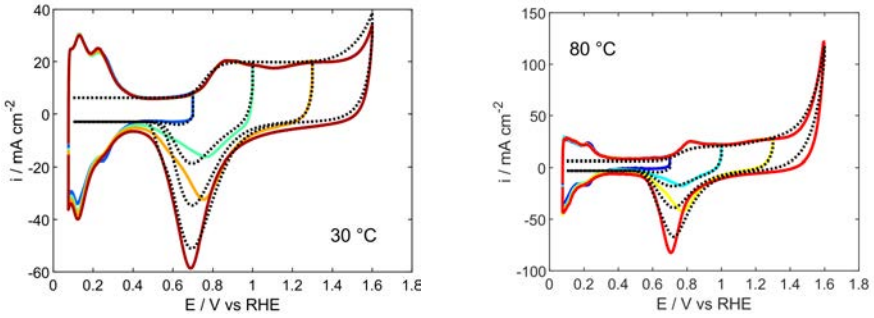

(a) Temperature 30°C **(b)** Temperature 80°C

Figure 3.28 – Comparison between Experimental CVs and Simulation. Operating conditions: 100/100% RH, $p_{out,anode} = p_{out,cathode} = p_{amb}$, $N_{N2} = N_{H2} = 60$ ml min^{-1}.

In figure 3.29 the comparison between experimental Holding test and simulation are reported. As previously stated PtOH kinetics is fast and reach a quasi-steady state after few seconds and barely increases during time. Conversely, PtO rate follow the logarithmic growth in time as predicted by theory. The experimental characteristic observed are related to reconstruction of platinum surface due to the formation of sub-surface oxide. The contribution to the total charge is probably related to Pt free site that become available for further oxidation when Pt-oxides formed in mono-layer surface flip into bulk metal. Although, the model developed cannot predict adeguately the Pt state reconstruction, it seems adequate to simulate current contributions of Pt Oxides over a wide range of time, and the increase of PtOx irreversibility which result in a change of rate equation for the associated kind of PtOx formed.

Finally, fast dynamics were considered. The evaluation of PtOx currents over a wide potential range and fast scan rate is representative of the real voltage cycling during Start-up operations. The results are reported in figure 3.30. Pseudo-capacitance has been used in place of current density to permit a reliable comparison at different scan rate. At low temperature the charge associated to anodic and cathodic reactions seems comparable at different

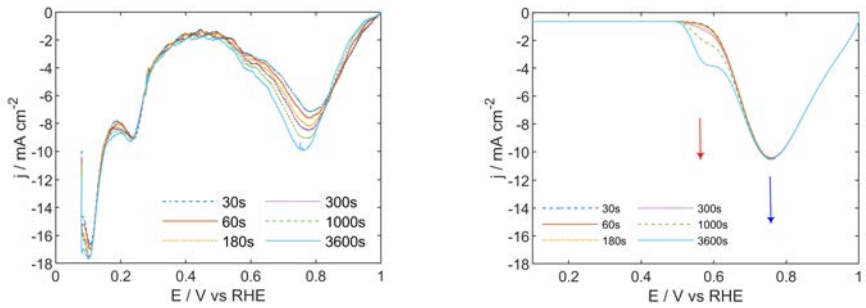

(a) Experimental **(b)** Simulated

Figure 3.29 – Comparison between Experimental LSVs and Simulation after Holding period at 1 V. Operating conditions: 100/100% RH, $p_{out,anode} = p_{out,cathode} = p_{amb}$, $N_{N2} = N_{H2} = 60$ ml min^{-1}.

scan rate. Looking at the simulation the reduction peak follows the same trend as observed in experiment, despite the shift is more evident. At 80°C the Pt oxides behaviour is more complex, both the anodic and cathodic feautures are deformated at higher scan rate with a clear broadening of reduction peak. The same behavior is quite good represented by the simulations. In similar way the model predict a shift of the reduction peak and a change of the shape. The simulation permits to clarify this phenomenon, due to the interaction between the two states of platinum oxides, the delay reduction of PtO, that have a slower kinetics, slows the reduction of the faster PtOH, causing the peaks separation, that were overlapped in the experiment.

The results of PtOx submodel implementation will be discussed in Section 7.2 where the current contributions during Start-up mitigated protocol will be analyzed in details.

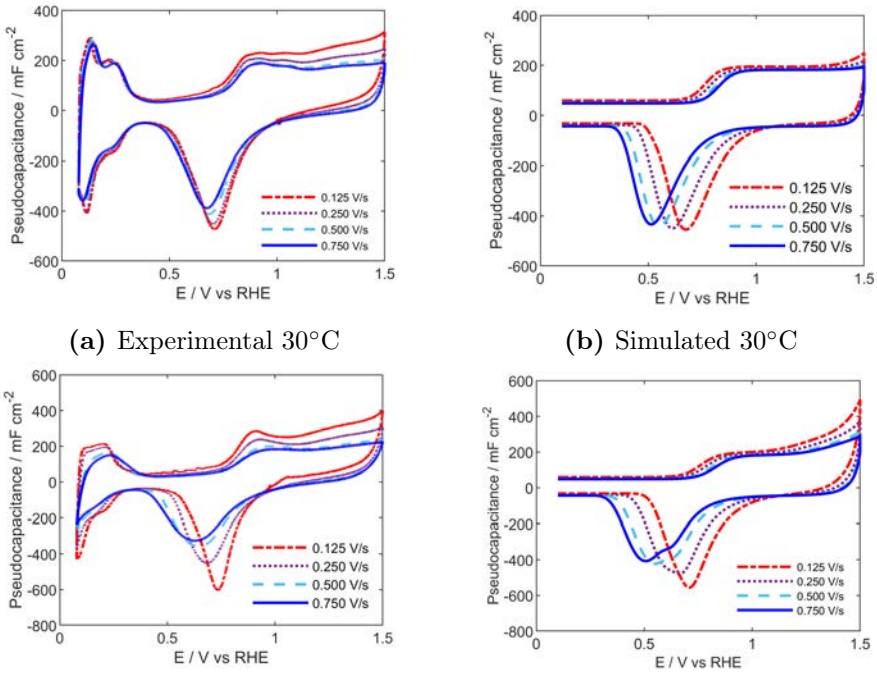

(a) Experimental 30°C

(b) Simulated 30°C

(c) Experimental 80°C

(d) Simulated 80°C

Figure 3.30 – Comparison between Experimental CVs and Simulation during fast dynamics. Operating conditions: 100/100% RH, $p_{out,anode} = p_{out,cathode} = p_{amb}$, $N_{N2} = N_{H2} = 60$ ml min^{-1}.

3.8 Summary of results and conclusions

In this first part of the work about start-up shut-down fundamentals, the combination of experimental RHEs and simulations ensured the understanding of the Start-up/Shut-down physics at a good level of detail.
First of all, the possibilities offered by both experimental and modelling tools have been clarified: both guarantee to track potentials as the transient phenomenon develops. Modeling matches with experimental evolution but gives also information about specific currents, both local and global, and about species distribution in channel and in porous layers. Analysing these tools results, a first insight in how start-up develops, and shut-down as well, is provided. Thereafter, testing operating conditions, it has emerged:

- *The effect of anode flow rate*
  - Both duration and peaks are increased as dry flows are reduced;
  - Equal total flows do not strictly end with same persisting of adverse conditions.
- *The role of O_2 at anode side*
  - Dilution of anode oxygen changes voltage peaks, modifying anode polarization state. The circulating currents are decreased and hence less carbon is corroded, as confirmed by the model;
  - Dilution of anode oxygen has shown an effect in terms of start-up and shut-down duration, suggesting that the amount of oxygen present at the catalyst layer regulates the phenomenon. It is even possible to consume all the reactant before front exits;
  - Changes in molecular diffusion of oxygen impact only on shut-down.
- *The impact of temperature*
  - The cathodic ORR during Start-up highlights a reduced current at low temperatures;
  - Results evidence the non-foregone higher COR/OER voltages at low temperatures.
- *The weight of capacitive and pseudo-capacitive effects*
  - The oxidation state, and the related PtOx currents, impacts on the potential peaks during consecutive Start-up/Shut-down: they progressively increase;

- Both PtOx and double-layer have a fundamental role in the lack of symmetry between start-up and shut-down and contribute to supply or drain most of the currents during start-up and Shut-down operations;
- Capacitive effects are responsible for the final inversion of current fluxes, due to a balancing process.

All the reported results suggest that the air-filled region of the anode electrode, and thus anodic ORR, mainly governs the reverse current and thus the carbon corrosion at the cathode. As the amount of oxygen is increased, voltage peaks are boosted and total amount of corroded carbon grows. During start-up the O_2 mass accumulated in CL influences the process, while shut-down depends on the dilution of entering reactant. The hydrogen front location is not the key feature to consider: O_2 consumption is the main point to focus on for an effective mitigation.
Residence time given by the plug-flow assumption is not thorough: it could be used as a first approximation, but for a deeper description of the events and to develop new strategies, a more complete analysis is required: effects of species consumption and gases diffusion must be considered, as well as the extra-time required by capacitive balancing.
Double-layer/pseudo capacitance effects are fundamental: they contribute both to explain duration, alterations with state of oxidation and discrepancies between start-up and shut-down.

The experimental setup has revealed effective in tracking the driving forces for carbon corrosion and in identifying how they are changed by operating conditions. Notably, RHEs at anode, that are hardly found in literature, give some useful hints since the importance of anodic passive part.
For the time being, CO_2 measurements and internal currents could not be recorded. Anyway, current measurements would have not been able to discern specific contribution. In this perspective, the model has proven capable of sustaining the results of the experiments, and distinguishing main reactions supplies.

Chapter 4

Start-up and shut-down cycling without mitigation strategies

4.1 Introduction

Evaluating the durability of a polymer electrolyte fuel cell under normal operating conditions requires several thousand hours of operation which makes the process inconvenient due to its high cost and long duration. Accelerated Stress Tests (ASTs) are a powerful way to degrade to degrade fuel cells focusing on single mechanisms. In the frame of ID-Fast project, appropriate procedures should be developed in order to finally predict real material ageing, under normal operation and transient operation (e.g. start-up/shut-down).

The aims of the work presented in this section are to clarify and measure the degradation caused by start-up/shut-down operation under un-mitigated conditions. The attention is focused on catalyst layer failure, since the most relevant issues regard such component. As first step of the work, standard AST protocols, developed by the US Department of Energy (DOE)[86], have been tested, trying to correlate their results with those given by start-up shut-down processes.

These investigations are carried out by means of a triple serpetine 25 cm^2 single-cell. The realized tests in this Chapter are:

- *Carbon Support AST*, for catalyst support.
  Degradation of cathode carbon support by collapse of the structure: both porosity and tortuosity of the carbon texture are progressively modified increasing gas transport resistances and worsening the triple phase boundary of the electrode; platinum nanoparticles are detached and thus isolated.

- *Electrocatalyst AST*, that stresses platinum dissolution.

Pt nanoparticles dissolution is enhanced, causing a reduction of catalyst surface area (ECSA) due to the combined effect of particle size growing and re-precipitation in the ionomer.

- *Unmitigated start-up and shut-down (SUSD) processes.*
  Real unmitigated process, caused by gas switching at the anode and thus front propagation. Aging that is intrinsically non-uniform: transient generates unequal detrimental conditions and therefore modifies materials characteristics with a varying local impact.

First of all, the impact of the single degradation mechanism have been studied by evaluating the impact of DoE ASTs on the performance evalution. then, the results have been compared to a succession of un-mitigated start-up/shut-down operation, to link the effects of a specific degradation mode (i.e. i.e Carbon corrosion and Platinum dissolution, section 1.3) and a real, non-uniform degradation operation mode. The ASTs operating conditions were the same (i.e. temperature and relative humidity) of the start and stop operation to simplify the interpretation of the results. However, they permit to reproduce in a controlled way a voltage profileover the entire MEA, despite of what happended during the real process, i.e. voltage profiles generated by front transient and not externally imposed. This allows easier interpretation of the results.

In addittion, to evaluate the evolution of local potentials and link the behaviour with the effect of the specific degradation mechanism few Start-up/Shut-down have been introduced at AST's stops, limiting the number of execution to avoid an alteration of the overall aging process.

4.2 Experimental Setup

The following experiments were performed with a triple serpentine 25 cm^2 single cell hardware. Three different catalyst coated membranes (CCMs) supplied by ION POWER(in the next Type A CCM) have been tested. The CCMs consisted of a perfluorosulfonic acid membrane and Pt/C electrodes with platinum loading of 0.3 mg Pt/cm^2/side. The CCM is sandwiched between anode and cathode gas diffusion layers (SGL-29BC having hydrophobic microporouss layer, SGL Group) and assembled in single cell hardware. The first two MEAs have been used for ASTs, in accordance with DOE protocols, reported in Sections 2.5.3 and 2.5.4. Un-mitigated start-up/shut-down procedure is instead tested on a third MEA. Temperature and relative humidity are set at values of 80 °C and 100% respectively, equivalent to ASTs. Five

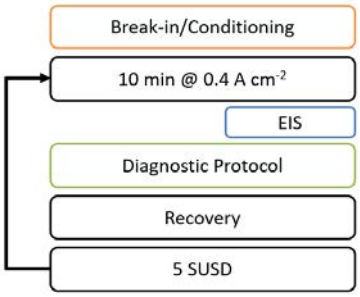

Figure 4.1 – Overview of the testing procedure for SUSD aging. The colours indicate at which cycle the operation is realized: every 5 SUSD (black), only at BOT (orange), every 20 SUSD (blue); at BOT, 60 SUSD and EOT (green).

start-up/shut-down are performed in sequence as previously described in Section 2.5.2, and testing procedure described in Figure 4.1 is repeated for each SUSD block. Notably, between one set of tests and the next, current is fixed at 0.4 A cm^{-2} for 10 min to allow MEA re-hydration and to check how performance degradation evolves in time. During such holding, EIS is also carried on, every four set of tests, to investigate materials evolution.
To recover the oxidation state of the catalyst surface, before every five cycles of start-up/shut-down and after the galvanostatic operation, a recovery procedure is introduced: the flux at cathode is interrupted and the voltage is let decrease due to H_2 crossover from the anode, reducing in this way the platinum oxides formed at cathode catalyst surface during high voltage excursion. This condition is held for 5 minutes from the point at which cell voltage reaches 100 mV. This permit to directly compare voltage evolution and local potential profile, as the test proceeds. Full diagnostic protocol, described in Section 2.5.2, is realized at BoT, after 60 cycles and at EoT, equal to 100 Start-up/Shut-down. the end of test was chosen considering a minimum performance of 0.3 V during galvanostatic operation at 0.4 A cm^{-2}.

4.3 Results of Accelerated Stress Testing

In this Section, state-of-art AST protocols, suggested by DOE, are utilized to follow and compare the evolution of performances as different mechanisms (platinum dissolution and carbon corrosion) are stressed.

First of all, the evolution of cyclic voltammety profile and ECSA measurement have been compared during standard ASTs. In Figure 4.2, as visible in the region between 0.1 V and 0.3 V, the hydrogen adsorption/desorption peaks are progressively reduced with the aging in both cases. However, the

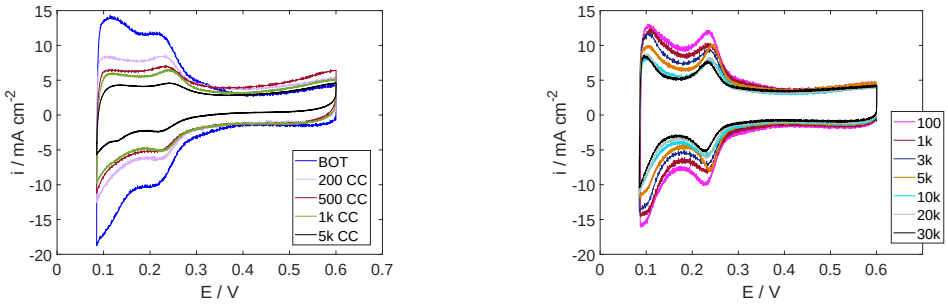

(a) Support AST **(b)** Electrocatalyst AST

Figure 4.2 – CV at different MEAs aging. RH = 100 %, T = 80 °C, p_{out} = p_{atm}, $N_{2,cathode}$ = 60 ml min^{-1}, $H_{2,anode}$ = 60 ml min^{-1}.

effect is more pronuanced during carbon support AST, where the peaks fastly collapse during voltage cycling. The ECSA is then computed integrating the anodic scan of voltammogramms, till the double-layer baseline in flat region between 0.4 V and 0.6 V. Electrochemical active surface area measurments are summarized in Figure 4.3: trends are close to literature profiles and in accordance with earlier works [95]. Due to the carbon corrosion, in Support AST, the ECSA value is strongly reduced and approaches a minimum after 5000 cycles, at which a reduction of 82.7% is computed. In contrast, platinum dissolution meccanism has a less impact, leading to a 67.0% reduction after 30k cycles of electrocatalyst AST. Double-layer capacitance instead is not altered in Electrocatalyst AST at all, suggesting that cathode electrode has not faced relevant structural changes. Support AST instead reveals two different features in the double-layer region:

- the double-layer capacitance strongly decrease after 2k/5k cycles. As reported in literature, the cathode electrode has faced a sudden thinning due to the structural collapse[24] that can be identified by capacitance reduction how is proportional to double layer interface and, indirectly, to catalyst layer thickness. Further, lot of particles could have lost ionomer/electrical contact.

- a deviation from the flat trend during the first anodic sweep towards higher currents. It could indicate some pollutants that block catalyst surface[61] or quinone/hydroquinone redox couple,made more visible during oxidation of carbon support[30]. This effect could be partially recoverable, as visible after high voltage exposition, in subsequent CV cycles;

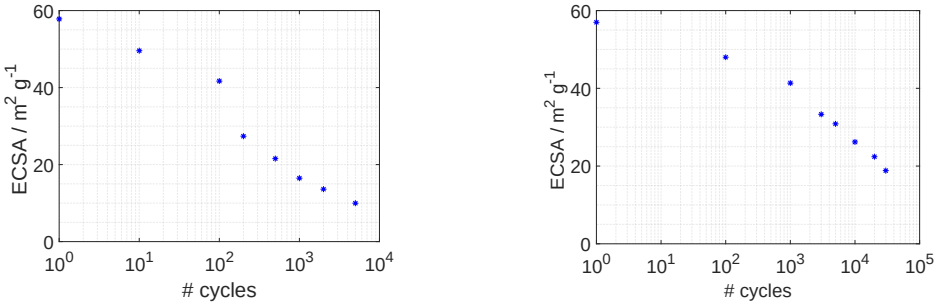

(a) Support AST **(b)** Electrocatalyst AST

Figure 4.3 – Electrocatalyst active surface area evaluated from CV as function of cycle number: comparison between carbon support and electrocatalyst ASTs.

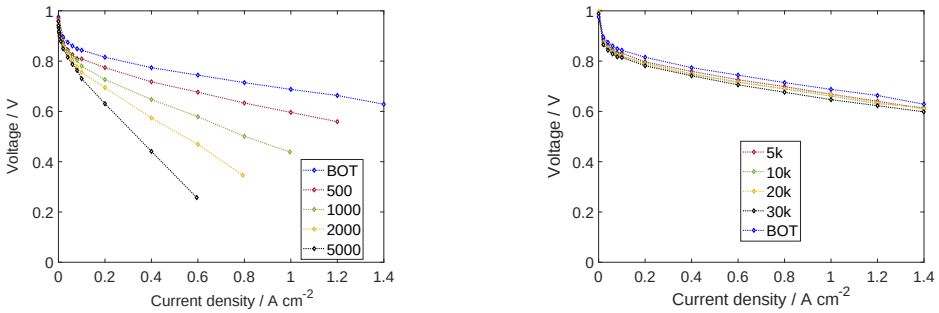

(a) Support AST **(b)** Electrocatalyst AST

Figure 4.4 – H_2/O_2 polarization curves during ASTs protocol. RH = 100 %, $p_{out} = p_{amb}$, $\lambda_a/\lambda_c \approx 2/19$.

Performance evolution has been evaluated by polarization curves, performed in H_2/air and H_2/O_2 gas feeding.

As visible in Figure 4.4 and 4.5, the effect of the electrocatalyst AST is mainly a translation of performance during ageing procedure. Conversely, significant ohmic and mass-transport losses rise in case of carbon support corrosion, larger at high current densities, at which they both count more, causing a curve rotation in this region.

To discriminate performance losses, the electrochemical impedance spectroscopy has been analyzed and results are depicted in Figure 4.6. Nyquist plots at 0.4 A cm^{-2} for pure oxygen confirm the differences between the degradation modes: Electrocatalyst AST does not evidence altered mass transport features, at low frequencies, as well as charge transfer loop undergoes just a small offset: failure of performance is mainly linked to catalyst surface loss. For a more detailed discussion of the mechanism see section 5.3.1) where the

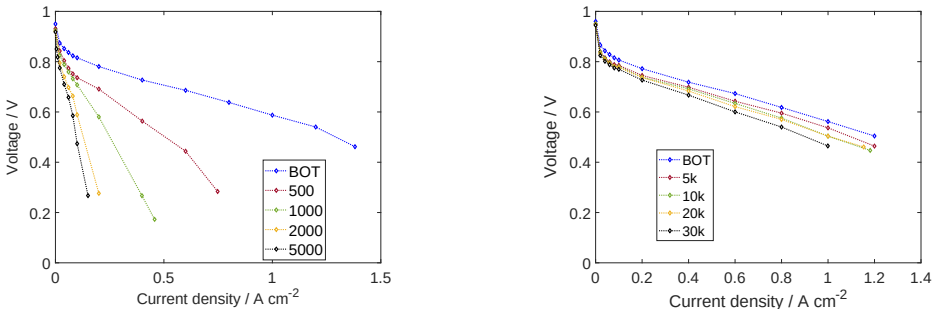

(a) Support AST **(b)** Electrocatalyst AST

Figure 4.5 – H_2/air polarization curves during ASTs protocol. RH = 100 %, $p_{out} = p_{amb}$, $\lambda_a/\lambda_c = 2/4$.

link between kinetic overpotential and ECSA losses have been analyzed.

Nyquist plot of Support AST instead shows a weakened cathodic ORR visible as a gradual alteration of the charge transfer circle, already from high frequencies. Also in this case, platinum nanoparticles may be no more in contact with ionomer, reducing thus the fraction of platinum available for the reaction. Flooding has become severe because both of hydrophilic groups generated by carbon corrosion and transport is lessen by loss of porosity[22] due to catalyst layer collapse. The effect is clearly visible as an increase of charge transfer circle and an alteration of the shape at low frequencies. This alteration is associated with appearance of a second circle, caused by oxygen transport resistances in the diffusion media or in the channel (i.e. channel impedance). Also the linear branch, related to CL ionomer, is more visible at a higher number of cycles. Two main effects are visible: the elongation of the linear branch, that could also alter the height of the charge transfer circle and an increase of the angle of the linear branch. Both could be related to a worsening of the total proton transport resistance but also the onset of heterogeneity of catalyst layer properties[**?**].

The reported alterations explain why results are so different in terms of performance even for approximately the same ECSA value: compare, for example, 20k cycles of Electrocatalyst AST and 500 cycles of Support AST, for which ECSA is equal to 22.4 and 21.55 $m^2\ g_{Pt}^{-1}$ respectively.

The increase of mass-transport resistance has been further investigated. From the limiting current test, the total oxygen transport resistance have been calculated following the procedure described in Section 2.4.5. Limiting current was measured for three oxygen dilutions and the resistance computed at each analysed pressure. The test have been repeated at each stop to record the evolution during aging. Results are outlined in Figures 4.7 (note the

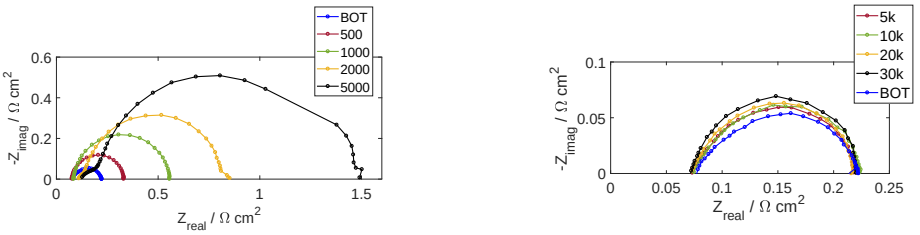

(a) Support AST **(b)** Electrocatalyst AST

Figure 4.6 – Nyquist plot recorded during ASTs protocol in H_2/O_2. RH = 100 %, T = 80 °C, $p_{out} = p_{amb}$, $\lambda_a/\lambda_c \approx 2/19$. Note the different scale of axes.

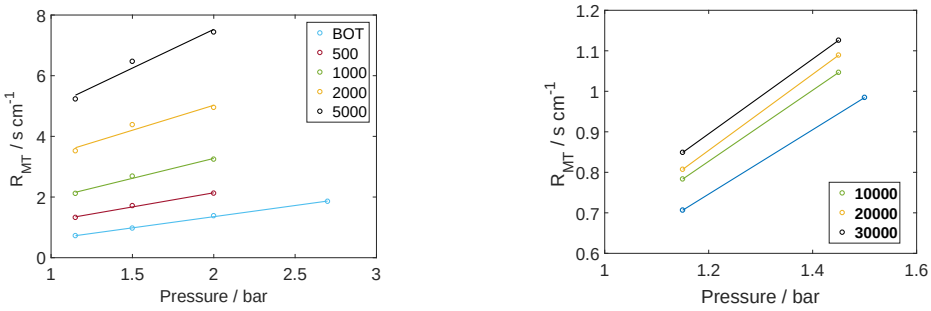

(a) Support AST **(b)** Electrocatalyst AST

Figure 4.7 – Total O_2 mass transport resistance as function of pressure for the two ASTs aging. Three dilutions have been tested to compute R_{MT}: 2, 3, 5 % O_2. RH = 100 %, T = 80 °C, $air_{cathode}$ = 3000 ml min^{-1}, $H_{2,anode}$ = 240 ml min^{-1}. Note the different y-axis.

different y-axis).

For Electrocatalyst AST, because of the only electrocatalyst dissolution, resistance to oxygen transport is just little varied, within 0.2 s cm^{-1}. The degradation mechanism causes an alteration of active catalyst distribution inside the catalyst layer, and a pronounced catalyst loss near the membrane. So, the result is compatible with a worsening, mainly, of the local transport resistance near the Pt particle. Instead, over the course of the voltage cycling, in Support AST, the oxygen transport resistance significantly increase. In this second case, limitations are largely boosted: at EoT, R_{MT} becomes 5.3/7.3 times larger than BoT, getting worse at high pressure. This measurements are coherent with the presumed collapse of cathode electrode. The main effect is a vertical translation in the chart, which means an increase of pressure-

independent resistance. Anyway, line slope deviates too, thus the pressure dependent component appears altered. Since carbon corrosion affects both the catalyst site availability and the gas pathway in the catalyst layer, a marked increment is associated with this mechanism. Moreover, molecular transport, that feels pressure variations, is much more relevant than local resistance at the nanoparticle. There may be also contributions in terms of water blockage inside the CL - consider that the test was carried on at 100% relative humidity.

Though, limiting current variations are small in case of Electrocatalyst AST the test could be very useful to evaluate the impact of catalyst loss. Specifically, resistance includes another contribution, which scales inversely with available platinum surface area as found by Greszler et al. [29]. By measuring limiting current over a wide range of platinum loadings (from 0.03 to 0.40 mg_{Pt} cm^{-2}) they showed that the electrode oxygen transport resistance is inversely proportional to platinum loading or, equivalently, platinum surface area because of the increase in local fluxes. They also highlighted that induced Ostwald ripening by voltage cycling caused similar results to what observed with different platinum loadings. The same kind of analysis is here proposed: once having computed the mass-transport during the protocol (i.e. at different ECSA values) and at two different pressures, results are reported as function of roughness factor inverse (Figure 4.8):

$$f_{Pt}\,[cm^2\,cm_{Pt}^{-2}] = 10\,ECSA\,[m^2\,g^{-1}]\,L_{Pt}\,[mg_{Pt}\,cm^2] \tag{4.1}$$

In our case, the local transport resistance is aroud 10.1 and 14.5 s cm^{-1}. The result is similar of what is found by Greszler et al.,i.e. 12 s cm^{-1} for resistive film covering the active platinum sites.

During carbon corrosion this kind of linear correlation does not subsist: after 1000 cycles, little changes of ECSA, and thus small variations of roughness factor, occur in parallel to very large increases of R_{MT}.

In conclusion, while in Support AST mass transport losses resulting from compaction of the cathode electrode, porosity reduction and hydrophobicity loss significantly reduce the limiting current, in case of platinum dissolution the small variations are linked to the reduction of available catalyst area.

4.4 Comparison between Support AST and Start-up/shut-down

The degradation mechanism caused by real start and stop transients is originated from front propagation in the anode compartment. During start-

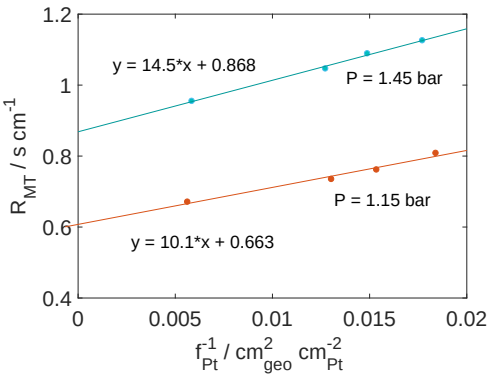

Figure 4.8 – Electrocatalyst AST: O_2 mass transport resistance as function of roughness factor inverse; f_{Pt} is proportional to L_{Pt} and ECSA. The latter is the varying parameter during the degradation.

up/shut-down, we the circulating currents are mainly determined by the operating conditions at anode side, as studied in Chapter 3. As long as operating conditions are the same, current remains unvaried, while the overpotentials of the reactions involved increases. Possible effects could be due to reversible mechanisms, like Pt oxidation, but also permanent degradation of materials. The reversible degradation is coherent with progressively increasing voltages in a single set of tests.

As reported in Figure 4.9, AST instead progressively reduces currents because potential profile is set at high voltages (1 V - 1.5 V), thus platinum gradually oxidises. Note that other factors could influence start-up/shut-down: the only partial platinum oxides reduction between one transient and the consecutive reduces the contribution of pseudo-capacitance but the exact impact on the COR catalysis could not be easily estimated(see Section 1.3). Some studies reported that oxidised species can even boost the reaction [63].

The scope of this section is to evaluate, in spite of physical differences, if the voltage cycling in Support AST is effective to predict the performance decay observed during start-up/shut-down. Since carbon corrosion should be the most relevant degradation mechanism in both the cases, a quantitive correlation is researched.

4.4.1 Results discussion

Firstly, performance indicatore of the status of cathode electrode, that should be the most affected component, are directly compared (Pt mass activity, ECSA, cathodic charge transfer resistance). Impedance spectroscopy and limiting current test have been finally used to quantify the mass transport losses.

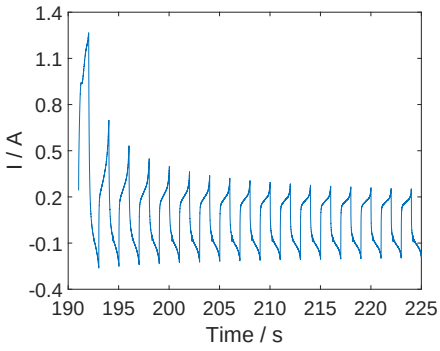

Figure 4.9 – Recorded current during Support AST for consecutive cycles between 1 V - 1.5 V in H_2/N_2.

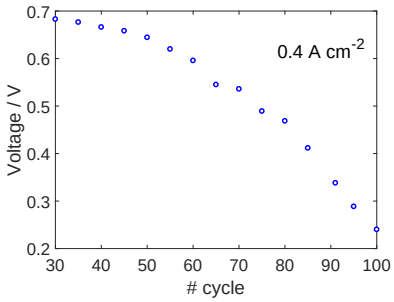

Figure 4.10 – Start-up/shut-down aging: recorded voltage at 0.4 A cm^{-2} immediately after each set of 5 SUSD. Test has been stopped as voltage decreased under 0.3 V.

After having evaluated these most relevant features, secondary contributions are checked to discriminate the differences between the protocols.
The comparison starts from the evaluation of performance loss in polarization curves as depicted in Figure 4.11 at different cycles.

Polarization curves at 60 start-up/shut-down are well reproduceced by 500 cycles of Support AST, and 100 start-up/shut-down by 1k cycles. Such correspondence, both in oxygen and air, allows to predict that, for the degradation rate, an almost 10 ratio exists (in detail, 9.6 ratio) in terms of cycles. Comparing instead the time for testing, AST accelerates real phenomena by a 10.3 factor. The high level of correspondence shows that Support AST accurately reproduces the performance loss caused by un-mitigated start-up/shut-down.
This is a positive strong conclusion about the representativeness of the Support AST to evaluate un-mitigated start-up/shut-down.

Then, performance evolution have been analyzed in deep to quantify the

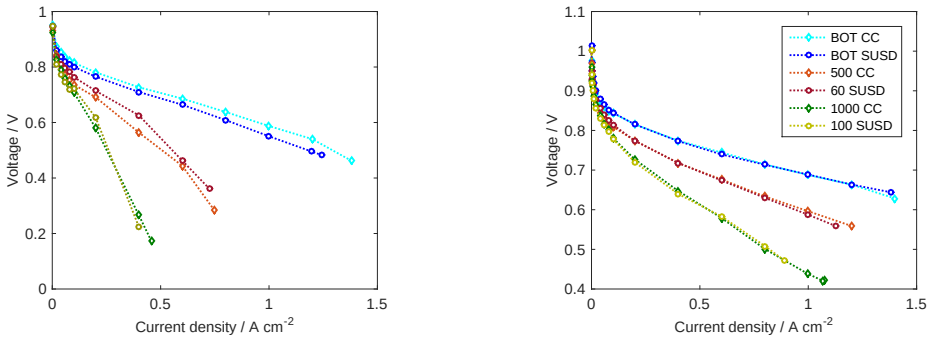

(a) Air polarization curves **(b)** O_2 polarization curves

Figure 4.11 – Comparison of polarization curves obtained aging MEAs with carbon support AST and start-up/shut-down procedure. RH = 100 %, T = 80 °C, $p_{a,out} = p_{c,out} = p_{atm}$. $\lambda_a/\lambda_c = 2/4$ for air and $\lambda_a/\lambda_c \approx 2/19$ for oxygen.

different contributions caused by carbon corrosion mechanism. The polarization curves in H_2/O_2 have been used to evaluate mass activity, following the protocol described in Section 2.4.6. This value represents the total ORR current per unit mass of platinum at cathode electrode. The results are strongly comparable, as visible in Table 4.1.

Table 4.1 – Mass activity changes during start-up/shut-down and Support AST.

Support AST		**SUSD**	
cycle [-]	**Mass activity [A/mgPt-1]**	**cycle [-]**	**Mass activity [A/mgPt-1]**
BoT	0.064	BoT	0.07
500	0.032	60	0.033
1000	0.025	100	0.021

Platinum utilization decreases significantly: at 100 Start-up/Shut-down/1k Support AST, mass activity is only the 30% and the 39% of the initial value, thus the degradation mechanism underlying starts and stops impacts drammatically on material. Comparing the first and the second row in the Table 4.1, the variation of mass activity is larger for the first half the test, with a reduction of almost 50% from BoT. The results suggest that the largest effects of Platinum loss or access to the active sites, occur in the first stage for both the processes.

Coherent results come from the evolution of ECSA reduction. Hydrogen

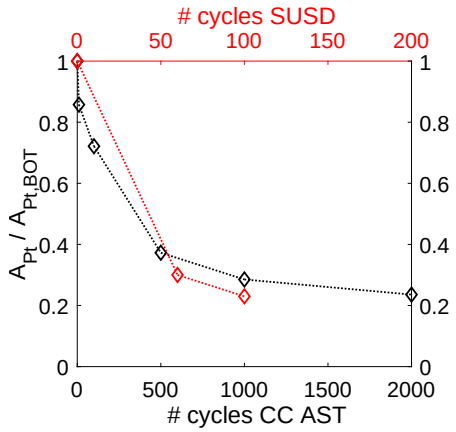

Figure 4.12 – Comparison of ECSA decrease between Support AST and Start-up/Shut-down aging procedures.

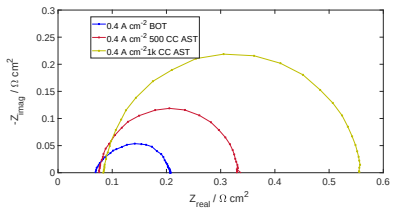

(a) Support AST

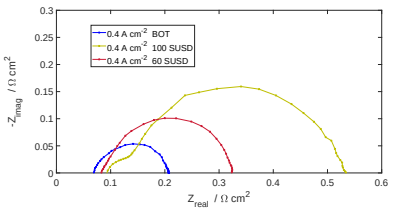

(b) Start-up/Shut-down

Figure 4.13 – Nyquist plots at 0.4 A cm^{-2} in H_2/O_2 at different aging levels of Support AST and Start-up/Shut-down. RH = 100 %, $p_{out} = p_{atm}$, $\lambda_a/\lambda_c \approx 2/19$.

desorption peaks are progressively reduced in both the cases resulting, as visible in the comparison of Figure 4.12, in similar ECSA variations. To make the chart more readable, ECSA at 5000 cycles of the Support AST has been omitted, but it remains, as shown before, almost constant: only minor changes occur since CCM has already reached a kind of lower-limit condition.

To complete the considerations on the activity of cathode electrode, EIS results have been checked. Figure 4.13 analyses the Nyquist plots in H_2/O_2. The cathodic charge transfer resistance is measured as the diameter of the main semi-circle. Despite to the observed similarities, the charge transfer resistance evolve quite differently in the two cases, as reported in Figure 4.14: the kinetic loss seems to increase more during the Support AST, while, at least as global behaviour, appears less reduced in Start-up/Shut-down.

Some other information can be extracted from the nyquist plot. The high

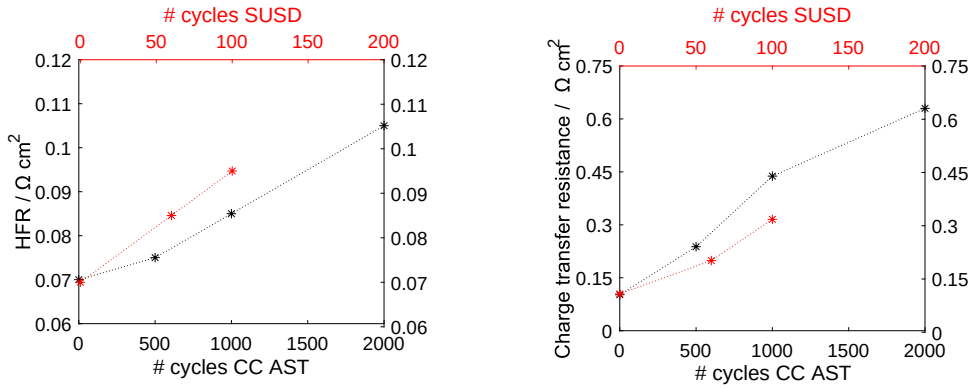

(a) High frequency resistance **(b)** Charge transfer resistance

Figure 4.14 – Evolution of HFR and charge transfer resistance for Support AST and Start-up/Shut-down aging procedures. Values are measured through Nyquist plots at 0.4 A cm^{-2} in H_2/O_2. RH = 100 %, T = 80 °C, $p_{out} = p_{atm}$, $\lambda_a/\lambda_c \approx 2/19$

frequency resistance increases in both cases. For the Start-up/Shut-down, such change is larger compared to Support AST (Figure 4.14.a). Ohmic resistance alterations could be due to membrane; to investigate if membrane thinning undergoes during the ageing, linear sweep voltammetry measurement is used to determine hydrogen crossover and short circuit resistance. As visible in Figure 4.15, during Start-up/Shut-down no changes of short-circuit resistance, neither hydrogen crossover are evident thus membrane condition is kept invariant. Same results are for support AST: only at 5k cycles a variation is detected. This is coherent also with OCV values in polarization curves: its decrease is small, less than 10 mV, for both the aging protocols, till 1k Support AST and 100 SUSD cycles. Instead, a decrease of 20 mV is reached at 5k cycles of support AST.

Since LSV analysis has not put in evidence membrane fault, the real impedance change seen before in Nyquist plots might be associated with electrodes degradation [93]:

- loss of carbon decreases electronic connectivity between carbon particles, making the CL more electrically tortuous;
- ionic connectivity between catalyst particles and membrane is worsen.

In the meanwhile, we cannot exclude that MEA is becoming progressively dehydrated, due to change of surface hydrophobicity or MPL crack formation, subsequent to carbon corrosion and/or mechanical failure due to electrode collapse.

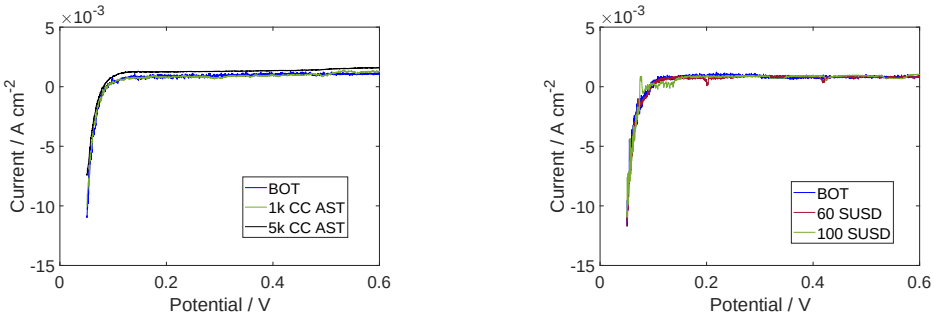

(a) Support AST **(b)** Start-up/Shut-down

Figure 4.15 – LSV plots at different MEAs aging. RH = 100 % , T = 80 °C, $p_{out} = p_{atm}$, $N_{2,cathode}$ = 60 ml min^{-1}, $H_{2,anode}$ = 60 ml min^{-1}.

In addition, despite a pure dissolution mechanism, other dominant effect of carbon corrosion concerns mass transport resistance, as extensively described previously. Limiting current test give relevant information about oxygen transport resistances. As appears in Figure 4.16, limiting current results for Start-up/Shut-down are well reproduced by Support AST. Only minor differences in terms of line slopes, that means in pressure-dependent behaviour, exist: in particular, a larger increase is found for Start-up/Shut-down. Notably, the almost identical value around the atmospheric pressure agrees with coincident i-V performances.

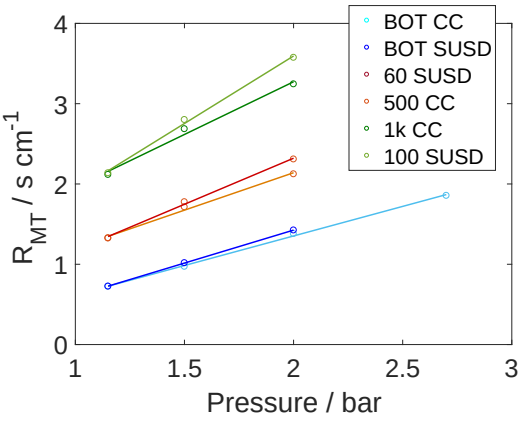

Figure 4.16 – Comparison of O_2 mass transport resistance vs. pressure obtained aging MEAs by carbon support AST and Start-up/Shut-down procedure. Three dilutions have been tested to compute R_{MT}: 2, 3, 5 % O_2. RH = 100%, T = 80 °C, $air_{cathode}$ = 3000 ml min^{-1}, $H_{2,anode}$ = 240 ml min^{-1}.

The contribution of mass transport resistance is in general visible at low

frequency part of the Nyquist plots. Looking at low frequency resistance, as the frequency response intercepts the real axis on the right side, Z_{real} is comparable between the two aging processes, thus the similar performances in the H_2/O_2 i-V chart. However, the semi-circles are not coincident: the shape is closer to a circle in case of Support AST, while for Start-up/Shut-down there is a noticeable deviation. The alterations can raise as degradation is not uniform: start-up and shut-down degrade more the inlet and the outlet of the CCM because these are the regions where largest detrimental conditions are generated and last longer. Therefore, the non-uniform shape might be the result of superposition of spectra, with larger effects at low frequencies. Moreover, some effects could be attributible to differences between rib and channel as observed by Gaumont et al. [26].

As supplementary study, alterations of protonic resistance has been better investigated through *on-line* control of what happens during Start-up/Shut-down transients. A general increase is clearly visible in Figure 4.17.

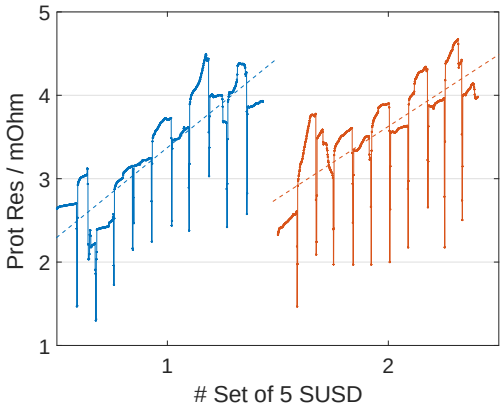

Figure 4.17 – Variation in HFR (at 1 kHz) during consecutive sets of start-up/shut-down. Reversible alteration is visible.

The high frequency resistance is reduced by consecutive set of cycles, during galvanostatic operation and refresh procedure, implying that the phenomenon is mainly reversible. Instantaneous drops correspond to a front passage. As reverse-current mechanism occurs, electrochemical reactions occur and heat is locally produced, causing progressive CCM dehydration.

The main difference between the EIS spectra, is observable as a more evident additional circle for Start-up/Shut-down, at high frequency of the Nyquist plot, reported in Figure 4.13. It exists both at low and high current densities and it appears closer to a circle, so it may be the anodic charge transfer, usually not visible because of the faster hydrogen oxidation reaction

kinetic compared to oxygen reduction reaction. In literature, similar EIS charts have been found for CO poisoning. It may be possible that gas permeability of the membrane allows the diffusion of carbon monoxide from the positive to the negative electrode [21]. Carbon monoxide is then adsorbed at the low H_2 potentials, and this adsorbed specie could not be completely oxidized when air flows in anode compartment during shut-down.

A further analysis should be required for a full comprehension; our main focus is, as told, on cathode electrode but, to better understand what happened at the anode in accordance with our experimental possibilities, an anodic cyclic voltammetry was performed; result is reported in Figure 4.18. Computation of ECSA assesses its reduction: considering that the fuel cell is symmetric, and thus the initial value corresponds to cathode side, the EoT value of 32 m^2 $g_{Pt}{}^{-1}$ indicates an almost halved electrocatalyst area. To explain this deterioration, it must be considered that real start-up and shut-down introduce air at anode electrode: gas shifting implies voltage cycling at the anode side between 0 and 1 V that does not exist in case of H_2/N_2 protocol. Voltage cycling induced ECSA loss, by the way of platinum dissolution as seen in Section 4.3.

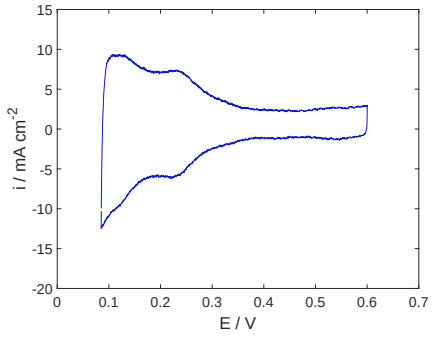

Figure 4.18 – Anodic CV for CCM degraded by Start-up/Shut-down procedure. RH = 100 %, T = 80 °C, $p_{out} = p_{atm}$, $N_{2,anode}$ = 60 ml min^{-1}, $H_{2,cathode}$ = 60 ml min^{-1}.

4.5 Combined effects of single degradation mechanisms and SUSD

The Start-up/Shut-down operation occur occasionally, in the real system, during the lifetime of the fuel cell. To evaluate the impact of such operation, in combination with other degradation mechanisms, few Start-up/Shut-down

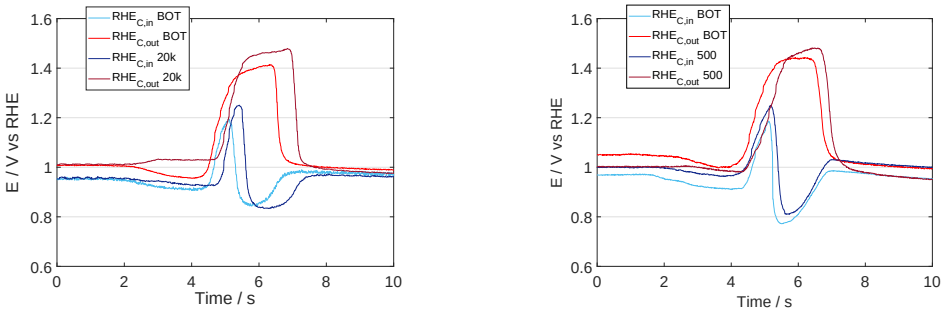

(a) Electrocatalyst AST **(b)** Support AST

Figure 4.19 – Variation of voltages, recorded by RHEs at cathode inlet and outlet, during Start-up at different ASTs degradation levels.

cycles have been introduced, during Electrocatalyst and Support ASTs, to check the effect, that such ASTs have on potential transient during Start-up/Shut-down. To make comparison reliable, a set of 3 Start-up/Shut-down has been reproduced consecutively and the third cycle compared in all the cases. In this way, the reversible effect of peaks alteration explained in Section 3.6 is mainly depleted.

It has been observed a general irreversible increase in the maximum voltage peaks for both the degradation processes. At the same time, the cathodic local potentials, in the active part of the cathode electrode has been decreased. From this local potentials, the oxygen reduction reaction overpotential evolution can be deduced, inferring its increase too.

In Figure 4.20, the alteration of the voltage peaks during start-up have been reported. The variation is almost linear for the platinum dissolution and for the carbon corrosion in the first cycles, while it slow down and suddenly drop, in the second case, after the degradation proceed. Moreover, looking at the same ECSA value, i.e. at 500 cycles of carbon corrosion (21.55 m^2 $g_{Pt}{}^{-1}$) and 2000 cycles (22.40 m^2 $g_{Pt}{}^{-1}$) of platinum dissolution, the maximum potential reached is similar in both cases.

Then, the model was exploited to evaluate the possible influence of catalyst sites reduction: simulations with a reduced cathodic ECSA were performed (see section 3.3). In this case, the ECSA value used for carbon oxidation reaction was proportionally reduced too, for the simulation. This, to taking into account the decreasing of the kinetics associated to the carbon corrosion, since the majority of reaction is expected to be catalysed. The potential variations, illustrated in Figure 4.21, are in accordance with the experiments: the increase of all the cathodic overpotentials is confirmed. In Figure 4.21.a the anodic potentials collected with RHEs are reported. Since no alteration of

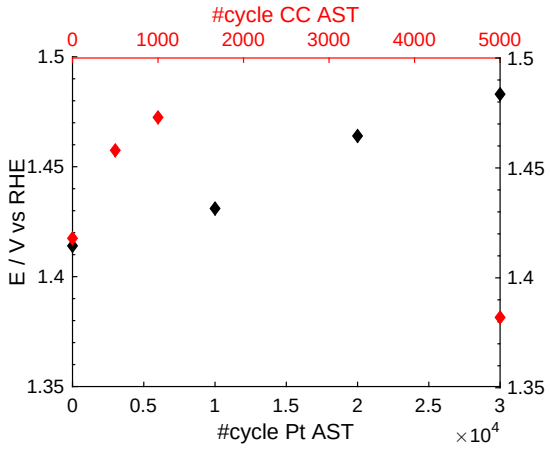

Figure 4.20 – Variation with cycle number of maximum voltage value during start-up for carbon support AST and electrocatalyst AST, measured with Reference electrode at cathode outlet position (see figure 4.19).

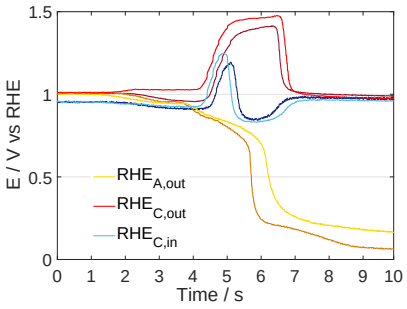

(a) Experimental: start-up at BOT (dark colour) and 20k cycles of Electrocatalyst AST (light colour)

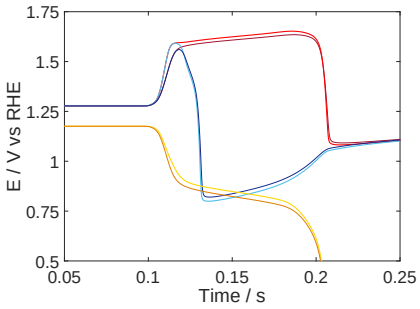

(b) Simulated: reference start-up (dark colour) and halved $ECSA_c$ case (light colour)

Figure 4.21 – Comparison between experimental (a) and model (b) results in case of reduced cathodic ECSA: at 20k Pt AST cycles, ECSA has become the 39% of BOT value, while it has been simulated a 50% ECSA reduction. For (a), test conditions are: T = 40 °C, RH = 100%, $air_{cathode}$ = 200 ml min^{-1}, air_{anode} = $H_{2,anode}$ = 100 ml min^{-1}, p_{out} = p_{atm}.

anode catalyst layer are expected during AST (i.e. anode remains always at the low H_2 potentials), the increased voltage when anodic oxygen reduction reaction is active indicates that the overall reverse-current is reduced. The same result is observed during simulations. When ECSA is halved, the total carbon oxidation reaction charge, predicted by the model, is reduced of 29%. Since the ECSA changes largely compared to the overall internal currents reduction, catalyst sites specific currents are higher. This explains the described alterations in terms of potentials and leads to conclude that, even if less carbon is corroded, catalyst is more stressed because of boosted local currents, as long as aging proceeds.

However, the model version used in this version does not take into account pseudo-capacitive contributions of platinum oxides, which can alter the currents balance. This could explain the smaller currents observed during simulation. Nevertheless, the key role played by ECSA has been confirmed. Anyway, the described variations detected during the tests are quite small in terms of voltages, thus the profile used in Support AST almost matches with Reference $\text{Electrode}_{C,out}$ profile during start-up till significant losses in performance. During AST cycling, cathodic oxygen reduction reaction peaks became lower for carbon corrosion with respect to electrocatalyst dissolution. For oxygen reduction reaction indeed, the reactant is a gas thus also mass transport losses induced by support deterioration are relevant.

Furthermore, it's noticeable the strong reduction of maximum potential visible at 5000 cycles of Support AST. Such result could be explained by a change in the limiting factor of the mechanism: the altered catalyst/electrolyte interface at the cathode and the weakened mass transport become more limiting than the anodic ORR. This is coherent with observations about double-layer reduction (Section 4.3) and HFR increase (Section 4.4). Consistent interpretations are found in literature [37].

In case of Start-up/Shut-down, the reduction of the anodic ECSA at EoT, that has been experimentally identified and reported before, could have an impact on potential profiles. To control it, this case has been simulated too: setting anodic ECSA equal to the 50% of its initial value, cathodic maximum potential is slightly decreased (not visible in experiments because decrease of cathode ECSA weights more and it has the opposite effect, as explained above). The main difference consists in the lower anode polarization, that decreases the voltage at which anodic oxygen reduction reaction occurs. This explains the results of Figure 4.22 from the two different CCMs used in the frame of this thesis work. Type B CCM is not symmetric, as Type A CCM; its ECSA is indeed lower as confirmed experimentally. It thus follows a down-shifted plateau during Start-up for Type B. Starting from carbon oxidation reaction global current, a reduction of corroded carbon was computed: the

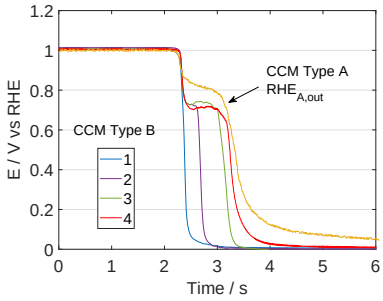

(a) Experimental: comparison between anodic voltages during start-up, measured by RHEs for the two different CCMs. Numbers in the legend indicate position along flow field: 4 of Type B must be compared to Type A.

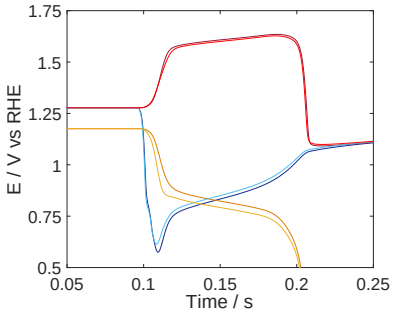

(b) Simulated: reference start-up (dark colour) and halved $ECSA_a$ case (light colour)

Figure 4.22 – Comparison between experimental (a) and model (b) results in case of reduced anodic ECSA. For (a), test conditions are: T = 40 °C, RH = 100%, $air_{cathode}$ = 200 ml min^{-1}, air_{anode} = $H_{2,anode}$ = 100 ml min^{-1}, p_{out} = atm.

new value is decreased by 19%. The impact of anodic ECSA seems lower than cathodic. Obtained results are summarized in Table 4.2.

Table 4.2 – Simulated results for Start-up, about ECSA variation: changes are reported w/r/t reference case. Voltage shifts are in accordance with experimental observations.

Parameter	**Δ**	**Global current**	**Max V COR**	**Min V $ORR_{,cat}$**	**$Plateau_{an}$ V $ORR_{,anode}$**	**ΔCorroded carbon**
$ECSA_{cathode}$	-50%	↓	↑	↓	↑	-29%
$ECSA_{anode}$	-50%	↓	↓	↑	↓	-19%

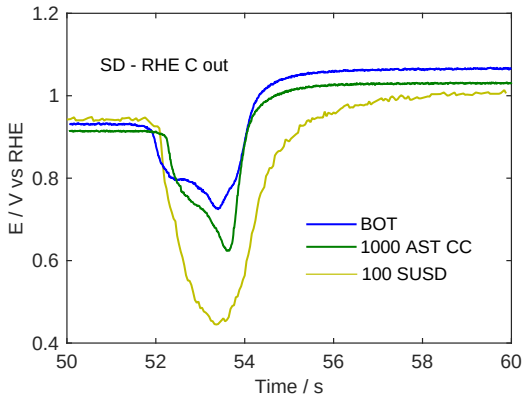

Figure 4.23 – Variation of minimum voltage, i.e. maximum oxygen reduction reaction overpotential, for cathode outlet during shut-down, in case of different degradation modes.

Comparing now Start-up/Shut-down local potentials during Support AST and real transient degradation, a difference is visible in cathodic overpotential during shut-down, reported in Figure 4.23. In case of unmitigated Start-up/Shut-down, the outlet of the cathode catalyst layer is subjected to the highest potentials and for longer, thus it is expected to degrade more: the large difference in the chart implies that the specific inlet region has performances much more reduced compared to what seen as average. In the meanwhile, also maximum voltages have increased more, till a maximum of 1.56 V during start-up at 100 cycles. This value is larger compared to what collected in Figure 4.20. We expect therefore that the active platinum area fell locally more during real mechanism than during the AST and besides, observing the largest deviations for oxygen reduction reaction, structure collapse should be harsher too, since it causes a higher mass transport resistance. All these results hint at the heterogeneity of the real process, against AST homogeneity.

4.6 Summary of results and conclusions

Reported results have shown the main differences between electrocatalyst degradation by its dissolution and carbon support degradation. Compare to the former, carbon corrosion shows much more reduced performances both in oxygen and air conditions. While Electrocatalyst AST mainly causes polarization curves translation due to ECSA loss, Support AST is largely damaging for the structure, such that high current density performances are

strongly lessen. The boosted mass transport losses are evident by Nyquist plots, derived from EIS, and by limiting current measurements that allowed oxygen transport resistance evaluation. All the results confirm that the expected processes of aging are consistently enhanced during protocols.

After having studied the failure modes of Type A CCM catalyst layer, results of real unmitigated start-up and shut-down at high temperature are compared.

Real process differs since:

- air subsists both at cathode and anode side, which faces a gas switching;
- anode is subjected to voltage cycling;
- detrimental conditions are not uniformly distributed but cathode inlet and outlet are the most stressed regions;
- voltage profile is not imposed but consequence of the circulating reverse current.

Regardless the differences in the mechanisms, the average performance of unmitigated Start-up/Shut-down is very well described by Support AST. Results are extremely close if one compares: i-V curve in H_2/air, i-V curve in H_2/O_2, Pt mass activity, and Oxygen mass transport resistance.
Differences instead emerge as Nyquist plots for Start-up/Shut-down are compared to AST: HFR increases faster, globally charge transfer resistance seems less weakened, additional features appear, both at low and high frequencies. These differences can be mainly attributed to a strong non-uniform degradation, that involves more inlet and outlet than middle region of the CCM. This is also confirmed by comparing the impact on Start-up/Shut-down transients of the two different ways of degradation: oxygen reduction reaction overpotential increases much more in Start-up/Shut-down, in particular for cathode outlet, suggesting higher locally damaged active area and transport properties.

The few Start-up/Shut-down introduced during ASTs help in understanding the impact of specific degradation on transients, hence the possible evolution with aging of the reverse-current mechanism. Variations in Start-up/Shut-down profiles, as ASTs go on, are limited: ECSA was supposed as the main parameter to have an impact. Model confirmed that such quantity shifts potentials in accordance with experiments, even if it is not able to fully describe the phenomena since CCM degradation cannot be easily represented. This tool permitted also to calculate the amount of corroded carbon: carbon oxidation reaction current is lowered with ECSA decline

(approximately 30% reduction for halved cathode catalyst area). All the degradation modes studied in this Chapter are so expected to progressively decrease the CO_2 produced; some proofs are found in literature [52]. Even though this reduction, platinum specific currents are boosted thus stressing electrocatalyst more. Similarly, simulating ECSA reduction at anode, which occurred during Start-up/Shut-down, a analogous impact in terms of start-up currents is found.

Chapter 5

Start-up and Shut-down cycling with mitigation strategies

5.1 Introduction

Recently, significant progress has been made in achieving reasonable fuel cell system lifetime for automotive applications. However, one of the main remaining tasks thereby is the heterogeneity of degradation of membrane electrode assemblies (MEAs) at the stack level, especially due to transient operation (e.g. load cycling, start-up, shut-down).

On a material level, changes in the load influence mainly the cathode and cause Pt dissolution when cycling between certain potentials. For instance, carbon corrosion and catalyst degradation of the cathode is higher under dynamic operation. Pei et al. demonstrated that start-ups, shut-downs and transient operation were the dominant sources of the performance decay in vehicle fuel cells, when comparing to the stationary procedures[65].

The simulated cycles of start/stop, presented in the previous chapter 4.4, without mitigation strategies are however not representative of the today applied mitigation strategies in stacks. In accordance with partners fleet data, shut-down is always fully mitigated while start-up is almost unavoidable only when rebooting after a long-time shut-down. Operating conditions for the real operations must be considered: the overview about the physics of the mechanism with the RHEs, which was drawn in chapter three, section 3.5, showed the impact of stressors on voltage profiles during transients. In this Chapter, a realistic test profile has been studied to reproduce in a Segmented Single Cell hardware the mechanism of the Long-Stop (Off-Specific event), based on the specifications of the ID-FAST project durability test program. Reflecting stack data, this simulates a stop-time before restart longer than

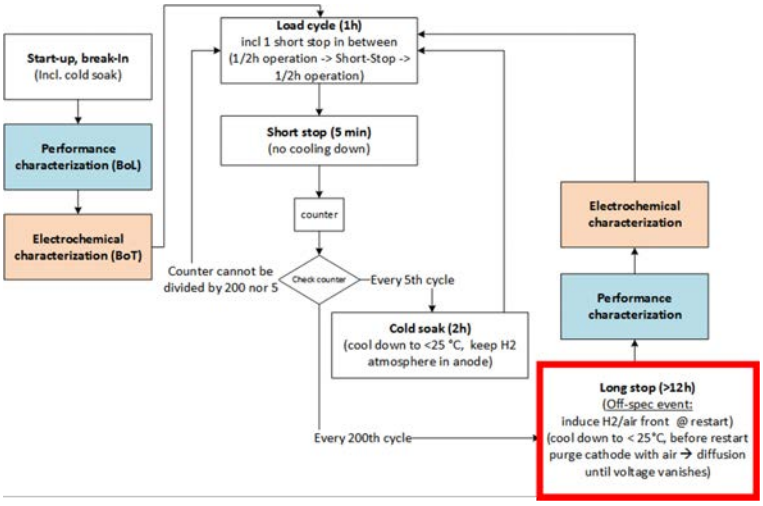

Figure 5.1 – ID-FAST durability test program

12 hours, which should occur every 200 operating hours, i.e. 25/30 times through the component lifetime.

A scheme of the real-world durability test program that will be used in ID-FAST project is shown in Figure 5.1, wherein Long-Stop and subsequent induced H_2/air front at Start-up is highlighted.

The next sections will clarify the results that the parameters close to real world have on performance as the degradation proceeds.

5.2 Experimental Setup

The triple serpentine Segmented Cell flow field has been used to study the degradation process (5.2). The hardware is structured with 4 graphite segments, at both anode and cathode side, designed in the frame of the Second Act project (FP7 FCH-JU 621216), by Rabissi et al. [69], in collaboration with IRD Fuel Cells A/S. The reference operating mode is galvanostatic: a total current is imposed and divided by a multi-channel electronic load among the segments, aiming to maintain their segments voltages at the same value. Such a configuration permits to identify the instantaneous contribution of each segment to the overall current density in the cell; four polarization curves are obtained (5.2). To guarantee a deeper insight into the start/stop process, the in-house custom hardware was upgraded in this work, introducing four per side Reference Hydrogen Electrodes; such setup has been used to evidence the local distribution of potentials of both cell segments and anodic/cathodic electrodes during operations, including fast transients. A more detailed

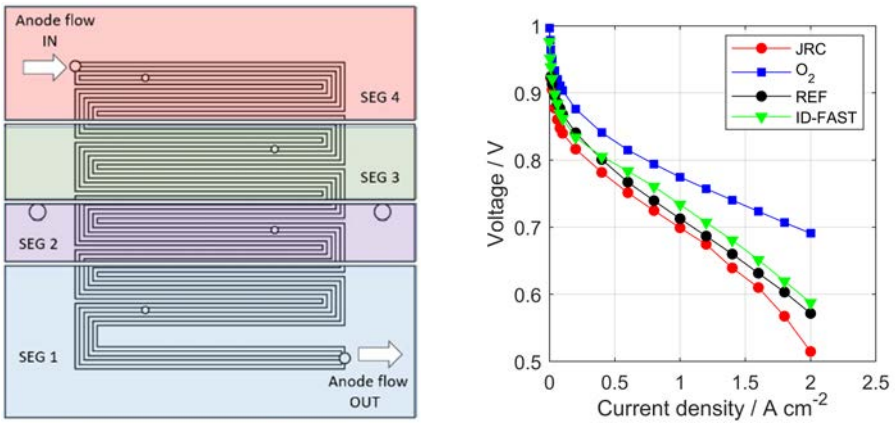

(a) Segmented flow-field **(b)** Global i-V curves

Figure 5.2 – (a) Cathode flowfield with segments highlighted. Anode flow direction is specified and counter-flow configuration is adopted for both ageing procedure and MEA characterization – (b) Example of iR-free polarization curves of the 4 segments. 100/100% RH, T = 80 °C, $p_{in,anode}/p_{in,cathode}$ = 2.5/2.3 bar, $\lambda_{anode}/\lambda_{cathode}$ = 2/4, minimum flux = 0.5 A cm^{-2} equivalent.

description is reported in chapter two, section 2.3.2.

Catalyst-coated membranes (CCMs) was used for this work: the project Johnson Matthey CCM with with Pt loading of 0.08/0.4 mg cm^{-2} for the anode/cathode side. The CCM was assembled with Freudenberg GDL H14CX483 without hot-pressing into segmented-cell hardware. The MEA compression was obtained using rigid gasket in PTFE and an optimal compression value of 80% was kept for the sample. The active area was controlled using PTFE sub-gasket, at fixed value of 25 cm^{-2} for macro segmented-cell.

To monitor the degradation of the MEA during start-up/shut-down cycling experiment, a set of polarization curves were recorded, following a structured protocol:

- H_2/Air polarization curve, named REF condition.
  This is the reference condition for the evaluation of performance loss and comparison with the results of the next chapter on AST. It consist of: 100/100% RH, T = 80 °C, $p_{in,anode}/p_{in,cathode}$ = 2.5/2.3 bar, $\lambda_{anode}/\lambda_{cathode}$ = 2/4, minimum flux = 0.5 A cm^{-2} equivalent.

- H_2/Oxygen polarization curve, named Oxygen condition.
  This is the oxygen feeded poalrization curve, used for the evaluation of activity loss. It consist of: 100/100% RH, T = 80 °C, $p_{in,anode}/p_{in,cathode}$ = 2.5/2.3 bar, $\lambda_{anode}/\lambda_{cathode}$ = 2/19 (constant flux of reference condition), minimum flux = 0.5 A cm^{-2} equivalent.

- H_2/air polarization curve, named ID-FAST condition
  This is the reference condition in the framework of ID-FAST project, agreed among the group for results comparison from stack to single-cell hardware. It consist of: 63.5/30% $RH_{an./ca.}$, T = 68 °C, $p_{in,anode}/p_{in,cathode}$ = 3.0/2.8 bar. Modified parameters for single-cell test $\lambda_{anode}/\lambda_{cathode}$ = 2/4, minimum flux = 0.5 A cm^{-2} equivalent.

- H_2/air polarization curve, named JRC condition
  This is the reference condition, proposed by the JRC, for the harmonization of european tests in stack and single-cell hardware. It consist of: 50/30% $RH_{an./ca.}$, T = 80 °C, $p_{in,anode}/p_{in,cathode}$ = 2.5/2.3 bar. Modified parameters for single-cell test $\lambda_{anode}/\lambda_{cathode}$ = 2/4, minimum flux = 0.5 A cm^{-2} equivalent.

5.2.1 Mitigated Start-up/Shut-down protocol

The start-up/shutdown ageing procedure is described in Figure 5.3. As reported, starting from H_2/air OCV, nitrogen is fluxed at cathode side for 300 s, during which cell voltage decreases till approximately 100 mV. Cathode electrode potential, evidenced by RHEs, follows the same trend, since anode operates with hydrogen. After the purging of the oxidant by the inert, that ensures full shut-down mitigation, air is fluxed for 120 s through the anode. Cell voltage immediately drops further, till 0 V, while cathode electrode potential increases to 1 V. Almost the same voltages are kept when air is introduced into the cathode: the after-long stop air/air condition is finally reached avoiding high cathodic potentials during the stop transient. After 120 s, a H_2/air front is finally generated at anode side; the unmitigated start-up causes cathode potential to increase up to 1.5 V. After 120 s again, the described procedure is repeated. According to the project specifications, the flux of hydrogen during start-up must be 1 A cm^{-2} equivalent. Using a 25 cm^2 CCM, N_{H2} = 175 ml min^{-1}; the same value has been adopted for the air flux at anode side. Applying this specification also to the cathode, it results $N_{N2} = N_{air}$ = 417 ml min^{-1}.

5.3 Results of Start-up/Shut-down durability testing

In order to identify the mechanisms promoting localized degradation and their related critical areas, performance characterization during Start-up/Shut-down cycling was evaluated. The ageing process caused the loss of platinum

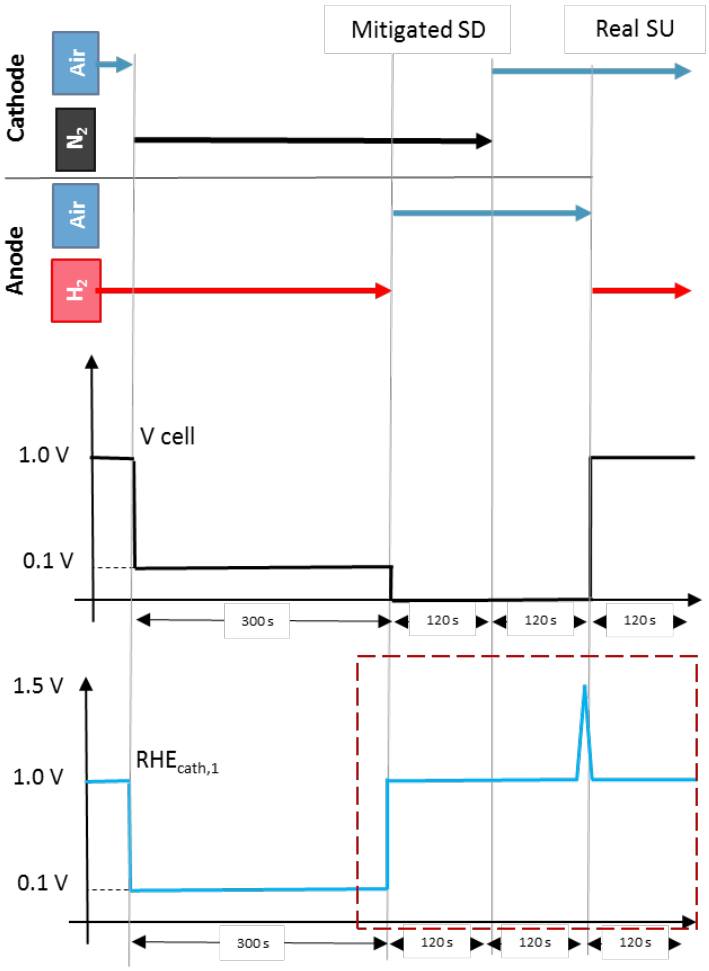

Figure 5.3 – Schematic representation of the procedure that reproduces the Start-up/Shut-down event. Shut-down is fully mitigated by an N_2 purge, while the H_2/air front mimics the start-up. The entire process is developed at 30 °C, 100/100% RH and ambient pressure. Cell voltage and local cathode inlet potential ($RHE_{cath,1}$) are here sketched.

active area, investigated though the cyclic voltammetry measurement. The average decrease for the entire CCM after 200 cycles of Start-up/Shut-down is 25%.

In detail, the local ECSA reduction has been computed thanks to the local cyclic voltammetry measurements, collected in Figure 5.4. The largest loss is evident for the first segment, since it undergoes the highest potentials and for longer during the start-up transient. The loss of ECSA (Table 5.1) is significant for the half of the cathode electrode closer to the anode outlet (i.e. segment 1 and 2) while segment 4, which encompasses the anode inlet

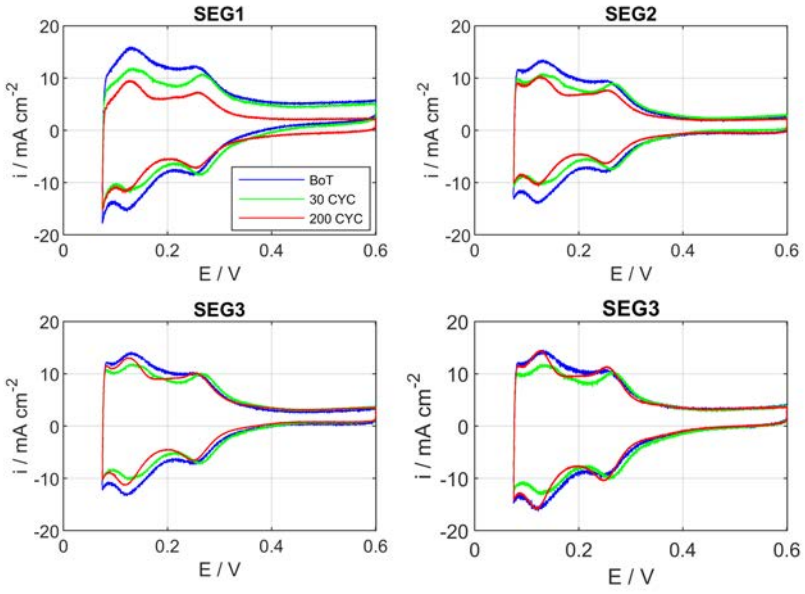

Figure 5.4 – Local CV measurement at BoT, 30 cycles and 200 cycles (for each segment). T = 30 °C, 100/100% RH, $p_{out,anode} = p_{out,cathode} = p_{amb}$, $N_{N2} = N_{H2} = 60$ ml min^{-1}.

position, faces just a very slight ECSA reduction.

Table 5.1 – Local ECSA measurement at BoT, 30 cycles and 200 cycles (for each segment). Comparison between segments and global ECSA loss os reported.

Local ECSA measurement				
SEGMENT	BoT	30 CYC	200 CYC	Relative ECSA loss
	m_2/g	m_2/g	m_2/g	%
1	41	40	26	-37
2	45	40	30	-33
3	45	42	36	-20
4	45	43	39	-13
Global	44	41	33	-25

The ECSA loss increases the kinetic losses: coherently, H_2/O_2 polarization curves are signed by performance reduction, visible as a vertical translation in the i-V chart. The larger voltage decrease regards segment 1 and 2 (close to anode outlet), within -10 mV and -8 mV, while the performance of the segment 4 is practically unchanged and even a bit promoted by the way of

current redistribution among the segments, within +4 mV.

To get more insight into the performance loss induced by start-up/shut-down cycling, H_2/air polarization curves were performed and the global results over the entire MEA are reported in Table 5.2.

Table 5.2 – Global performance loss under operating conditions reported in 5.2

Global performance Loss				
Type	Current density	ΔV %:BoT - 30 CYC	ΔV %:BoT - 200 CYC	ΔV %:30 CYC - 200 CYC
	mA cm^{-}22	mV	mV	mV
REFERENCE	0.1	-4	-12	-9
	1.8	14	3	-12
Oxygen	0.1	-3	-6	-3
	1.8	2	-2	-4
ID-FAST	0.1	20	4	-16
	1.8	7	-9	-16
JRC	0.1	18	-1	-19
	1.8	5	3	-2

Here, two differents results can be observed between the first 30 cycles and the the remaining ones until 200 cycles:

- first 30 cycles:
  a slight increase of performance was observed, in particular at mid-high current density. This could be related to a "cleaning" of the catalyst, as a probable consequence of voltage cycling. The effect is more pronuanced in dry conditions (i.e. ID-FAST and JRC i-V curves), suggesting an improvement of protonic transport and/or oxygen mass transport due to a better water management or an increase of diffusion media porosity. Such phenomenon, not observable with harsher decay protocols, appears reproducible and requires further dedicated studies, in view of break-in and refresh procedures.

- last 170 cycles:
  Deviations are limited for the average performance: within 12 mV in air and 6 mV in oxygen. Nevertheless, the maximum performance loss measured between 30 and 200 cycles is within -19 mV in the worst case. This performance loss is equivalent to 112 μV/cycle in the last 170 cycles. This has non-trivial effects and could also be dramatically higher in real automotive tests programme when Off-load events are taken into consideration, if proper mitigation strategies were not applied. To be thorough, I have to highlight that the degradation associated to start-up/shut-down cyclying is compatible with 1000 hours (i.e. 1h = 1 cycle, and total amount is 20% of lifetime) of operation under NEDC automotive cycles, as reported in [59].

Moreover, to evaluate the dispersion of current density distribution, a heterogeneity level index ϵ of the current density i is calculated as[70]:

$$\varepsilon[\%] = \frac{i_{SEG,i-th}}{i_{GLOBAL}} \cdot 100\% \tag{5.1}$$

where i_{GLOBAL} is the current density of the overall cell, while i$i_{SEG_{i-th}}$ is the values of current density provided by the each segment. The index ϵ-i will be used in the following to quantify the impact on current density heterogeneity of operating parameters for the polarization curves. Moreover, it will permit to quantify the current density redistribution during start-up/shut-down cycling.

Results for heterogeneity index, calculated for the 4 segments in all the operating conditions, are reported in Table 5.3.

Table 5.3 – Heterogeneity measurements at BoT, and 200 cycles (for each segment). Comparison between segments is reported for all the operating conditions tested.

Heterogeneity current index								
	BoT				EoT			
Type	SEG 1	SEG 2	SEG 3	SEG 4	SEG 1	SEG 2	SEG 3	SEG 4
	%	%	%	%	%	%	%	%
REFERENCE	115	94	95	97	103	94	100	104
	105		*96*		*98*		*102*	
Oxygen	108	93	97	103	101	87	98	115
	101		*100*		*94*		*106*	
ID-FAST	115	94	96	96	102	93	101	103
	105		*96*		*98*		*102*	
JRC	110	93	100	97	99	91	104	104
	101		*98*		*95*		*104*	

Looking at the results, two main considerations may be inferred:

- The heterogeneity index shows inhomogeneity in current density, already noticeable from low current density values despite the high stoichiometries applied, revealing a higher current density localized at cathode inlet and cathode outlet. Local EIS analysis permit to further investigate this phenomena. Focusing, on the high frequency resistance features(HFR) it's clear how the the outermost segments presented the lowest resistance value and this contributes to their higher performance, in all the operating conditions. The performance heterogeneity, could be ascribed to water distribution among the segments caused by triple serpentine flow field, or inhomogeneous MEA compression, that could affect mass transport resistance or contact resistances between the components.

- The comparison between the heterogeneity indexes, mediated on the two half-MEA (italic number in table 5.3), clearly reveal a current redistrubution after start-up/shut-down cycling, for the cathode outlet part (i.e. segment 3 and 4). As seen in section 3.4, the potential evolution during start-up/shut-down, is strongly heterogeneous, with a potential peak around 1.5 V vs RHE in the first cathode segment (close to anode outlet in counter-flow configuration). Voltage cycling leads to a loss of catalyst surface area, which result in an ORR kinetics controlled voltage loss.

To get more insight into the performance loss due to start-up/shut-down cycling, a more complete analyse of the first MEA segment (i.e. cathode inlet/anode outlet) will be described in the next section.

5.3.1 Local degradation investigation

Focusing the analysis on the first MEA segment that, as previously told, undergoes the largest potential variations, a clear performance loss appears in H_2/air polarization curve as depicted in Figure 5.5.

Comparing the results of local polarization curves, is clearly visible that the first region is affected by the main degradation. Mean performance loss for the four segmets are respectively: -18 mV, - 4 mV and pratically null for the third and fourth segment.

The kinetic performance loss due to platinum dissolution can be estimated based on the decrease of catalyst surface area (i.e. ECSA / $m^2_{Pt}g^{-1}_{Pt}$). According to Tafel kinetics:

$$\eta_{ORR} = \frac{2.303RT}{\alpha F}\log\left(\frac{i_{geo}}{i_0 \cdot ECSA \cdot L_{Pt} \cdot 10}\right) \tag{5.2}$$

where α, is the cathodic trasnfer coefficient (that is assumed equal to 1 at high voltage[89]), i_{fc} the current density in galvanostatic operation (units, A/cm^2), i_0 the exchange current density (units, A/cm^2_{Pt}), L_{Pt} the cathode platinum loading (units mg_{Pt}/cm^{-2}), and 10 a unit correction factor for the roughness factor (i.e $r.f.[\frac{cm^{-2}_{Pt}}{cm^{-2}}] = ECSA * L_{Pt} * 10$).

After start-up/shut-down cycling the theoretical effect of platinum dissolution can be estimated by ECSA decline, according to:

$$\Delta\eta = \frac{2.303 \cdot RT}{\alpha F}\log\left(\frac{ECSA_{BoT}}{ECSA_{EoT}}\right) \tag{5.3}$$

For the first segmented the theoretical voltage loss and measured one in H_2/O_2 polarization curve are respectively, -14 mV and -10 mV, in good

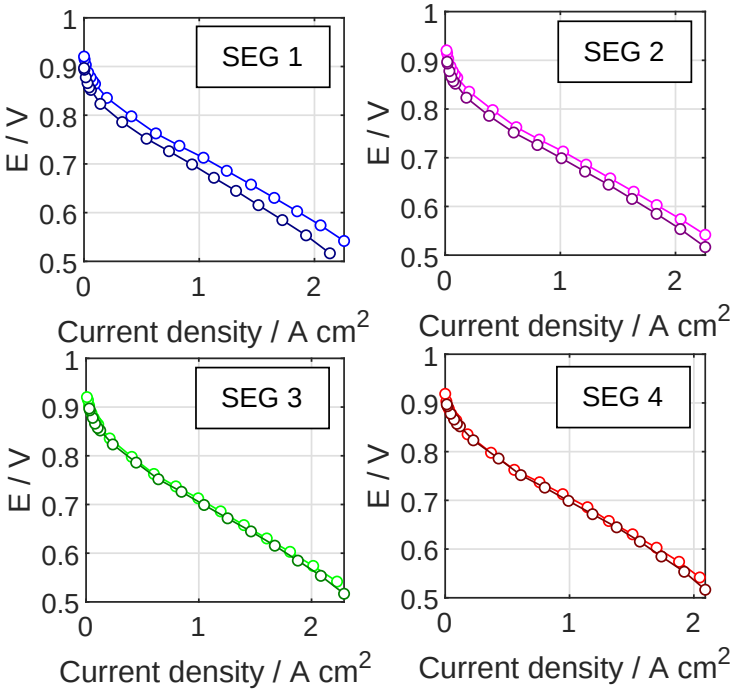

Figure 5.5 – Performance comparison at BoT and after 200 cycles of Start-up/Shut-down obtained by polarization curves of the 4 segments. Light colors BoT, dark colors curves after 200 cycles. Reference condition: 100/100% RH, T = 80 °C, $p_{in,anode}/p_{in,cathode}$ = 2.5/2.3 bar, $\lambda_{anode}/\lambda_{cathode}$ = 2/4, minimum flux = 0.5 A cm^{-2} equivalent.

accordance. Similar results are confirmed for the other segments, though the measured performance loss is slightly smaller than the theoretical one.

To complete the characterization of performance loss, Electrochemical impedance Spectroscopy have beeen analyzed, and the results are reported in Figure 5.6.

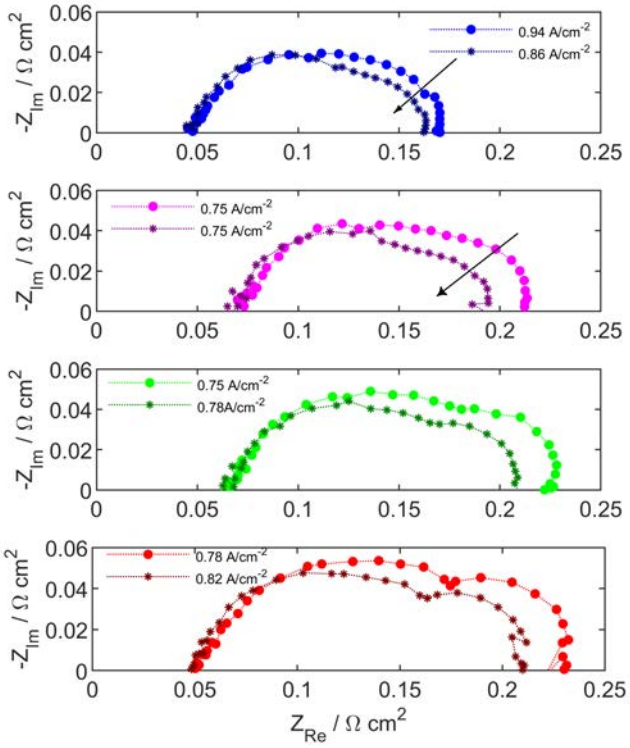

Figure 5.6 – Local EIS comparison at BoT and after 200 cycles of Start-up/Shut-down obtained by polarization curves at 0.8 A/cm^{-2}. Light colors BoT, dark colors curves after 200 cycles. Reference condition: 100/100% RH, T = 80 °C, $p_{in,anode}/p_{in,cathode}$ = 2.5/2.3 bar, $\lambda_{anode}/\lambda_{cathode}$ = 2/4, minimum flux = 0.5 A cm^{-2} equivalent.

Local EIS measurments confirmed in details, what that has been previously stated. All the EISs shown a reduced spectra, due to different phenomena:

- For the third and fourth segment, two main causes occurs: an increase of local current density that is in accordance with a reduction of charge transfer feature, due to current redistribution after start-up/shut-down cycling and the enhancement of oxygen transport as clearly visible as a reduction low frequencies features, associated with flow-field geometrical feautures;

- For the first and second segment, on the opposite, current redistribution induced a reduction of the current density at which EIS is performed. Despite, also in that case the impedance spectra, at low frequencies appears to be reduced, suggesting an improvement of mass transport resistance. This result could be in accordance with the improvement of performance observed after 30 start-up/shut-down cycles;

- Heterogeneous performance observed between middle and outermost segments, may be justified by the higher High frequency resistance observed in the middle of the MEA. Such effect, as previously told, can be attributed to an inhomogeneous MEA compression or water management and temperature distribution.

A more rigorous characterization requires a correction of voltage loss induced by the voltage cycling by the oxygen mass-transport loss through the diffusion medium, which can be clarified by limiting current measurements. The limiting currents were measured at 30 cycles and 200 cycles during start-up/shut-down cycling in order to determine the total transport resistance R_{Total} at different ECSA values, as defined in equation:

$$R_{Total} = \frac{4F}{RT}\frac{P_{O_2}}{i_{\lim}} \tag{5.4}$$

The evaluation of total transport resistance is not trivial in segmeted cell, because the evaluation of oxygen partial pressure in the channel required the computation of oxygen consumption and pressure drop in serpentine flow-fields. Therefore, the impact of oxygen mass-trasnport resistance is here presented in term of limiting curren measurment at different oxygen concentration, since the its evaluation can be performed without data processing, that which could introduce unintended artifacts.

Results of the limiting current test are shown in Figure 5.7 and reveal segments heterogeneity.

At 30 cycles, the limiting current density is a bit improved for all the segments but the first, while at 200 cycles the two halves of the MEA (close to anode inlet and to anode outlet) show an opposite alteration: the current is reduced in case of firts and second segment, with notably largest changes at the first, while the third and fourth segment exhibit contrarily improved perfomance. The net result is the overall MEA unvaried behavior.

As reported in literature by Caulk and Baker[13] a change in the oxygen transport resistances dependent on the water content of the diffusion medium (DM): in a dry DM, the entire pore volume can be used for oxygen transport, while in a water saturated DM, the amount of open pores for gas transport

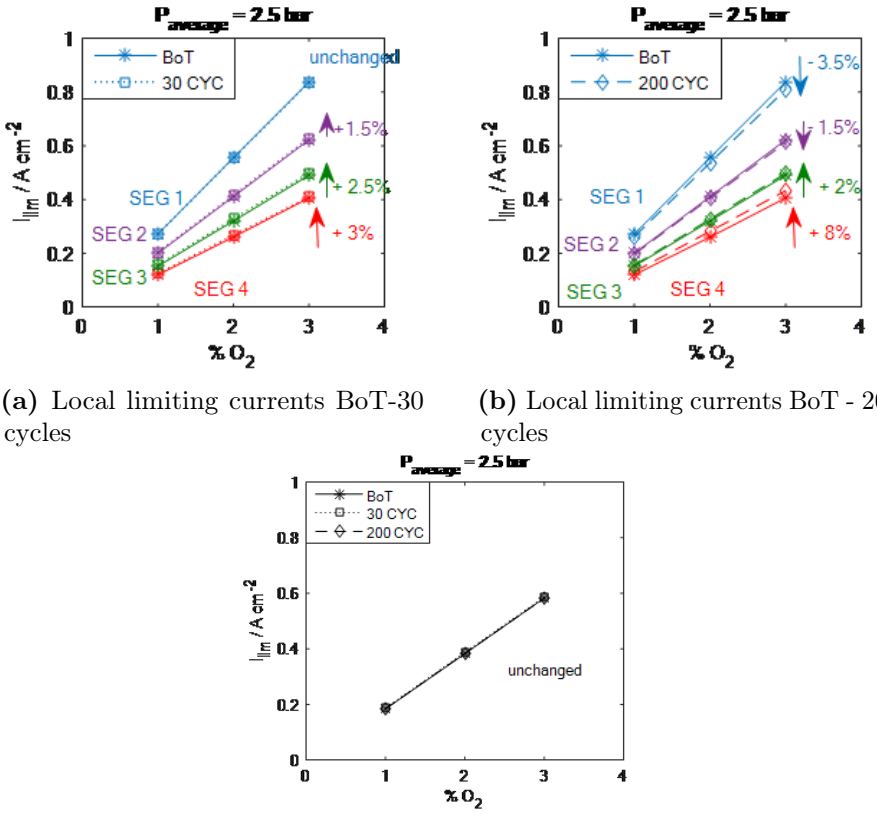

(a) Local limiting currents BoT-30 cycles

(b) Local limiting currents BoT - 200 cycles

(c) Global limiting currents BoT - 200 cycles

Figure 5.7 – Limiting current vs oxygen concentration measured at BoT, 30 cycles, 200 cycles for each segment and for the entire MEA (in black). The average percentage variation of the limiting current for each segment is indicated.

is significantly lower. Then it's reasonable to assume, that start-up/shut-down cycling in mitigated operating conditions could led to a cleaning of catalyst surface or ionomer or, alternatively, to a change of diffusion media hydrophobicity or open pore that boost gas transport.

5.4 Summary of results and conclusions

In conclusion, the first cathode segment (close to anode outlet) suffers the strongest degradation due to start-up operation. At 30 cycles, electrocatalyst surface decay and performance changes are minor (within 10% variation and 5 mV respectively) and the limiting current is unchanged.

At 200 cycles, which is a quite high number of long start-up compared to what expected in a real stack, the local ECSA loss is relevant (-37%) while the performance is reduced by a maximum of 20 mV. For the second half of the MEA (near anode inlet/cathode outlet), despite a slight reduction of electrocatalyst surface, the performance is even a bit improved. Even if this result could be attributed to a redistribution of the currents among the segments because of a more pronounced degradation in the segment 1 and 2, also a positive effect of condtioning can be attributed to voltage cycling at the part of MEA at cathode outlet.

Chapter 6

Experimental characterization of AST in Zero-gradient cell

6.1 Introduction

The main obstacle for a full commercialization of PEMFC vehicles in the near future is the reduction of system cost, mainly associated to the amount of platinum, meanwhile meeting long-term durability (see Chapter 1.2). Despite recent achievements in lowering platinum loading of cathode catalyst layer below to 0.1 mg_{Pt}/cm^2[41], additional overpotential occurs at low loadings and high current density, and the origin of this phenomena is still debated[33, 62, 79].
Moreover, it is well-known that MEASs degraded under dynamic load-cycles, and Off-load operation, such as Start-up/Shut-down, due to associated voltage cyclings. This means that voltage cycling tests are frequently applied as accelerated stress test to evaluate the materials durability.
The protocols developed by the American Department of Energy (DoE) are the main applied and investigated in literature. Such a protocols are: the square wave (SW) potential cycling, for the evaluation of Electrocatalyst durability, developed to reproduce voltage cycling during normal operation, and designed to accelerate the degradation mechanism of platinum dissolution; the Triangular wave (TW) potential cycling, for the evaluation of support materials, intended to reproduce start-up/shut-down Off-load operation and fuel starvation, and designed to accelerate the degradation mechanism of carbon corrosion due to potentials rises over 1.5 V (see Chapter 3.4 and [72]). However, DoE ASTs are performed at very specific parameters (e.g. 80 °C, 100% RH), not representative of real-world operations, which are instead characterized by a high heterogeneity of conditions that make the degradation

heterogeneous too as seen in previous in Section 5.3. In addition, ASTs don't reproduce the typical parameters of the today-adopted operative modes, like the mitigation procedures for start-up/shut-down (based on low temperatures, high flow rate and oxygen consumption).

In this chapter, as a basis for the development of the new AST protocols for start-up/shut-down impact evaluation, DOE ASTs were evaluated. All material testing results have been realized adopting new single cell design (named Zero-gradient cell hardware), designed to characterize material properties under uniform operating conditions, without any effect of the flow-field design.

6.2 Experimental Methodology

6.2.1 The Electrocatalyst and Support AST protocols

In the first Sections the effects of degradation are studied separately for the catalyst layer and the carbon support using DoE stress protocols. Next, the SU-AST protocol, is presented and the results were validated.
Here, common details were presented, such as tested materials and assembly, diagnostics protocols and hardware. ID-FAST furnished Catalyst-coated membranes (CCMs) was used for this work: a Johnson Matthey CCM with with Pt loading of 0.08/0.4 mg cm^{-2} for the anode/cathode side assembled with Freudenberg GDL H14CX483 without hot-pressing into Zero-Gradiente hardware. The active area was controlled using PTFE sub-gasket, at fixed value of 10 cm^{-2}. A more detailed description is reported in Chapter 2.2.

As first the effects of Carbon Corrosion and Platinum dissolution are evaluated with protocols reported in Table: 6.1.

Table 6.1 – Electrocatalyst and Support AST protocols

	Electrocatalyst AST	Support AST
Cycle	Square wave: steps 0.6 V (3 s) - 0.95 V (3 s) rise time 0.5 s	Triangular sweep: 1.0 - 1.5 V sweep rate 500 mV/s
Number	30000 cycles	5000 cycles
Cycle time	6 s	2 s
Temperature	80°C	
Relative Humidity	Anode/cathode 100%	
Fuel/Oxidant	H_2/N_2 at 60 mL/min	
Pressure	Atmospheric	

Detailed informations about the overall degradation can be derived from the comparison characterization procedure performed at the Beginning and End of test: the polarization curves presented in 2.4 show the change of fuel cell response at different working conditions after the degradation procedure.

All MEAs were conditioned prior to testing, using a galvanostatic procedure (H_2/air flows fixed stoichiometry $\lambda_{\text{anode}}/\lambda_{\text{cathode}} = 2/4$ at 65°C, 100% relative humidity (RH), ambient pressure): 0.5 A/cm^{-2} for 60 min, 2 min at 0.2 A/cm^{-2}, and 2 min at 0.8 A/cm^{-2}. This sequence was repeated 10 times, after which constant performance was reached.

For performance characterization differential flow polarization curves were recorded in galvanostatic mode at Beginnig of Life and End of life,following the indications presented in Chapter 2.4. To evaluate the course of degradation ID-FAST and Reference polarization curve are carried out at each degradation steps (i.e. Electrocatalyst AST: BoL - 5k - 20k - 30k cycles; Support AST: BoL - 200 - 1k - 2k - 5k cycles).

The ORR kinetics (i.e. mass activity and Tafel slopes) were determined from Oxygen polarization curve, after application of corrections for: ohmic voltage drop (iR-free), determined by Electrochemical Impedance Spectroscopy (EIS) measurment of High frequency resistance at a specific current density; ohmic short-circuit of the membrane and hydrogen crossover, determined by Linear Sweep Voltammetry measurment.

Cyclic voltammogram (CV) were recorded at cathode electrode at each stop (H_2/N_2 flor rate 60 mL/min at 30°C, 100% relative humidity (RH), ambient pressure) and Electrochemical Active Surface Area (ECSA) was calculated integrating H-desorption charge (using a specific charge of 210 $\mu C/cm_P^{-2}t$) and averaging over 5 voltammograms. The Oxygen mass transport resistance (R_{ToT}) was calculated from limiting current measurements at 80°C and 100% RH under fixed flow conditions (2 nl/min of H_2 and 4 nl/min of O_2/N_2 mixtures) at three different oxygen concentration (i.e. 1 - 2 - 3 $\%_{drygas}$).

Moreover, EISs are used to evaluate the effects of activation, ohmic and mass transport losses of performance at 0.4 $A\ cm^{-2}$, 1 $A\ cm^{-2}$ and 2 $A\ cm^{-2}$, at different operating conditions.

6.3 Catalyst Support Accelerated Stress Testing

As presented in Chapter 2.5.4, the catalyst support protocol uses a rapid triangle wave cycle to accelerate the corrosion of the catalyst support minimizing the degradation of the catalyst itself. The potential range of the protocol is similar to start-up or shut-down unmitigated one. Carbon Support AST forces the mechanism of carbon oxidation, which led after several cycle at the electrode collapse [78]. The porosity and the tortuosity of the carbon texture

change, the gas transport resistance increases and the triple phase boundary of the electrode gets worse because of Pt nanoparticles detaching.

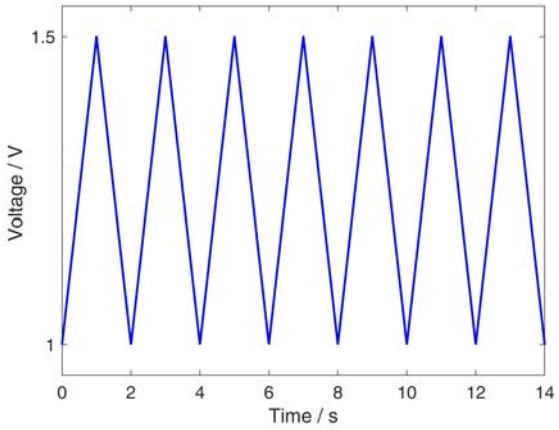

Figure 6.1 – Voltage profile for carbon support AST

Additional information about the effects of temperature can be derived by carrying out the same AST at lower temperature (T_{cell} = 30 °C).

6.3.1 Effects of carbon support degradation

The evolution of the cyclic voltammetry profile and ECSA, at different AST stops are reported in Figure 6.2.

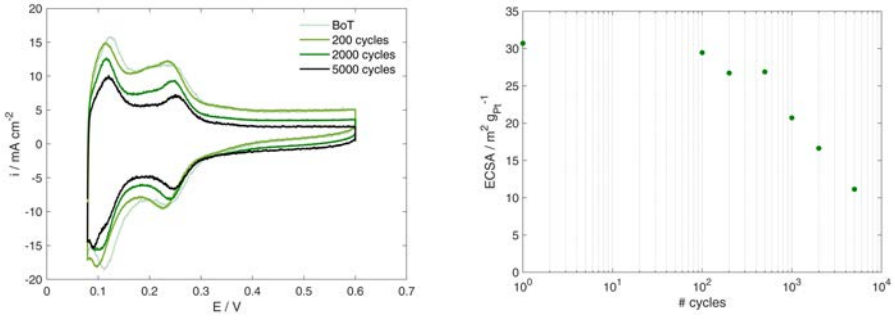

(a) CV **(b)** ECSA evolution

Figure 6.2 – CV and ECSA measurements during Support AST. T = 30 °C, 100/100% RH, $p_{out,anode} = p_{out,cathode} = p_{amb}$, $N_{N2} = N_{H2}$ = 60 ml min^{-1}.

The ECSA reduces by 17% between 1 and 1000 cycles and decreases by 41 % in the last 4k cycles referring to the initial value of active area. The

wide change of peaks, in accordance with scientific literature[53], indicates that platinum loss due to carbon corrosion is boosts by high temperature effects and high potential cycling.

Moreover, the reduction of current width at 0.4 V, in the last 3k cycles, suggests the reduction of double-layer capacitance, mainly due to carbon corrosion of catalyst support, which led to a reduction of support area. The effect seems more evident after 2000 cycles, when, probably, electrode structure collapses, with a strong reduction of ionomer/carbon contact.

To evaluate mass activity loss during voltage cycling oxygen polarization curves were collected at BoL and EoL and results were compared in Figure 6.3.

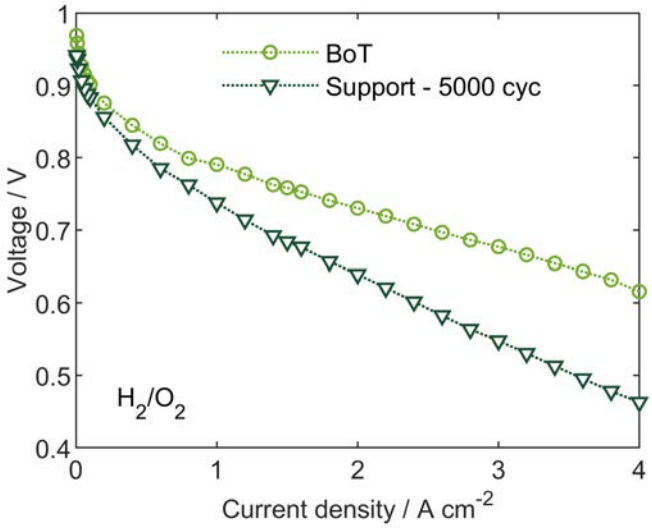

Figure 6.3 – Comparison between oxygen polarization curves during Carbon Support AST cycling. Operating conditions: 100/100% RH, T = 68 °C, $p_{in,anode}/p_{in,cathode}$ = 3.0/2.8 bar, $\lambda_{anode}/\lambda_{cathode}$ = 2/19 (constant flow rate of air i-V curve), minimum flux = 0.5 A cm^{-2} equivalent.

Platinum utilization decreases significantly: after 5000 cycles of carbon support AST, mass activity is only the 50% of the initial value, thus ageing is quite destructive in term of performance as the following Table 6.2 shows:

To evaluate the performance loss induced by voltage cycling, H_2/air polarization curves were performed and the results at BoL and at each stop are reported in Figure 6.4, for the reference and the ID-FAST operating conditions. In both cases in the first 1k cycles MEA performance gets better probably because the Break-in procedure does not guarantee a complete activation of the MEA, or few cycles at high potential have a beneficial

	ECSA	**Mass Activity**
	m^2/g_{Pt}	A/mg_{Pt}
BoT	30	0.31
EoT	11	0.15

Table 6.2 – Mass activity and ECSA variation during Carbon Support AST

effect, as observed in previous chapter during start-up/shut-down cycling (see Section 5.3). After 2000 cycles, the effects of degradation is stronger: significant ohmic and mass transport losses can be recognised by the i-V curves.

The kinetic performance loss due to platinum dissolution can be estimated based on the decrease of catalyst surface area (i.e. ECSA / $m^2_{Pt}g^{-1}_{Pt}$). According to Tafel kinetics:

$$\eta_{ORR} = \frac{2.303RT}{\alpha F} \log\left(\frac{i_{geo}}{i_0 \cdot ECSA \cdot L_{Pt} \cdot 10}\right) \tag{6.1}$$

After 5000 cycles at high voltage, the theoretical voltage loss is -31 mV. In experimental results obtained in Reference, ID-FAST and Oxygen polarization curves are respectively: -87 mV, -74 mV and -46 mV. This values are higher compared to the theoretical one, suggesting that also worsening of proton and oxygen transport are involved.
Again, the maximum voltage loss is visible at high current densities, for the fully humidified curves (i.e. maximum voltage loss for: reference test = -252 mV; oxygen test = -153 mV; ID-FAST test = - 88 mV).

To clarify performance losses, Electrochemical Impedance Spectroscopy were analyzed and results are presented in 6.20.
The Nyquist plots confirm the degradation modes recognized in the polarization curves and ECSA measurments. High Frequency Resistance decreases in the first cycles of Support AST because of the improvement of membrane proton conductivity during first conditioning phase.
Despite, in the next cycles, at high frequency, the gradual increases of resistances (associated to *linear branch* feature[45]) is indicative of a dehydration of the MEA or worsening of proton conductivity, probably caused by electrode collapse or change of hydrophobicity of electrode/MPL materials, due to a decrease of water retention.
Similar results are reported in literature, where increasing hydrophilic effect of carbon surface oxidation are observed[22]. Then, after 2000 cycles *linear branch* is less evident, resulting in a more circular shape. As far as the author knows this effect is stil not clarified in literature.

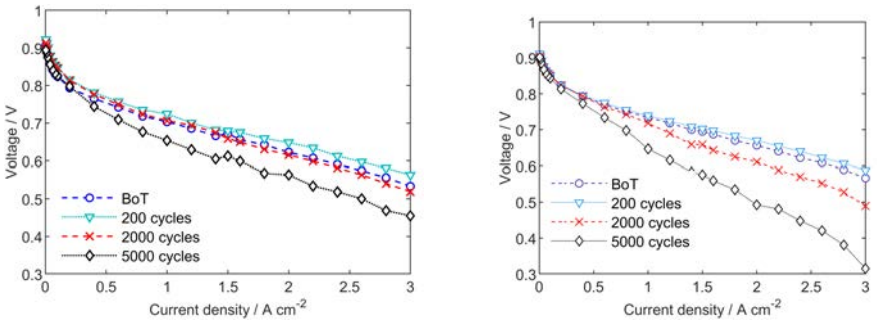

(a) ID-FAST polarization curves **(b)** Reference polarization curves

Figure 6.4 – Polarization curves during Support AST. ID-FAST: T = 68 °C, 63.5/30% RH, $p_{out,anode} = p_{out,cathode} = 3.0/2.8$ bar; Reference condition: 100/100% RH, T = 80 °C, $p_{in,anode}/p_{in,cathode} = 2.5/2.3$ bar. In each test, $\lambda_{anode}/\lambda_{cathode} = 2/4$, minimum flux = 0.5 A cm^{-2} equivalent.

The main differences between BoL and EoL spectra are visible at low frequencies, where the the feauture related to charge transfer resistance increased and a second inductive lopp become more pronuanced with the increased of degradation. This effect, mainly attributible to a worsening of oxygen mass transport resistance in the diffusion media, is also more evident at fully humidified conditions respect to polarization curves with feeded gas at low RH (see Figures: 6.20 - 6.23).

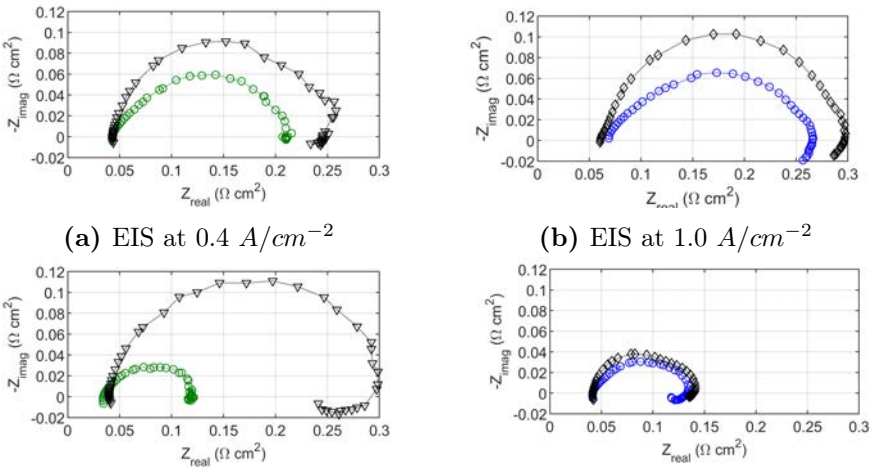

(a) EIS at 0.4 A/cm^{-2} **(b)** EIS at 1.0 A/cm^{-2}

(c) EIS at 2.0 A/cm^{-2} **(d)** EIS at 3.0 A/cm^{-2}

Figure 6.5 – EIS spectra evolution during Support AST at Reference (left) and ID-FAST (right) conditions.

Limiting current test, performed as presented in Chapter 2.4.5, allows

the computation of the total oxygen transport resistance for three different oxygen dilutions and pressures. Comparing the R_{MT} at BoT and EoT a wide change can be recognised.

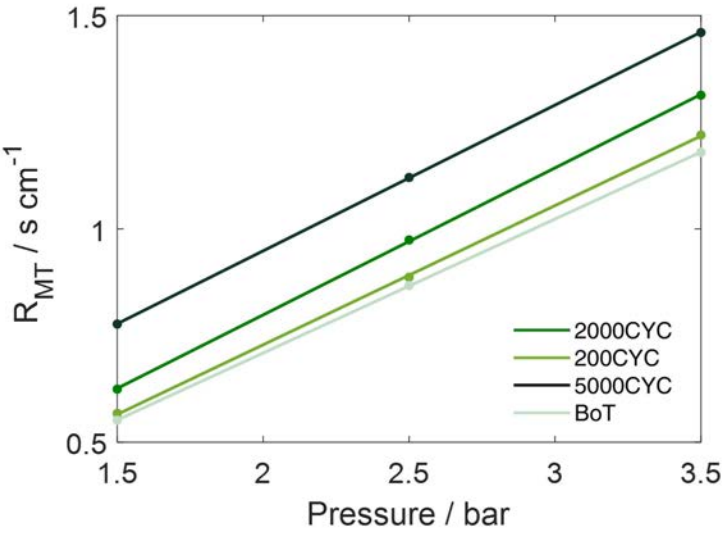

Figure 6.6 – Total O_2 mass transport resistance at different pressures during Support AST cycling

The effects of non-Fickian transport resistance, can be recognised in the vertical shift of the chart and corresponds to an increase of pressure-independent resistance.
The deviation of the line slope stands for an increase of resistance in molecular transport, is affected by pressure change and is relevant in diffusion media.

Greszler et al. [29] express the local resistance of mass transport from the distribution of the inverse of the roughness factor (defined in equation 6.2) and the total mass transport resistance.

$$f_{Pt}[cm^2 cm_{Pt}^{-2}] = 10\ ECSA[\ m^2 g^{-1}] L_{Pt}[mg_{Pt} cm^2] \tag{6.2}$$

They demonstrate that oxygen transport resistance is inversely proportional to platinum loading, or the equivalent platinum surface area. This effect could be usefull to discriminate between the mechanism of carbon oxidation and platinum dissolution, because their effect involved, respectively, a simple reduction of roughness factor during cycling, or others effect like support structure reconstruction.

The change of the Mass Transport Resistance has not exactly a linear change during Support AST, because after 1k cycles a small change of ECSA,

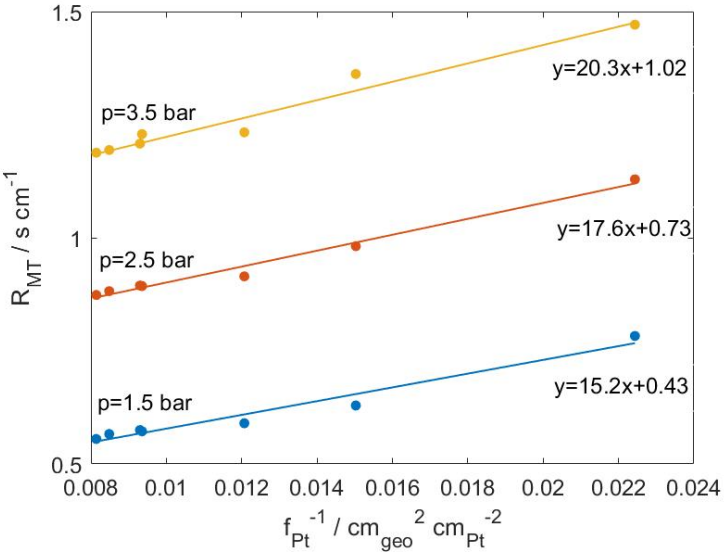

Figure 6.7 – O_2 mass transport resistance as function of roughness factor inverse during Support AST cycling

and proportionally of roughness factor, occur in parallel to a larger increase of mass transport resistance from the initial trend. ECSA changes in the last 4k cycles and defines the high value of the line slope. But to simplifiy the numerical analysis, a linear fit was here used and the results were compared with available literature data. From the Figure 6.7, the transport resistance on the surface of the platinum, can be determined. The slope of R_{O_2} vs $\frac{1}{f_{Pt}}$, are respectively: 5.5 for the Electrocatalyst AST (see 6.4) and 15-20 for the Support AST.

The values registered are higher than Greszler results [29], however the result of this test will be used to compare different AST's, presented in the next sections and underline the differences in the occurrence of specific degradation mechanism (i.e. carbon oxidation and platinum dissolution). In conclusion, carbon corrosion AST causes an increase of mass transport resistance, higher than the expected value for a simple platinum reduction.

A complete set of polarization curves at different working conditions is here presented as supplementary information, to evaluate the impact of carbon support oxidation at the end of Support AST, on the performance that occurs at the different zone of a stack single cell, that operate under driving load profile. First of all, voltage losses at different operating conditions are compared, and results are reported in Table 6.3.

Table 6.3 – Voltage losses during support AST cycling

Voltage Loss as a function of operating condition			
Test Condition	RH cathode %	ΔV mean	ΔV max
	%	mV	mV
Reference	100	-87	-252
Cath. Out - Low Load	100	-83	-186
Cath. Out - High load	77	-68	-155
Cath. In - Low Load	30	-46	-88
Cath. Out - High load	30	-39	-120

The comparison of the *Polarization A*[1] (i.e. cathode in - low loading operating condition: $T = 68°C$, $p_{C/A} = 2.8/3.0\ bar$, $RH_{C/A} = 30/63.5\%$) at the beginning and at the end of the test shows a small change in the activation losses region: the affects of degradation are more visible in the ohmic and mass transport controlled region as discussed previously.

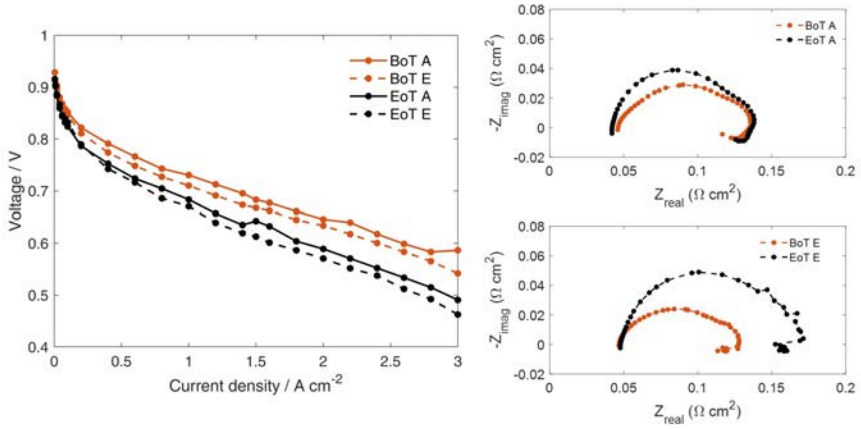

Figure 6.8 – EIS at 2 $A\ cm^{-2}$ (right) and Polarization A and E (left) at BoT and EoT of Support AST

The same result can be noticed in the evolution of *Polarizations E* (i.e. cathode in - high loading operating condition:$T = 85°C$, $p_{C/A} = 2.8/3.0\ bar$, $RH_{C/A} = 30/100\%$) demonstrating that carbon oxidation effects, in cathode inlet section (low relative humidity), are the same at low or high load operations.

[1]To simplify the legend notation, hereinafter polarization curves are denoted with capital letter and the associated operating conditions are reported in the text.

The operating conditions have impact on the EIS, which Nyquist plot is reported below at 2 $A\ cm^{-2}$. Due to the lowest RH_A, polarization A at BoT shows a more pronounced high frequency arc, as well as an higher R_{CT} and transport resistance feauture due to the lowest operating temperature of polarization E. In both cases degradation leads to a change of the spectrum that assumes a circular shape.

The effects of carbon corrosion in cathode outlet section are comparable at low or high load as well. The MEA degrades more homogeneously in the two conditions: a vertical shift can be recognized at low current density and the ohmic losses increases as well. The reduction of membrane proton conductivity and the reduction of reactants diffusivity compromise the effects of mass transport. The slope of the polarization curve increases slightly in middle region but mass transport losses are the most visible both in *Polarization C* (i.e. cathode out - low loading operating condition: $T = 68°C$, $p_{C/A} = 1.4/1.9\ bar$, $RH_{C/A} = 100/50\%$) and *Polarization F* (i.e. cathode in - low loading operating condition: $T = 95°C$, $p_{C/A} = 2.8/3.0\ mbar$, $RH_{C/A} = 77/40\%$). As previously seen for cathode inlet operations, linear branch is less visible due to degradation. Moreover, voltage cycling causes an increase of HFR in polarization F, that is the less humidified.

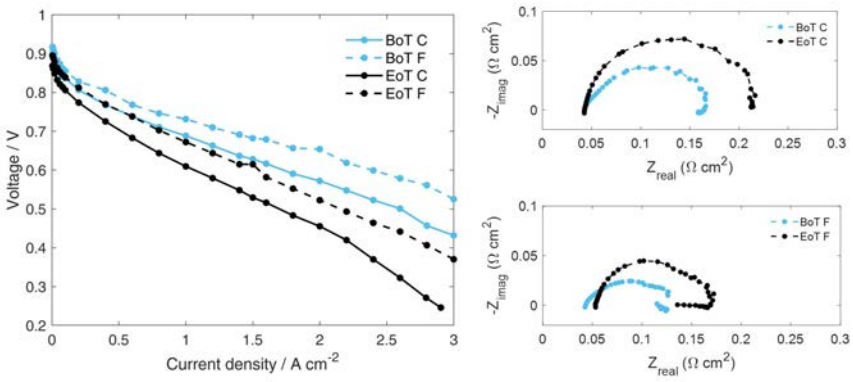

Figure 6.9 – EIS at 2 $A\ cm^{-2}$ (right) and Polarization C and F (left) at BoT and EoT of Support AST

The effects on the performance of the reduction of the diffusivity of reactants are stressed in *Polarization* C_{extra} (i.e. cathode out - low loading operating condition:$T = 68°C$, $p_{C/A} = 1.4/1.9\ bar$, $RH_{C/A} = 100/50\%$, $x_{O_2/H_2} = 10/100\%$) and *Polarization* F_{extra} (i.e. cathode in - low loading operating condition: $T = 95°C$, $p_{C/A} = 2.8/3.0\ bar$, $RH_{C/A} = 77/40\%$,

$x_{O_2/H_2} = 10/100\%$): the results at the end of the test show a heavy reduction of the limiting current and a slight increase of activation losses. At both BoT and EoT, these two tests are characterized by higher R_{CT} caused by the lower oxygen partial pressure, but this effect is more pronounced in *Polarization* C_{extra} due to the lower operating temperature.

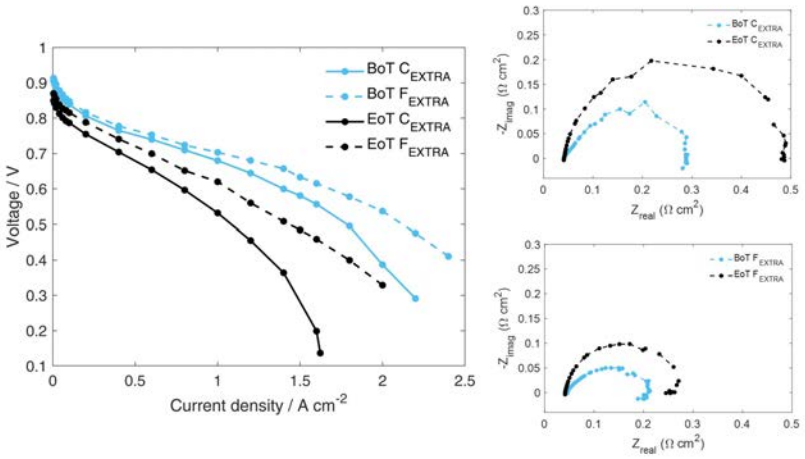

Figure 6.10 – EIS at 2 A/cm^{-2} (right) and Polarization C_{extra}e and F_{extra} (left) at BoT and EoT EIS of CC AST

A lower hydrogen content in reactants does not change the evolution of degradation: the effects visible in *Polarization E* are confirmed in *Polarization* E_{extra} (i.e. cathode in - high loading operating condition: $T = 85°C$, $p_{C/A} = 2.8/3.0\ mbar$, $RH_{C/A} = 30/100\%$, $x_{O_2/H_2} = 70/21\%$).

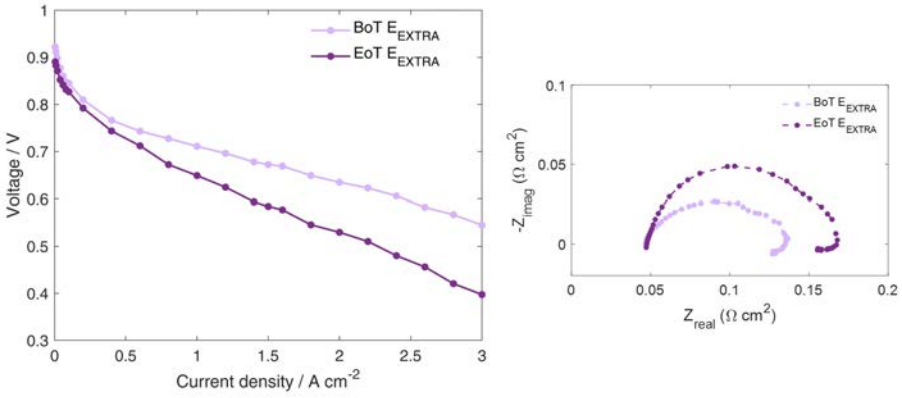

Figure 6.11 – EIS at 2 A/cm^{-2} (right) and Polarization E_{extra}(left) at BoT and EoT EIS of Support AST

The figure below presents the change of voltage loss at different cycles for Reference (operating condition: $T = 80°C$, $p_{C/A} = 2.3/2.5\ bar$, $RH_{C/A} = 100/100\%$) and ID-FAST (i.e. cathode in - low loading operating condition: $T = 68°C$, $p_{C/A} = 2.8/3.0\ bar$, $RH_{C/A} = 30/63.5\%$) polarization curve. The rate of degradation is computed as the ratio of the total voltage loss between BoT and EoT and the total duration of the AST. The degradation rates are respectively for Reference and ID-FAST operating conditions: -17 $\mu V/cycle$, with a maximum of -50 $\mu V/cycle$ at high current density, and - 9 $\mu V/cycle$, with a maximum of -37 $\mu V/cycle$ at high current density.

In conclusion the evaluation of performance evolution, under different operating conditions, is fundamental for: discriminate which kind of voltage loss is more stressed (i.e. kinetics, ohmic, transport overpotentials), and in particular, to evaluate how the operating conditions combined their effect with degradation in order to predict the response of materials at different zone of a full scale MEA (i.e. heterogeneity effect, see Chapter 5.3).

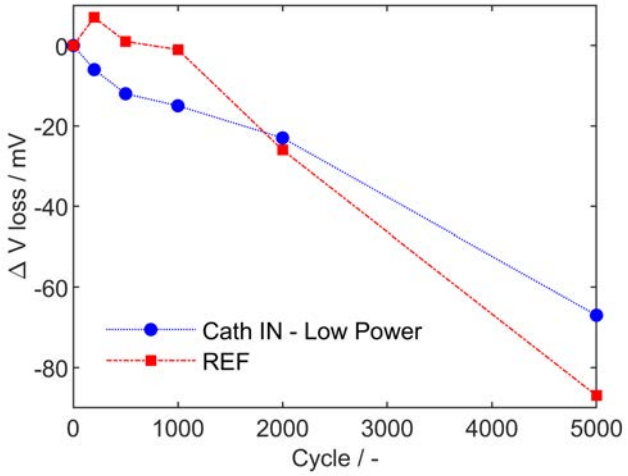

Figure 6.12 – Degradation rate during Support AST for Polarizations

6.3.2 Effects of temperature on carbon support AST

In the previous section a complete characterization of carbon support AST was presented. The analysis conducted in this chpater started from carbon oxidation mechanism, because this is main known cause that affect performance loss during start-up/shut-down cycling. A well-defined correlation between the two types of operation (i.e. voltage cycling during AST and start-up/shut-down) was found in Chapter 4.4.

In the next sections the analysis will be addressed and consideration will be given to explain how the mitigation strategies, involved in real world Start-up/Shut-down cycling, affetcs the degradation process. First of all, the stressor effect of temperature is analyse by repeating Support AST at 30 °C.

Low Temperature Carbon Support AST presents different results in terms of degradation effects than high temperature AST. Cyclic voltammetries and ECSA measurements are reported in 6.13. The active area increases uniformly during AST. In the first 500 cycles ECSA can be considered constant and reach the maximum value after 1000 cycles. Only at EoL, after 5000 cycles, a small reduction is computed, but the ECSA value is 14% higher than beginning of test. In terms of ECSA, a degradation effect is not recognised and this confirms the key role of the temperature, which has a strong impact on carbon corrosion kinetics. Moreover, it seems that at 30 °C, the MEA underwent an addittional activation process.

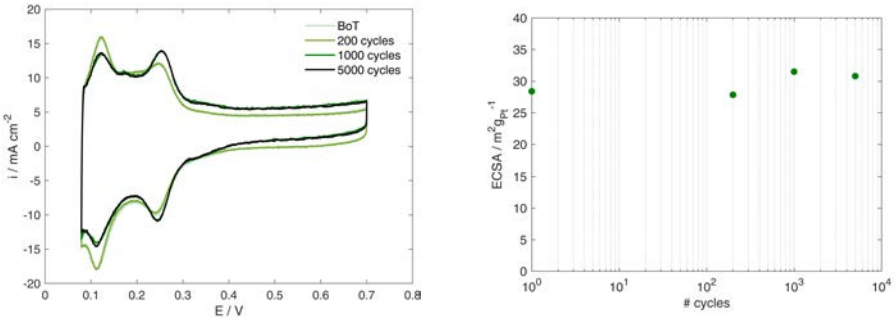

(a) CV **(b)** ECSA evolution

Figure 6.13 – CV and ECSA measurements during Support AST performed at T = 30 °C. CV protocol: T = 30 °C, 100/100% RH, $p_{out,anode} = p_{out,cathode} = p_{amb}$, $N_{N2} = N_{H2} = 60$ ml min^{-1}.

The increasing trend of platinum surface concides also with boosted performances, as revealed by i-V curve 6.14. reasons of phenomena are unknown: it may come from electrocatalyst re-crystallization, a larger availability of platinum active sites - previously not accessible - and modifications in the

ionomer. Moreover, high voltage cycling is known to be a method for reversible recovery of ECSA after degradation; sulphur based pollutants can be effectively removed[64, 80, 100].

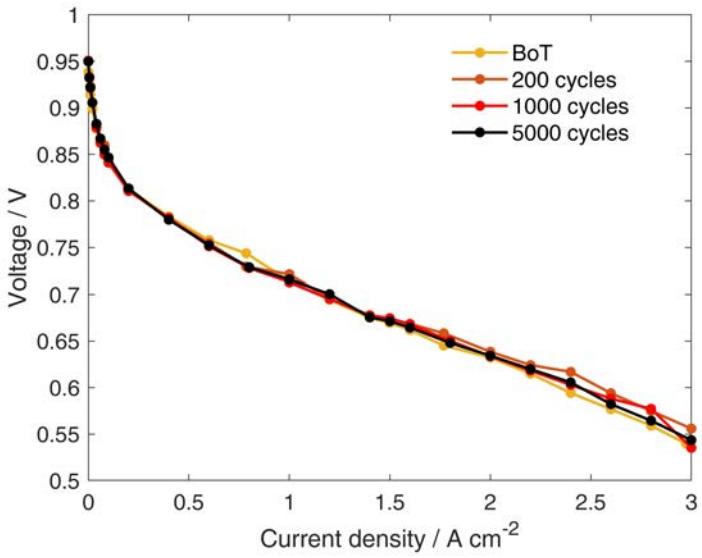

Figure 6.14 – Polarization A during low temperature CC AST cycling

Limiting current test results are depicted in 6.15. Test results demonstrate that no changes in mass transport resistance and limiting current are visible. Instead, a negative slope is reported, but the small differences taken into considerations limit the validity of the results and interpretation.

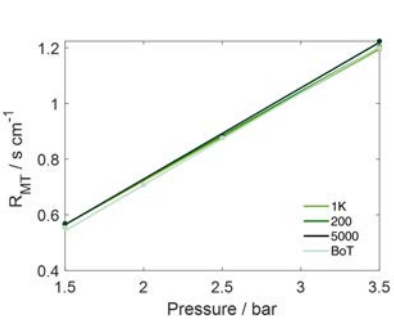

(a) Pressure effect on R_{tot,O_2}

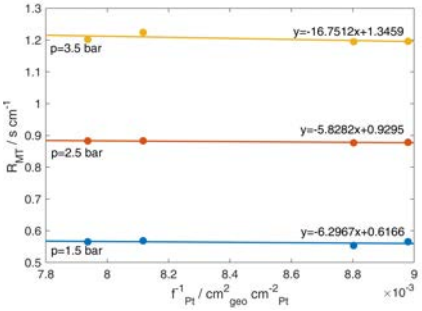

(b) Roughness factor effect on R_{tot,O_2}

Figure 6.15 – Variation of total oxygen mass transport resistance with pressure (a) and inverse of roughness factor (b) during low temperature Support AST

About the aforementioned initial recovery mechanism, the complete characterization suggests that something changed in transport characteristics, not only in terms of ECSA. It is difficult to understand alterations; however, recovery seems higher at 1000 cycles in atmospheric air than oxygen and mainly for high currents. Similarly, checking the trend at 2.5/2.3 bar, 500 cycles and 1000 cycles are characterized by boosted performances than BOT, most of all at high current densities. Being aware that voltage changes during this test are such small that results must be carefully interpreted, for what concerns this work we can conclude that cycling at high voltages and ambient temperature induces initially a non-negligible recovery compared to successive losses. It is necessary a very large number of cycles to see carbon corrosion degradation, that however seems to still exist.

6.4 Electrocatalyst Accelerated Stress Testing

During electrocatalyst AST protocol 30000 square wave potential cycles are imposed in order to accelerate the catalyst degradation. The main phenomenon occurring is Pt dissolution that causes the agglomeration of Pt particles, mainly due to Ostwald ripening, and the migration within the membrane[23, 81]. Data collected in this section will be used to discriminate which degradation mechanism prevails under start-up/shut-down cycling. Particular emphasis will be posed on the evaluation of kinetics losses.

Analyzing the evolution of CV profile during ageing, a reduction of adsorption/desorption peaks, and so a change of active area, is visible. Double-layer capacitance does not seem to be altered, leading to think that AST does not lead to structural changes of cathode electrode. With respect to Carbon Corrosion, Platinum Dissolution has a lower impact on the ECSA value: the reduction at 30000 cycles is about 50%.

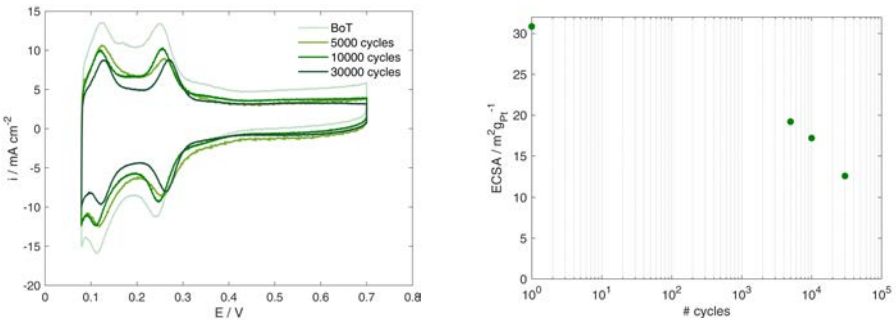

(a) CV **(b)** ECSA

Figure 6.16 – CV and ECSA measurements during Electrocatalyst AST performed at T = 30 °C. CV protocol: T = 30 °C, 100/100% RH, $p_{out,anode} = p_{out,cathode} = p_{amb}$, $N_{N2} = N_{H2} = 60$ ml min^{-1}.

The ECSA loss calculated correspong to a theoretical voltage loss of 26 mV (see 5.3). Thus, the mean change in oxygen polarization curve correspong to -36 mV, that is in quite good agreement with the prediction based on ECSA measurment.

Analyzing the trend of the H_2/O_2 polarization, the 50% reduction of mass activity is then consistent with the ECSA value at BoT and EoT (see 6.4).

	ECSA	**Mass Activity**
	m^2/g_{Pt}	A/mg_{Pt}
BoT	31	0.44
EoT	13	0.20

Table 6.4 – Mass activity and ECSA variation during Electrocatalyst AST

In both ID-FAST polarization curve (i.e. cathode in - low loading operating condition: $T = 68°C$, $p_{C/A} = 2.8/3.0\ bar$, $RH_{C/A} = 30/63.5\%$) and Reference one (operating condition: $T = 80°C$, $p_{C/A} = 2.3/2.5\ bar$, $RH_{C/A} = 100/100\%$) the degradation causes a vertical translation of the curve between BoT and EoT, even if degradation is slightly more pronounced in high current region. Similarly to the previous AST, Reference curve gets better during the first 5000 cycles, probably due to activation, and then it begins to worsen.

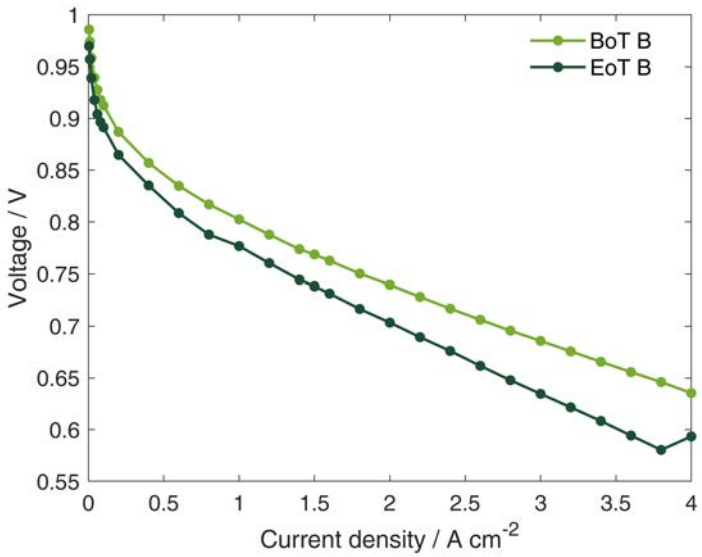

Figure 6.17 – H_2/O_2 polarization curve during Electrocatalyst AST cycling. Operating conditions: 100/100% RH, T = 68 °C, $p_{in,anode}/p_{in,cathode}$ = 3.0/2.8 bar, $\lambda_{anode}/\lambda_{cathode}$ = 2/19 (constant flow rate of air i-V curve), minimum flux = 0.5 A cm^{-2} equivalent.

LSV measurements validate the polarizations trend: after keeping constant during the first cycles, LSV slope decreases after 10000 cycles leading to a decrease of ohmic resistance (i.e. less short-circuit resistance).

The overall trend previously discussed is corroborated by EIS analysis. HFR remain quite constant during the AST, without causing an increase of ohmic overpotential.

The R_{CT} increase between BoT and EoT, that is more pronounced at low current densities, while at high current densities (e.g. at 2 and 3 A/cm^2) the amplitude of the imaginary component is quite invariated. This effect could be related to a second loop, probably caused by oxygen oscillation in the diffusion media, in similar ways to channel impedance[76]. In general, platinum dissolution seems to have no impact on the the linear branch keeps constant during degradation, compared to what happened in Support AST at high temperature.

Resistance to oxygen transport is just a little varied, less than 0.1 $s\ cm^{-1}$ (see 6.21). While a vertical translation is observed, the pressure independent term is increasing. The pressure dependent component keeps constant during degradation meaning that the small R_{MT} variation during Electrocatalyst AST is only due to the loss of available catalyst area.

The chart that represents the oxygen transport resistance as a function

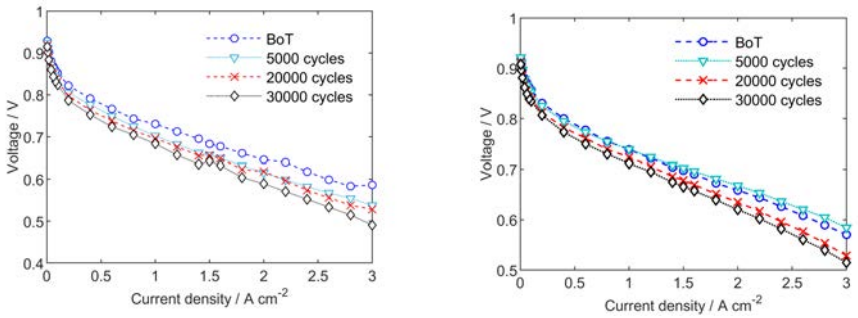

(a) ID-FAST polarization curve **(b)** Reference polarization curve

Figure 6.18 – Polarization curves during Support AST. ID-FAST: T = 68 °C, 63.5/30% RH, $p_{out,anode} = p_{out,cathode}$ = 3.0/2.8 bar; Reference condition: 100/100% RH, T = 80 °C, $p_{in,anode}/p_{in,cathode}$ = 2.5/2.3 bar. In each test, $\lambda_{anode}/\lambda_{cathode}$ = 2/4, minimum flux = 0.5 A cm^{-2} equivalent.

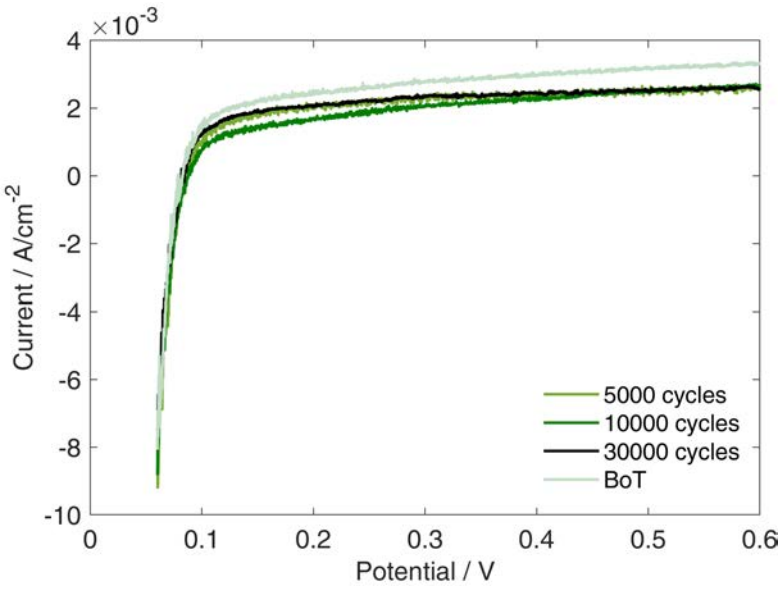

Figure 6.19 – LSV during Electrocatalyst AST cycling

of roughness factor, shows that the slopes of the curves are the same for the three pressures tested. This is consistent with what has been previously said: the pressure dependent component keeps constant during degradation meaning that the small R_{MT} variation during Electrocatalyst AST is only due to the loss of available catalyst area. The fact that the total resistance does not change significantly during AST indicates that carbon corrosion is negligible under voltage cycling profile applied.

As previously observed for ID-FAST (Polarization A: cathode in - low load-

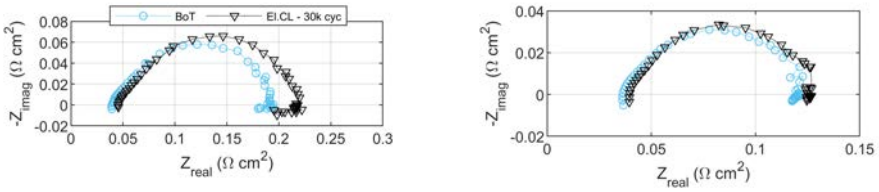

(a) EIS at 0.4 A/cm^{-2}

(b) EIS at 1.0 A/cm^{-2}

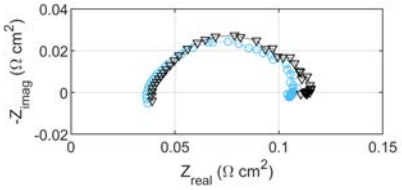

(c) EIS at 1.5 A/cm^{-2}

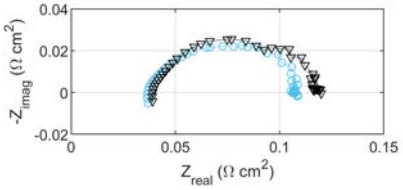

(d) EIS at 3.0 A/cm^{-2}

Figure 6.20 – EIS spectra evolution during Electrocatalyst AST at Reference condition: 100/100% RH, T = 80 °C, $p_{in,anode}/p_{in,cathode}$ = 2.5/2.3 bar, $\lambda_{anode}/\lambda_{cathode}$ = 2/4, minimum flux = 0.5 A cm^{-2} equivalent.

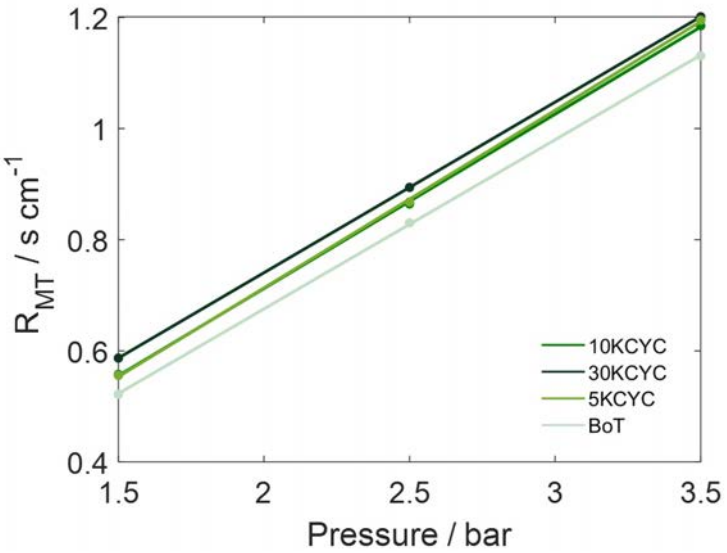

Figure 6.21 – Total O_2 mass transport resistance at different pressures during Electrocatalyst AST cycling

ing operating condition:$T = 68°C$, $p_{C/A} = 2.8/3.0\ bar$, $RH_{C/A} = 30/63.5\%$) and Reference polarization curves, Electrocatalyst AST causes a vertical translation of polarization curves, with a voltage loss that is slightly stronger in mass transport region. At cathode inlet section this trend is confirmed for

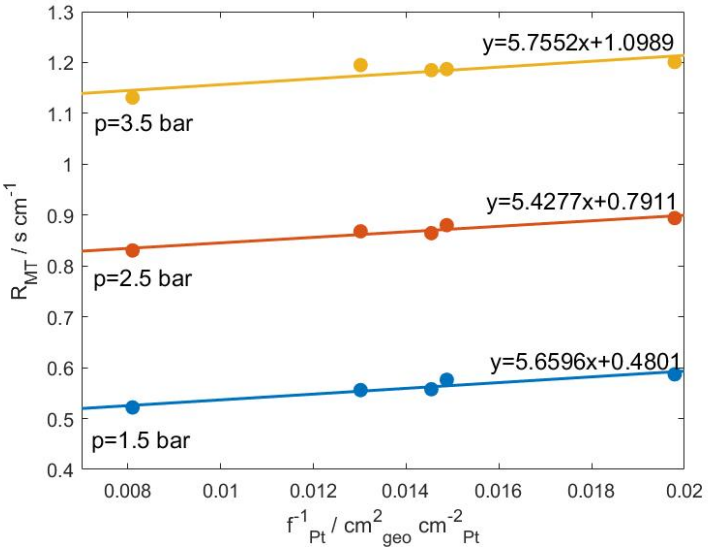

Figure 6.22 – O_2 mass transport resistance as function of the inverse of roughness factor during Electrocatalyst AST cycling

both the high and low load, as shown in Figure 6.23.
These two polarizations are characterized by a low cathode humidification that has impact on EIS spectrum that shows a strong low frequency arc, both at BoT and EoT. The effect of degradation is more visible at high temperature (Polarization E: cathode in - high loading operating condition:$T = 85°C$, $p_{C/A} = 2.8/3.0\ bar$, $RH_{C/A} = 30/100\%$) that shows an higher HFR at EoT.

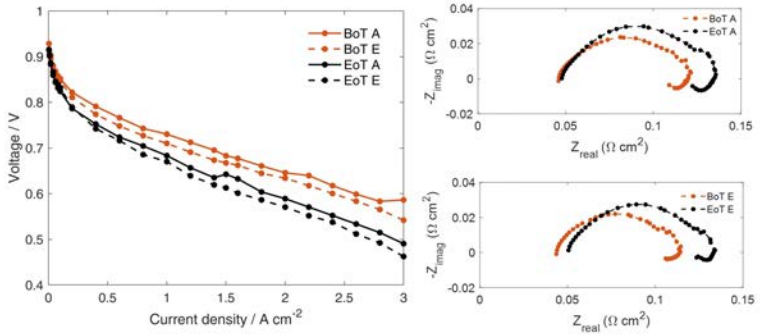

Figure 6.23 – EIS at 2 $A\ cm^{-2}$ (right) and Polarization A and E (left) at BoT and EoT of Electrocatalyst AST

The effects of Pt dissolution in cathode outlet section are comparable

at low or high load as well. The MEA degrades homogeneously in the two conditions: a vertical shift can be recognized at low current density and the ohmic losses increase as well. The reduction of membrane proton conductivity and the reduction of reactants diffusivity compromise the mass transport region with a double of voltage losses. Probably, ECSA reduction leads to a flux concentration at high current densities, and this is visible in the mass transport region particularly at cathode outlet, that represents a critical operation.

There are voltage losses located in middle region of polarization curve but mass transport losses are the most visible both in *Polarization C* (i.e. cathode out - low loading operating condition: $T = 68°C$, $p_{C/A} = 1.4/1.9\ bar$, $RH_{C/A} = 100/50\%$) and *Polarization F* (i.e. cathode in - low loading operating condition: $T = 95°C$, $p_{C/A} = 2.8/3.0\ mbar$, $RH_{C/A} = 77/40\%$).

While degradation doesn't influence linear branch, it leads to an increase of charge transfer resistance (and transport resistance loop) in both the operating conditions. Degradation has an higher impact on Polarization F due to the lower humidification, resulting in a more pronounced low frequency arc and an higher HFR.

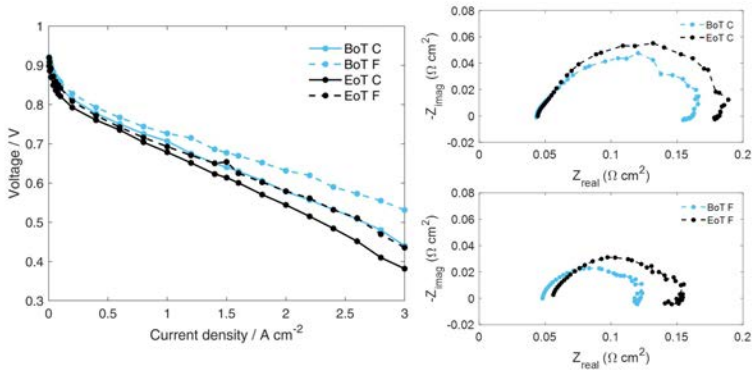

Figure 6.24 – EIS at 2 $A\ cm^{-2}$ (right) and Polarization C and F (left) at BoT and EoT of Electrocatalyst AST

The effects on the performance of the reduction of the diffusivity of reactants are stressed in *Polarization* C_{extra} (i.e. cathode out - low loading operating condition:$T = 68°C$, $p_{C/A} = 1.4/1.9\ bar$, $RH_{C/A} = 100/50\%$, $x_{O_2/H_2} = 10/100\%$) and *Polarization* F_{extra} (i.e. cathode in - low loading operating condition: $T = 95°C$, $p_{C/A} = 2.8/3.0\ bar$, $RH_{C/A} = 77/40\%$, $x_{O_2/H_2} = 10/100\%$): the two tests at the end of the test show a heavy reduction of the limiting current and a slight increase of activation losses.

The lowest oxygen partial pressure that characterizes these two tests results in a higher R_{CT} with respect to the other operating conditions, both at BoT and EoT. R_{CT} increase is more pronounced in polarization C, due to the lower temperature.

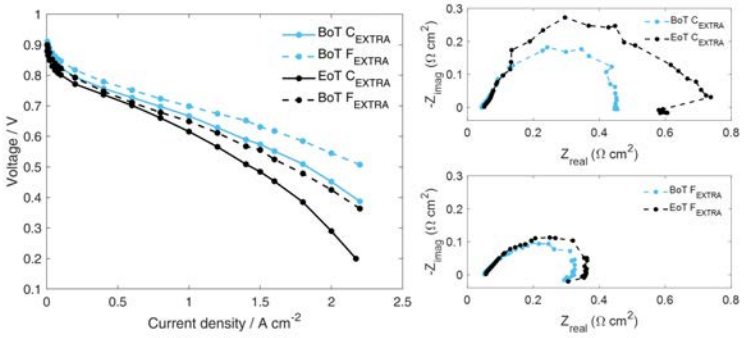

Figure 6.25 – EIS at 2 $A\ cm^{-2}$ (right) and *Polarization* C_{EXTRA} *and* F_{EXTRA} (left) at BoT and EoT of Electrocatalyst AST

The different oxygen partial pressure tested in *Polarization* C_{extra} and F_{extra} doesn't lead to a vertical shift, as observed for the other test. Degradation causes a voltage decrease located mainly in the mass transport region. However, even in this case, the performance loss in Pt dissolution is lower than in Carbon Support AST, and could be probably associated to

In *Polarization* E_{extra} a different anode feeding is tested (70% of H_2 instead of 100%) and this does not influence cathode degradation, as visible is polarization evolution, that has the same trend of *Polarization E*.

The occurrence of Platinum dissolution phenomena is affected by different degradation rates variable with the current density. The figure below summaries this aspect: it reproduces, as for Support AST, the voltage losses for different operating conditions at EoT. The following curves are reported: Reference conditions Reference one (operating condition: $T = 80°C$, $p_{C/A} = 2.3/2.5\ bar$, $RH_{C/A} = 100/100\%$) and theoretical voltage loss derived by ECSA measurment; to compare low and high stack power conditions *Polarization C* (i.e. cathode out - low loading operating condition: $T = 68°C$, $p_{C/A} = 1.4/1.9\ bar$, $RH_{C/A} = 100/50\%$) and *Polarization F* (i.e. cathode in - low loading operating condition: $T = 95°C$, $p_{C/A} = 2.8/3.0\ mbar$, $RH_{C/A} = 77/40\%$); to evaluate oxygen depletation at cathode outlet in real stack, *Polarization* C_{extra} (i.e. cathode out - low loading operating condition:$T = 68°C$, $p_{C/A} = 1.4/1.9\ bar$, $RH_{C/A} = 100/50\%$,

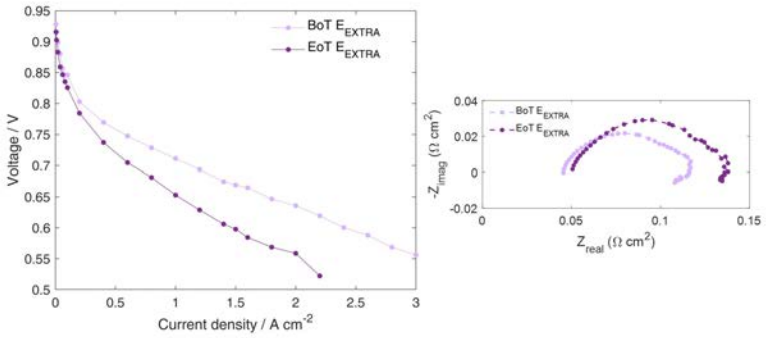

Figure 6.26 – EIS at 2 $A\ cm^{-2}$ (right) and Polarization E_{extra} (left) at BoT and EoT of Electrocatalyst AST

$x_{O_2/H_2} = 10/100\%$) and *Polarization* F_{extra} (i.e. cathode in - low loading operating condition: $T = 95°C$, $p_{C/A} = 2.8/3.0\ bar$, $RH_{C/A} = 77/40\%$, $x_{O_2/H_2} = 10/100\%$). Until 1 A/cm^2 the voltage losses are quite compatible with the theoretical calculated value, underlying that loss are principally kinetics controlled. Similar performance occurs at EoT both at low and high power mode, instead at low oxygen concentrantation, over 1 A/cm^2 to overpotentials start to be mass transport controlled. This aspect must be taken in proper consideration when performance at full scale cell are considered, starting from differential cell analysis, because the performance degradation due to platinum dissolution is boosted for the cathode outlet zone.

6.5 Summary of results and conclusions

Two different degradation phenomena, mainly related to cathode electrode , have been investigated through proper AST protocols in order to quantify the response of the materials to the single degradation mechanisms. The results obtained have to be used in order to understand how the single degradation mechanisms impact on the performance of the fuel cell.

The effect of carbon support oxidation is mainly attributible to a performance loss due to catalyst loss and worsening of oxygen transport in the diffusion media. Differently, platinum dissolution degradation affects the response of the fuel cell at all current densities as a kinetically controlled voltage loss. In particular, the increase of oxygen transport resistance was found as the main indicator to distinguish the contribution of each degradation mechanism on aged material response.

The performance indicators here discussed will be compared in the next Chapter, when a new AST protocol will be proposed to reproduce in a con-

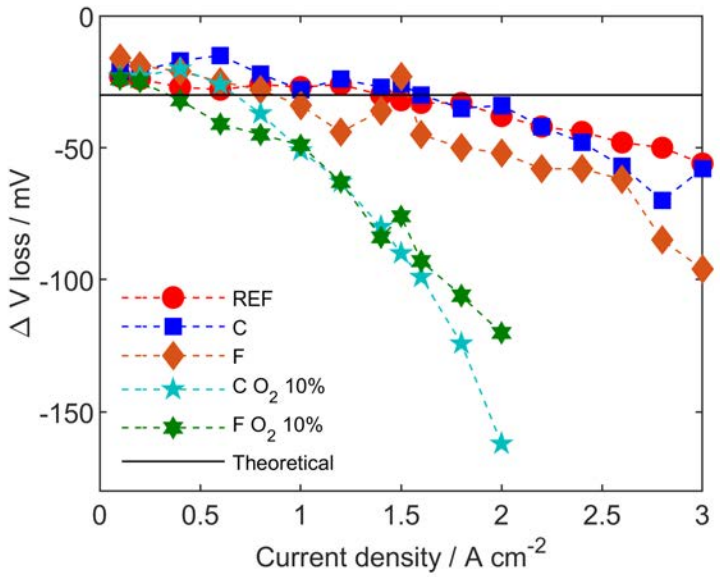

Figure 6.27 – Comparison between Voltage losses at different operating conditions

trolled way, the Start-up/Shut-down operation in zero-gradient cell hardware.

Chapter 7

Design of an accelerated stress test for start-up operation

7.1 Introduction

Finally, the principal result of this work, the new AST protocol (hereinafter defined *Start-up Accelerated Stress Test*, SU-AST) is presented, in order to reproduce the degradation mechanism observed under real Start-up/Shut-down cycling, when mitigation strategies are applied (see Chapter 5.1). The goal is to reproduce a realistic test, based on the specifications of the ID-FAST project durability test program. To summarise, the Start-up event should occur every 200 operating hours, i.e. 25/30 times through the component lifetime. In this range, the mitigation strategies applied, results effective to limit the effect of Start-up/Shut-down operation on components degradation (see Section 5.3). However, to better understand the impact of such a procedure, 200 cycles were tested, and results reported a localized performance degradation in the first half of the MEA. In particular, the aim of the SU-AST protocol is to mimic the degradation mechanism, underlying the Start-up/Shut-down cycling of the first segment of MEA (i.e. anode outlet/cathode inlet).

The analysis of the SU-AST, which reproduces the phenomena of Start-up/Shut-down under mitigation strategies, is the starting point to individuate the most effective phenomena cause of degradation of the fuel cell working in this condition. The effects of Platinum dissolution and Carbon Corrosion have been studied in the previous chapter, using DoE standard protocol in Zero-Gradient cell hardware. In this last section the degradation associated to these two phenomena are compared to the effects of Start-up/Shut-down degradation and the most effective phenomena is individuated. To confirm

the experimental results, the aged samples after 200 cycles were analysed by ex-situ characterization. Finally, the possibility to increase the acceleration factor of SUSD AST is studied. The role of Platinum Oxides is discussed while high voltage is hold. The formation of Platinum oxides is studied at different holding times and a new accelerated profile is provided.

7.2 The Start-up AST protocol

The details about start-up operation in segmented-cell, i.e. operating conditions, sequence and duration were reported in Section 5.2.1. A description of methodology applied in this chapter can be found in section 6.2.

To summarise, 200 cycles of start-up, at low temperature (i.e. 30 °C) were performed in sequence, using the segmented-cell with 8 reference electrodes, 4 at the anode and 4 at the cathode to collect local information. In Figure 7.1, the local potentials profiles, during the first 30 cycles, were reported.

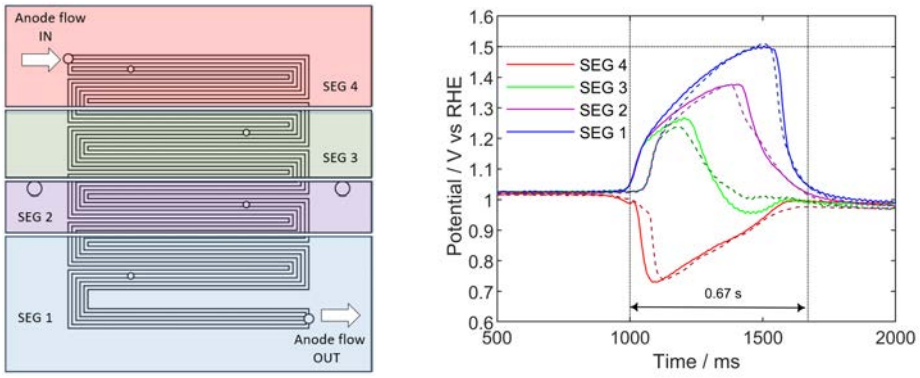

(a) Segmented-cell **(b)** Cathode potentials measured withe RHE

Figure 7.1 – (a) Scheme of segmented-cell (Start-up/Shut-down are performed in counter-flow); (b) Local potential profiels collected with RHEs at cathode electrode during the first 30 cycles of Start-up

The cathode segment that reach a maximum potential of 1.5 V vs RHE, during the start-up, is the cathode inlet (corresponding to anode outlet in counter-flow configuration). Since, the main degradation in full-scale cell is located in at cathode inlet, the main effort was so far concentrated primarily on trying to reproduce the impact of start-up operation on this specific zone.

The target of this work, is the definition of a new AST protocol able to describe Start-up/Shut-down process with a reliable, replicable and fast test in Zero-Gradient cell. In this first attempt an acceleration factor of one has been chosen. The new SU-AST proposed is performed at low temperature

(i.e. T = 30 °C as the mitigated start-up/shut-down cycling) and in inert atmosphere with the fuel cell fed with $60ml/min$ of N_2 at the cathode and $60ml/min$ of H_2 at the anode. The voltage profile of the real process at segment 1 is mimic along the entire AST cycle (see 5.3).

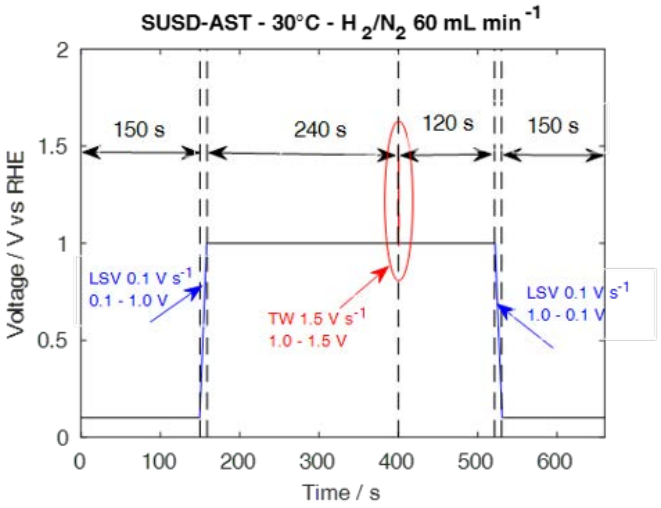

Figure 7.2 – New AST protocol for evaluation of Start-up operation

To simplify the shape of the voltage profile in real start-up, a triangular sweep cycle is used. The potential was fixed between 1.0 V and 1.5 V vs RHE and symmetric scan-rate, equal to 1.5 V/s is imposed. The description of Start-up AST protocol is reported in table 7.1, and a real representation of voltage profile in time is depicted in figure 7.2.

Cycle	1) Holding at 0.1 V for 2.5 min 2) Transaction with scan rate 0.1 $V\ s^{-1}$ 3) Holding at 1 V for 4 min 4) Transaction with scan rate 1.5 $V\ s^{-1}$ 5) Peak at 1.5 V 6) Transaction with scan rate 1.5 $V\ s^{-1}$ 7) Holding at 1 V for 1 min 8) Transaction with scan rate 0.1 $V\ s^{-1}$ 9) Holding at 0.1 V for 2.5 min
Cycle time	678 s
Cell temperature	30 °C
Relative Humidity	AN/CAT 100%
Pressure	Atmospheric
H_2/N_2	60/60 $ml\ min^{-1}$
Metric	**Frequency**
Polarization curves (A and P)	0, 30, 100, 200 cycles
Cyclic Voltammetry	0, 30, 100, 200 cycles
Limiting Current	0, 30, 100, 200 cycles

Table 7.1 – Start-Up AST

7.3 The validation of Start-up AST

7.3.1 Local current densities

In the last part of this dissertation, the Start-up AST protocol is validated respect the results of Start-up/Shut-down cycling obtain in segmented-cell, under real process (see 5.3). In both cases 200 degradation cycles have been studied, and a complete diagnostic procedure is applied.

First of all, a comparison between current measured during SU-AST and real process is reported in Figure 7.3.

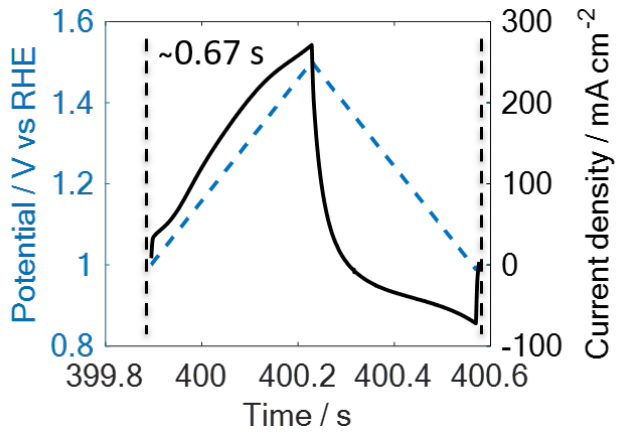

(a) Segmented-cell

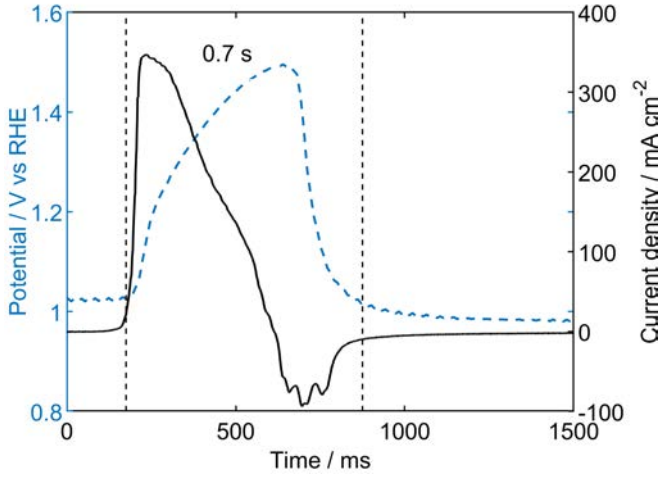

(b) Cathode potentials measured withe RHE

Figure 7.3 – (a) Triangular sweep during SU-AST; (b) Local potential and current density profiles collected with RHEs and multi-potentiostat at cathode inlet segment, during real Start-up/Shut-down cycling

During real Start-up/Shut-down cycling, the voltage profile depends on balancing of capacitance and faradic currents, generated by the reverse-current mechanisms (see section 3.4). Moreover, the voltage profile in real process depends strongly to the operating conditions that were applied (see section 3.5) and the exactly mechanisms cannot be reproduce in a controlled way by common potentiostat. Anyway, the comparison between the two process highlight a very good agreement among duration and current density peak. This is a good indicator of how the AST can reproduce the stress on cathode electrode as observed during real process.

To elucidate the underlying mechanism of start-up/shut-down under mitigation strategies, a simulation of Start-up operation has been done with the PEMFC model (see section 3.7). Faradic and capacitive current densities profile are obtained at the same operating conditions of real start-up and the results here presented are mediated over mesh region corresponding to cathode inlet segment in segmented-cell. In figure 7.4, the results are reported.

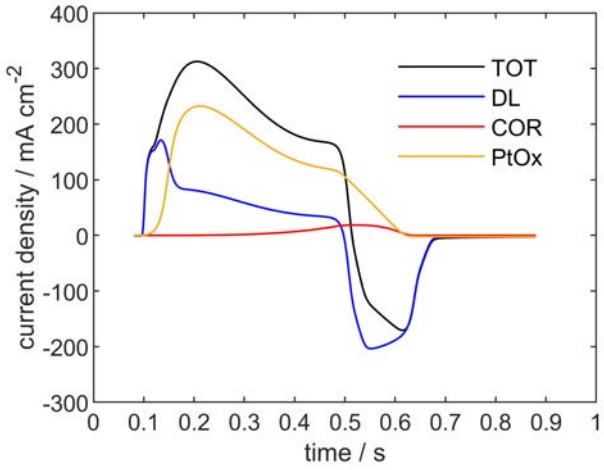

(a) Simulated current densities

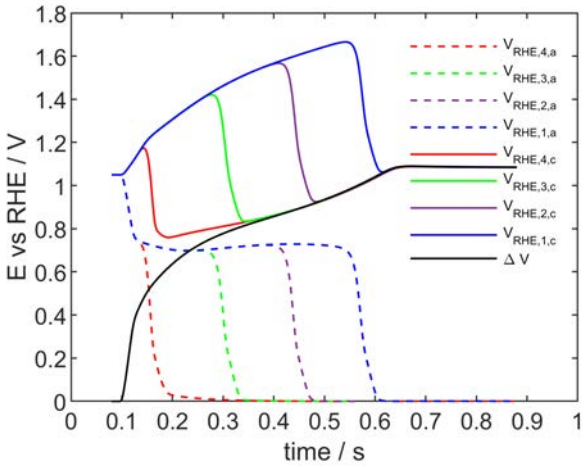

(b) Simulated RHE's potentials

Figure 7.4 – (a) Simulated currents profile of cathode inlet positions during start-up. (b) simulated potentials at RHE's probe. Operating conditions: T = 30 °C, 100/100% RH, $p_{out,anode} = p_{out,cathode} = p_{amb}$, $N_{H2} = 175$ ml min^{-1}.

The contribution of carbon oxidation reaction is minimum, compared to capacitive currents (here intended as doble-layer and platinum oxides

contributions), which means a current peak of 18 mA/cm^2 relative to the toal value of 300 mA/cm^2. The COR production, at 30 °C, is in good agreement with data reported by Mittermeier et al.[58].
Moreover, the simulation permits to distinguish the contribution of double-layer and platinum oxides current densities. At first, double-layer contributes to sustain the reverse-current mechanism due to fast potential rise. Platinum oxides, subsequently, start to be formed and still until maximum potential is reached, while double-layer currents follows the time derivative of potential and slow down at half-peak. Due to hydrogen front moving, in anode compartment, before maximum potential is reached at cathode inlet segments, the capacitive currents are reversed, and it's only in this phase that carbon oxidation current start to be significant. Thus, the negative contribution of capacitive currents boosts the carbon oxidation reaction which must close the charge balance.

7.3.2 Performance losses

Finally, the performance comparison between real start-up cycles in segmented-cell and SU-AST is here described. In terms of ECSA loss, the degradation obtained at 200 cycles of the SU-AST is comparable with the one obtained in the first segment, as presented in Table 7.2.

Table 7.2 – ECSA losses of Segmented-cell and Zero-Gradient cell compared

	ECSA LOSS SEGMENTED	ECSA LOSS ZERO-G
SEG 4	13%	-
SEG 3	20%	-
SEG 2	33%	-
SEG 1	37%	31%

Relative ECSA trend over the two cycling protocols is depicted in figure 7.5.

the ECSA loss in real start-up operation, obtained with segmented cell, is compared with the one observed with SU-AST in New reference single cell: the obtained values are similar, suggesting a high representativeness of the proposed AST; the ex-situ characterization of the samples is presented in 7.5 to further confirm that the same degradation mechanism is occurring.

The performance in terms of voltage loss are not directly comparable because of the different hardwares used: the two flow-fields are different and the Zero-Gradient cell operates with high flow rates in order to ensure

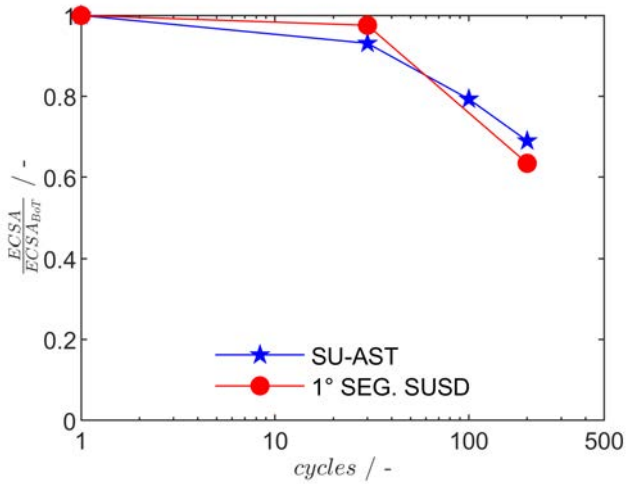

Figure 7.5 – Relative ECSA measurements during Start-up/Shut-down cycling in real process and AST. T = 30 °C, 100/100% RH, $p_{out,anode} = p_{out,cathode} = p_{amb}$, $N_{N2} = N_{H2} = 60$ ml min^{-1}.

homogeneous conditions, while the Segmented-cell is highly heterogeneous. In order to make possible the comparison between tests on different hardware, iR-free polarization curves are calculated and only current densities are taken into consideration. The voltage is corrected using High Frequency Resistance taken from the EIS Nyquist plots, while the effective current density is evaluated adding hydrogen cross-over current to the fuel cell current density.

$$\Delta V_{iR\,free} = \Delta V + i \cdot HFR \tag{7.1}$$

This correction makes acceptable the comparison between the two hardwares, at least, till 1 A/cm^2. Results are reported in figure 7.6.

As clearly visible, the performance loss after 200 cycles of start-up in real system can be effectively reproduced with the proposed SU-AST.

Then, EIS are compared, to give an insight of performance evolution due to the two process. In figure 7.7 are reported the results obtained at 0.4 A/cm^2 at BoT and after 200 cycles of SU-AST on Zero-Gradient and of real Start-up/Shut-down cathode inlet (first segment in segmented-cell).

At BoT the spectra are comparable even if HFR is slighly higher in segmented-cell, probably due to the different hardware. The same results is obtained after 200 cycles - that is, the shape of the spectras are not varied. Since, degradation doesn't affect the EIS spectra, as it happens in polarization curves and CV, the main cause of performance loss is probable a kinetics reduction, the effect of which is explained as a vertical translation of the

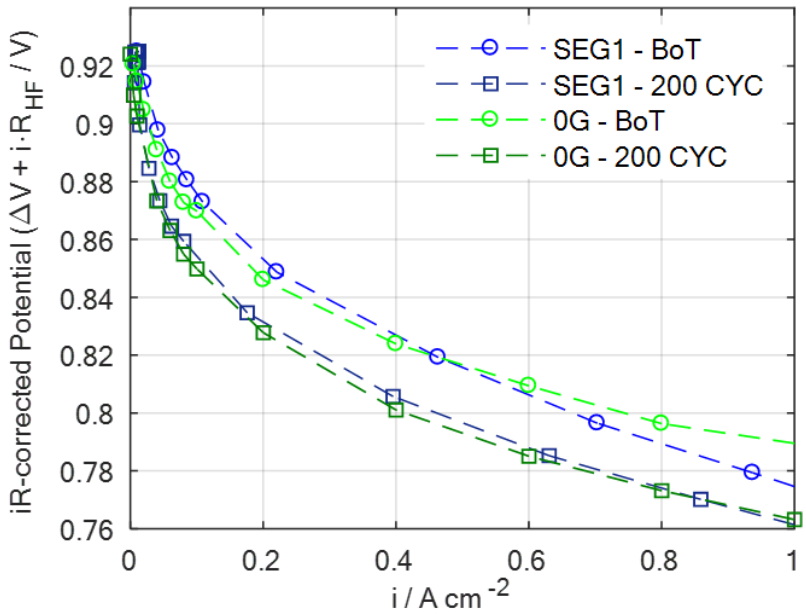

Figure 7.6 – Comparison between Start-up/Shut-down in segmented-cell (cathode inlet segment) and SU-AST. iR-free Reference polarization curve: 100/100% RH, T = 80 °C, $p_{in,anode}/p_{in,cathode}$ = 2.5/2.3 bar. In each test, $\lambda_{anode}/\lambda_{cathode}$ = 2/4, minimum flux = 0.5 A cm^{-2} equivalent.

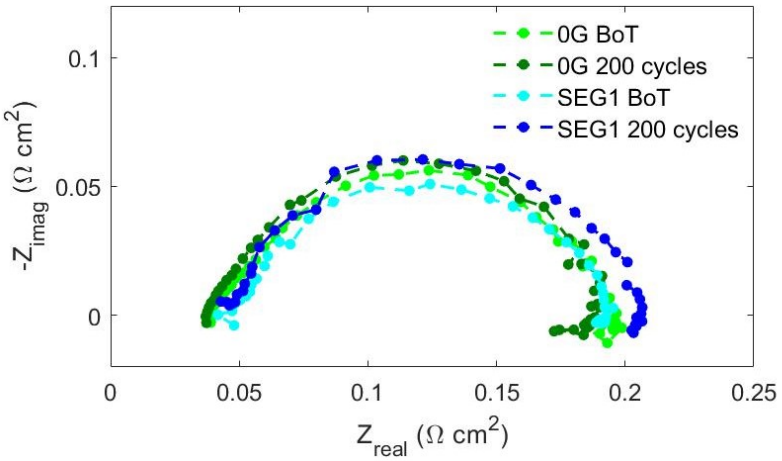

Figure 7.7 – EIS comparison, 0.4 $A\ cm^{-2}$, between Start-up/Shut-down in segmented-cell (cathode inlet segment) and SU-AST. Operating conditions: 100/100% RH, T = 80 °C, $p_{in,anode}/p_{in,cathode}$ = 2.5/2.3 bar. In each test, $\lambda_{anode}/\lambda_{cathode}$ = 2/4, minimum flux = 0.5 A cm^{-2} equivalent.

polarization curve.

To conclude, the evolution of oxygen mass transport resistance over the inverse of roughness factor is compared, to highlight ECSA evolution effect on performance. In figure 7.8 results are reported. It is important to point out that the shape of the two hardware flow-fields are different, moreover the rib of segmented flow-field is almost three times the rib of Zero-Gradient flow-field (0.8 mm against 0.25 mm). For this reason limiting currents are lower in the segmented-cell leading to higher R_{MT}. However in both real Start-up/Shut-down and SU-AST a linear trend is visible and the slopes of the curves are comparable, validating a similar oxygen mass transport resistance evolution during the degradation cycles.

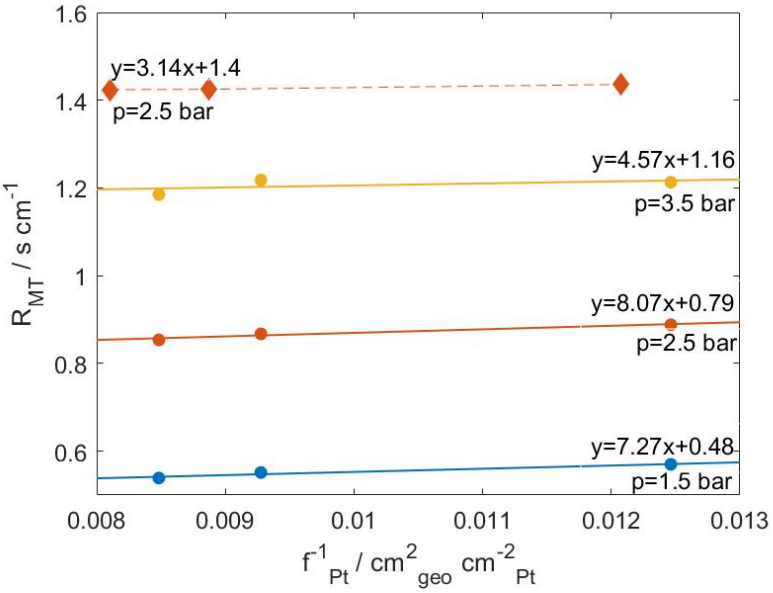

Figure 7.8 – Oxygen mass transport resistance as function of the inverse roughness factor for SU-AST on Zero-Gradient cell (circles) and real Start-up/Shut-down on segmented-cell (diamond)

So, a direct correlation between real-world operation and proposed AST is found: the acceleration factor is close to 1. In the last section, a higher acceleration factor is proposed, by the evaluation of platinum formation/reduction mechanism.

Moreover, the evolution of the performance of the MEA during Start-up/Shut-down cycling is affected by a series of degradation phenomena related to the voltage profile of the AST. The influence of Carbon Corrosion in Start-Up and Shut-Down process is known from literature [72], despite the

contribution of Platinum dissolution is lacking, due to the few studies done at low temperature or applyng mitigation strategies. The continuous voltage cycling during the AST (from 0.1 V to 1 V) and the presence of voltage peak (at 1.5 V) as well suggest the occurrence of platinum dissolution and carbon corrosion respectively. However, when the performance loss has been analyzed, for two processes, they were in good accordance. Since performance loss seems kinetically-controlled, is probably the platinum dissolution mechanism that causes the material degradation observed in both cases.

7.4 Elucidating the degradation mechanism under Start-up/Shut-down cycling

To better understand the underlying mechanism of Start-up/Shut-down cycling, when mitigation are applied and further validate the SU-AST developed a deep analysisys is here presented.

Firstly, the performance degradation associated to the Start-up AST is evaluated through the analysis of in-situ measurments. The aim is to highlight the main performance losses in term of kinetics, and mass-transport resistance. Then the results SU-AST are compared with Electrocatalyst AST and Support AST ones, in order to distinguish the effects of the degradation mechanisms on performance evolution.

Next, by ex-situ investigation, aged materials are analysed and results are discussed to elucidate the effects of degradation mechanisms involved. Samples, after 200 cycles of start-up in segmented-cell and under AST, were compared and the similarities and differences are highlighted.

7.4.1 Start Up AST results

The effects of SU-AST cycling are studied considering the change of ECSA, CV and polarization performance as the previous AST's results analysis. The evolution of CV profile (see figure 7.9) progressively reduce during voltage cycling and after the first 30 cycles seems follow a logarithmic profile as the AST proceeds.

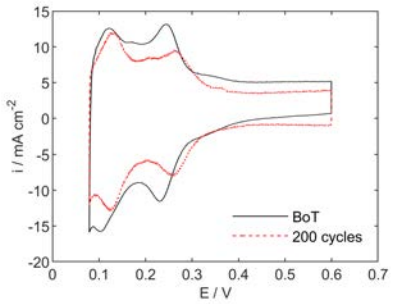

(a) Cyclic voltammetry during SU-AST cycling

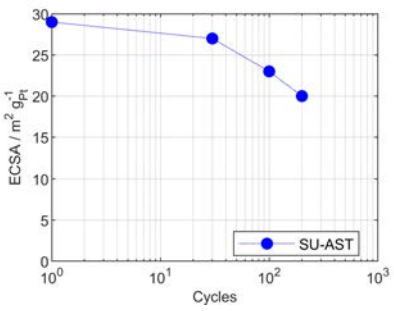

(b) ECSA variation during AST cycling

Figure 7.9 – (a) Start-up AST cyclic voltammetry results; (b) ECSA evolution. Operating conditions, T = 30 °C, 100/100% RH, $p_{out,anode} = p_{out,cathode} = p_{amb}$, $N_{N2} = N_{H2} = 60$ ml min^{-1}.

The change of active area is quite regular with AST cycling. In the first 30 cycles the 2% of the initial ECSA is lost. In the end cycling, each 100 cycles correspond to a lost of 5% of the active area. According to the evolution of the active area an uniform decrement of the performance would be expected in different working conditions, when the main degradation mechanism involved is associated to platinum loss as a result of Platinum dissolution.

As explained in Section 2.4.1, ECSA values reported in figure 7.9 can be obtained integrating the area under H-desorption peak in the voltammogramm, that is performed only during AST stop (i.e. at BoT, 30, 100 and 200 cycles).

However, with the SU-AST protocol, ECSA can be estimated in every cycle by integration of the adsorption peak obtained in the potential sweep from 1 V to 0.1 V (represented in red in figure 7.10). Even if the integration of H-adsorption (i.e. absolute ECSA value) is different from the one obtained during desorption, a quite good agreement is found (i.e. 27% vs 31% measured during characterization). The results are reported in figure 7.10.

The protocol permits to monitor constantly the ECSA loss during cycling, and make it possible to stop the test at a specific ECSA value. ECSA loss keeps almost constant in the first 30 cycles and then it starts to strongly increse with a logarithmic trend.

However, some spurios effects are visible before and after each stops. After intermediate characterization tests, the ECSA value slightly increases probably due to a sort of refresh mechanism.

Degradation caused by SU-AST is visible also in the evolution of current density during Start-up peak, that is represented in figures 7.11 as function

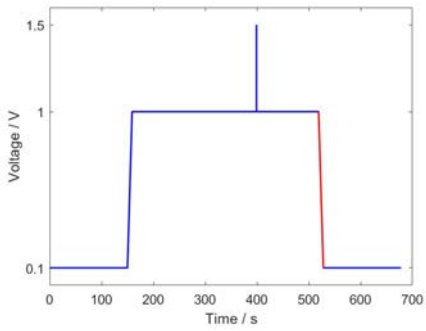

(a) Voltage profile

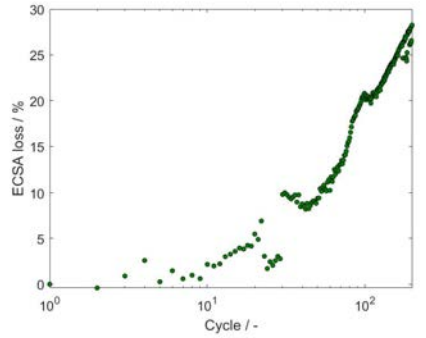

(b) ECSA loss

Figure 7.10 – (a) SU-AST voltage profile; (b) ECSA loss during SU-AST.

of voltage and time. In accordance to ECSA evolution, current density registered at 1.5 V is quite constant in the first 30 cycles and then it decreases, in accordance with platinum sites available for oxidation reaction

Looking at the performance evolution (see figure 7.12) a vertical shift in the polarization curve is visibile at EoT, in accordance with ECSA loss, as previously stated.

To complete the characterization, EIS spectra were analysed and results are reported in figure 7.13. During voltage cycling, are visible some small deviations at high frequency (linear branch zone) at low current density, while the spectra at high current density seems to enlarge. Due to the little differences observed is difficult to conclude that other mechanism, other than ECSA loss occurs. Moreover the slight change of linear branch could be compatible with the depletion of platinum in the catalyst layer region next to the membrane, as is found by Baricci et al. [6]. However, as observed during Support AST, it could be also an indication of carbon support oxidation (see section 6.3), despite it seems a very small effect.

To clarify the impact of AST cyclcing, polarization curves and EIS were

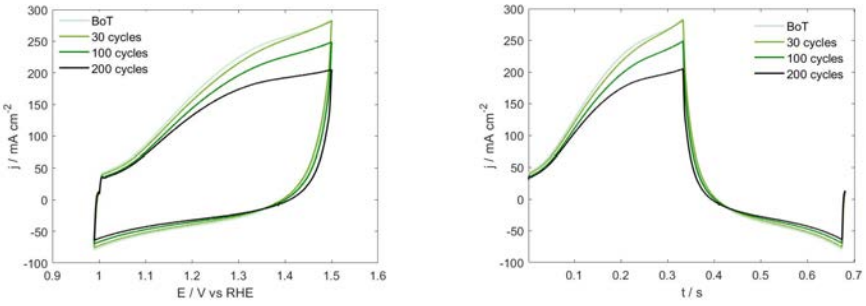

(a) i-V graph **(b)** i-t graph

Figure 7.11 – (a) Start-up current density evolution during AST as function of voltage; (b) and time.)

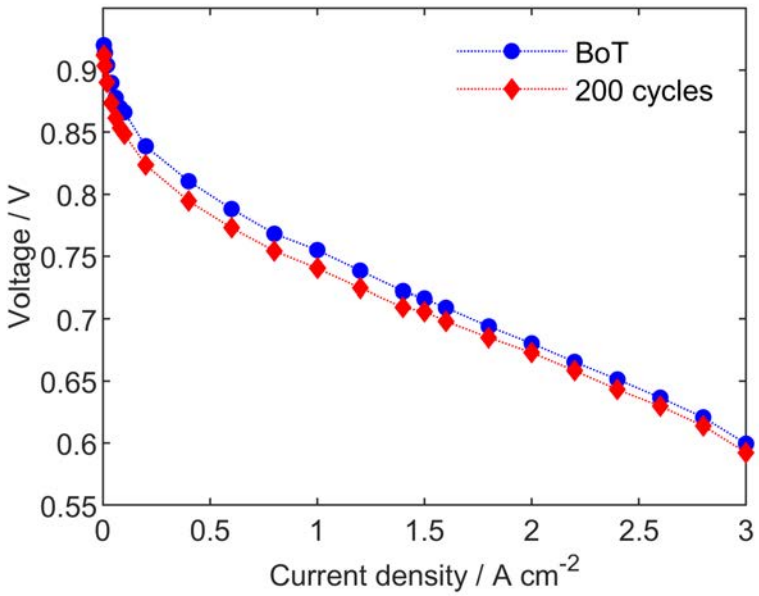

Figure 7.12 – Reference polarization during SU-AST cycling. Operating conditions: $T = 80°C$, $p_{C/A} = 2300/2500\ mbar$, $RH_{C/A} = 100\%$

analysed at lower oxygen concentration, from *Polarization* C_{extra} (i.e. cathode out - low loading operating condition:$T = 68°C$, $p_{C/A} = 1.4/1.9\ bar$, $RH_{C/A} = 100/50\%$, $x_{O_2/H_2} = 10/100\%$). The results are reported in figure 7.14.

The reduction of oxygen content in cathode feeding does not affect particularly the performance of the MEA, despite a shift of the performance is visible at high current density and from EIS at low frequencies. The exactly explanation could be due to the combination of oxygen content and high current (high overpotential), that alter the current profile in the cathode electrode,

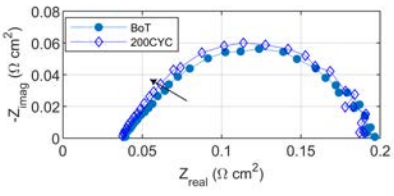

(a) EIS at 0.4 A/cm^2

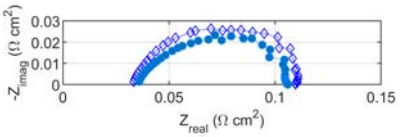

(b) EIS at 3.0 A/cm^2

Figure 7.13 – EIS spectra recorded for reference polarization curve during SU-AST cycling. Operating conditions: $T = 80°C$, $p_{C/A} = 2.2/2.5\ bar$, $RH_{C/A} = 100\%$

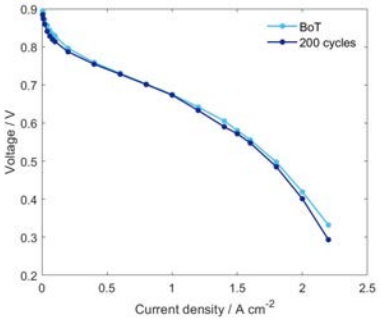

(a) Polarization curve

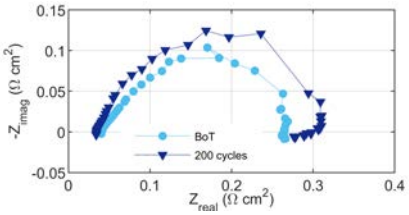

(b) EIS at 0.4 A/cm^2

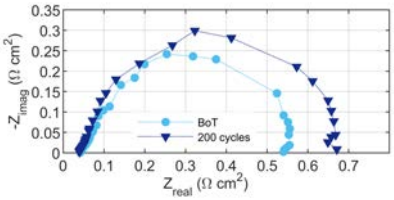

(c) EIS at 2.0 A/cm^2

Figure 7.14 – (a) Polarization curve and EIS at (b) 1.0 and (c) 2.0 A/cm^{-2} during SU-AST. Cathode out - low loading operating condition:$T = 68°C$, $p_{C/A} = 1.4/1.9\ bar$, $RH_{C/A} = 100/50\%$, $x_{O_2/H_2} = 10/100\%$

increasing the production near the membrane, were platinum dissolution effect are worsened [6, 60, 92].

7.4.2 Comparison between Support and Start-up AST

The effects of Start-up as well for Support in ASTs, at low and high temperature protocols, are here presented. Carbon corrosion at high temperature makes the ohmic losses and the mass transport effect more effective and

responsible of the major loss of performance during cycling (section6.3). The effects of degradation at low temperature Support AST are negligible, see section 6.3.2. The aim of this last investigation is the comparison of Carbon Support and SU-AST's effects in order to demonstrate the possible occurrence of carbon corrosion during Start-up/Shut-down operation, in real system and AST. In this perspective the performances of the MEAs during Support AST and SU-AST are discussed in terms of i-V curve (*Reference Polarization*), mass activity derived from *Oxygen Polarization curve*, EIS, ECSA measurements, and mass transport effects.
To make a reliable comparison, due the different cycles performed, the data at 200 cycles of Start-up (EoT) and after 2000 cycles of Support AST are analysed, when ECSA loss are comparable. Their respective values are: 20 m^2/g_{Pt} for SU-AST (31% ECSA loss - BoT = 29 m^2/g_{Pt}) and 21 m^2/g_{Pt} for Support AST (32% ECSA loss - BoT = 31 m^2/g_{Pt}).

During Start-up AST, ECSA is reduced after 30 cycles following a quite linear trend over cycles, while in support AST, it follows a more logarithmic trend. Despite, the reduction of active area after 5000 cycles of Support AST is higher, approximately 60% of ECSA loss, the degradation effect in Start-up AST is faster (over cycles). This suggests that the effects of Platinum dissolution, involving, agglomeration, particle growth and detachment stress more the catalyst layer than expected, despite mitigation strategies are adopted.

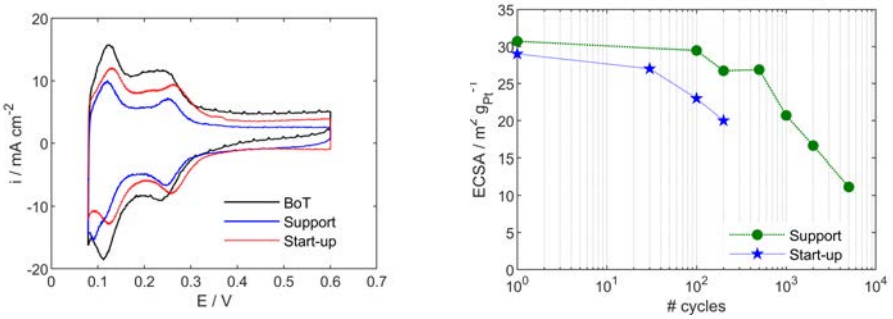

(a) Cyclic voltammetry **(b)** ECSA measurements

Figure 7.15 – (a) Cyclic voltammetry; (b) ECSA evolution; comparison between Support (80 °C) and Start-up ASTs. Operating conditions, T = 30 °C, 100/100% RH, $p_{out,anode} = p_{out,cathode} = p_{amb}$, $N_{N2} = N_{H2} = 60$ ml min^{-1}.

However, the degradation mechanism related to Start-up/Shut-down affects MEA performance while it causes a uniform reduction of voltage in all the regions of the polarization curve (see 7.16). On the other hand, the effect of carbon corrosion is not uniform over cycling: the degradation occurs

drastically after 2000 cycles influencing mainly the high current density region while low current densities present a similar variation of performance of Start-up AST. When performance are mainly kinetically-controlled, for both the mechanisms, the ECSA loss is the dominant parameter, instead at high current densities (over 0.8 A/cm^2) are the mass-transport resistances that play the dominant role.

The H_2/Air performance curves do not shift uniformly over the range of current densities, and at high current densities, the limiting current

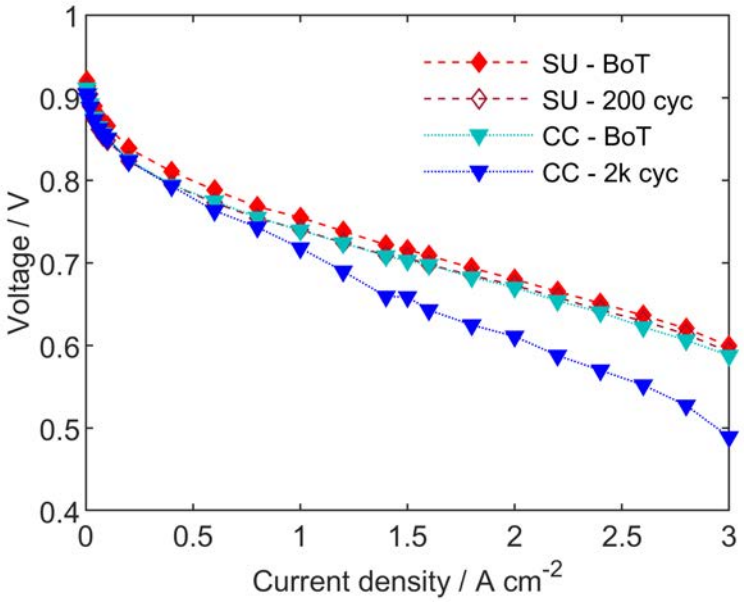

Figure 7.16 – Reference polarization comparison. Operating conditions: $T = 80°C$, $p_{C/A} = 2.3/2.5\ bar$, $RH_{C/A} = 100\%$

Since, the H2-air performance curves do not shift uniformly over the range of current densities in Support AST, at high current densities, higher mass-transport resistance are expected.This effect can been recognized in the evolution of EIS, reported in figure 7.17. Ff in SU-AST no drastically change of spectrum are recognised, the Support AST is responsible of an increase of R_{CT} and oxygen transport feauture at low frequencies. No visible change of the HFR are visible, states that the membrane properties do not change. Due to carbon corrosion occurrence, the linear branch changes: at the end of Support AST the spectrum has a circular shape. This trend demonstrates that Carbon Corrosion mainly affects mass transport region differently from Start-up/Shut-down operations, considered here, which causes quite an homogeneous performance degradation over the range of current

densities.

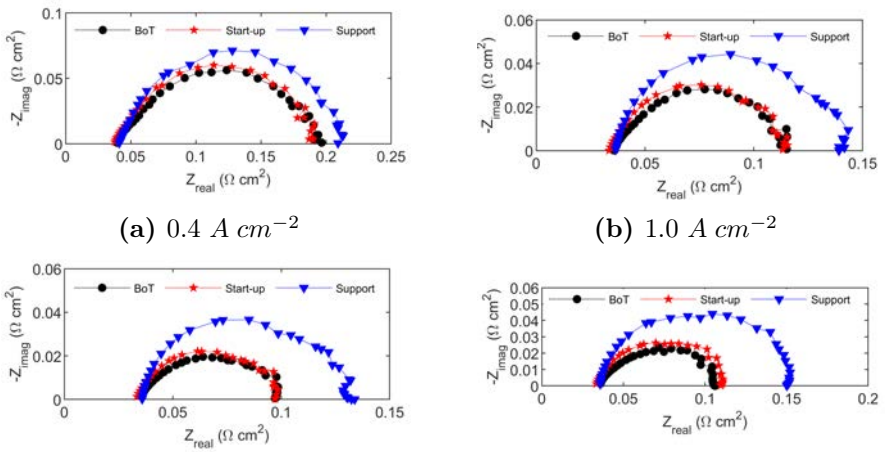

(a) 0.4 $A\ cm^{-2}$ **(b)** 1.0 $A\ cm^{-2}$

(c) 2.0 $A\ cm^{-2}$ **(d)** 3.0 $A\ cm^{-2}$

Figure 7.17 – Comparison of EIS evolution during Support and Start-up ASTs at reference operating conditions: $T = 80°C$, $p_{C/A} = 2.2/2.5\ bar$, $RH_{C/A} = 100\%$

The result of limiting current test is depicted in Figure 7.22. The change of oxygen transport resistance is much higher for Support AST, despite a quite linear correlation is found for each test. The slope of R_{O_2} vs $\frac{1}{f_{Pt}}$, are respectively: 6.6 and 17.6 for the SU-AST and Support AST. However, for Start-up cycling this dependency is quite constant at different pressures while it increases, with the pressure, in Support AST. While, carbon oxidation attack catalyst layer structure, worsening molecular gas transport, in Start-up AST, due to platinum dissolution mechanisms, the catalyst sites fluxes are increased. This increases the effects of non-Fickian transport resistance, that can be recognised in the vertical shift of the chart and corresponds to an increase of pressure-independent resistance.

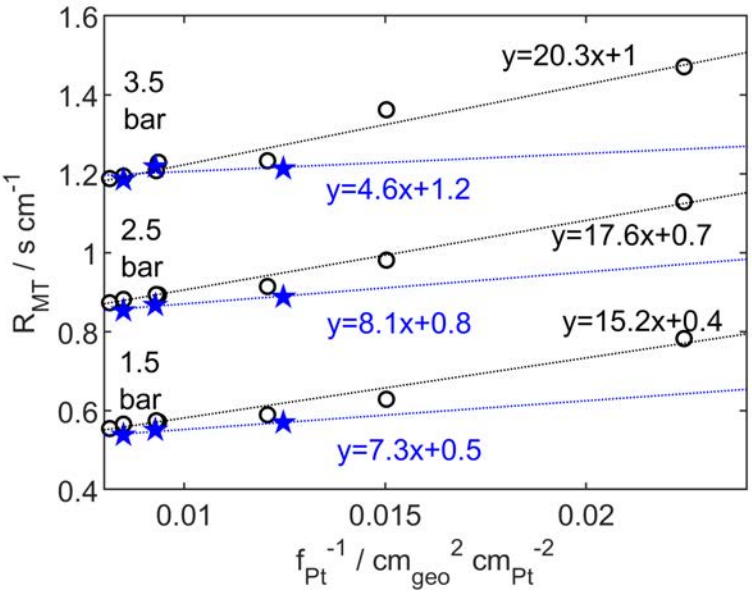

Figure 7.18 – O_2 mass transport resistance as function of the inverse of roughness factor during Support (open circle - black) and Start-up (Full pentagram - blue) AST cycling. Linear fitting curve (dotted lines) and equations are reported in the graph.

7.4.3 Comparison between Electrocatalyst and Start-up ASTs

The analyse of the last sections exclude, the carbon corrosion, as the major degradation phenomena that affects start-up cycling. So, in order to understand the impact of platinum dissolution, an accurate comparison between Electrocatalyst and Start-up AST was made. In this case, the end of life performance in Start-up ASt were compared with the performance in Electrocatalyst ASt after 20000 cycles.

The cyclic voltammetry profiles for the two protocols seems to be similar: both are characterized by a decrease of absorption/desorption peaks and a double layer zone almost constant. The results are reported in figure 7.19. The corrsponding ECSA values are: 20 m^2/g_{Pt} for Start-up (31% ECSA loss - BoT = 29 m^2/g_{Pt}) and 17 m^2/g_{Pt} for Electrocatalyst ASTs (43% ECSA loss - BoT = 30 m^2/g_{Pt}).
In Start-up AST th effect of degradation isn't particularly visible in cyclic voltammetry and probably this is due to the small number of steps considered, but an increase of the number of cycles will probably lead to a stronger effect as visible by extrapolation of the ECSA loss - cycles trend. As for the Support

AST, also the Electrocatalyst AST show a slower ECSA reduction, over cycles, respect to the Start-up AST.

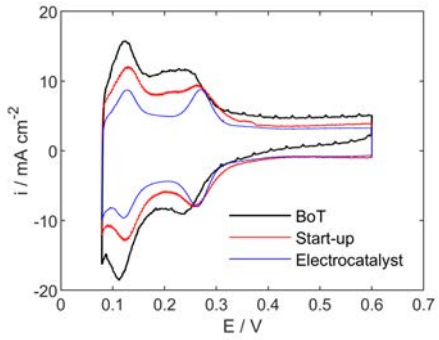

(a) Cyclic Voltammetry

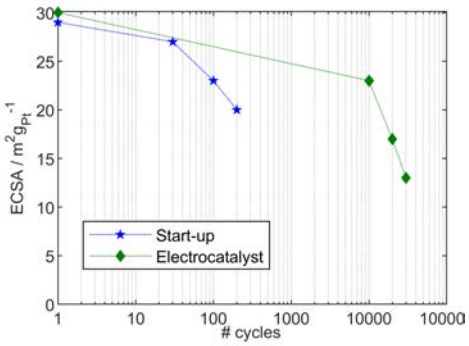

(b) ECSA measurements

Figure 7.19 – (a) Cyclic voltammetry; (b) ECSA evolution; comparison between Support (80 °C) and Start-up ASTs. Operating conditions, T = 30 °C, 100/100% RH, $p_{out,anode} = p_{out,cathode} = p_{amb}$, $N_{N2} = N_{H2} = 60$ ml min^{-1}.

As previously said, Electrocatalyst AST causes a vertical translation of polarization curve, with a voltage loss that is almost constant in all the three polarization regions (i.e. activation, ohmic and concentration overpotentials). In SU-AST, a similar phenomenon is visible. After an initial improvement of performances due to conditioning, a 12 mV mean voltage loss is present in activation, ohmic and mass transport regions (compatible with 11 mV loss predicted by ECSA trend). The voltage loss isn't particularly strong probably due to the small number of degradation cycles, but as explained this number it's compatible with the occurance in real systems. Performance comparison is reported in figure 7.20.

The evolution of the spectra during Start-up and Electrocatalyst AST's cycling support what is derived from the analysis of the polarization curve at fully humidified condition: the degradation is uniform in both cases. Visible

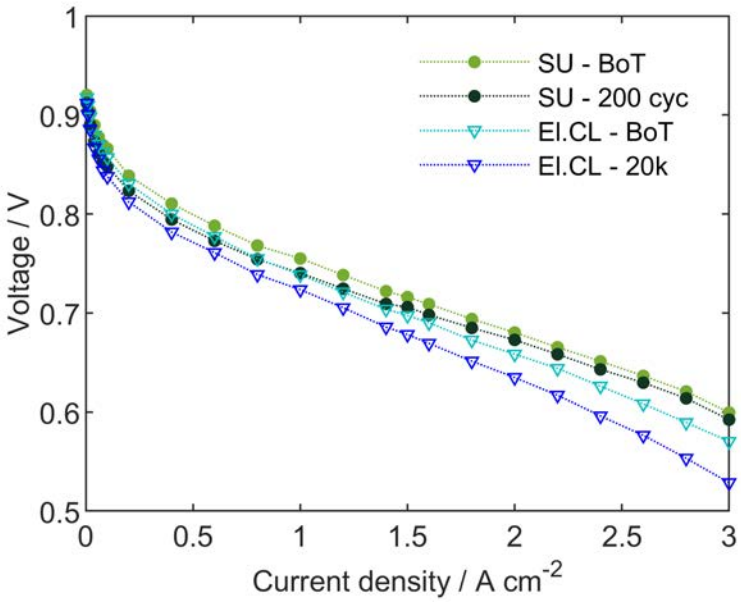

Figure 7.20 – Reference polarization comparison between Start-up and Electrocatalyst AST. Operating conditions: $T = 80°C$, $p_{C/A} = 2.3/2.5\ bar$, $RH_{C/A} = 100\%$

and homogeneous losses can be recognized in all regions. The evolution of the polarization curve is compatible with the change of EIS: no change of low frequency zone and moderate increase of R_{CT}. The evolution of the spectra are coherent: the evolution of the linear branch is the same making for the same influence of the two degradation phenomena (see figure 7.24).

A really compatible evolution of oxygen transport resistance is confirmed from the $R_{MT} - f^{-1}$ chart in Figure 7.22: the lines obtained during Electrocatalyst and Start-up AST's are comparable, there is just a vertical translation at high pressure, while the slope is almost the same in the two cases.

The slope of R_{O_2} vs $\frac{1}{f_{Pt}}$, are respectively: 6.6 and 5.6 for the SU-AST and Electrocatalyst AST, while for Support AST it was 17.6. The increase of oxygen transport resistance can be ascribed to non-Fickian transport resistance, that can be recognised in the vertical shift of the chart and corresponds to an increase of pressure-independent resistance[29].

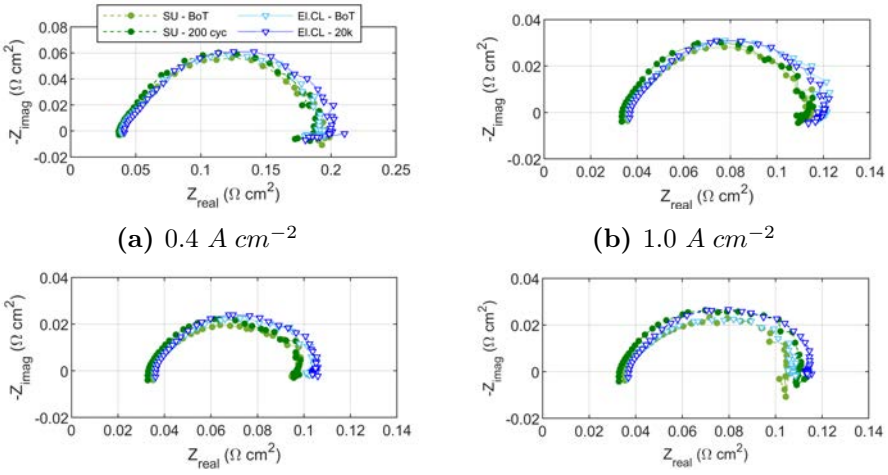

(a) 0.4 $A\ cm^{-2}$ **(b)** 1.0 $A\ cm^{-2}$

(c) 2.0 $A\ cm^{-2}$ **(d)** 3.0 $A\ cm^{-2}$

Figure 7.21 – Comparison of EIS evolution during Electrocatalyst and Start-up ASTs at reference operating conditions: $T = 80°C$, $p_{C/A} = 2.2/2.5\ bar$, $RH_{C/A} = 100\%$

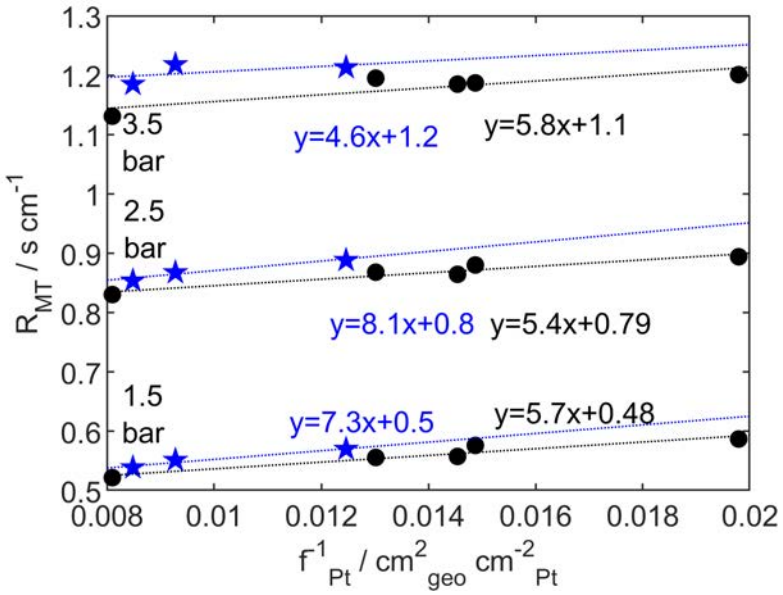

Figure 7.22 – O_2 mass transport resistance as function of the inverse of roughness factor during Electrocatalyst (closed circle - black) and Start-up (Full pentagram - blue) AST cycling. Linear fitting curve (dotted lines) and equations are reported in the graph.

7.4.4 Combined Electrocatalyst/Start-up AST

The combined effect of different degradation mechanisms was evaluated by adopting a proper sequence of different ASTs. The proposed Start-up AST was then performed on the MEA aged by the Electrocatalyst-AST protocol. The combined effect of performance loss due to Electrocatalyst AST and SU-AST is reported in Figure 7.16.

Despite the small number of cycles introduced a further ECSA decrease was observed: the ECSA value after Electrocatalyst AST was 13 m^2/g_{Pt}, after Start-up AST 11 m^2/g_{Pt}.

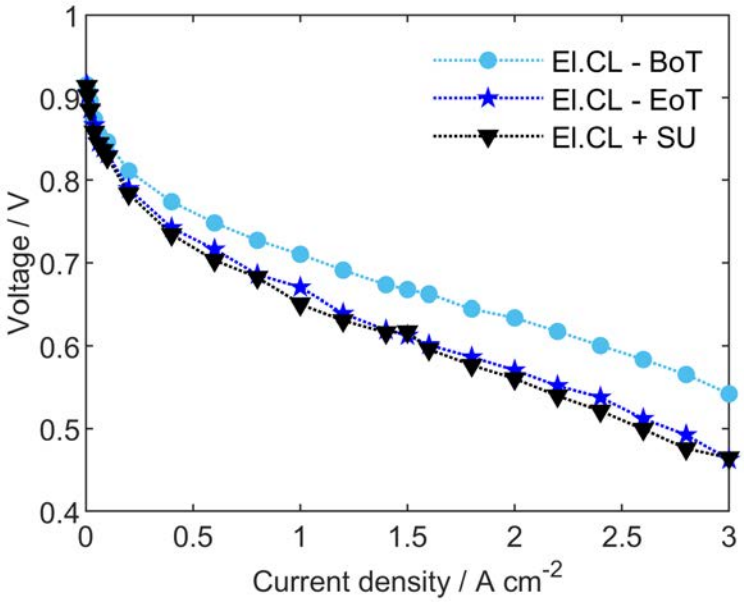

Figure 7.23 – Evolution of *Polarization E* during Electrocatalyst/Start-up combined AST

For performance analysis, *Polarizations E* (i.e. cathode in - high loading operating condition:$T = 85°C$, $p_{C/A} = 2.8/3.0\ bar$, $RH_{C/A} = 30/100\%$) was the one chosen for the comparison, because it allowed to evaluate the effect of the combined Electrocatalyst/Start-up AST on cathode inlet, that is the most stressed region under start-up and shut-down in real operating condition, as described in Chapter 5.3. Results are depicted in figure 7.23. From the polarization curve analysis, is clear that 200 Start-up cycles seem a direct continuation of the previous 30000 ones: a vertical translation is visible, with a voltage loss proportional to the small number of degradation cycles. Under cathode inlet operating conditions the degradation due to SU-AST appears

comparable in case of single AST and combined AST, with an observable rate of 40 µV/cycle and 45 µV/cycle respectively.

This trend is confirmed by EIS analysis. For all the current density values,the last 200 Start-up cycles causes an increase of HFR and R_{CT} comparable to the one generated after the only Electrocatalyst AST.

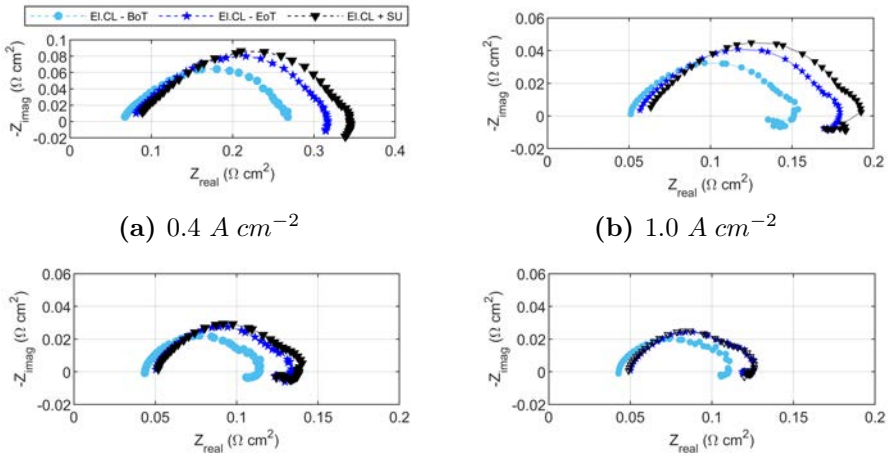

(a) 0.4 $A\ cm^{-2}$ **(b)** 1.0 $A\ cm^{-2}$

(c) 2.0 $A\ cm^{-2}$ **(d)** 3.0 $A\ cm^{-2}$

Figure 7.24 – EIS evolution during combined Electrocatalyst/Start-up AST at reference operating conditions: $T = 80°C$, $p_{C/A} = 2.2/2.5\ bar$, $RH_{C/A} = 100\%$

While ECSA variation isn't particularly strong because it already approah the minimum after the 30000 cycles of Electrocatalyst AST, the most interesting result is the correlation between mass transport resistance and ECSA value. The point obtained at 200 Start-up cycles lies perfectly on the line obtained for the only Electrocatalyst AST. That confirms that the two degradations lead to the same oxygen transport resistance change.

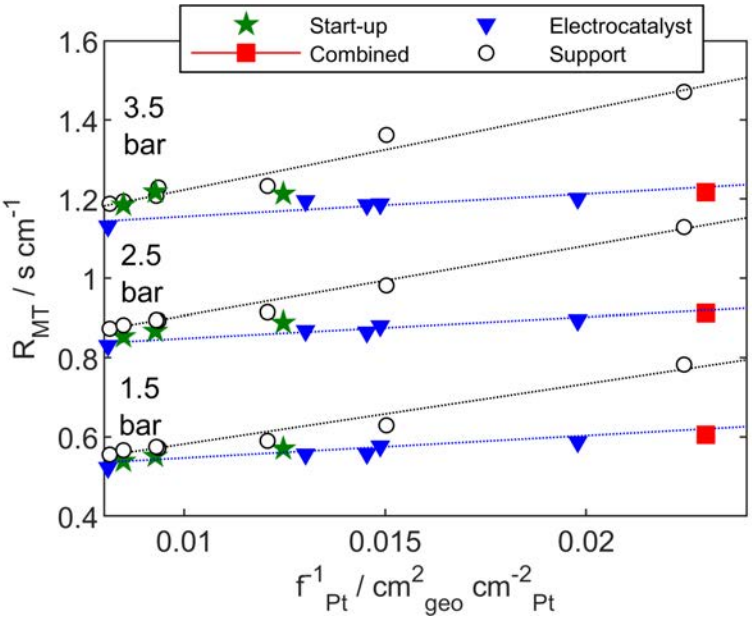

Figure 7.25 – O_2 mass transport resistance as function of the inverse of roughness factor during Combined (Full square - red), Start-up (Full pentagram - green), Electrocatalyst (Full triangle - blue), Support (open circle - black) AST's cycling. Linear fitting curve (dotted lines) for Electrocatalyst and Support ASTs are reported in the graph.

From the results analysed so far, the evolution of performance due to Start-up AST cycling is the same as Electrocatalyst AST cycling. Given the substantial similarities between the two degradetion processes, the platinum dissolution mechanism is confirmed to be the relevant mechanism of degradation of cathode electrodes during mitigated Start-up/Shut-down cycling and Start-up AST.

7.5 Ex - situ analysis

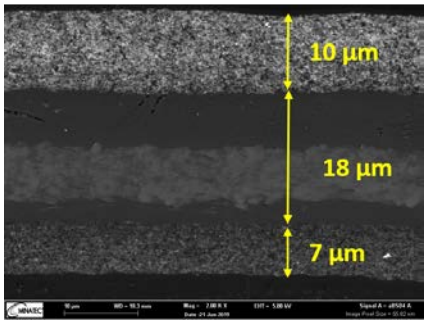

(a) SEM

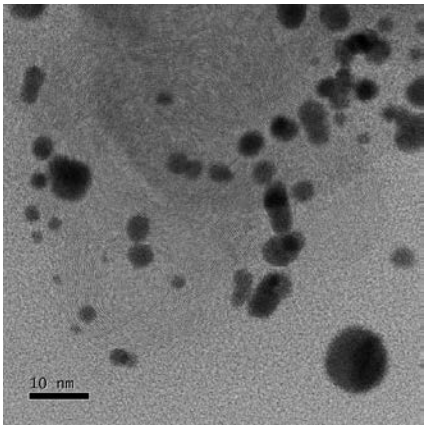

(b) TEM

Figure 7.26 – Fresh MEA pictures. SEM/TEM samples analyzed after conditioning.

To clarify the underlying degradation mechanism, during Start-up/Shutdown cycling an ex-situ characterization was done on aged MEAs. The analysis were conducted in collaboration with the CEA centre of Grenoble, which provided Scanning Electron Microscopy (SEM) and Transmission Electron Microscopy (TEM) images. The pristine Pt/carbon CCM and cross-sectional SEM/TEM samples were prepared from the cycled MEA, under Start-up operation in segmented-cell and in zero-gradient cell. Three cross-sectional thin slices were observed for segmented-cell, at cathode inlet, middle and outlet position, while one sample were prepared from zero-gradient cell.

In the figures 7.26 are reported SEM and TEM images of a fresh MEA. In SEM image the CCM components thickness are highlighted (i.e. anode below) and the membrane reinforcement is visible. Looking at the TEM image, platinum nanoparticle seems to agglomerate, and formed clusters on the carbon surface, compatible with a graphitized carbon support[2].

Results of Start-up operation in segmented-cell (i.e. H_2/Air operations) and Zero-gradient cell (H_2/N_2 operations) are depicted in Figure 7.27.

After 200 cycles, cathode thinning does not seem to happen, so severe carbon corrosion can be excluded, in both the operations. Heterogeneous Platinum dissolution from the cathode causes the formation of a Pt band[46]. Platinum precipitates, with different intensities, in all the segmented-cell regions. While a higher intensity of the Pt band characterizes the air inlet, it is less pronounced in the middle and almost absent in the air outlet section.

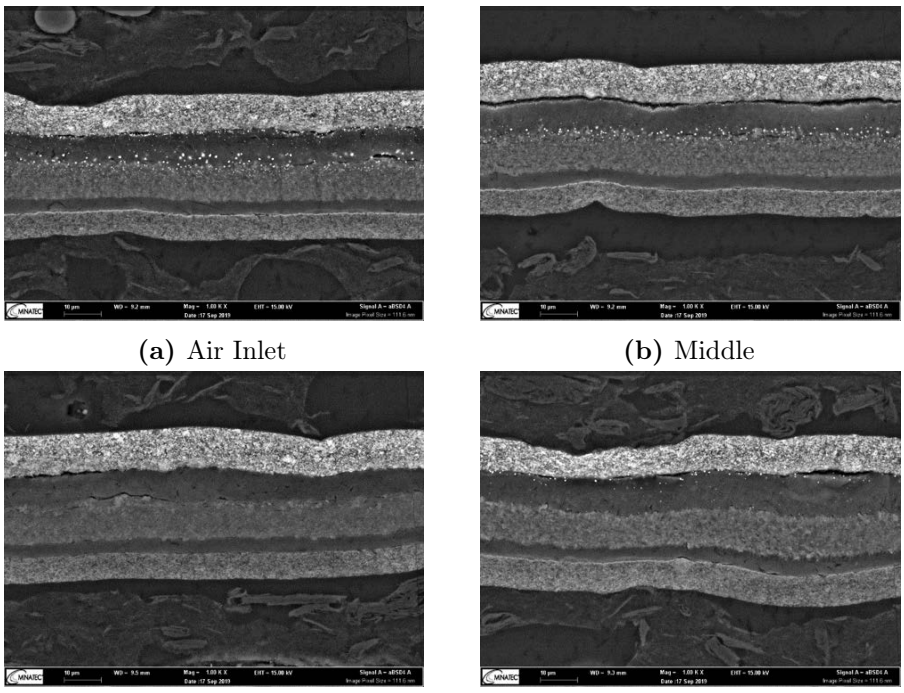

(a) Air Inlet **(b)** Middle

(c) Air Outlet **(d)** SU-AST

Figure 7.27 – SEM images of the cross-sections of MEAs after the durability evaluations: (a-c) under Start-up in segmented-cell at cathode inlet, middle, outlet positions (anode cross-flow configuration); (d) cathode under Start-up AST in H_2/N_2 operations.

Moreover these enlarged images evidence that the Pt band position depends on gases feeding. At high hydrogen concentration the Pt band is located near the membrane catalyst layer interface, while in presence of oxygen, the reduced hydrogen concentration move the Pt band near the reinforcement. The intensity of Pt dissolution mechanism seems in good accordance with maximum potential reached during operation: higher dissolution for cathode inlet and AST samples, and a limited effect at cathode outlet zone. Despite the entire cathode electrode sweep to high potentials (more than 1 V), it is the cathode inlet zone that reach 1.5 V. This accelerate the platinum dissolution and the subsequent platinum redeposition in the polymer electrolyte.

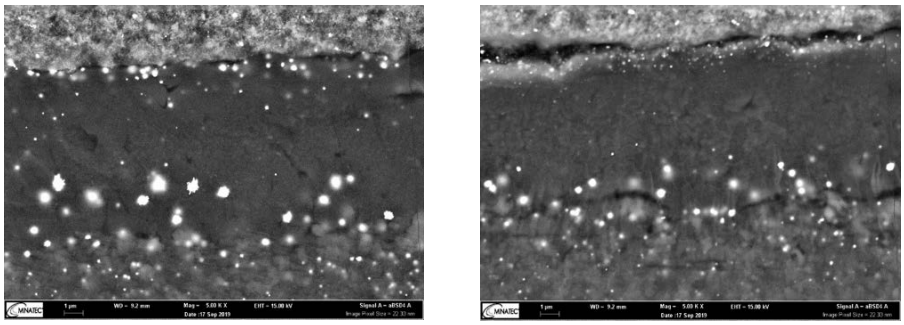

(a) Air Inlet **(b)** Middle

Figure 7.28 – Enlarged SEM images of aged MEAs under H_2/Air operations.

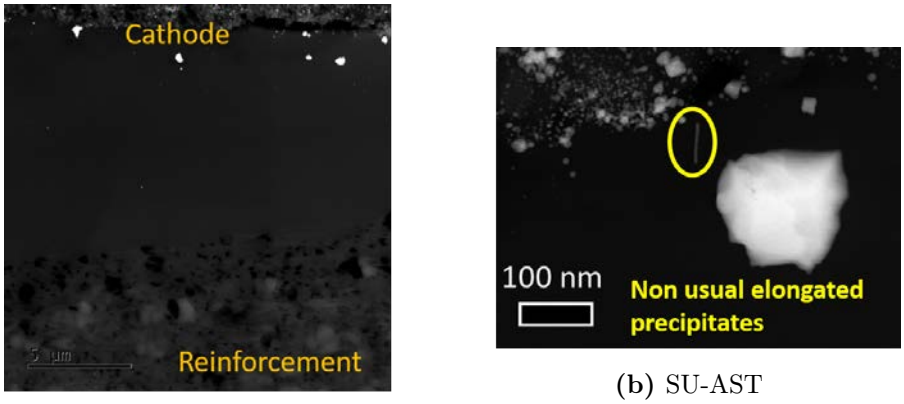

(a) Air Inlet **(b)** SU-AST

Figure 7.29 – TEM images of aged MEAs under H_2/N_2 operations.

In Figures 7.28-7.29 SEM/TEM images of CCM aged in segmented-cell and Zero-gradient-cell are reported. Large Pt agglomerates are visible in both pictures (i.e. 200-300 nm Pt agglomerates). Moreover, regular shaped

particles, are located in the membrane (near the reinforcement) when the anode is fed with H_2 and the cathode with air, while the Pt band is shifted in the cathode/membrane interface or in the catalyst layer (inside the ionomer) in the case of H_2/N_2 operations when high hydrogen concentration is reached also at the cathode side. In particular, elongated precipitates were found in the case of Start-up AST. The formation of such a large precipitate could be characteristic of the fast voltage sweep and wide potential window adopted, unlike what observed in others works on AST [94].

Regarding the Pt ions precipitation at the membrane anode/interface, observed for cathode inlet/ middle samples and SU-AST, but not for cathode outlet sample, it could be related to the large amount of Pt ions that diffuses/migrates through the membrane (and don't precipitate over the reinforcement). They were smaller respect to larger precipitate at cathodic side and could indicates that some ions cross the membrane without being reduce by hydrogen crossover.

In conclusion, despite the differences observed in the Pt band formation in air and inert atmosphere, that could enhance the degradation over a larger number of Start-up cycles, the mechanism of platinum dissolution and diffusion/precipitation within the polymer electrolyte, under wide voltage cycling at low temperature, is clearly the dominant physical process underlying performance loss observed in Start-up operations.

Particle size distribution from TEM images

Transmission electron microscopy (TEM) provide two-dimensional images of nanoparticles. These images can be used to calculate the average particle size and particle size distribution. For effective characterization, high-angle annular dark-field (HAADF) images were analysed to enhanced contrast between Pt nanoparticles and substrate (i.e. carbon support, ionomer and resin) . Only images captured at high magnification were analysed (640K magnification, and pixel size of 0.03586 nm) using automatic method. All images were elaborated using ImageJ, an open source software with a suite of analysis routines (http://rsbweb.nih.gov/ij/download.html). The procedure steps were as follows:

- Set the measurement scale using measurement of pixel size;
- Crop the image to remove scale bars and other image artefacts that might affect contrast or particle analysis.
- Check and correct brightness and contrast to ensure that all images have histograms centred.

- Apply color threshold and correct brightness and contrast (see effects in figure 7.30). Due to the thresholding operation, that reduced image quality (e.g. uneven background, rough particles or spotted zones) the despeckle operation was applied. No other operations or filters were used.
- Touching particles were not elaborated by using automated separation algorithms (such as the *Watershed*). Rather, all particle were recorded, and touching particles were removed from the spreadsheet of the results using an aspect ratio (AR) threshold (i.e. particles with AR more than 1.25 were excluded from fitting.
- Some measurands were taken into consideration when analyze particle routine was runned (such as area, shape descriptors, Feret's diameter).
- Analyse the particles (ImageJ specific settings should include the following: show outlines, display results, include holes and exclude on edges).
- Each image file was then saved (filename.tif) with the relative the spreadsheet (Results.xls), which reports all measurand values.

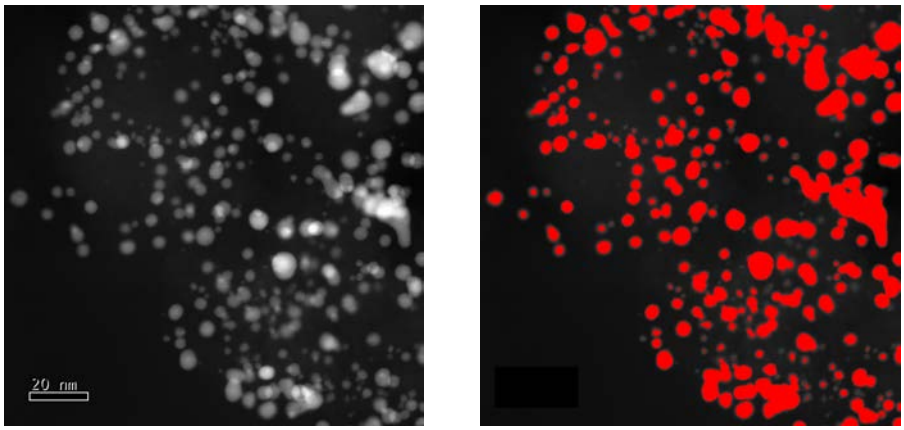

(a) Raw **(b)** Processed

Figure 7.30 – Digital processing of TEM images

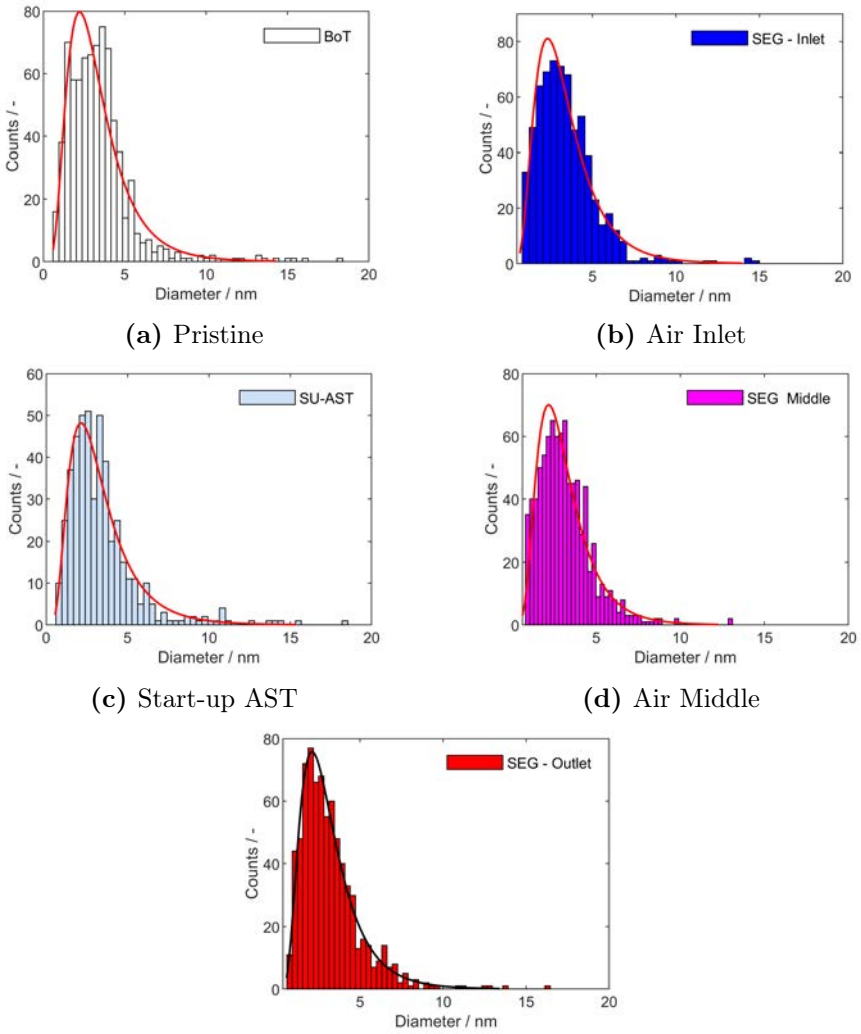

(a) Pristine **(b)** Air Inlet

(c) Start-up AST **(d)** Air Middle

(e) Air Outlet

Figure 7.31 – Pt particle size distributions of pristine and aged samples

The size distribution is expressed through a Gaussian or log-normal function, characterized by the mean (μ) and standard deviation (σ). To evaluate the particle size the area-equivalent diameter was chosen as the most appropriate measurands. Finally, the data fitting was done in matlab, using the automatic routine *fitdist*, for both the probability density functions described. The hystograms of Pt particle size distribution are reported in Figures 7.31. To be reliable, the automatic counting must consider a large number of particles. For this analysis, total particles analyzed are more than 5000 and for each samples are: Pristine = 1187; Segmeted-cell inlet = 922; Segmented-cell Middle = 1241; Segmented-cell Outlet = 1179; Start-up AST

= 685.

The probability density functions are reported in table 7.3:

	Normal Distribution		**Log-Normal Distribution**	
	E(x)	STD(x)	E(x)	STD(x)
Pristine	3.4	1.4	3.4	1.9
Air Inlet	3.4	1.4	3.4	1.9
Air Middle	3.1	1.2	3.1	1.7
Air Outlet	3.2	1.3	3.2	1.8
Start-up AST	3.4	1.5	3.4	2.0

Table 7.3 – Particle size distribution results.

The average particle values are quite similar for all the samples and around 3 nm. Looking at the aged samples, the protocols showing the main similiraties are collected at the cathode inlet of the segmented-cell and during Start-up AST. They show the same mean particle diameter (i.e. 3.4 nm) and a wider particle distribution. In particular, larger particles (out of 20 nm abscissa scale in the hystogram) were detected, in contrast with the other samples.

However, the pristine material has the same distribution of the most stressed zones and this complicates the experimental analysis as larger nanoparticles might have different properties from smaller ones. As reported in literature[10, 11], due to voltage cycling, the particle size tends to increase for the Otswald-ripening mechanism. Probably due to the small number of cycles, the effect on particles size distribution are indistinguishable.

In conclusion, the presence of large Pt agglomerate and the pronounced ECSA loss, are quite good indicator that the catalyst material is severely stressed under wide voltage cycling, also at low temperature. Considering the mitigation effect of low temperature on carbon corrosion mechanism, Pt dissolution/detachment appears to be the major cause of degradation, under operating conditions considered in this work.

7.6 The accelerated protocol for Start-Up AST

A general approach to identify transfer function from zero-gradient cell AST to real-world operation on full-scale cell was here proposed.

It is based on the achievement through the investigation of physics of the mechanisms of reverse-current during start-up and shutdown, and the analysis of local performance losses, under the specific protocol developed, introducing

mitigation strategies to mimic real automotive stack start-up/shut-down operation.

To develop the AST, the real world representativeness has been privileged rather than a high acceleration factor. So far, the new AST proposed for start-up operation, presents a transfer function close to 1, till the number of start-up events is limited to few hundreds. The necessity to reduce the time required to perform the AST must be carefully evaluated, because it imply a more complex transfer function. In fact, in general, the higher the acceleration factor, the lower is the AST representativeness of real world, so less accurate will result the transfer function. In this last section a new Accelerated Stress Test procedure is proposed, capable to properly reproduce the Start-up/Shut-down phenomena in a reasonable timeframe.

By the investigation till here conducted, the platinum dissolution has been recognised as the major cause of materials degradation under mitigated Start-up operation. Since, platinum loss is strongly related to the mechanism of platinum oxidation/reduction, and accelerated by voltage cycling, the impact of the different zones of voltage profile (see figure 7.32) during a cycle of Start-up AST has been studied.

In the regions one and three of SU-AST the MEA is kept at 1 V for 240 and 120 seconds respectively. From literature, is known that high voltage holding accelerate the degradation caused by Pt dissolution[101]. In order to reduce this time interval and accelerate the AST, the role of voltage holding time on platinum oxides formation has been investigated.

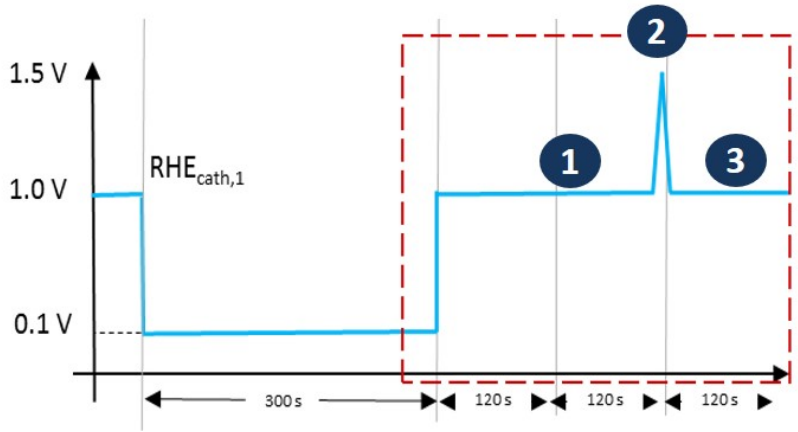

Figure 7.32 – SUSD AST profile

7.6.1 Procedure description

In order to study the formation of platinum oxides (PtO_x) a proper sequence of tests is performed, measuring oxides formation, at the end of each voltage steps of the AST cycle, by Linear Sweep Voltammetry (LSV). Tests were performed at same operating conditions of AST: with a 60 ml/min flux of H_2 at the anode and N_2 at the cathode, ambient pressure and at 30 °C. The adopted protocol is outlined in Table 7.4.

Simulation region	*Type of test*	*Holding time*	*LSV's UPL*	*LSV's LPL*
1	1 V Holding	30-60-180-300-1000-3600 s	1 V	0.079 V
2	1.5 V Peak	-	1 V	0.079 V
3	1 V Holding	10-30-45-60-120 s	1 V	0.079 V

Table 7.4 – LSV operating conditions

7.6.2 Holding time effects before Start-up

In order to simulate region 1, an holding time variable between 30 s and 3600 s at 1 V vs RHE was applied. LSV was performed right after in order to investigate the reduction peaks. Looking at the results is evident that, in terms of PtO_x formation, the holding time at 1 V cause a progressive increase of platinum reduction charge. However, keeping the MEA at 1 V for 30 seconds or 1 hour doesn't change significantly the peak formation. Platinum oxides reach a quasi steady-state after few seconds at high potential, and the subsequent increase in reduction charge follow a logarithmic profile in time, as explained in seminal works of Conway [16, 17, 28]. After every test a negative peak, around 0.8 V is visible, moreover the different holding time seem to shift this peak at lower potential, suggesting the formation of a more stable platinum oxide.

The simulation of regions one and two together was performed introducing the 1.5 V peak (red curve) after a 240 s holding at 1 V. In Figure 7.34 the comparison between protocol one and two are presented. The result obtained is really interesting: less than a second at 1.5 V causes a dramatic increase of the reduction charge associated to the oxides respect as seen in the previous operations.

Finally, all the three regions were simulated together and the results are shown in Figure 7.35. After a 240 s holding at 1 V and the 1.5 V peak, the

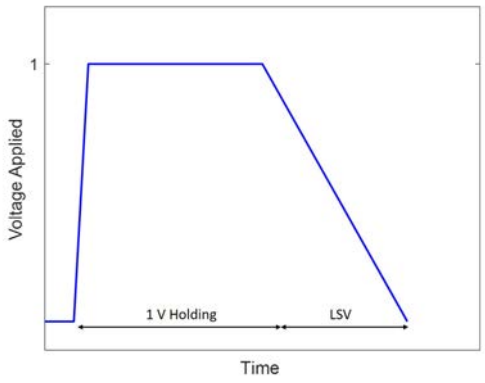

(a) Holding

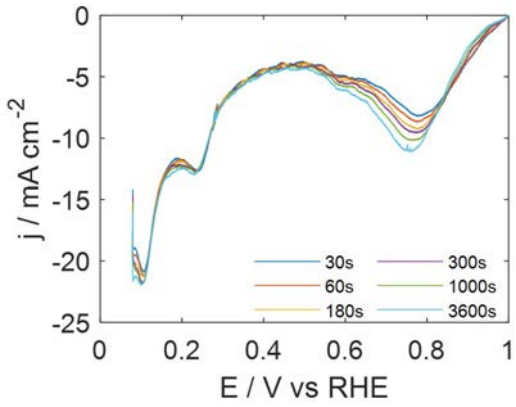

(b) LSV

Figure 7.33 – Simulation of region 1 and LSV result

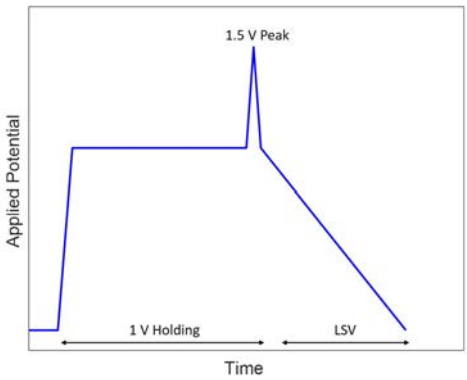

(a) Holding and SU peak

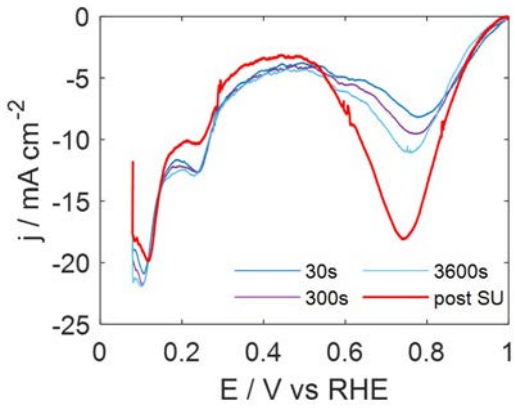

(b) LSV

Figure 7.34 – Simulation of regions 1-2 and LSV result

MEA was kept again at 1 V for an holding time variable between 10 and 120 seconds to evaluate the effect of OCV period after start-up operation. The results previously obtained for region 1 are confirmed: PtO_x formation isn't significantly affected by the holding time at 1 V, as its increase doesn't alter the reduction peak previously caused by the high voltage sweep.

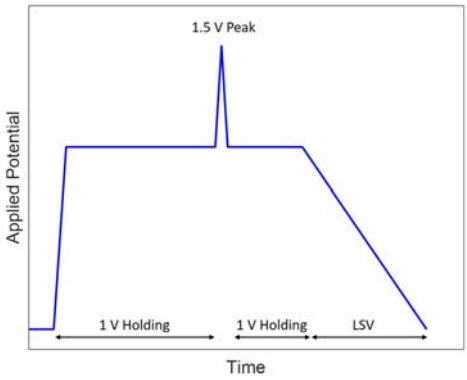

(a) Holding, SU peak, Holding

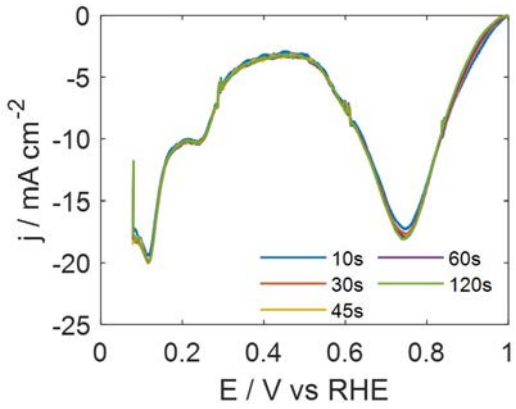

(b) LSV

Figure 7.35 – Simulation of regions 1-2-3 and LSV result

7.7 Conclusion

Starting from the analyses of Start-up/Shut-down operation under mitigation strategies a new AST protocol was designed to reproduce the performance degradation in Zero-gradient cell. The characterization of physical processes, that involved materials aging, confirmed that Platinum dissolution is the most influent phenomenon during Start-up cycling here considered. Moreover, the representativeness of Start-up AST, respect to real world operation was here validated, with an acceleration factor equal to one. While the AST accurately reproduces the real process, it isn't able to accelerate the operations, limiting the usability at a larger number of cycles. With the purpose to accelerate the AST protocol, platinum oxides studies were performed and a new accelerated Start-up AST was proposed, as illustrated below.

	$Refresh$ $at\ 0.1\ V$	$Holding$ $at\ 1\ V$	$Peak$ $at\ 1.5\ V$	$Holding$ $at\ 1\ V$	$Total$ $Time$
SUSD AST	300 s	240 s	0.6 s	120 s	660 s
Accelerated SUSD AST	30 s	30 s	0.6 s	10 s	70 s

Table 7.5 – SUSD ASTs time parameters

The proposed AST has the same shape of the previous one, but with with shorter timeframes that allow to simulate a number of cycles higher than 200. The acceleration factor permits to test a material, with a reduction in time from 37 hours (for 200 cycles) to less than 4 hours.

Conclusions

A detailed investigation of local performance degradation during Start-up/Shut-down operation has conducted. An in-house custom setup based on a segmented cell-like approach was modified and manufactured applying eight Reference Hydrogen Electrode (four at the anode and four at the cathode side) in order to investigate the local potential profile during Start-up/Shut-down. The test bench was developed to monitor a unique fuel cell with four segments (both anode and cathode flow-fields) and eight RHEs during start/stop operation. To permit fast gas switching and transient potential acquisition (transient duration < 0.5 s, frequency data acquisition 100 Hz) a Labview program was designed ad-hoc. Continuous improvements to the experimental setup have been carried out during the activity itself to permit a deeper detail of the most interesting aspect highlighted during the experimental activity itself and to increase measurement reliability. A two dimensional transient model was developed to study the reverse-current mechanism under start-up/shut-down operating conditions for a PEMFC. The solved domain is divided into five regions, to simulate both anode and cathode electrodes: anodic and cathodic gas diffusion layers (GDL's), anodic and cathodic catalyst layers (CL's) and the polymer membrane. Conservation equations are implemented in each layer, along with phenomenological equations to provide a physical description of the major phenomena. The hydrogen oxidation reaction (HOR) and oxygen reduction reaction (ORR) occur in the anode active layers while oxygen reduction/evolution reactions (ORR/OER) and carbon oxidation reaction (COR) occur in the cathode active layer: The model relies on the following assumptions: 1) differences between local regions under the channel, and under the ribs of the gas distributor are neglected; 2) Liquid water transport and energy conservation are not solved, neglecting the blocking effect of liquid water on species transport and heating of porous media; 3) Conservation of water in the ionomer phase is not solved, thus water crossover across polymer membrane is neglected and ionic conductivity is calibrated as a constant parameter, consistently with the fully humidified condition that is set in the experiment; 4) Pseudo-Capacitive currents due to platinum oxida-

tion/reduction were introduced in the last version to increase the simulation accuracy. Assumptions (2) and (3) are acceptable, as first approximation, in the light of fast dynamic behaviour that were investigated in this work (< 5 s). The model can simulate both steady state operation (polarization curves) and the transient operation (voltammetries and start-up/shut-down operation). The use of a 2D model had the consequence of being able to simulate up to a single straight channel, the length of which was set to be 50 mm to limit memory usage and computational time, without losing the representativeness of the simulations. Probe points have been implemented on the interface between CLs and GDLs along the channel length (at start, 1/4, 1/2, 3/4, end of the channel) to mimic the measurement performed with the local RHEs. The model is solved with COMSOL Multiphysics® 5.4 with secondary current distribution module and reacting flow in porous media module.

In the first task, the physics of the mechanisms of reverse-current during start-up and shutdown was analysed. The goal of the task is to evaluate the impact of specific stressors, on start-up and shutdown operation, such as the temperature, the flow rate, the reactants concentration. Through a dedicated experimental campaign performed with reference hydrogen electrodes different start-up (shutdown) operating conditions has been evaluated. Thus, modelling setups has been applied to distinguish the current contributions to the reverse-current mechanism underlying start-up (shutdown) operation. One of the highlights of the research project is to extend available literature on the governing mechanisms underlying start-up/shut-down operation in PEMFC. The approach starts incorporating mass-transport effects by simulating them with a fully coupled 2D model and validate results obtained by experimental local RHE's profile. First, potential profiles provided by the model approximately match with experiments, providing a general consistency between model and experiment. The rest of the analysis is mainly focusing on start-up, which is more relevant from a technological point of view, considering that several mitigation strategies exist for shut-down. Under Start-up, a fast rise in cell potential is observed initially and, the cathode electrode sustains the process by, initially, double-layer capacitive currents during potential rise, until potential is high enough to have carbon corrosion current maintaining the process. When hydrogen reaches the active site, instead, it shifts rapidly down the local anode electrode potential, therefore anode capacitance generates a negative anodic current which sums up to anodic ORR. The cathode electrode at the position where the H_2/air front is located, switches from passive (COR) to active operation (ORR). Since the reverse current circulating across the cell progressively fades, as expected from the moment that the passive region becomes smaller as the front proceeds,

the local cathode potential of the active region raises towards OCV and the capacitive current changes from positive to negative until leading, in the end, to a current flowing in the opposite direction. The concentration of the reactants in time and space is also studied. By simulation results, it is possible to see how, during Start-up, the movement of the hydrogen front in the channel is not matched by the hydrogen progress in the catalyst layer, in disagreement with the plug-flow assumption usually used in the literature. The consumption of oxygen in the CL affects the profile of the outgoing oxygen front in the catalyst layer. The current density associated to carbon corrosion during start-up is split into the contribution of four segments (numbered from 1 to 4) reporting the spatial distribution of the support degradation over all active surface. It is found that degradation is strongly heterogeneous, consistently with the local potential profiles discussed above. In particular, the inlet region (cathode zone opposite to anode inlet - co-flow configuration) is not affected by this degradation mechanism, while the outlet region (cathode zone opposite to anode outlet – co-flow configuration) for about 50% of the degradation occurring. The last results are of fundamental importance for the study of performance degradation. Stressing factors (or stressors) are analysed to improve the understanding of carbon corrosion degradation mechanism under start-up and shut-down under real operating conditions. Those are: temperature, gas flow rate, hydrogen concentration in anode, oxygen concentration in anode, oxygen concentration in cathode and gas mixture composition (with synthetic air in N_2 and He). Furthermore, these specific parameters were analysed for their relevance in the investigation of performance degradation and AST development. Since the kinetics of electrochemical reactions is strongly influenced by the temperature, this parameter has been necessarily considered between stressors. In the simulation, the effect of the temperature is implemented in the exchange current density with reaction-specific Arrhenius terms. It is found that a higher cathode peak potential is reached when temperature is lowered, both in experiments and simulations. According to Arrhenius description of temperature dependency of kinetics of COR, it is argued that temperature should reduce exponentially the impact of carbon corrosion. But, during start-up, this effect is opposed to an increase of the local outlet potential because of the dynamics of the process. The analysis of the potential in the active part of the cathode, where ORR occurs, suggests that current density should increase at high temperature: the lower potential for cathodic ORR during start-up at high temperature clearly indicates that current of the active region (and consequently of the passive region) is increasing, since kinetic losses are indeed reduced as temperature goes up. When increasing the temperature, the dry gas flow rates are reduced because relative humidity is unchanged, as was done in the experimental, to

maintain the same residence time. Instead, the partial pressure of hydrogen and oxygen vary significantly when temperature is changed, this should be considered in the physical interpretation of the results. In particular, the oxygen mass in the anode compartment before the start-up increases. This effect, combined with a reduced reverse-current at low temperature, explained the growth of time required to finish the start-up operation. Anyway, to generate a certain current, mainly determined as seen by anodic ORR and thus by anodic oxygen, COR/OER peak changes: as visible from the plots, voltage can raise even though current is lower at a different temperature. Different dry flows have been tested, while keeping constant the relative humidity (i.e. RH 1/1 – T 40 °C). Tests results highlight the decrease of maximum reached potentials and duration of transient phenomena when gas flow rate is increased. In addition, the minimum voltage increases, suggesting a reduced overpotential of cathodic ORR. The gas flow rate is a well-known mitigation parameter used in real system operation, and it will be taken in great consideration for the calibration of new AST protocol as reported below. The last stressors that was considered is the oxygen concentration in the anode compartment. The collected experimental profile, at high oxygen concentration (50% O_2) in the dry gas, shows an increase of the duration of the start-up, an increase in the value of peak potential in the cathode passive zone and a decrease of the minimum potential observed in the cathode active zone. The same trend is well reproduced by the simulation. The same trend under high oxygen concentration, at the anode in the passive zone was confirmed. The local potential suggests that high concentration of oxygen causes an increase of the total current flowing due to the reverse-mechanism, boosting carbon corrosion. A better explanation of the contribution of this stressor could be obtained looking at the current profile simulated. The global COR current highlights the fundamental contribution of the anode in the passive zone to control the start-up mechanism. Decreasing the oxygen concentration, the reverse-current is strongly mitigated, lowering at the same time the total carbon corroded. Furthermore, the simulation done at very low oxygen concentration has revealed the basic role played by the capacitive phenomena during start-up. With nitrogen feeding in the anode compartment, the anodic ORR in the passive zone was switched off. Though anodic ORR was removed in the passive part of the cell, the reverse-current mechanism is fed by capacitive currents due to anodic/cathodic double-layer. In that case, carbon corrosion current was reduced at 20% respect to the air feeding, but the reverse-current mechanism is not completely inhibited.

Since the objective of this research project is to reproduce real-world operation (such as start-up) using ASTs, a comparison between degradation under repetitive start-up and shutdown operation and ASTs was preliminary

performed using SoA protocols. Firstly, start-up/shutdown operation in unmitigated cycles (at 80 °C – small flow rate) were compared with DoE ASTs, then a specific protocol, developed in the framework of ID-FAST project (introducing mitigation strategies to mimic real automotive stack start-up/shut-down) was investigated and local performance losses were analysed. This part of the work starts with the analysis of the SoA ASTs protocols for the catalyst layer. It has been developed as a preliminary study, necessary to better comprehend the contribution of the different single degradation mechanisms, i.e. the platinum dissolution and the carbon support corrosion in real degradation: the DoE AST protocols were analysed and the results compared with consecutive start-up and shutdown cycles. The goal of this activity was to evaluate which mechanism prevail on the degradation during the Start-up/Shut-down operation and to estimate an empirical correlation between the performance indexes (mass activity, ECSA, polarization curves, limiting current) through the different ageing operation. Three different MEA of 25 cm^2 active area have been degraded using a single cell setup (triple serpentine flow-fields). The first two have been used for ASTs, in accordance with DOE protocols. Unmitigated Start-up/Shut-down procedure is instead tested on a third MEA. Temperature and relative humidity are set equivalent to ASTs, at values of 80 °C and 100% respectively. Five Start-up/Shut-down are reproduced in a row: this procedure does not involve any kind of mitigation. It consists in applying a constant air flow (200 $mlmin^{-1}$) to the cathode and fluxing alternatively (every 60 s) a hydrogen and an air flow of 50 $mlmin^{-1}$ to the anode. Notably, between one set of tests and the next, current is fixed at 0.4 A/cm^2 for 10 min to allow MEA re-hydration and to record data about how degradation evolves in time. In order eliminate the influence of the oxidation state to the catalyst surface, after the galvanostatic operation a recovery is introduced. A full diagnostic protocol is realized at Beginning of Test (BoT), after 60 Start-up/Shut-down and at End of Test (EoT), equal to 100 Start-up/Shut-down. EoT was chosen considering a minimum performance of 0.3 V at the 0.4 A/cm^2 applied current. Reported results show the main differences between electrocatalyst degradation by its dissolution and carbon support degradation. Compare to the former, carbon corrosion leads to much more reduced performances both in oxygen and air operations. While electrocatalyst AST mainly causes polarization curves translation due to ECSA loss, support AST is largely damaging for the structure, affecting both gas and ionic transport properties, hence high current density performances are strongly weakened. The larger mass transport losses are evidenced by the limiting current measurements, on which oxygen transport resistance up to platinum surface is evaluated. As declared by the Fuel Cell Technology Office of DoE, the carbon corrosion

AST exploits a potential range like which would occur in an unmitigated system start-up or shut-down. The analysis of the ageing results shows a very good agreement between such DoE carbon support protocol and the unmitigated real operation in terms of polarization curves (both in air and oxygen), Platinum active area and mass transport resistance in spite of the physical differences between the two mechanisms (different involved gases at cathode, gas switching - and related voltage cycling - at anode, a voltage profile not uniformly distributed during start/stop as well as during the AST). A clear quantitative correlation is therefore found: an almost 10 ratio (9.6) exists between AST cycles and Start-up/Shut-down, while AST accelerates the deterioration in time by a 10.3 factor. The strong similarity suggests that, even though start-up/shutdown is a heterogeneous mechanism, the absence of mitigation for both the operations makes the impact quite homogenous, such that the overall MEA indexes are very well described by the uniform ageing due to the carbon support AST.

To evaluate real world operations a realistic test profile has been arranged to reproduce in a Segmented Single Cell hardware the mechanism of the Long-Stop (Off-Spec Event), based on the specifications of the ID-FAST project durability test program. Reflecting partner test fleet data, this simulates a stop-time before restart longer than 12 hrs. Which should occur every 200 operating hours, i.e. 25/30 times through the component lifetime. For significant validation here the results are extended to 200 cycles. A triple serpentine Segmented Cell flow field (i.e. with four graphite segments, at both anode and cathode side) has been used to study the degradation process. To guarantee a deeper insight into the start/stop process, the in-house custom hardware was upgraded, introducing four per side Reference Hydrogen Electrodes; such setup has been used to evidence the local distribution of potentials of both cell segments and anodic/cathodic electrodes during operations, including fast transients. The start-up/shut-down ageing procedure consists in starting from H_2/air OCV, nitrogen is fluxed at cathode side for 300 s, during which cell voltage decreases till approximately 100 mV. After the purging of the oxidant by the inert, that ensures full shut-down mitigation, then cell voltage immediately drops further, till 0 V, while cathode electrode potential increases to 1 V. Almost the same voltages are kept when air is introduced into the cathode: the after-long stop air/air condition is finally reached avoiding high cathodic potentials during the stop transient. After 120 s, a H_2/air front is finally generated at anode side; the unmitigated start-up causes cathode potential to increase up to 1.5 V. After 120 s again, the described procedure is repeated. According to the project specifications, the flux of hydrogen during start-up must be 1 A/cm^2 equivalent. The same specification was adopted for the air flux at the anode and cathode sides. The ageing process caused

the loss of Pt active area, investigated though the CV measurement. The global decrease, after 200 cycles, is around 25%. In detail, the local ECSA reduction has been computed thanks to the local CV measurements. The largest loss is evident for the first segment (i.e. SEG 1 – 37% ECSA loss), since it undergoes the highest potentials and for longer during the start-up transient. The loss of ECSA is significant for the half of the cathode electrode closer to the anode outlet, i.e. segment 1 and 2 (i.e. SEG 2 – 33% ECSA loss) while segment 4, which encompasses the anode inlet position, faces just a very slight ECSA reduction (i.e. SEG 3/4 - 20%/13% ECSA loss). The ECSA loss increases the kinetic losses: coherently, H_2/O_2 polarization curves are signed by performance reduction as a vertical translation in the polarization curve. The larger voltage decrease regards segment 1 and 2 (close to anode outlet), while the performance of the segment 4 is practically unchanged and even a bit promoted by the way of current redistribution among the segments. H_2/air polarization curves suggest instead a slight increase of performance after 30 cycles at mid-high current density. This could be related to a "cleaning" of the catalyst, as a probable consequence of voltage cycling. Such phenomenon, not observable with harsher decay protocols, appears reproducible and requires further dedicated studies. Deviations are limited for the average performance: within 12 mV in air and 6 mV in oxygen. Focusing on the first region instead, the impact is even doubled: 18 mV and 10 mV respectively as maximum loss. Results of the limiting current test reveal segments heterogeneity. At 30 cycles, the limiting current density is a bit improved for all the segments but the first, while at 200 cycles the two halves of the cell (close to anode inlet and to anode outlet) show an opposite alteration: the current is reduced in case of segment 1 and 2 (largest changes at the first), while segments 3 and 4 boost their performance. This outcome hints at a redistribution of the currents among the segments because of degradation: the net result is the overall MEA unvaried behaviour. In conclusion, the first cathode segment (close to anode outlet) suffers the strongest degradation due to start-up operation. At 30 cycles, ECSA decay and performance changes are minor (within 5 mV and 10% variation respectively) and the limiting current is even a bit improved. At 200 cycles, which is a quite high number of long start-up compared to what expected in a real stack, the local ECSA loss is relevant (-37%) while the performance is reduced by a maximum of 18 mV.

As a basis for the development of the AST protocols all material testing results should be realized by the same test hardware and testing procedures. Therefore, new single cell design studied by the working group coordinated by JRC with the aim to contribute defining an international standard was considered in this work. The developed single cell (hereinafter also known as Zero-Gradient test cell) permits to evaluate material properties under uniform

operating conditions, without any effect of the flow-field designs. Such a result was achieved minimizing gradients regarding gas concentration, humidity, and temperature. An in-house version of the Zero-Gradient hardware was defined, developed, and realized in this research project. The new reference single cell hardware is conceived to keep the operative conditions as homogeneous as possible along the MEA, and all its different part were designed to achieve this objective, as clearly stated by JRC. As with state-of-the-art CCMs very high current densities up to 5 A/cm^2 (at potentials below 400 mV) and fast dynamics (4 C/min) are realized, an efficient cooling of the test cell hardware was implemented adopting liquid cooling endplate along with the implementation of an additional thermostatic bath in the test bench. Flow-fields is designed in accordance with JRC specifications. The selected hardware had to be validated to ensure the highest standards in measurements and reproducibility among partners. For this task, separate measurements with the POLIMI prototype and with commercial test cell hardware version (test performed by project partner) were done. Finally, the most distinctive results are presented, the Accelerated Stress tests were performed in the new hardware, the so-called Zero-gradient test cell, which was specifically designed to compare components during AST and real-world operation on full-scale cell. First, a new Start-up AST (SU-AST) has been developed and transfer functions correlating accelerated degradation to real world has been validated. In general, a long stop implies an ambient temperature start-up: since temperature is known to be a key-role stressor and since the maximum transient potential is close to DoE AST upper potential limit even at low temperature, temperature was the first parameter studied by simply changing its value in the carbon support AST. First of all, two different AST protocol were compare: the DoE support AST and a modified protocol, with temperature fixed at 30 °C, instead of 80 °C. Preliminary, the Pt active surface area was analysed. In case of 80°C test, the ECSA value is the 46% of BOT with respect to the 17% found in the previous test campaign on (material A). This is a first sign that the impact of carbon corrosion is less intense than on the previous MEA. In case of 30 °C test, repercussions are totally different: ECSA remains larger than BOT till 2000 cycles. Only at 5000 cycles, a small reduction is computed. Polarization curves for air at 2.5/2.3 bar for both the tests have shown differences in performance evolution very marked. According to ECSA trend, at low temperature the performance initially increases and finally comes back to BoT. At high temperature instead, kinetic and diffusion losses are both boosted. From these observations, the real process appears to impact differently from low temperature AST; therefore, this second is not able to appropriately reproduce real degradation. Note that the relation found above between DoE AST and unmitigated, high temperature Start-

up/Shut-down is no more respected in this case. To explain the discrepancy, we observed that the main difference is the voltage range. The mitigation strategy allows to skip shut-down but, in the meanwhile, nitrogen transition brings down cathodic potential to 100 mV; hence, the cathodic voltage range during the test is enlarged. As reported in literature, Pt dissolution is strongly dependent on differences between maximum and minimum potentials. In conclusion, we suppose that Pt dissolution has occurred more in case of real process such that low temperature AST fails in reproducing the mechanism: it is probably better to reduce the lower limit with respect to the one of DoE AST to ensure a better representativeness. Then, the new AST protocol, named Start-up AST, is proposed. It consists in a voltage profile similar to the one recorded with reference electrode in start-up operation but performed in an inert atmosphere (i.e. H_2/N_2 for anode/cathode – flow rates equal to 60 $mLmin^{-1}$). To simplify the shape of the voltage profile in real start-up, a triangular sweep cycle is used. The potential was fixed between 1.0 V and 1.5 V vs RHE and symmetric scan-rate, equal to 1.5 V/s is used. A comparison between current measured during Start-up AST and current simulated for real start-up confirmed good agreement between the two mechanisms. Also considering such simplification of voltage profile a good agreement between current measured during Start-up AST and current simulated during real start-up was achieved. To elucidate the currents contribution underlying the process the simulation was performed using the advanced version with Pt oxides submodule. The contribution of carbon oxidation reaction is minimum, compared to capacitive currents (here intended as doble-layer and platinum oxides contributions), which means a current peak of 18 mA/cm^2 relative to the total value of 300 mA/cm^2. A performance comparison between real start-up cycles in segmented-cell and Start-up AST was conducted. To make possible the comparison between tests on different hardware, only the specific segment that undergoes the maximum potential is considered, as of interest for the degradation. The performance loss after 200 cycles of start-up in real system can be effectively reproduced with the proposed Start-up AST. Then, the ECSA loss in real start-up operation, obtained with segmented cell, is compared with the one observed with Start-up AST (i.e. 37% and 31%): the obtained values are similar, suggesting a high representativeness of the proposed AST. So, a direct correlation between real-world operation and proposed AST was found but the acceleration factor is close to one. The combined effect of different degradation mechanisms has been evaluated by adopting a proper sequence of different ASTs. The proposed Start-up AST was then performed on the MEA aged by the Electrocatalyst AST protocol. The specific loss caused by Start-up AST can be disentangled and evidenced if it is compared to the decrease of performance induced on another MEA sample

by the single Start-up AST. First, the performance losses were evaluated at operating conditions that mimic cathode inlet of real operating system to quantify the impact of combined AST on the specific degraded zone under start-up. Under cathode inlet operating conditions, the degradation due Start-up AST appears comparable in case of single AST and combined AST, with an observable rate of 40 µV/cycle and 45 µV/cycle, respectively. The comparison between single and combined ASTs at low oxygen concentration was than evaluated to highlight the coupling effect on cathode catalyst layer of the degradation mechanisms. In both the tests the mass transport losses were exacerbated at high current density and even more in the combined AST. In the combined AST, the ECSA value slightly decreased, that reached the minimum after the first Electrocatalyst AST but rather deteriorated the performance when the mass transport effect became limiting. To better understand the mass-transport effects visible during aging of the components, the method of limiting current was applied for Start-up (in segmented-cell and in AST), and Electrocatalyst, Support and Combined ASTs. The total mass transport resistance at limiting current (when the oxygen concentration on the platinum catalyst approaches zero) consider: channel, porous media, catalyst layer and interfacial resistance from primary pore trough the ionomer to Pt nanoparticle. As clearly visible a strong linear correlation was found respect to the inverse of catalyst surface active area, with a very similar slope between all the tests (5/10 scm^{-1} - 1.5/3.5 bar) except for the 80 °C Support AST (15/20 scm^{-1} - 1.5/3.5 bar), where electrode reconstruction worsen oxygen transport resistance. The results confirm that the platinum dissolution mechanism is the main responsible of performance losses.

To evaluate the impact of degradation on materials aging several Ex-Situ analysis have been performed in cooperation with CEA (French Alternative Energies and Atomic Energy Commission) and DLR (German Aerospace Centre) on the aged MEAs. SEM analyses revealed no severe MEA microstructure evolution, such as in carbon corrosion AST. Only a band of Pt precipitates was observed in the membrane, the intensity of the band differs for the different studied MEA regions: a higher precipitate density is located in the air inlet region compared to the middle zone whereas quite no precipitate was visible in the air outlet zone. Observation of TEM images highlighted the presence of large Pt agglomerates, caused by Start-up. In air atmosphere regular shaped particles (i.e. 200-300 nm Pt agglomerates) are in the membrane (near the reinforcement) while in inert atmosphere they precipitate into the ionomer. Despite the differences observed in the Pt band formation in air and inert atmosphere, that could enhance the degradation over a larger number of Start-up cycles, the mechanism of platinum dissolution and diffusion/precipitation within the polymer electrolyte, under wide

voltage cycling at low temperature, is clearly the dominant physical process underlying performance loss observed in Start-up operations.

Appendix

In this Appendix, a description of the main tools and devices introduced in the Experimental chapter is reported. Their technical specifications, relevant for the measurements performed during the whole work, could be here checked.

Electronic load

During the conditioning phase and in most diagnostic measurements, a an electronic load is used. It dissipates the power produced by the cell in such a way as to control either voltage or current. On the segmented cell a multi-channel electronic load was employed (CHROMA 63610-80-20) while on single cell hardware and Zero-Gradient cell a single module was used (CHROMA 63600-80-80) :

Model	CHROMA 63610-80-20	CHROMA 63600-80-80
Voltage range	0 ÷ 6 V	0 ÷ 6 V
Current Range	0 ÷ 20 A	0 ÷ 80 A
Voltage resolution	1 mV	0.1 mV
Current resolution	1 mA	1 mA
Voltage set accuracy	0.05% + 6 mV	0.05% + 6 mV
Current set accuracy	0.1% + 20 mA	0.1% + 80 mA
Voltage read accuracy	0.025% + 0.6 mV	0.025% + 0.6 mV
Current read accuracy	0.05% + 10 mA	0.05% + 40 mA

Single-channel potentiostat

A potentiostat was employed to perform CV, LSV and AST. The use of such device is needed as it is able either to provide or absorb power, continuously changing between the two working modes.

Model	Metrohm AUTOLAB PGSTAT30
Voltage range	$0 \div \pm 10$ V
Current Range	$0 \div 20$ A
Voltage resolution	30 muV
Current resolution	1 muA
Accuracy	0.02% + 3 mV

Multi-channel potentiostat

This second type of potentiostat is used to perform local measurements of CV and LSV in case of Segmented Cell hardware. It permits to control each portion independently by the way of separate channels, ensuring also a high accuracy.

Model	NI PXIe-4139
Voltage range	$0 \div 60$ V
Current Range	$0 \div 3$ A
Voltage resolution	10 muV
Current resolution	1 muA
Accuracy	0.02% + 3 mV

Flow meters

Flow meters allow to regulate the amount of gaseous streams: setting the volumetric flow desired, a valve is open of a percentage of the full scale to suitably fulfill the requirement. Two different types of flow meters have been used, since they are distinguished by the gas type: N_2/air and H_2 flow meters.

Type	H2
Model	BROOKS 5850s
Range	$0 \div 0.3/2$ nl/min
Accuracy	0.7% + 0.2% F.S.

Type	Air/N_2
Model	BROOKS 5850s
Range	$0 \div 3/15$ nl/min
Accuracy	0.7% + 0.2% F.S.

Bubblers

Bubblers provide the correct humidification of gases. All the gases - air, O_2, N_2, H_2 - enter a small porous tube immersed in the water inside the bubbler. The flow is fully humidified at the bubbler temperature, that must be set equal to the desired flows dew point; in this way the necessary water vapour content is achieved.

Thermocouples

Thermocouples are used to perform temperature measurements. Two of them are put inside anode and cathode aluminum plates, to check cell temperature. Other three are used instead to take under control the temperature of the bubblers and therefore the dew point of flows.
The two type of thermocouples used are:

Type	K
Material	Chromel, Alumel
Range	-270 ÷ 1370 °C
Calibration interval	40 ÷ 90 °C
Accuracy	0.2 °C

Type	J
Material	Iron, Constantan
Range	-40 ÷ 750 °C
Calibration interval	40 ÷ 90 °C
Accuracy	0.2 °C

T-controllers

Temperature controllers have the function of setting the temperature of the connected devices to a desired value. They are connected to a thermocouple that constantly measures the temperature and to an electrical cartridge heater that provides the thermal power. The power side of the circuit is decoupled from the control side by means of a relay. The device uses a PID logic and the output is a low voltage signal that drives the opening and closing of the relay, in order to allow reaching the rate value of the temperature in a fast and smooth way, thus avoiding thermal stress to the heated device.

Model	ASCON LineaM3 Serie γ2
Input voltage	220 ÷ 240 V AC
Temperature input	Thermocouple (type)
Control logic	PID
Resolution	0.1 K
Accuracy	0.25% ± 1 digit

Tubes and connections

All the fluids, both gases and liquid water, course through tubes made of Teflon® PFA (perfluoroalkoxy); it is a flexible and corrosion-resistant material, behaving as an inert and able to operate in a wide range of temperatures. The typical size is 1/8" OD. There are anyway few exceptions: the heated line between the bubblers and the cell is 1/4" OD as well as the outlet anode tube. To reduce as much as possible the pressure drops at cathode outlet, which is typically subjected to higher flows, a 3/8" OD tube has been chosen. The tubes connections are made by stainless steel junctions and fittings furnished by Swagelok®.

DAQ hardware

A multifunction I/O board is used to sample voltage signals and generate digital and analog outputs. The selected device is a National Instrument USB-6218 board. The data were than logged and saved on a PC using LabVIEW.

Pressure transducer

Pressure transducers were used to monitor and log pressure at various position, depending on the set-up employed.

Model	GE Unik 5000
Range	$0 \div 5$ bar
Accuracy	0.04% F.S.

Reference Hydrogen Electrodes

The reference hydrogen electrodes used are Gaskatel Hydroflex reference electrodes. To verify that the set up utilized had a fast enough response, the voltage profile of the reference electrodes during a CV was compared to the imposed potential, as visible in figure 36.

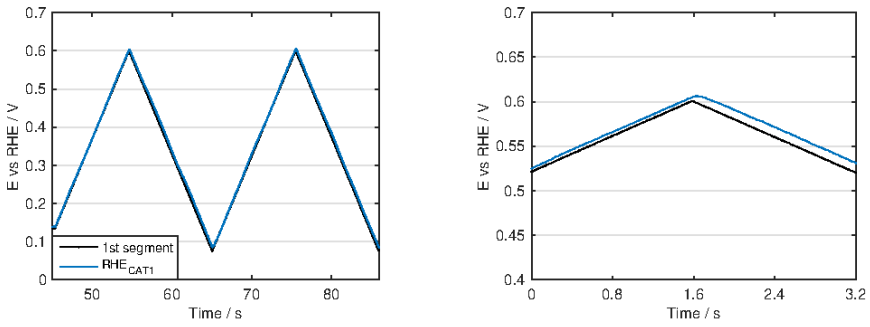

(a) Responsiveness of RHE **(b)** Figure detail

Figure 36 – Example of responsiveness of a RHE. Voltage profile of the first RHE w/r/t an imposed CV profile. LPL = 0.075 V, UPL = 0.6 V, Sc = 50 mV s^{-1}

Nomenclature

Acronym

Acronym	Description
AST	Accelerated Stress Test
BoT	Beginning of test
CCM	Catalyst-Coated Membrane
CL	Catalyst Layer
COR	Carbon Oxidation reaction
DL	Double-Layer
DoE	U.S. Department of Energy
ECSA	Electrochemical Active Surface Area
EIS	Electrochemical Impedance Spectroscopy
EoT	End of Test
FCEV	Fuel Cell Electric Vehicle
GDL	Gas Diffusion Layer
HFR	High Frequency resistance
HOR	Hydrogen Oxidation Reaction
LSV	Linear Sweep Voltammetry
LPL	Lower Potential Limit
MEA	Membrane Electrode Assembly
MPL	Micro Porous Layer
OCV	Open Circuit Voltage
OER	Oxygen Evolution Reaction
ORR	Oxygen Reduction Reaction
PEEK	Polyether-ether-ketone
PEMFC	Polymeric Electrolyte Membrane Fuel Cell
PTFE	Polytetrafluoroethylene
PGM	platinum Group Metal
RH	Relative Humidity

RHE	Reference Hydrogen Electrode
SUSD	Start-up and Shut-down
UPL	Upper Potential Limit

Variables and Symbols

Variable	Description
a_x	Activity of species x
c_x	Concentration of species x
c_{dl}	Double-layer capacitance
d_x	Height of component x
D_x	Diffusivity of species x
$D_{eff,x}$	Effective diffusivity of species x
e	Electron charge, $1.602 * 10^{-19}$ C
E	Voltage
$E_{iR-free}$	Ohmically-corrected cell voltage
E_0	Standard potential of reaction x
E_x	Equilibrium potential of reaction x
F	Faraday's constant, 96485 C/mol
f_{Pt}	Roughness factor
i	Current density
i_{eff}	Exchange current density
i_{lim}	Limiting current density
i_{x,H_2}	Hydrogen crossover current density
L_{Pt}	Platinum Loading
L_x	Length of component x
N_x	Flux of species x
M_x	Molecular mass of species x
$PtOx$	Platinum oxides
R	Gas constant, 8.314 J mol^{-1} K^{-1}
R_{MT}	Total oxygen mass transport resistance
$r_{Pt/C}$	Platinum/carbon ratio
Sc	Scan rate
T	Temperature
t_{res}	Residence time

Bibliography

[1] R. K. Ahluwalia, S. Arisetty, J.-K. Peng, R. Subbaraman, X. Wang, N. Kariuki, D. J. Myers, R. Mukundan, R. Borup, and O. Polevaya. Dynamics of Particle Growth and Electrochemical Surface Area Loss due to Platinum Dissolution. *Journal of the Electrochemical Society*, 161(3):F291–F304, jan 2014.

[2] Ermete Antolini. Carbon supports for low-temperature fuel cell catalysts. *Applied Catalysis B: Environmental*, 88(1-2):1–24, 2009.

[3] A J Appleby. Theory of Successive Electron Transfer Steps in Cyclic Voltammetry: Application to Oxygen Pseudocapacitance on Platinum. *Journal of The Electrochemical Society*, 120(9):1205, 1973.

[4] Radoslav T. Atanasoski, Ljiljana L. Atanasoska, David A. Cullen, Gregory M. Haugen, Karren L. More, and George D. Vernstrom. Fuel Cells Catalyst for Start-Up and Shutdown Conditions: Electrochemical, XPS, and STEM Evaluation of Sputter-Deposited Ru, Ir, and Ti on Pt-Coated Nanostructured Thin Film Supports. *Electrocatalysis*, 3(3):284–297, 2012.

[5] Daniel R. Baker, David A. Caulk, Kenneth C. Neyerlin, and Michael W. Murphy. Measurement of oxygen transport resistance in PEM fuel cells by limiting current methods. *Journal of the Electrochemical Society*, 156(9), 2009.

[6] Andrea Baricci, Matteo Bonanomi, Haoran Yu, Laure Guetaz, Radenka Maric, and Andrea Casalegno. Modelling analysis of low platinum polymer fuel cell degradation under voltage cycling: Gradient catalyst layers with improved durability. *Journal of Power Sources*, 405:89–100, nov 2018.

[7] US) Bekkedahl, Timothy A. (Loveland, CO, US), Bregoli, Lawrence J. (Southwick, MA, US), Breault, Richard D. (North Kingstown, RI,

US), Dykeman, Emily A. (Cheyenne, WY, US), Meyers, Jeremy P. (West Hartford, CT, US), Patterson, Timothy W. (East Hartford, CT, U. Reducing fuel cell cathode potential during startup and shutdown, 2005.

[8] Wolfgang Bernhart, Stefan Riederle, Manuel Yoon, and Wilfried G. Aulbur. Fuel Cells — A Realistic Alternative for Zero Emission? *Auto Tech Review*, 3(2):20–23, feb 2014.

[9] Denis Bona, Dennis E. Curtin, Francesco Pedrazzo, and Elena Maria Tresso. Using a Stack Shunt to Mitigate Catalyst Support Carbon Corrosion in Polymer Electrolyte Membrane Fuel Cell Stacks During Start-Stop Cycling. *Journal of Fuel Cell Science and Technology*, 11(1):011010, nov 2013.

[10] Rod Borup, Jeremy Meyers, Bryan Pivovar, Yu Seung Kim, Rangachary Mukundan, Nancy Garland, Deborah Myers, Mahlon Wilson, Fernando Garzon, David Wood, Piotr Zelenay, Karren More, Ken Stroh, Tom Zawodzinski, James Boncella, James E. McGrath, Minoru Inaba, Kenji Miyatake, Michio Hori, Kenichiro Ota, Zempachi Ogumi, Seizo Miyata, Atsushi Nishikata, Zyun Siroma, Yoshiharu Uchimoto, Kazuaki Yasuda, Ken-ichi Kimijima, and Norio Iwashita. Scientific Aspects of Polymer Electrolyte Fuel Cell Durability and Degradation. *Chemical Reviews*, 107(10):3904–3951, oct 2007.

[11] Rod L. Borup, John R. Davey, Fernando H. Garzon, David L. Wood, and Michael A. Inbody. PEM fuel cell electrocatalyst durability measurements. *Journal of Power Sources*, 163(1):76–81, dec 2006.

[12] Steven G. Bratsch. Standard Electrode Potentials and Temperature Coefficients in Water at 298.15 K. *Journal of Physical and Chemical Reference Data*, 18(1):1–21, jan 1989.

[13] David A. Caulk and Daniel R. Baker. Heat and Water Transport in Hydrophobic Diffusion Media of PEM Fuel Cells. *Journal of The Electrochemical Society*, 157(8):B1237, 2010.

[14] Li Chen, Gang Wu, Edward F. Holby, Piotr Zelenay, Wen Quan Tao, and Qinjun Kang. Lattice boltzmann pore-scale investigation of coupled physical-electrochemical processes in C/PT and non-precious metal cathode catalyst layers in proton exchange membrane fuel cells. *Electrochimica Acta*, 158:175–186, 2015.

[15] Richard G Compton and Craig E Banks. *Understanding Voltammetry*. IMPERIAL COLLEGE PRESS, 2nd edition, nov 2010.

[16] B. E. Conway, B. Barnett, H. Angerstein-Kozlowska, and B. V. Tilak. A surface-electrochemical basis for the direct logarithmic growth law for initial stages of extension of anodic oxide films formed at noble metals. *The Journal of Chemical Physics*, 93(11):8361, 1990.

[17] B.E. Conway. Electrochemical oxide film formation at noble metals as a surface-chemical process. *Progress in Surface Science*, 49(4):331–452, aug 1995.

[18] Robert M. Darling and Jeremy P. Meyers. Kinetic Model of Platinum Dissolution in PEMFCs. *Journal of The Electrochemical Society*, 150(11):A1523, 2003.

[19] J. Dillet, D. Spernjak, A. Lamibrac, G. Maranzana, R. Mukundan, J. Fairweather, S. Didierjean, R.L. Borup, and O. Lottin. Impact of flow rates and electrode specifications on degradations during repeated startups and shutdowns in polymer-electrolyte membrane fuel cells. *Journal of Power Sources*, 250:68–79, mar 2014.

[20] Julien Durst, Adrien Lamibrac, Frédéric Charlot, Jérome Dillet, Luis F. Castanheira, Gaël Maranzana, Laetitia Dubau, Frédéric Maillard, Marian Chatenet, and Olivier Lottin. Degradation heterogeneities induced by repetitive start/stop events in proton exchange membrane fuel cell: Inlet vs. outlet and channel vs. land. *Applied Catalysis B: Environmental*, 138-139:416–426, jul 2013.

[21] Simon Erbach, Bernhard Pribyl, Merle Klages, Lena Spitthoff, Khanik Borah, Sebastian Epple, Lorenz Gubler, Alexandra Pătru, Martin Heinen, and Thomas J. Schmidt. Influence of operating conditions on permeation of CO2 through the membrane in an automotive PEMFC system. *International Journal of Hydrogen Energy*, 44(25):12760–12771, may 2019.

[22] Joseph D. Fairweather, Dusan Spernjak, Adam Z. Weber, David Harvey, Silvia Wessel, Daniel S. Hussey, David L. Jacobson, Kateryna Artyushkova, Rangachary Mukundan, Rodney L. Borup, Power Systems, and British Columbia Vjj. Effects of Cathode Corrosion on Through-Plane Water Transport in Proton Exchange Membrane Fuel Cells. *Journal of the Electrochemical Society*, 160(9):F980–F993, 2013.

[23] P. J. Ferreira, G. J. la O', Y. Shao-Horn, D. Morgan, R. Makharia, S. Kocha, and H. A. Gasteiger. Instability of PtC Electrocatalysts in Proton Exchange Membrane Fuel Cells. *Journal of The Electrochemical Society*, 152(11):A2256, 2005.

[24] Farisa Forouzandeh, Xiaoan Li, Dustin W. Banham, Fangxia Feng, Siyu Ye, and Viola Birss. Understanding the Corrosion Resistance of Meso- and Micro-Porous Carbons for Application in PEM Fuel Cells. *Journal of The Electrochemical Society*, 165(6):F3230–F3240, 2018.

[25] Hubert A. Gasteiger, Shyam S. Kocha, Bhaskar Sompalli, and Frederick T. Wagner. Activity benchmarks and requirements for Pt, Pt-alloy, and non-Pt oxygen reduction catalysts for PEMFCs. *Applied Catalysis B: Environmental*, 56(1-2 SPEC. ISS.):9–35, 2005.

[26] T. Gaumont, G. Maranzana, O. Lottin, J. Dillet, S. Didierjean, J. Pauchet, and L. Guétaz. Measurement of protonic resistance of catalyst layers as a tool for degradation monitoring. *International Journal of Hydrogen Energy*, 42(3):1800–1812, 2017.

[27] Bostjan Genorio, Ram Subbaraman, Dusan Strmcnik, Dusan Tripkovic, Vojislav R. Stamenkovic, and Nenad M. Markovic. Tailoring the Selectivity and Stability of Chemically Modified Platinum Nanocatalysts To Design Highly Durable Anodes for PEM Fuel Cells. *Angewandte Chemie International Edition*, 50(24):5468–5472, jun 2011.

[28] D. Gilroy and B. E. Conway. Surface oxidation and reduction of platinum electrodes: Coverage, kinetic and hysteresis studies. *Canadian Journal of Chemistry*, 46(6):875–890, 1968.

[29] T. a. Greszler, D. Caulk, and P. Sinha. The Impact of Platinum Loading on Oxygen Transport Resistance. *Journal of the Electrochemical Society*, 159(12):F831–F840, 2012.

[30] E. N. Gribov, N. V. Maltseva, V. A. Golovin, and A. G. Okunev. A simple method for estimating the electrochemical stability of the carbon materials. *International Journal of Hydrogen Energy*, 41(40):18207–18213, 2016.

[31] Wenbin Gu, Robert N. Carter, Paul T. Yu, and Hubert A. Gasteiger. Start/Stop and Local H2 Starvation Mechanisms of Carbon Corrosion: Model vs. Experiment. *ECS Transactions*, 11(1):963–973, 2007.

[32] Wenbin Gu, Paul T Yu, Robert N Carter, Rohit Makharia, and Hubert A Gasteiger. *Modeling of Membrane-Electrode-Assembly Degradation in Proton-Exchange-Membrane Fuel Cells – Local H2 Starvation and Start–Stop Induced Carbon-Support Corrosion*, pages 45–87. Springer New York, New York, NY, 2009.

[33] L. Hao, K. Moriyama, W. Gu, and C.-Y. Wang. Modeling and Experimental Validation of Pt Loading and Electrode Composition Effects in PEM Fuel Cells. *Journal of the Electrochemical Society*, 162(8):F854–F867, 2015.

[34] Gregor S. Harzer, Jan N. Schwämmlein, Ana Marija Damjanović, Sourov Ghosh, and Hubert A. Gasteiger. Cathode Loading Impact on Voltage Cycling Induced PEMFC Degradation: A Voltage Loss Analysis. *Journal of The Electrochemical Society*, 165(6):F3118–F3131, mar 2018.

[35] G. Hinds and E. Brightman. In situ mapping of electrode potential in a PEM fuel cell. *Electrochemistry Communications*, 17(1):26–29, apr 2012.

[36] Edward F. Holby, Wenchao Sheng, Yang Shao-Horn, and Dane Morgan. Pt nanoparticle stability in PEM fuel cells: influence of particle size distribution and crossover hydrogen. *Energy & Environmental Science*, 2(8):865, 2009.

[37] Yuta Ishigami, Kenji Takada, Hiroshi Yano, Junji Inukai, Makoto Uchida, Yuzo Nagumo, Tsuyoshi Hyakutake, Hiroyuki Nishide, and Masahiro Watanabe. Corrosion of carbon supports at cathode during hydrogen/air replacement at anode studied by visualization of oxygen partial pressures in a PEFC—Start-up/shut-down simulation. *Journal of Power Sources*, 196(6):3003–3008, mar 2011.

[38] Thomas Jahnke, Georg A Futter, Andrea Baricci, Claudio Rabissi, and Andrea Casalegno. Physical Modeling of Catalyst Degradation in Low Temperature Fuel Cells: Platinum Oxidation, Dissolution, Particle Growth and Platinum Band Formation. *Journal of The Electrochemical Society*, 167(1):013523, nov 2020.

[39] Fei Jia, Liejin Guo, and Hongtan Liu. Mitigation strategies for hydrogen starvation under dynamic loading in proton exchange membrane fuel cells. *Energy Conversion and Management*, 139:175–181, may 2017.

[40] S. Komini Babu, D. Spernjak, J. Dillet, A. Lamibrac, G. Maranzana, S. Didierjean, O. Lottin, R.L. Borup, and R. Mukundan. Spatially

resolved degradation during startup and shutdown in polymer electrolyte membrane fuel cell operation. *Applied Energy*, 254(October 2018):113659, nov 2019.

[41] Anusorn Kongkanand and Mark F. Mathias. The Priority and Challenge of High-Power Performance of Low-Platinum Proton-Exchange Membrane Fuel Cells. *The Journal of Physical Chemistry Letters*, 7(7):1127–1137, apr 2016.

[42] Anusorn Kongkanand and Joseph M. Ziegelbauer. Surface platinum electrooxidation in the presence of oxygen. *Journal of Physical Chemistry C*, 116(5):3684–3693, 2012.

[43] Stefan Kreitmeier, Alexander Wokaun, and Felix N. Büchi. Local Catalyst Support Degradation during Polymer Electrolyte Fuel Cell Start-Up and Shutdown. *Journal of The Electrochemical Society*, 159(11):F787–F793, jan 2012.

[44] A.A. Kulikovsky. A physical model for catalyst layer impedance. *Journal of Electroanalytical Chemistry*, 669:28–34, 2012.

[45] A.A. A. Kulikovsky. A physical model for catalyst layer impedance. *Journal of Electroanalytical Chemistry*, 669:28–34, mar 2012.

[46] Sumit Kundu, Max Cimenti, Stephen Lee, and Dmitri Bessarabov. Fingerprint of automotive fuel cell cathode catalyst degradation: Pt band in PEMs. *Membrane Technology*, 2009(10):7–10, 2009.

[47] A. Lamibrac, G. Maranzana, J. Dillet, O. Lottin, S. Didierjean, J. Durst, L. Dubau, F. Maillard, and M. Chatenet. Local degradations resulting from repeated start-ups and shutdowns in Proton Exchange Membrane Fuel Cell (PEMFC). *Energy Procedia*, 29:318–324, 2012.

[48] A. Lamibrac, G. Maranzana, O. Lottin, J. Dillet, J. Mainka, S. Didierjean, A. Thomas, and C. Moyne. Experimental characterization of internal currents during the start-up of a proton exchange membrane fuel cell. *Journal of Power Sources*, 196(22):9451–9458, 2011.

[49] Y. Li, K. Moriyama, W. Gu, S. Arisetty, and C. Y. Wang. A One-Dimensional Pt Degradation Model for Polymer Electrolyte Fuel Cells. *Journal of the Electrochemical Society*, 162(8):F834–F842, 2015.

[50] Nicolas Linse, Günther G. Scherer, Alexander Wokaun, and Lorenz Gubler. Quantitative analysis of carbon corrosion during fuel cell

start-up and shut-down by anode purging. *Journal of Power Sources*, 219:240–248, dec 2012.

[51] S. Maass, F. Finsterwalder, G. Frank, R. Hartmann, and C. Merten. Carbon support oxidation in PEM fuel cell cathodes. *Journal of Power Sources*, 176(2):444–451, feb 2008.

[52] Natalia Macauley, Dennis D. Papadias, Joseph Fairweather, Dusan Spernjak, David Langlois, Rajesh Ahluwalia, Karren L. More, Rangachary Mukundan, and Rodney L. Borup. Carbon Corrosion in PEM Fuel Cells and the Development of Accelerated Stress Tests. *Journal of The Electrochemical Society*, 165(6):F3148–F3160, 2018.

[53] Natalia Macauley, Dennis D. Papadias, Joseph Fairweather, Dusan Spernjak, David Langlois, Rajesh Ahluwalia, Karren L. More, Rangachary Mukundan, and Rodney L. Borup. Carbon Corrosion in PEM Fuel Cells and the Development of Accelerated Stress Tests. *Journal of The Electrochemical Society*, 165(6):F3148–F3160, 2018.

[54] G. Maranzana, A. Lamibrac, J. Dillet, S. Abbou, S. Didierjean, and O. Lottin. Startup (and Shutdown) Model for Polymer Electrolyte Membrane Fuel Cells. *Journal of The Electrochemical Society*, 162(7):F694–F706, apr 2015.

[55] Josef C. Meier, Carolina Galeano, Ioannis Katsounaros, Angel A. Topalov, Aleksander Kostka, Ferdi Schüth, and Karl J J Mayrhofer. Degradation Mechanisms of Pt/C Fuel Cell Catalysts under Simulated Start–Stop Conditions. *ACS Catalysis*, 2(5):832–843, may 2012.

[56] Jeremy P. Meyers and Robert M. Darling. Model of Carbon Corrosion in PEM Fuel Cells. *Journal of The Electrochemical Society*, 153(8):A1432, 2006.

[57] Thomas Mittermeier, Alexandra Weiß, Frédéric Hasché, and Hubert A. Gasteiger. PEM Fuel Cell Start-Up/Shut-Down Losses vs Relative Humidity: The Impact of Water in the Electrode Layer on Carbon Corrosion. *Journal of The Electrochemical Society*, 165(16):F1349–F1357, dec 2018.

[58] Thomas Mittermeier, Alexandra Weiß, Frédéric Hasché, Gerold Hübner, and Hubert A. Gasteiger. PEM Fuel Cell Start-up/Shut-down Losses vs Temperature for Non-Graphitized and Graphitized Cathode Carbon Supports. *Journal of The Electrochemical Society*, 164(2):F127–F137, dec 2017.

[59] F. Nandjou, J. P. Poirot-Crouvezier, M. Chandesris, J. F. Blachot, C. Bonnaud, and Y. Bultel. Impact of heat and water management on proton exchange membrane fuel cells degradation in automotive application. *Journal of Power Sources*, 326:182–192, 2016.

[60] Nobuaki Nonoyama, Shinobu Okazaki, Adam Z. Weber, Yoshihiro Ikogi, and Toshihiko Yoshida. Analysis of Oxygen-Transport Diffusion Resistance in Proton-Exchange-Membrane Fuel Cells. *Journal of The Electrochemical Society*, 158(4):B416, 2011.

[61] Michael Obermaier, Aliaksandr S. Bandarenka, and Cyrill Lohri-Tymozhynsky. A Comprehensive Physical Impedance Model of Polymer Electrolyte Fuel Cell Cathodes in Oxygen-free Atmosphere. *Scientific Reports*, 8(1):4933, dec 2018.

[62] J. P. Owejan, J. E. Owejan, and W. Gu. Impact of Platinum Loading and Catalyst Layer Structure on PEMFC Performance. *Journal of the Electrochemical Society*, 160(8):F824–F833, 2013.

[63] A. Pandy, Z. Yang, M. Gummalla, V. V. Atrazhev, N. Y. Kuzminyh, V. I. Sultanov, and S. Burlatsky. A Carbon Corrosion Model to Evaluate the Effect of Steady State and Transient Operation of a Polymer Electrolyte Membrane Fuel Cell. *Journal of the Electrochemical Society*, 160(9):F972–F979, 2013.

[64] Baturina OA. Gould BD Lyons KS. Patent. Performance recovery of a fuel cell, 2017.

[65] Pucheng Pei and Huicui Chen. Main factors affecting the lifetime of Proton Exchange Membrane fuel cells in vehicle applications: A review. *Applied Energy*, 125:60–75, jul 2014.

[66] R. Petrone, D. Hissel, M. C. Péra, D. Chamagne, and R. Gouriveau. Accelerated stress test procedures for PEM fuel cells under actual load constraints: State-of-art and proposals. *International Journal of Hydrogen Energy*, 40(36):12489–12505, 2015.

[67] Yanling Qiu, Hexiang Zhong, Meiri Wang, and Huamin Zhang. Effect of relative humidity cycles accompanied by intermittent start/stop switches on performance degradation of membrane electrode assembly components in proton exchange membrane fuel cells. *Journal of Power Sources*, 283:171–180, 2015.

[68] C. Rabissi, E. Brightman, G. Hinds, and A. Casalegno. In operando measurement of localised cathode potential to mitigate DMFC temporary degradation. *International Journal of Hydrogen Energy*, 43(20):9797–9802, may 2018.

[69] C. Rabissi, P. Gazdzicki, L. Guétaz, S. Escribano, L. Grahl-Madsen, A. Baricci, and A. Casalegno. A locally resolved investigation on direct methanol fuel cell uneven components fading: Steady state and degradation local analysis. *Journal of Power Sources*, 397(July):361–373, sep 2018.

[70] C. Rabissi, M. Zago, P. Gazdzicki, L. Guétaz, S. Escribano, L. Grahl-Madsen, and A. Casalegno. A locally resolved investigation on direct methanol fuel cell uneven components fading: Local cathode catalyst layer tuning for homogeneous operation and reduced degradation rate. *Journal of Power Sources*, 404(October):135–148, 2018.

[71] Erin L. Redmond, Brian P. Setzler, Faisal M. Alamgir, and Thomas F. Fuller. Elucidating the oxide growth mechanism on platinum at the cathode in PEM fuel cells. *Physical Chemistry Chemical Physics*, 16(11):5301, 2014.

[72] Carl A. Reiser, Lawrence Bregoli, Timothy W. Patterson, Jung S. Yi, J. Deliang Yang, Mike L. Perry, and Thomas D. Jarvi. A Reverse-Current Decay Mechanism for Fuel Cells. *Electrochemical and Solid-State Letters*, 8(6):A273, 2005.

[73] Tatyana V. Reshetenko and Jean St-Pierre. Separation Method for Oxygen Mass Transport Coefficient in Gas and Ionomer Phases in PEMFC GDE. *Journal of the Electrochemical Society*, 161(10):F1089–F1100, aug 2014.

[74] Cynthia A. Rice, Patrick Urchaga, Antonio O. Pistono, Bryce W. McFerrin, Benjamin T. McComb, and Jingwei Hu. Platinum Dissolution in Fuel Cell Electrodes: Enhanced Degradation from Surface Area Assessment in Automotive Accelerated Stress Tests. *Journal of The Electrochemical Society*, 162(10):F1175–F1180, 2015.

[75] Steven G. Rinaldo, Wendy Lee, Jürgen Stumper, and Michael Eikerling. Mechanistic Principles of Platinum Oxide Formation and Reduction. *Electrocatalysis*, 5(3):262–272, 2014.

[76] I A Schneider, D Kramer, A Wokaun, and G G Scherer. Oscillations in Gas Channels - II. Unraveling the Characteristics of the Low Frequency Loop in Air-Fed PEFC Impedance Spectra. *Journal of The Electrochemical Society*, 154(8):B770, 2007.

[77] I A Schneider and S von Dahlen. Start-Stop Phenomena in Channel and Land Areas of a Polymer Electrolyte Fuel Cell. *Electrochemical and Solid-State Letters*, 14(2):B30, 2011.

[78] Hendrik Schulenburg, Bernhard Schwanitz, Nicolas Linse, Günther G. Scherer, A. Wokaun, Julijana Krbanjevic, Roman Grothausmann, and Ingo Manke. 3D Imaging of Catalyst Support Corrosion in Polymer Electrolyte Fuel Cells. *The Journal of Physical Chemistry C*, 115(29):14236–14243, jul 2011.

[79] Tobias Schuler, Anamika Chowdhury, Anna T. Freiberg, Brian Sneed, Franz B. Spingler, Michael C. Tucker, Karren L. More, Clayton J. Radke, and Adam Z. Weber. Fuel-Cell Catalyst-Layer Resistance via Hydrogen Limiting-Current Measurements. *Journal of The Electrochemical Society*, 166(7):F3020–F3031, feb 2019.

[80] Vijay A. Sethuraman and John W. Weidner. Analysis of sulfur poisoning on a PEM fuel cell electrode. *Electrochimica Acta*, 55(20):5683–5694, aug 2010.

[81] Y. Shao-Horn, W. C. Sheng, S. Chen, P. J. Ferreira, E. F. Holby, and D. Morgan. Instability of supported platinum nanoparticles in low-temperature fuel cells. *Topics in Catalysis*, 46(3-4):285–305, 2007.

[82] Qiang Shen, Ming Hou, Dong Liang, Zhimin Zhou, Xiaojin Li, Zhigang Shao, and Baolian Yi. Study on the processes of start-up and shutdown in proton exchange membrane fuel cells. *Journal of Power Sources*, 189(2):1114–1119, apr 2009.

[83] Zyun Siroma, Naoko Fujiwara, Tsutomu Ioroi, Shin ichi Yamazaki, Hiroshi Senoh, Kazuaki Yasuda, and Kazumi Tanimoto. Transient phenomena in a PEMFC during the start-up of gas feeding observed with a 97-fold segmented cell. *Journal of Power Sources*, 172(1):155–162, 2007.

[84] Hao Tang, Zhigang Qi, Manikandan Ramani, and John F. Elter. PEM fuel cell cathode carbon corrosion due to the formation of air/fuel boundary at the anode. *Journal of Power Sources*, 158(2):1306–1312, aug 2006.

[85] Georgios Tsotridis, Alberto Pilenga, Giancarlo De Marco, and Thomas Malkow. *EU Harmonised Test Protocols for PEMFC MEA Testing in Single Cell Configuration for Automotive Applications; JRC Science for Policy report.* 2015.

[86] US Department of Energy (DOE). "Fuel Cells 2016 - Multiyear research, development, and demonstration plan," 2016. 2015:1–58, 2016.

[87] US Pat. 2005/0074649. Fuel Cell Voltage Control, 2005.

[88] S. Vengatesan, Michael W. Fowler, Xiao Zi Yuan, and Haijiang Wang. Diagnosis of MEA degradation under accelerated relative humidity cycling. *Journal of Power Sources*, 196(11):5045–5052, 2011.

[89] Jia X. Wang, Junliang Zhang, and Radoslav R. Adzic. Double-Trap Kinetic Equation for the Oxygen Reduction Reaction on Pt(111) in Acidic Media †. *The Journal of Physical Chemistry A*, 111(49):12702–12710, dec 2007.

[90] Xiaoping Wang, Romesh Kumar, and Deborah J. Myers. Effect of Voltage on Platinum Dissolution. *Electrochemical and Solid-State Letters*, 9(5):A225, 2006.

[91] Michael A. Yandrasits, Matthew J. Lindell, and Steven J. Hamrock. New directions in perfluoroalkyl sulfonic acid–based proton-exchange membranes. *Current Opinion in Electrochemistry*, 18:90–98, dec 2019.

[92] Wonseok Yoon and Adam Z. Weber. Modeling Low-Platinum-Loading Effects in Fuel-Cell Catalyst Layers. *Journal of The Electrochemical Society*, 158(8):B1007, 2011.

[93] A. P. Young, J. Stumper, and E. Gyenge. Characterizing the Structural Degradation in a PEMFC Cathode Catalyst Layer: Carbon Corrosion. *Journal of The Electrochemical Society*, 156(8):B913–B922, 2009.

[94] Haoran Yu, Andrea Baricci, Andrea Bisello, Andrea Casalegno, Laure Guetaz, Leonard Bonville, and Radenka Maric. Strategies to mitigate Pt dissolution in low Pt loading proton exchange membrane fuel cell: I. A gradient Pt particle size design. *Electrochimica Acta*, 247:1155–1168, 2017.

[95] Haoran Yu, Andrea Baricci, Andrea Bisello, Andrea Casalegno, Laure Guetaz, Leonard Bonville, and Radenka Maric. Strategies to mitigate Pt dissolution in low Pt loading proton exchange membrane fuel cell: I.

A gradient Pt particle size design. *Electrochimica Acta*, 247(860):1155–1168, sep 2017.

[96] P. T. Yu and F. T. Wagner. Procedures for shutting down fuel cell system by using air purge at low cell temperature., 2007.

[97] Yi Yu, Hui Li, Haijiang Wang, Xiao-Zi Yuan, Guangjin Wang, and Mu Pan. A review on performance degradation of proton exchange membrane fuel cells during startup and shutdown processes: Causes, consequences, and mitigation strategies. *Journal of Power Sources*, 205:10–23, may 2012.

[98] Jianlu Zhang, Huamin Zhang, Jinfeng Wu, and Jiujun Zhang. Chapter 3 - Techniques for PEM Fuel Cell Testing and Diagnosis. In Jianlu Zhang, Huamin Zhang, Jinfeng Wu, and Jiujun Zhang, editors, *Pem Fuel Cell Testing and Diagnosis*, pages 81–119. Elsevier, Amsterdam, 2013.

[99] Jianlu Zhang, Huamin Zhang, Jinfeng Wu, and Jiujun Zhang. Chapter 6 - Hydrogen Crossover. In Jianlu Zhang, Huamin Zhang, Jinfeng Wu, and Jiujun Zhang, editors, *Pem Fuel Cell Testing and Diagnosis*, pages 171–185. Elsevier, Amsterdam, 2013.

[100] Xu Zhang, Liejin Guo, and Hongtan Liu. Recovery mechanisms in proton exchange membrane fuel cells after accelerated stress tests. *Journal of Power Sources*, 296:327–334, nov 2015.

[101] Patrick Zihrul, Ingmar Hartung, Sebastian Kirsch, Gerold Huebner, Frédéric Hasché, Hubert A. Gasteiger, Frédéric Hasché, and Hubert A. Gasteiger. Voltage Cycling Induced Losses in Electrochemically Active Surface Area and in H 2 /Air-Performance of PEM Fuel Cells. *Journal of The Electrochemical Society*, 163(6):F492–F498, mar 2016.

Acknowledgement

First, I would like to thank my supervisors, Prof. Andrea Casalegno and Dr. Andrea Baricci, whose insight and knowledge into the subject matter steered me through this research.

Thanks to Dr. Matteo Zago and Dr. Claudio Rabissi for their collaborative effort during the years we spent together. The meetings and conversations were vital in inspiring me to think outside the box, and their personal support and encouragement was invaluable.

Furthermore, I would like to thank the rest of the research team: Elena, Mirko, Marco, Amedeo, Gabriele and the graduate students who followed me in these academic years: Marco, Giacomo, Alice, Jacopo and Giorgia. I simply could not have done this without you.

And my biggest thanks to my family and friends for all the unconditional support in this very intense adventure. A special thank you to Chiara, for all your love and patience.